CANADIAN THESES

THÈSES CANADIENNES

NOTICE

The quality of this microfiche is heavily dependent upon the quality of the original thesis submitted for microfilming. Every effort has been made to ensure the highest quality of reproduction possible.

If pages are missing, contact the university which granted the degree.

Some pages may have indistinct print especially if the original pages were typed with a poor typewriter ribbon or if the university sent us an inferior photocopy.

Previously copyrighted materials (journal articles, published tests, etc.) are not filmed.

Reproduction in full or in part of this film is governed by the Canadian Copyright Act, R.S.C. 1970, c. C-30.

AVIS

La qualité de cette microfiche dépend grandement de la qualité de la thèse soumise au microfilmage. Nous avons tout fait pour assurer une qualité supérieure de reproduction.

S'il manque des pages, veuillez communiquer avec l'université qui a conféré le grade.

La qualité d'impression de certaines pages peut laisser à désirer, surtout si les pages originales ont été dactylographiées à l'aide d'un ruban usé ou si l'université nous a fait parvenir une photocopie de qualité inférieure.

Les documents qui font déjà l'objet d'un droit d'auteur (articles de revue, examens publiés, etc.) ne sont pas microfilmés.

La reproduction, même partielle, de ce microfilm est soumise à la Loi canadienne sur le droit d'auteur, SRC 1970, c. C-30.

THIS DISSERTATION
HAS BEEN MICROFILMED
EXACTLY AS RECEIVED

LA THÈSE A ÉTÉ
MICROFILMÉE TELLE QUE
NOUS L'AVONS REÇUE

SOME PROPERTIES OF THE SEMIMAGNETIC SEMICONDUCTOR ALLOY $Cd_xZn_yMn_zTe$ $(x+y+z=1)$

by

TOM DONOFRIO

Thesis

presented to the University of Ottawa

in partial fulfillment of the

requirements for ~~the~~ degree of

Doctor of Philosophy

Department of Physics

Faculty of Science and Engineering

University of Ottawa

Ottawa, Ontario, 1986

ISBN 0-315-33310-3

UNIVERSITÉ D'OTTAWA
UNIVERSITY OF OTTAWA

ABSTRACT

Some of the crystallographic, optical and magnetic properties of the pseudo-ternary alloy system, $Cd_xZn_yMn_zTe$, $(x+y+z=1)$, have been investigated in this report. These alloys belong to the class of materials known as semimagnetic semiconductors, an intermediate type which lies between non-magnetic and magnetic semiconductors.

Samples with different compositions were produced and Debye-Scherrer x-ray photographs were used to determine the the lattice parameters for each. These values were plotted as a function of composition and thus the range of single phase solid solution was determined.

The direct energy gap was measured as a function of composition and temperature by wavelength modulated reflectance. A "blue shift" was observed at low temperature which increased with Mn concentration. The extra increase in the energy gap was estimated by extrapolating the high temperature behaviour. The results were then analyzed using an equation which depended on the magnetic transition temperatures, T_g.

Measurements of magnetic susceptibility were carried out using a SQUID magnetometer and the T_g values were determined as a function of composition. As well, values for the Curie-Weiss parameters, θ and C, were determined. Non Curie-Weiss behaviour was investigated and it was found that a

qualitative explanation based on superparamagnetism and isolated paramagnetic ions, could explain the results. A study of the exchange interaction using the T_g values, suggested that the magnetic spins were indirectly coupled to each other by a mechanism which involved a virtual transition between the valence band and a Mn 3d level. Predictions of the exchange energy, based on these results, agreed with those of other researchers. As well, predictions of the Curie-Weiss temperature, also agreed with the measured values obtained in this work.

The ESR linewidth was studied as a function of composition and temperature. An asymmetric broadening was observed at lower temperatures, the onset of which varied systematically with composition. The linewidth was observed to increase with decreasing temperature and became too large to measure at temperatures well above any magnetic transition point. The results were analyzed using a theory based on inhomogeneous broadening.

ACKNOWLEDGEMENTS

I would like to express my thanks to Dr. J.C. Woolley for his assistance throughout the course of this work and for his many unique insights; to Dr. G. Lamarche for his aid in the magnetic susceptibility measurements and for the many useful discussions with him; and to Dr. A. Manoogian for the discussions with him as well as his assistance on the ESR measurements.

I would also like to thank Samir Chehab and Miguel Quintero for the considerable number of beneficial discussions with them on many of the aspects of this work. As well I wish to thank Doug Beckett and Ziba Kamal for providing a few of the samples used in the measurements.

Finally, I would like to give special thanks to Jen Majid and Ricardo Brun Del Re, for producing a large fraction of the samples and to Bei Wah Chan for handling the technical aspects of the ESR measurements.

TABLE OF CONTENTS

List of Figures

List of Tables

CHAPTER 1

INTRODUCTION

In recent years, there has been considerable interest in a group of alloys which form an intermediate class of materials between non-magnetic and magnetic semiconductors. They have become known as either semimagnetic semiconductors, (SMSC), or as diluted magnetic semiconductors, (DMS). The first term was coined by Galazka, (4), while the second is a name suggested by Furdyna, (130). The greatest part of the work has been done on pseudo-binary alloy systems containing manganese such as

$$Cd_{1-z}Mn_zTe$$

$$Zn_{1-z}Mn_zTe$$

$$Cd_{1-z}Mn_zSe$$

$$Hg_{1-z}Mn_zTe$$

$$Hg_{1-z}Mn_zSe$$

with $0 \leq z \leq 1.0$. The electronic configuration of Mn includes five tightly bound and unpaired d-level electrons, ($3d^5$), which give the atom a net magnetic moment. In these systems, the cases when z=0 correspond to ordinary semiconductors with well known properties. The cases for which z=1.0, correspond to magnetic semiconductors with magnetic properties which are also well understood. Mixing these two types of materials results in a new kind of material, (80), with properties which are different from both.

The presence of localized moments in the semiconductor crystal leads to an interaction of these electrons with the band

electrons and with impurity electrons. This in turn leads to new effects in those measurements which depend on the splitting of these electronic levels in a magnetic field. The most dramatic of them being the observation of anomalously large magneto-optical phenomena such as giant Faraday rotation and Zeeman splitting of the electron bands in $Cd_{1-z}Mn_zTe$, (5, 131). The magnitude of these effects are between 100 and 1000 times larger than those associated with ordinary semiconductors, (80), and are affected by the intensity of the field as well as the temperature and composition. Thus the localized magnetic moments act as an amplifying mechanism for an applied magnetic field. In magnetic semiconductors, the strong interaction between the magnetic ions dominates over the response to a normal magnetic field such as that used in the examples mentioned above. Consequently, in order to overcome the internal field, a very strong external field would be necessary to control the magneto-optical behaviour. Another example of a large anomalous effect is observed in the transport properties of $Hg_{1-z}Mn_zTe$ crystals in a magnetic field, (132). In this case, the effect of the interaction between the localized electrons and the valence band leads to the observation of a giant negative magnetoresistance. A more complete discussion of this along with other unique electrical and optical properties of SMSC in a magnetic field, is contained in the text and references of several review articles, (4, 80, 130, 132-134), and will not be dealt with any further in this report.

The magnetic properties of these materials have also

provoked a great deal of interest. Over a certain range of temperature and composition, an interaction between magnetic moments causes the spins to become frozen into random orientations. This spin glass state was first observed in metallic alloys such as Au:Fe and Cu:Mn, (39), where in each case, the concentration of magnetic impurity is between one and ten percent. Since then, a large amount of effort has gone into trying to understand this behaviour using a variety of measurement techniques. A comprehensive overview of spin glasses is presented in the following review papers; references 39, 52, 66, and 135.

Briefly, the characteristic properties of spin glasses are, the observation of a cusp in the temperature dependent magnetic susceptibility, the lack of any feature corresponding to this cusp in the thermal dependence of the specific heat, and the existence of a time dependent remanent magnetization at temperatures below the cusp point. The sharpness of the susceptibility cusp implies that some form of phase transition is occurring at a well defined temperature. However, the existence of such a phase change is not verified by the specific heat measurements. In fact, it seems as though the various bulk properties of spin glass materials can be divided into two groups, those such as magnetic susceptibility, the hall effect and the Mossbauer effect, which show definite anomalies at the spin glass temperature, and those such as heat capacity, thermoelectric power and ESR linewidth, which do not. Thus, a good deal of effort has been applied to trying to determine the nature of the spin glass transition, (136).

Most of the theoretical and experimental work has been done on metallic alloys where the interaction between the localized spins occurs through the conduction electrons. This RKKY, (Ruderman, Kittel, Kasuya, Yosida), interaction is responsible for the spin glass state in these materials. The presence of these conduction electrons also adds their own effects to the measurement of the bulk properties. However, the opportunity to study spin glasses without such effects was introduced by de Seze, (23), when it was shown that spin glass behaviour could be exhibited by magnetic ions on a dilute face centered cubic, (FCC), lattice with only antiferromagnetic interaction. Some of the candidates for such materials with very small carrier concentrations are the pseudo-binary SMSC alloys, $Cd_{1-z}Mn_zTe$ and $Zn_{1-z}Mn_zTe$.

As indicated previously, most of the work on SMSC has been done on pseudo-binary alloys. This allows one to observe how the properties of the material change when the composition changes. However, because there is only one composition variable, all of these properties are inseparably coupled and so cannot be controlled independently of each other. This may be remedied somewhat by comparing two similar alloy systems such as $Cd_{1-z}Mn_zTe$ and $Cd_{1-z}Mn_zSe$. A better solution would be to provide a continuous change in composition between two such alloy systems as was done by Debska et al, (143), for the alloy system $Cd_xHg_yMn_zTe$, $(x+y+z=1)$. The work which is to be presented in this report is part of the work done by a research group working on SMSC alloys such as;

$Cd_xZn_yMn_zSe$	(ref. 92)
$Cd_{1-z}Mn_zTe_{1-y}Se_y$	(ref. 91)
$Cd_{2x}(CuIn)_yMn_{2z}Te_2$	(ref. 114)
$Cd_{2x}(AgIn)_yMn_{2z}Te_2$	(ref. 114)
$Zn_{2x}(CuIn)_yMn_{2z}Te_2$	(ref. 115)

In each of these cases, any two properties of the material can be controlled independently of each other.

In the present work, an investigation of some of the optical and magnetic properties of the pseudo-ternary alloy system, $Cd_xZn_yMn_zTe$, (with x+y+z=1), will be presented. The composition of this semimagnetic semiconductor may be represented by a triangle such as that illustrated in fig. 1.1. Each point in the triangle represents a particular value of x, y and z in triangular coordinates, and hence a particular composition. In this case, the left and right edges of the triangle represent the pseudo-binary SMSC alloys, $Cd_{1-z}Mn_zTe$ and $Zn_{1-z}Mn_zTe$, while the bottom edge represents the pseudo-binary semiconductor alloy $Cd_{1-y}Zn_yTe$. The corners of the triangle represent the pure compounds, MnTe, ZnTe, and CdTe. Any straight line drawn within the triangle which intersects the point where z=1.0, represents a particular y:x composition ratio. For $Cd_xZn_yMn_zTe$, each of these ratios is also a pseudo-binary alloy system. This feature will be used in the next chapter to determine the limits of solid solution.

The measurements which were carried out were as follows. First the variation of the lattice parameters with composition were measured. In doing so, the limits of solid solution were also

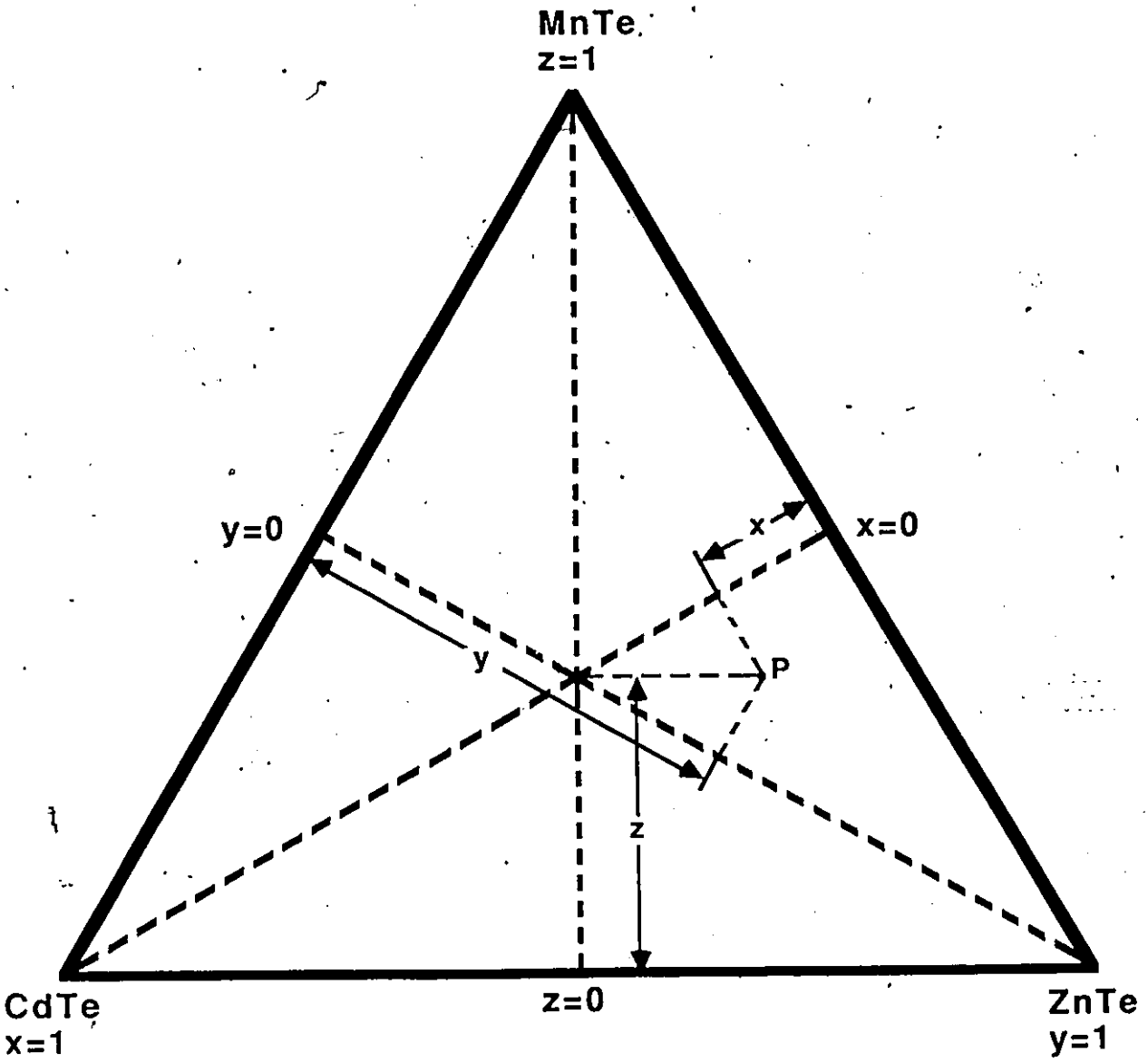

FIGURE 1.1 Triangular Coordinate System.
Any point 'P' in the diagram represents a sample of composition (x, y, z).

determined. Next, the variation of the energy gap was determined both as a function of composition and of temperature. Finally the magnetic susceptibility and ESR linewidth were measured also as a function of composition and temperature.

Polycrystalline samples were produced rather than the single crystals which other researchers, in this field, usually used. Since a large number of samples of different compositions were required, it was decided that growing single crystals for each one would be too time consuming. Comparisons of some of the results obtained in this work with those of other researchers, showed that in most of these cases, there was no significant difference between the results obtained from polycrystalline samples, and those obtained from single crystals. The sole exception of this was one aspect of the ESR measurements and will be discussed in chapter 5.

CHAPTER 2

X-RAY MEASUREMENTS

2.1 PREPARATION OF SAMPLES

To produce the polycrystalline samples, the appropriate amounts of each element were weighed out to an accuracy of approximately 0.2 mg., and melted in a quartz tube, which was sealed under vacuum. These tubes had an inner diameter of 0.5 cm with 0.1 cm walls. The lengths of the sealed tubes were generally between four and five cm. A total of half a gram of each sample was found to be enough, in most cases, for the various types of measurements that were to be made.

It was found that during the melting process, the material reacted with the quartz to such an extent that the tubes broke open and no sample could be obtained. To protect the samples from this reaction, the insides of the quartz tubes were covered with a layer of carbon. This was accomplished by the following process. A piece of absorbent paper, about two centimeters square, was folded and inserted into the end of a quartz tube whose other end had been previously sealed. The end of the tube with the absorbent paper, was then placed in a beaker full of acetone and left to soak. After a few minutes, the tube was removed and the sealed end heated over an open flame. When the concentration of acetone vapours inside the tube was high enough, a layer of red hot carbon would begin to collect at the hot end. Care was taken to keep the hot end from coming in contact with the acetone liquid. The soaking and heating processes were repeated until the carbon was thick

enough to make that end of the tube opaque under a strong light.

The melting temperatures of the various elements, and compounds which make up this system are listed in Table I, (43). Melting temperatures for various concentrations of the alloy system, $Cd_xZn_yMn_zTe$ are not expected to differ much from the range of values suggested by the binary compounds, CdTe, ZnTe and MnTe in the table. For the case of $Cd_{1-z}Mn_zTe$, Triboulet and Didier, (45), have determined that the melting temperature is lowered by no more than about 40°c when Mn is substituted for Cd in CdTe. These high melting points approached the highest temperature which could be attained by the melting furnace. Consequently, the samples would have to be held at this highest temperature for a period of time to allow any portion which had not melted to be completely dissolved.

The temperature of the melting furnace was between 1150 and 1200°c. To insure that uniform materials were produced, the samples were left at this temperature for 20 to 30 minutes. Subsequently, the quartz tubes containing the samples were transferred to another oven and left to anneal at 800°c for two weeks. The temperature controller kept the samples to within 25°c of this over the annealing period.

The above process usually yielded good solid samples, which could be sliced for modulated reflectance measurements. There were some problems with some of the samples from the Zn side of the pseudo-ternary diagram with high Mn concentrations, (fig. 2.1). In these cases, the reflectance signal due to the optical energy gap

	Melting Point (^{o}c)
Cd	450
Mn	1200
Te	600
Zn	500
CdTe	1098
ZnTe	1293
MnTe	1165

TABLE I Melting points of the elements and compounds of the $Cd_xZn_yMn_zTe$ alloy system, (ref. 43).

was too small to be detected except at the lowest temperatures. This failure to detect the energy gaps may be partly a result of the higher melting points required for these materials. Attempts were made to improve these samples by trying to reach as high a melting temperature as was possible and also, to use different annealing times and annealing temperatures, but these did not result in any improvement with the detection of the energy gap. The other sets of measurements, susceptibility and ESR were found to be successful for all cases.

For x-ray measurements, pieces from each sample were crushed to a fine powder. The colour of this powder was black for most compositions. However, when ZnTe dominated the alloy, the powder was reddish in appearance. Most of the samples were in good equilibrium. The exceptions were those with high Mn concentrations, (greater than 70%). Diffraction lines observed in the Debye Scherrer x-ray powder photographs of these samples, showed a blurring and faintness which was not present in the alloys with smaller concentrations of Mn. This blurring was not serious enough to prevent measurements of the positions of the lines from being carried out. It is likely that a better state of equilibrium could be attained by annealing under different conditions.

2.2 RESULTS OF X-RAY ANALYSIS

The range of sample composition which was studied is shown in fig. 2.1. In general, the compositions were chosen so that properties along lines of constant z and along lines of constant x:y ratio could be studied. Two regions, with different crystal behaviours were observed, in the ternary phase diagram. The broken line, in fig. 2.1, represents the boundary between the two regions. Samples which lie below this line were found to have a zinc blende structure, fig 2.2. In this structure the anions, which in this case happen to be Te, lie on the sites of face centered cubic sublattice. The cations, which are a mixture of Cd, Zn and Mn, lie on the sites of a different FCC sublattice. A translation of a quarter body diagonal separates the two sublattices. The cations and anions are tetrahedrally bonded to each other in this diamond like structure. Above the broken line in fig. 2.1, the samples were found to consist of two phases, a zinc blende phase and an hexagonal nickel arsenide phase.

The x-ray diagrams of some of the two phase samples were measured, but only to determine the limits of solid solution. This will be described fully, later in this section. All of the other types of measurements were performed only on samples which lay in the single phase region.

Lattice parameters were determined from the x-ray powder photographs by making use of the Bragg condition for diffraction, which, for a general cubic structure, may be expressed as follows, (31);

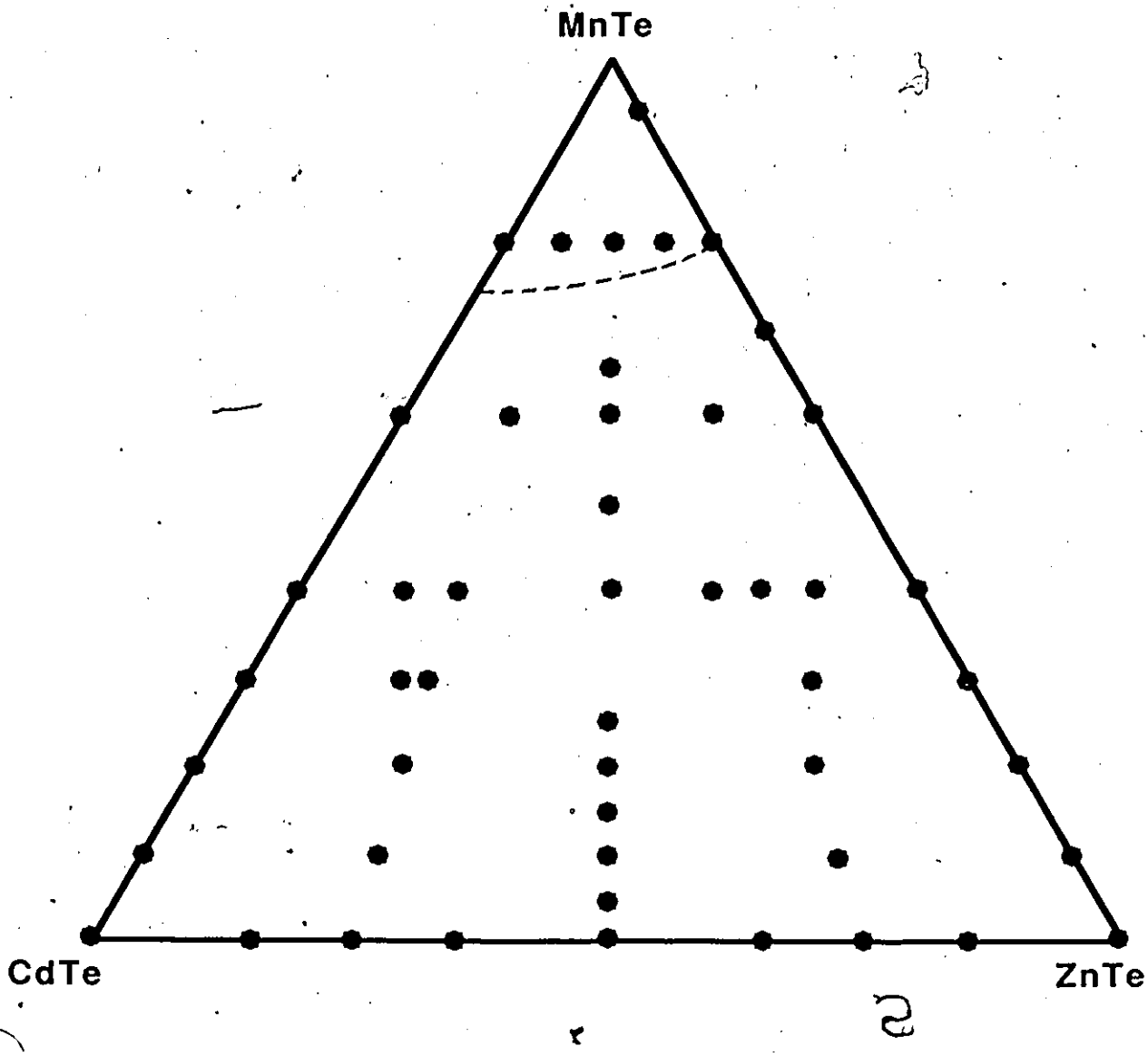

FIGURE 2.1 Samples studied by powder x-ray photographs. The curved line at the top of the diagram represents the limits of solid solution.

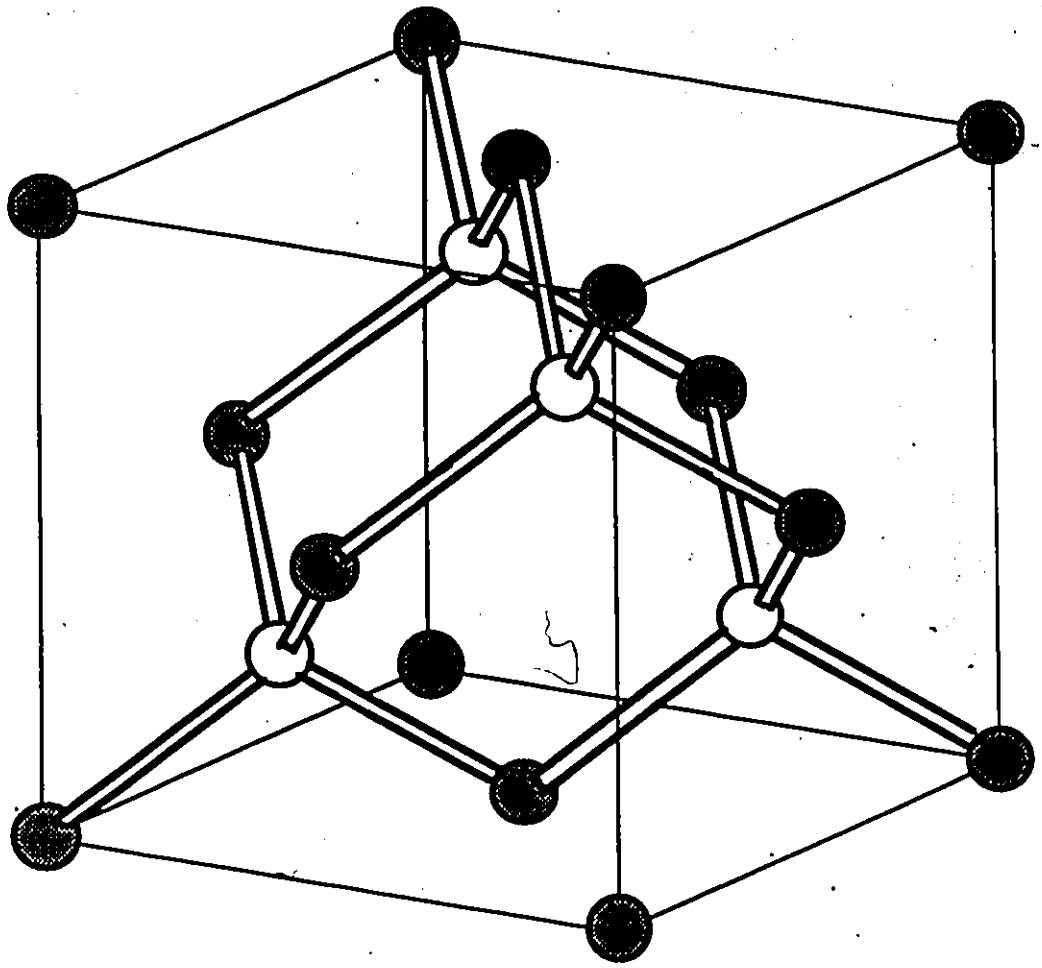

FIGURE 2.2 Zinc Blende Structure

$$a^2 = \frac{N \lambda^2}{4 \sin^2\theta} \qquad (2.1)$$

where "a" is the lattice parameter, λ is the x-ray wavelength, and θ is the Bragg angle. N is an integer and is equal to $(h^2+k^2+l^2)$, where h, k and l are the Miller indices for the scattering planes. In a simple cubic lattice, all possible combinations of h, k and l are allowed, but for a face centered cubic lattice, systematic absences will appear in the sequence of values of N. Lines for which h, k and l are neither all odd nor all even will not occur, (31). Furthermore, the reduction in symmetry of a zinc blende lattice as compared to an FCC lattice causes some of these lines to become quite faint. This results in the following sequence of values of N; 3, 8, 11, 16, etc., each representing a strong line in the x-ray diffraction pattern, (32). Each successive value is obtained by alternately adding three or five to the preceding value. For a given x-ray wavelength, the maximum value of N depends upon the lattice parameter. In the present case, the largest value of N turned out to be 59. The wavelength used in all x-ray photographs was 0.15405nm.

Due to absorption effects, the values of "a" obtained from equation 2.1 after measuring θ, tended to increase as N increased. This absorption disappears at $\theta = 90^{\circ}$. The Nelson-Riley extrapolation method, (1), was used to predict what value "a" would have at $\theta = 90^{\circ}$. Values of "a" were plotted against a function $f(\theta)$;

$$f(\theta) = \frac{1}{2}\left\{\frac{\cos^2\theta}{\sin\theta} + \frac{\cos^2\theta}{\theta}\right\} \qquad (2.2)$$

The straight line intercept on the "a" axis, where $\theta = 90^{\circ}$, gives the value of the lattice parameter.

The lattice parameter results are shown in figs. 2.3 and 2.4. First of all, fig. 2.3, in which the variation of "a" with y for constant z was plotted, shows that the variation is linear, in agreement with Vegard's law, (113). These lines of "a" vs. y turn out to be parallel to each other, within experimental limits. The broken line on the graph is drawn so as to intersect all the lines at the points where x=0. This line can be extrapolated to y=0, the lattice parameter of MnTe in the zinc blende phase.

Looking now at fig. 2.4, the results for five different x:y ratios are shown. They also turned out to be straight lines, again within experimental limits and therefore in agreement with Vegard's law, (113). But in this case, the lines extrapolate to a single point at $z=1_c$. This would also be the lattice parameter of MnTe in the zinc blende phase and is comparable to the value obtained in fig. 2.3. The error bars for each point were estimated from uncertainties in composition which were derived from the error in weighing the correct mass of the constituent elements, mentioned at the beginning of this chapter.

Since MnTe has an hexagonal nickel arsenide structure the extrapolated point represents a fictitious value. However such a value can be useful when investigating other alloy systems derived from MnTe which also have a zinc blende phase. Examples of such

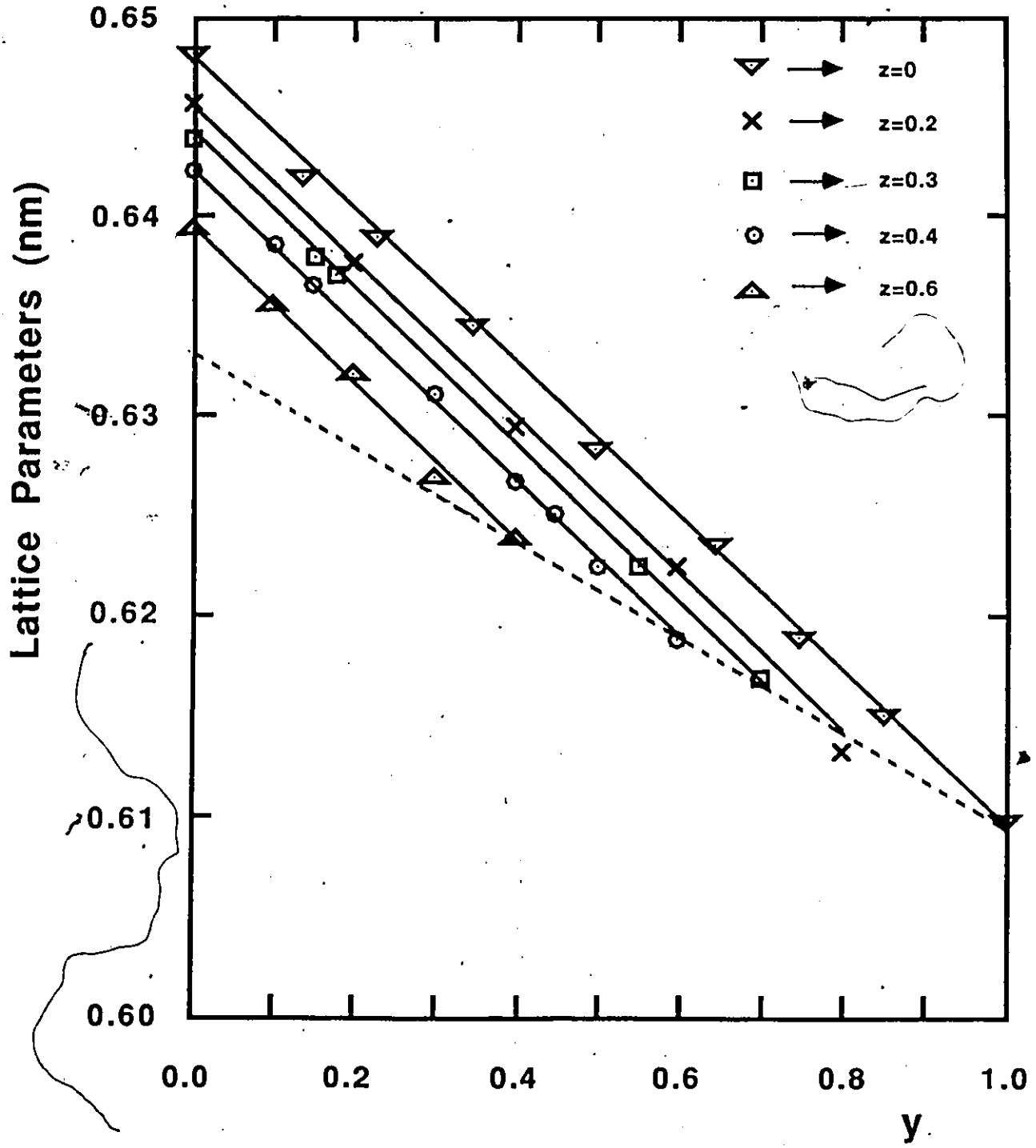

FIGURE 2.3 Lattice parameter as a function of y. The solid lines were fitted using the polynomial equation. The broken line represents the x=0 edge.

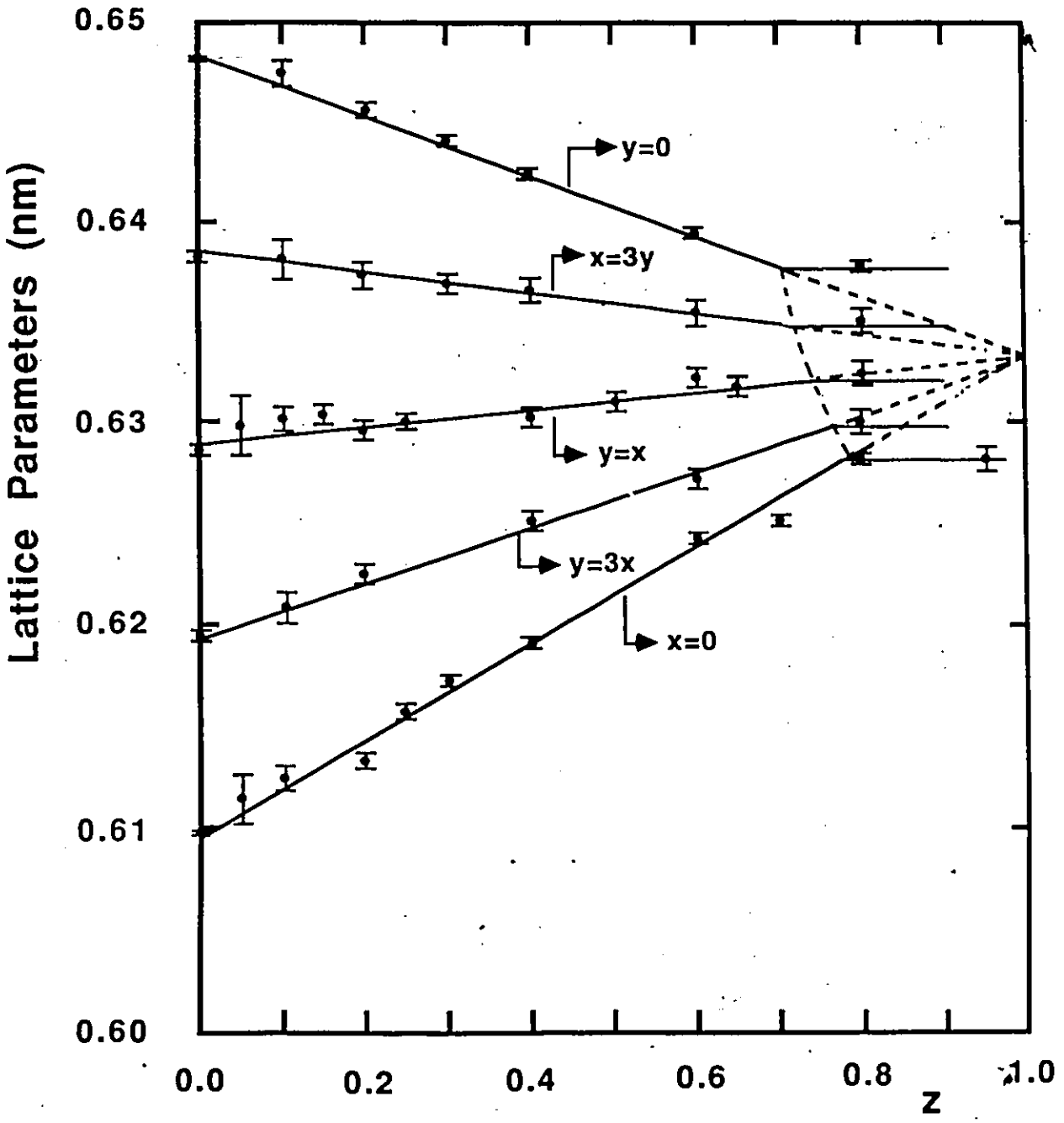

FIGURE 2.4 Lattice parameter as a function of z. The solid lines were fitted using the polynomial equation. The broken lines represent the two phase region.

alloys include systems investigated by other members of this research group such as $Cd_{2x}(CuIn)_yMn_{2z}Te_2$ and $Cd_{2x}(AgIn)_yMn_{2z}Te_2$, (114) as well as $Zn_{2x}(CuIn)_yMn_{2z}Te_2$, (115). In these cases, an extrapolation of the lattice parameter in the zinc blende phase to z=1.0, should coincide with the value obtained in figs. 2.3 and 2.4.

The x-ray diagrams of the two phase samples contain many lines in addition to the zinc blende lines, fig. 2.3(b). These extra lines belong to the hexagonal structure of MnTe. An x-ray picture of MnTe was taken to be used as a comparison in order to confirm this. The two phase region of the composition diagram consists of a MnTe phase and a $Cd_xZn_yMn_zTe$ phase. Since the alloy system is a pseudo-ternary, the boundary between the single phase and two phase regions may be determined from these two phase samples.

Consider the quaternary alloy system made up Cd, Zn, Mn and Te. The system being investigated represents the special case for which the molar concentration of Te atoms is equal to the combined molar concentrations of the other elements. To be considered a pseudo-ternary, such a system must have all of its phases satisfy this last condition. A violation of this might occur in a multi-phase concentration range by one or more of the phases.

To explain this further, take the example of a simple binary system, A_xB_{1-x}. If a two phase region existed for say x between 0.4 and 0.7, then the two phases would consist of $A_{0.4}B_{0.6}$ and $A_{0.7}B_{0.3}$ which are the compositions of the extremities of the

miscibility region. A change in x within this region results only in changing the relative concentrations of the two constituents without changing their compositions. An example of a pseudo-binary might be the $A_xB_{1-x}C$ system, which is a section of a ternary diagram for which the concentration of one of the elements, C, is constant, (fig. 2.5). In order for it to be classified as a pseudo-binary, the phase relationship between the two phases are the same as they would be with an ordinary binary diagram. So all phases in the pseudo-binary must lie on the line drawn in fig. 2.5. If this last condition is not obeyed, then the system cannot be considered a pseudo-binary.

In the present case the limit of solid solution for y=0 occurs at z=0.72. Since this section is a pseudo-binary, the zinc blende phase within the two phase region, retains the composition which it possessed at the phase boundary no matter what the initial amount of Mn. This is represented by the sudden leveling off at the phase boundary of the lattice parameters in fig. 2.4. The same result occurs for the other lines in the diagram. Since the composition of the zinc blende phase remains constant for a particular x:y ratio, the value of the lattice parameter will remain constant and equal to the lattice parameter of the last single phase material on that line. Hence the position of the horizontal lines in the figure, can be determined by measuring the lattice parameters of the zinc blende phases of various two phase samples. This in turn will give the position of the boundary between the single phase and two phase regions by extrapolating

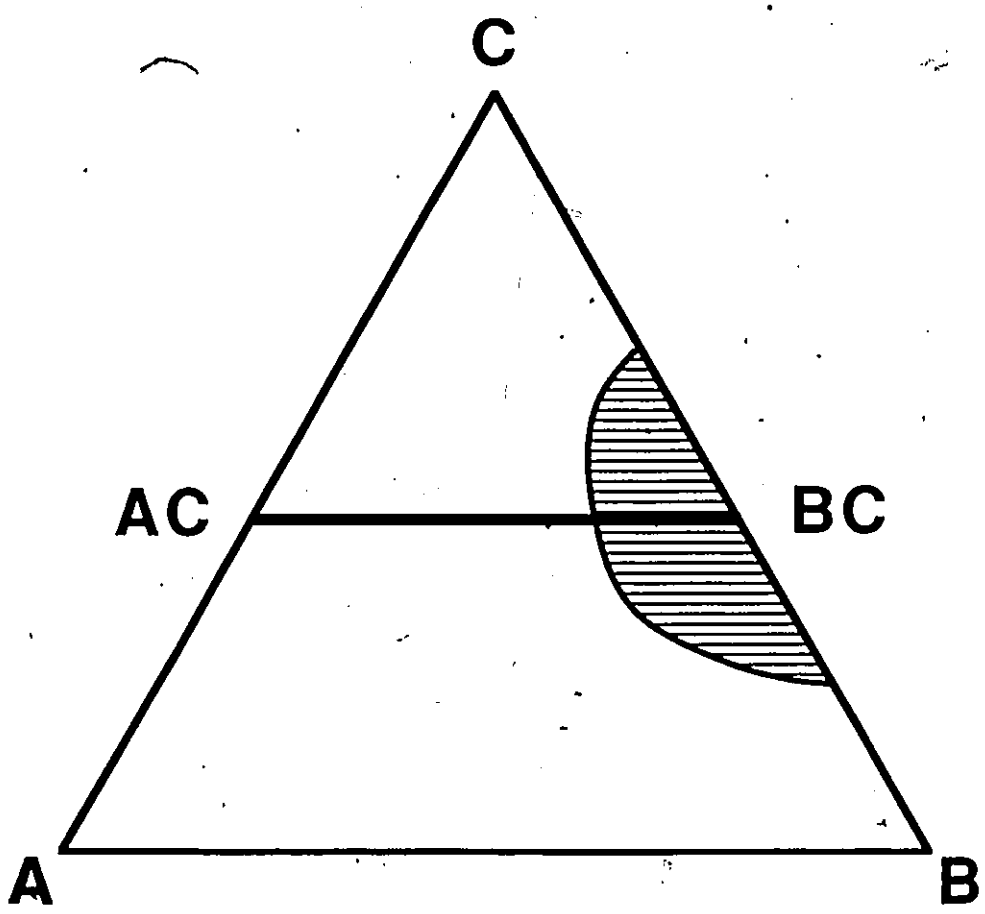

FIGURE 2.5 An example of the relation between a pseudo-binary and a ternary system. The triangle represents the ternary system $A_xB_yC_{1-x-y}$. The heavy line represents the pseudo-binary system $A_xB_{1-x}C$.

back to intersect with the original fitted lines. The boundary is represented, in the figure, by the broken curve crossing the juncture of the fitted lines and the horizontal lines.

The results obtained in this work for the solid solution phase diagram of the $Cd_{1-z}Mn_zTe$ system agree with that of the previous work on these materials by Triboulet and Didier, (45). As well, values of the lattice parameter for this edge agree with those reported by Galazka, (2). The results of Furdyna et al., (137), for $Zn_{1-z}Mn_zTe$ alloys also agree with those obtained here.

2.3 FIT TO X-RAY DATA

To draw lines of constant "a", the data may be fitted to an equation which is a function of the composition. The equation is derived from a general power series. The linear variations of the lattice parameter, discussed above, will alone reduce the power series to an equation containing only linear terms;

$$a = A + B\,y + C\,z + D\,x$$

This can be further reduced to;

$$a = A + B\,y + C\,z \qquad (2.3)$$

by the relation, $x + y + z = 1$.

In addition to determining the lines of constant "a", the collected data may be used to test the interpolation equations proposed by Williams et al., (3) for a pseudo-ternary system. These equations allow one to predict the values of lattice parameter for the interior of the composition triangle using only the data from the edges. The same procedure was also used with the

room temperature energy gap results to be presented in chapter 3.

In the method proposed by Williams et al, complete solid solution is assumed so that any given parameter will vary smoothly with composition. The lattice parameters are then linearly interpolated from the following binary equations;

$$\begin{aligned} T_{12}(x) &= xB_2 + (1-x)B_1 \\ T_{23}(y) &= yB_3 + (1-y)B_2 \\ T_{31}(z) &= zB_1 + (1-z)B_3 \end{aligned} \tag{2.4}$$

which represent the variation in lattice parameter for the following pseudo-binary systems;

$$Cd_{1-x}Zn_xTe$$
$$Mn_{1-y}Zn_yTe$$
$$Cd_{1-z}Mn_zTe$$

The value of the parameter for the pure compounds, (the corners of the composition triangle of fig. 2.1) are represented by B_1, B_2 and B_3 in equation 2.4. For any point in the system, the value of the lattice parameter may be written as;

$$Q(x\ y\ z) = \frac{xy\ T_{12}(u) + yz\ T_{23}(v) + zx\ T_{31}(w)}{x\ y + y\ z + z\ x} \tag{2.5}$$

where u, v and w are determined by;

$$\begin{aligned} u &= (1-x+y)/2 \\ v &= (1-y+z)/2 \\ w &= (1-z+x)/2 \end{aligned} \tag{2.6}$$

The exact origin of this equation is not explained by Williams et al.

If equations (2.4) and (2.6) are substituted into equation

(2.5), then the expression is reduced to equation (2.3) with the constants in the equations related as follows;

$$B_1 = A$$
$$B_2 = A + B$$
$$B_3 = A + C$$

So in this case there is no distinction between the two methods of determining the lines of constant lattice parameter. A least squares fit of equation (2.3) to 47 data points gives the following result;

$$a = 0.6483 - 0.0388y - 0.0150z \text{ nm} \qquad (2.7)$$

The lines shown in figs. 2.3 and 2.4 are fitted from this equation. The broken lines in both diagrams represent extrapolations to the expected value of the lattice parameter of MnTe if it existed with the zinc blende structure. The standard deviation of the experimental points from this equation was calculated to be 0.0005 nm.

A test of the "goodness" of the fit was done using the reduced chi-squared function, (104), which is defined as follows;

$$\chi^2_\upsilon = \frac{1}{\upsilon}\sum \frac{(y_i - y(x_i))^2}{\sigma_i^2} \qquad (2.8)$$

In this equation, the measured values are represents by x_i and y_i while the fitting function is represented by $y(x_i)$. The number of degrees of freedom, υ, is given by $\upsilon = N-n-1$ where N is the number of sets of values and n is the number of constants in the fitting equation. The uncertainty for each set of data is taken into account by σ_i. The sum is taken over the complete

set of data points. In simple terms, eq. 2.8 represents a ratio of the deviation of the experimental values, from what is predicted, to the experimental uncertainty in determining these points. A value of χ^2_υ close to 1.0 is indicative of a good fit while a value much greater than this would suggest that the fitting equation does not describe the data very well and so may not be valid.

Using the uncertainty stated at the beginning of section 2.1, which is due only to errors in weighing out the correct amounts of each element, the value of the reduced χ^2 was calculated to be approximately 1.01. This not only indicates that eq. 2.3 is valid for this data, but also that most of the error in figs. 2.3 and 2.4 are due to the reason cited earlier. With the validity of eq. 2.7 established, values of constant "a" could be calculated. These were plotted in fig. 2.6.

The results obtained in this section show that there is a large variation in the lattice parameter when y is varied while holding the Mn fraction constant. This feature will be used to study the effects on the magnetic properties, of changing the separation between magnetic ions.

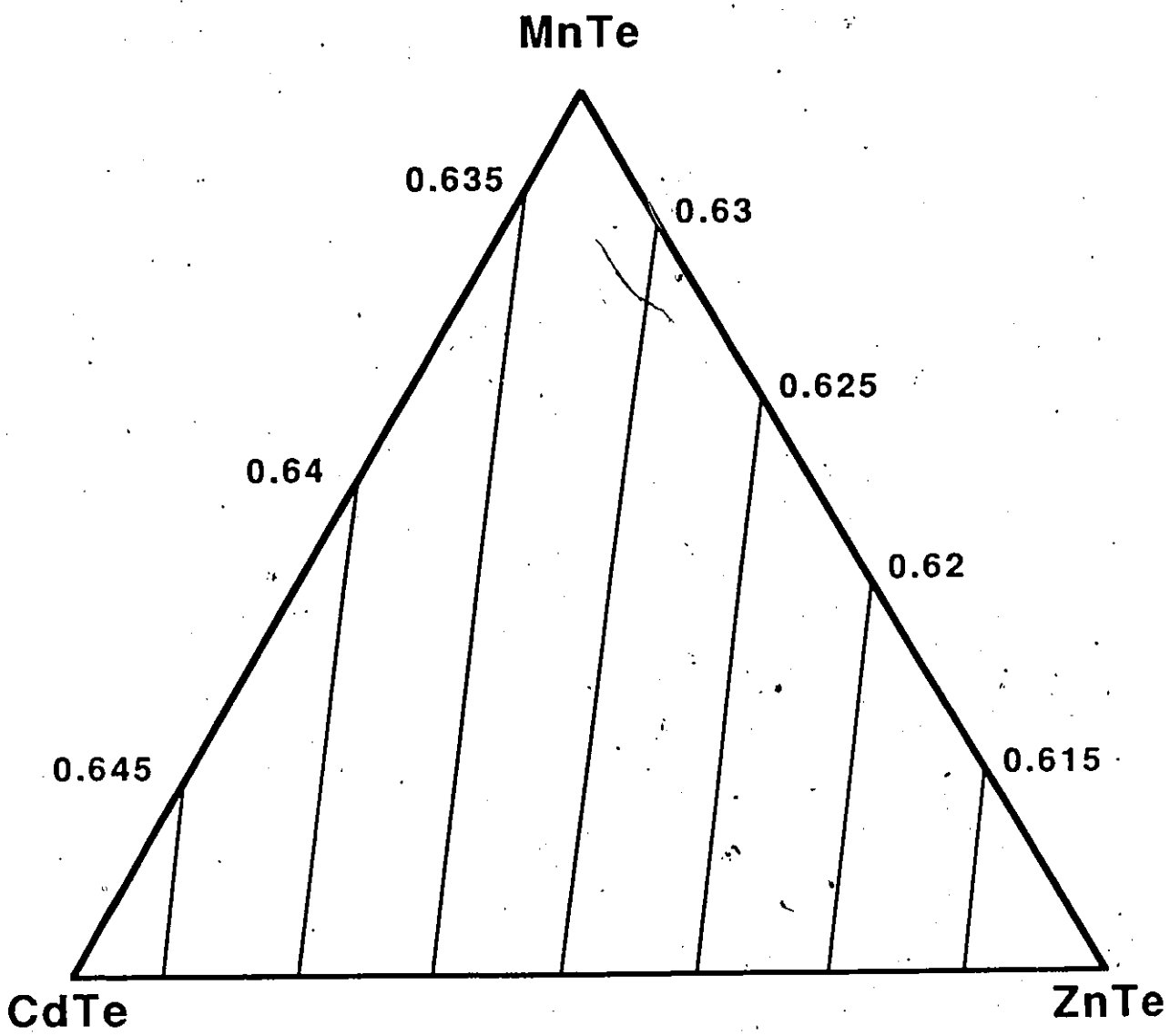

FIGURE 2.6 Values of Constant Lattice Parameter. The values indicated are in units of nanometers.

CHAPTER 3

ENERGY GAP MEASUREMENTS

3.1 INTRODUCTION

Once the phase diagram was established, other properties of $Cd_xZn_yMn_zTe$, in the range of solid solution, could be investigated. In this chapter, measurements of the direct energy gap as a function of temperature and composition will be presented.

The form of the band structure in this material, (fig. 3.1), is typical of substances with a diamond like or adamantine structure. The principal band gap is situated at the center of the brillouin zone, (9-13), with an s-like conduction band and a p-like valence band. The valence band is split by spin-orbit coupling at k=0. For CdTe and ZnTe the energy gap is direct, consequently the lowest minimum of the conduction band occurs at k=0. With Mn added to the alloy, measurements of absorption, (117), and reflectance, (108), have indicated that the band gap remains direct. There is also no evidence of a major change in the band structure such as the metal-semiconductor transition observed in $Hg_{1-z}Mn_zTe$, (132).

The simplest method of measuring the energy gap of a sample is to measure its absorption spectrum. Limitations in this technique usually arise from the inability of some materials to transmit enough light to be measurable, unless the sample is polished down to an extremely small thickness. This was not a problem in the present case. This material proved to be quite transparent since transmission of light could be detected from

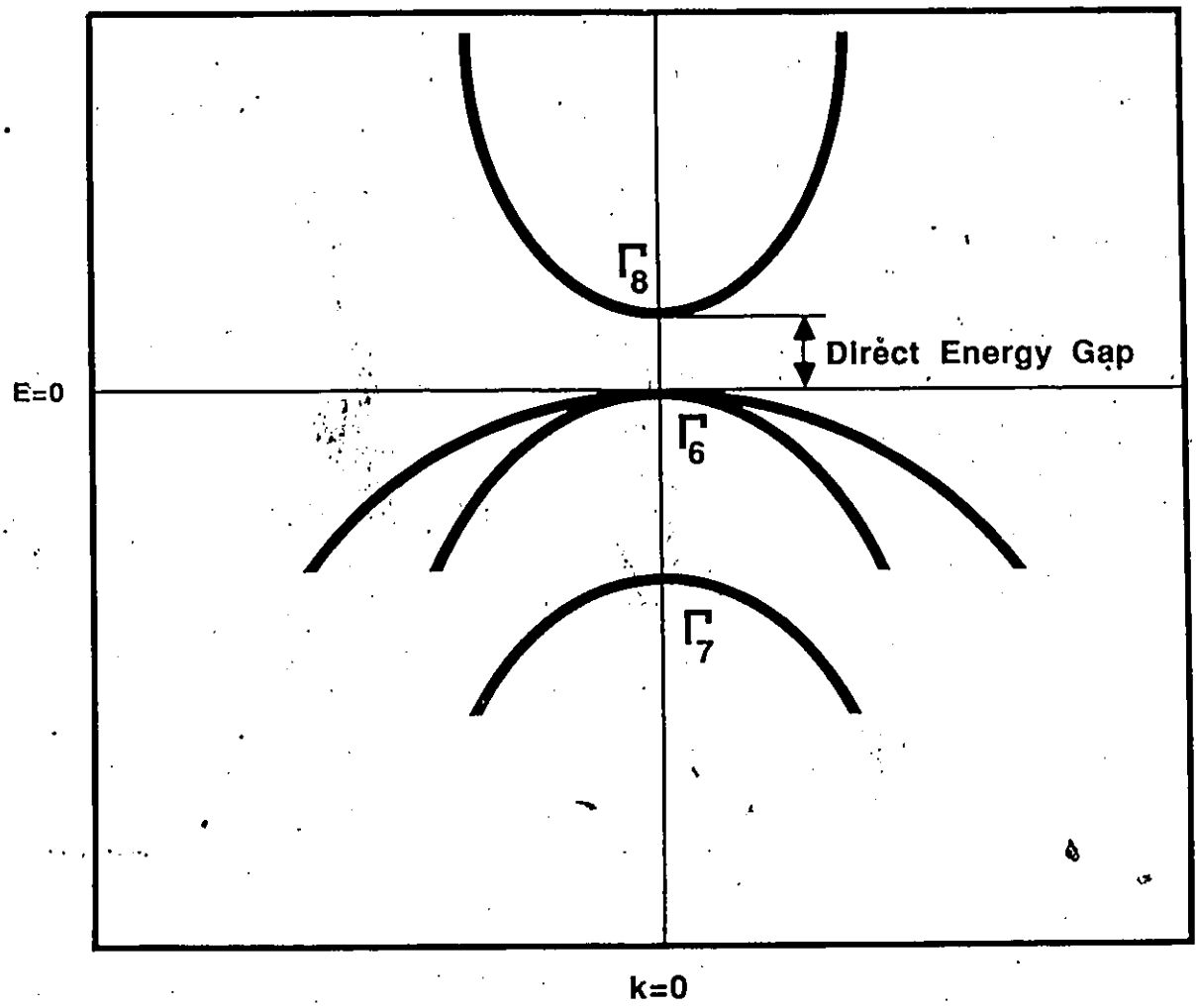

FIGURE 3.1 Band structure at the center of the Brillouin zone.

samples whose thickness was as large as several tenths of a millimeter. However, the usefulness of absorption was severely limited by another factor. It became impossible to observe the energy gap when it became larger than a certain value. This effect had already been observed in the $Cd_{1-z}Mn_zTe$ system, (30). The edge was observed to increase linearly with Mn concentration until it became "pinned" at a value of approximately 2.05eV. Although the precise mechanism for this effect has yet to be identified, suggestions have been made which attribute it to transitions between localized Mn levels, (30, 138). An alternate proposal has been introduced by Abreu et al, (8). This involves a transition from the valence band to a Mn level which appears at a lower energy than the conduction band in the samples with higher Mn concentrations. A third group of researchers, (117), relate this effect to defect levels. Recently, absorption measurements have been carried out by Amrani et al., (116), on samples which have been polished down to a thickness of about two microns. Both the energy gap and the so called manganese transition were observed at high Mn concentrations. Unfortunately, very high quality samples would be needed to duplicate this achievement. It would have been impossible to polish the polycrystalline samples down to the same thickness.

Since a large majority of the samples would have had energy gaps which would have caused the absorption edge to be pinned, a different approach was necessary. For this reason, reflectance was used to determine the gaps.

3.2 WAVELENGTH MODULATED REFLECTANCE

The dielectric function, ϵ, describes the electronic state of a solid, thus, the response of crystal to an electromagnetic field can be understood in terms of it. Since both the absorption spectra and the reflection spectra can be related to ϵ, (15), then they may be used as tools in evaluating the band structure of a semiconductor.

The condition for absorption in a semiconductor is;

$$E_c - E_v \geq \hbar\omega$$

where E_c and E_v, are the energies of the conduction and valence bands. At the threshold of absorption, where only the equality holds, the reflection becomes a maximum. In fact, the reflectance becomes a maximum at all critical points in the band structure for which;

$$\nabla_k(E_c(k) - E_v(k)) = 0 \quad \text{and} \quad E_c - E_v = \hbar\omega$$

or, in other words, for which the conduction band is parallel to the valence band in k-space, (14).

In order to determine experimentally the reflectance, R, of a sample as a function of incident photon energy, the intensity of reflected light, I, is measured. These two quantities are related by the following; $I = R\ I_o$, where I_o is the intensity of the incident light. However, the peaks of the reflectance spectra are not very strong in most cases. This may make it difficult to observe a structure which is related to an optical transition, as well as determining accurately the energies of the transitions once they are identified. One remedy for this is to use a modulation

technique. In such a procedure, some property of the sample, which affects the energy gap is varied cyclically. The result of this is that the derivative of the peak is measured. Examples of this are electroreflectance and stress modulation, (46, 47).

Another way in which this may be accomplished is by using wavelength modulated reflectance where the derivative with respect to λ is carried out directly. If the derivative of $I=RI_o$ is taken with respect to wavelength, one obtains;

$$\frac{dI}{d\lambda} = R\frac{dI_o}{d\lambda} + I_o\frac{dR}{d\lambda} \qquad (3.1)$$

The quantity we want to investigate is $dR/d\lambda$. The quantity which can be measured, however, is $dI/d\lambda$. This can present a problem in that the term, $dI_o/d\lambda$ may be much stronger than the $dR/d\lambda$ term. Not only that, the two terms are also multiplied by R and I_o, respectively. For the moment let us assume that these last two quantities are constant in comparison to their derivatives. The first term on the right hand side depends on the spectral response of the incident light. Ideally, I_o, should be flat in terms of its response to changes in wavelengths. This of course is not possible. It depends greatly on the characteristics of the light source and the diffraction grating used in the monochromator, as well as, (to a lesser degree), any mirrors used to focus the light in various parts of the system. Basically, any significant change in the response of these elements will give enormous derivative curves that may virtually wipe out any trace of the wanted signal in that particular region of the spectrum.

The usual way to get around this is to split the incident light into two beams. One of the beams will be reflected by the sample as usual, while the other is measured directly, (48). The latter signal should contain only the $dI_o/d\lambda$ term, while the former would contain both. The two signals are then subtracted using some kind of feedback arrangement in order to keep the two $dI_o/d\lambda$ terms at the same amplitudes. However, in order to be able to accomplish this, the two detectors used, must have identical responses. If they don't, the two $dI_o/d\lambda$ terms will be different and so will not subtract properly.

In the case of $Cd_xZn_yMn_zTe$, the signal was strong enough to be seen in most regions of the spectrum without any subtraction. When it did become necessary, a separate measurement of $dI_o/d\lambda$ was performed by substituting a small mirror for the sample.

It should be mentioned that the method described here is different from the normal procedure of measuring $1/R\ dR/d\lambda$ which is obtained by further dividing the output by the D.C. part of the signal. However, it was found that in using the simpler method, the values obtained for the energy gaps did not differ significantly from those of other researchers, (106, 108, 116, 139), using different types of measurements.

3.3 APPARATUS USED FOR ENERGY GAP MEASUREMENTS

3.3.1 WAVELENGTH MODULATED REFLECTANCE

Monochromatic light from a monochromater was used as the incident light, I_o. In order to measure the derivative of the reflectance, this light may be modulated by a small amount $\Delta\lambda$, in wavelength. If this is done, then this small modulation, continuously sweeps out a small portion of the reflectance curve, (see fig. 3.2). When $\Delta\lambda$ is small enough, it will approximately measure the slope of the curve at the point P, which is proportional to the derivative at that point.

A schematic diagram of the experimental setup is shown in fig. 3.3. The light from the source is focused on a slit whose aperture is set at 1.0mm. From there, it is reflected on to a grating and then usually would be reflected on to the exit slit. But instead, it is directed on to a mirror, which can be continuously oscillated through a small angle. This is where the wavelength modulation takes place.

A small motor controls the oscillation frequency of the mirror. With the frequency of oscillation set to zero, the light reflecting off the mirror is directed on to the exit slit. Since the light has been split into its different components by the grating, there is a spatial distribution in wavelength along the wall around the exit slit. So only the wavelength that happens to be directly incident on the slit is permitted through. The angle of the diffraction grating determines what this wavelength is. With the oscillating motor on, the mirror vibrates back and forth,

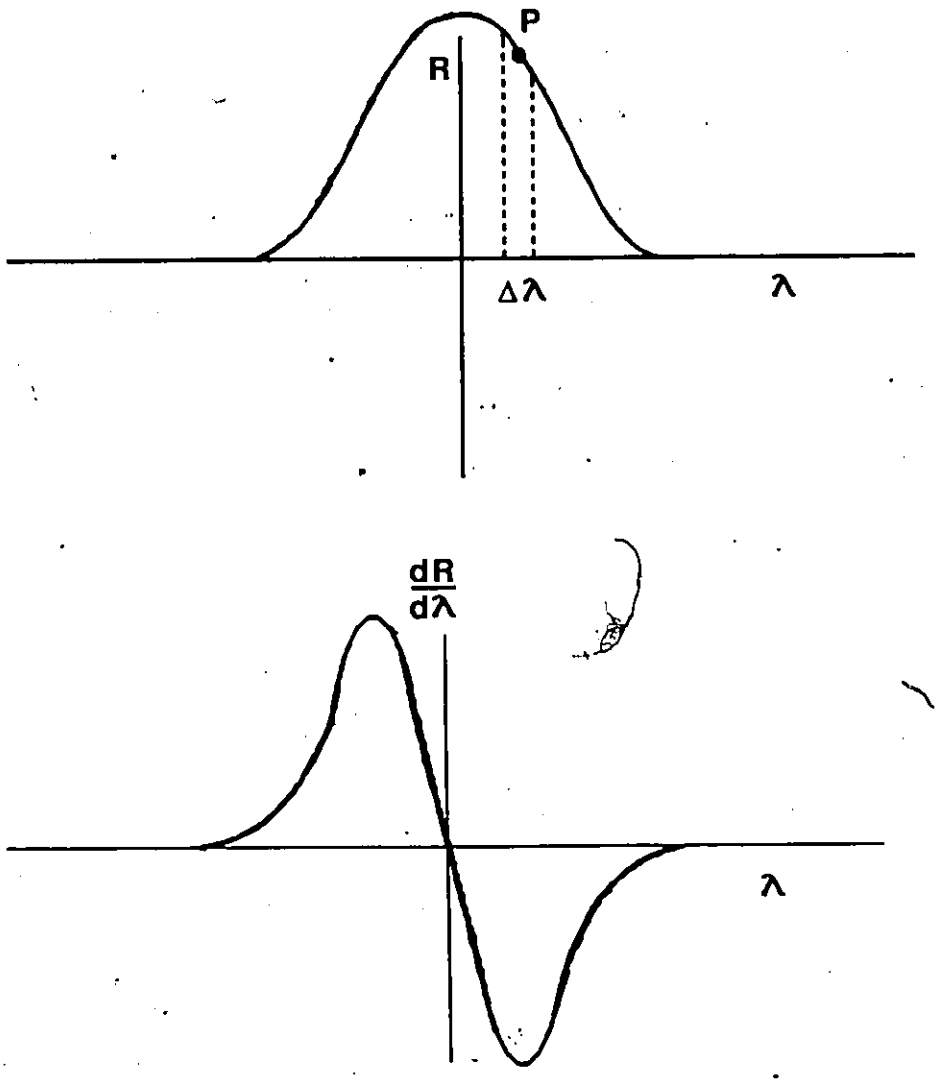

FIGURE 3.2 Derivative of a Reflectance Maxima

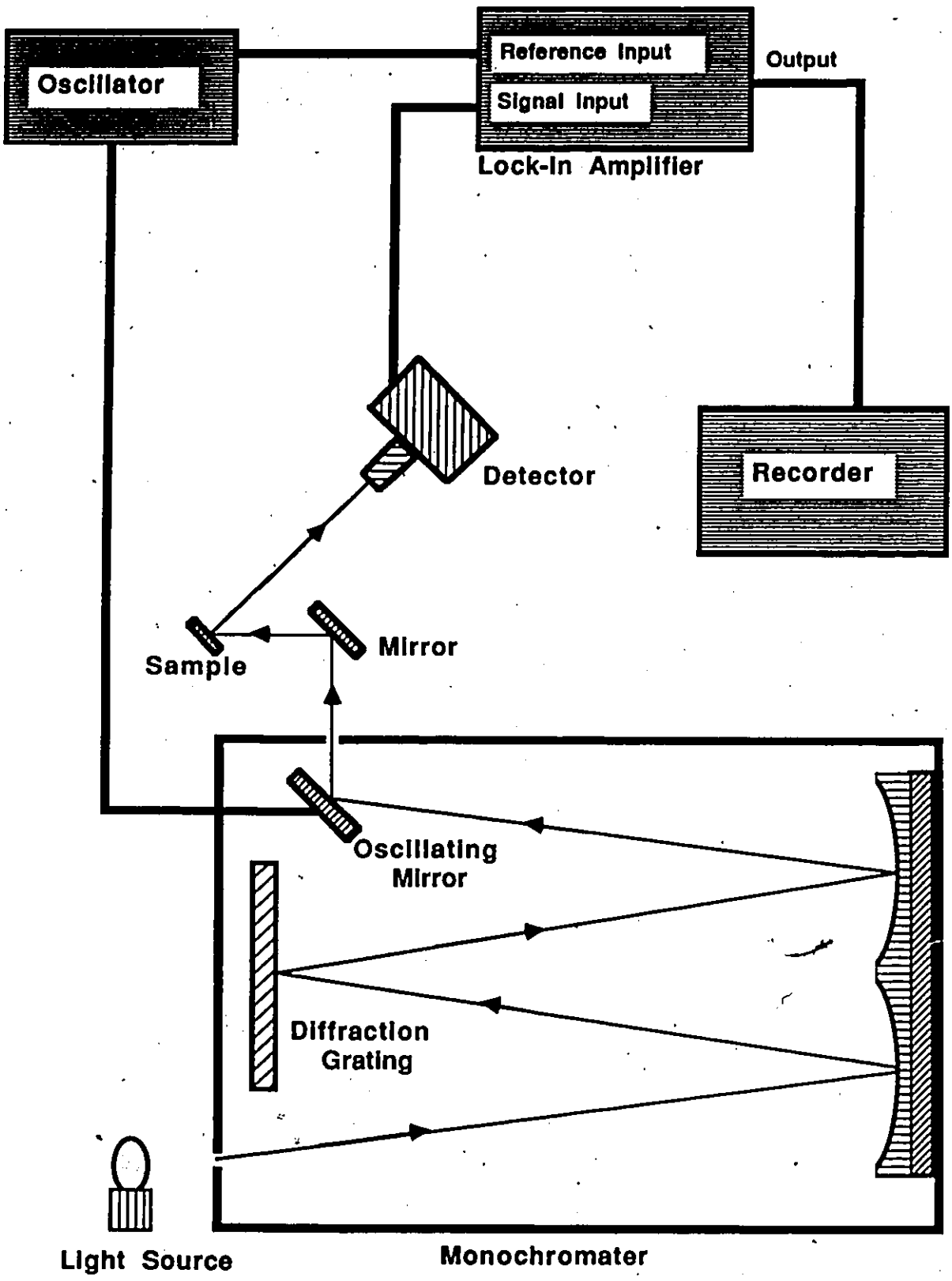

FIG. 3.3 Modulated Reflectance Apparatus.

shifting the entire spectrum on the exit wall back and forth, which in turn shifts the wavelength of the admitted light by a small amount $\Delta\lambda$.

The modulated "monochromatic" light is then focused on to a sample, with the reflected light measured by a photomultiplier. Two different photomultipliers were used. An RCA 4832 was used for most of the preliminary room temperature measurements. Later a more sensitive 1P28 photomultiplier was used in measurements done as a function of temperature. The photomultiplier signal was fed into a lock-in amplifier which was locked on to the oscillation frequency of the mirror. In this way, only the modulated signal was read by the lock-in. The output signal was in turn fed into an x-y recorder or, a signal analyzer, which essentially served the same purpose as the chart recorder.

The main difficulties with this system is encountered when the energy gap lay near a large structure due to $dI_o/d\lambda$. Since such structures were, for the most part, caused by the response of the grating and the light source, two different gratings and light sources were used. The two diffraction gratings had 600 and 1200 lines/mm respectively. Some of the strong curves in the spectrum of one grating, did not occur in that of the other, (at least not in the same place). So by changing the grating, a previously unsurveyable region in the spectrum became measurable.

The same effect was observed with the two different light sources. One was a 650 watt quartz-iodide lamp. The second light source was a tungsten filament bulb, which had a maximum power of

about 40 watts. A focusing mirror built into the tungsten light assembly, increased the effective light intensity so that it was more comparable, (but still not equal), to that of the quartz-iodide lamp.

Together, in various combinations, the two diffraction gratings and the two light sources, provided essentially four different "background" spectrums with different $dI_o/d\lambda$ structures, thus opening up most of the visible spectrum to investigation without too much interference. However, in switching gratings, an error in the calibration of up to two nanometers could be introduced despite frequent checks with a mercury vapour lamp. Because of this, the same grating and light source was used for all the various temperature measurements of any one sample.

3.3.2 CYOGENIC APPARATUS

For measurements below room temperature, a CTI-CRYOGENICS model 21SC CRYODYNE cryocooler was used. A schematic diagram of the entire system is presented in fig. 3.4. The system employs Joule-Thompson expansion of He gas to cool down to just below 10K. The compressor is connected to the cold head by He supply and return lines. Together, they compress and expand the gas and so provide cooling for the cold station below the cold head. The cold station, fig. 3.5, is divided into two stations, where two different stable temperatures can be maintained. For the present set of measurements, only the second stage cold station was used in order to reach the lowest possible temperature.

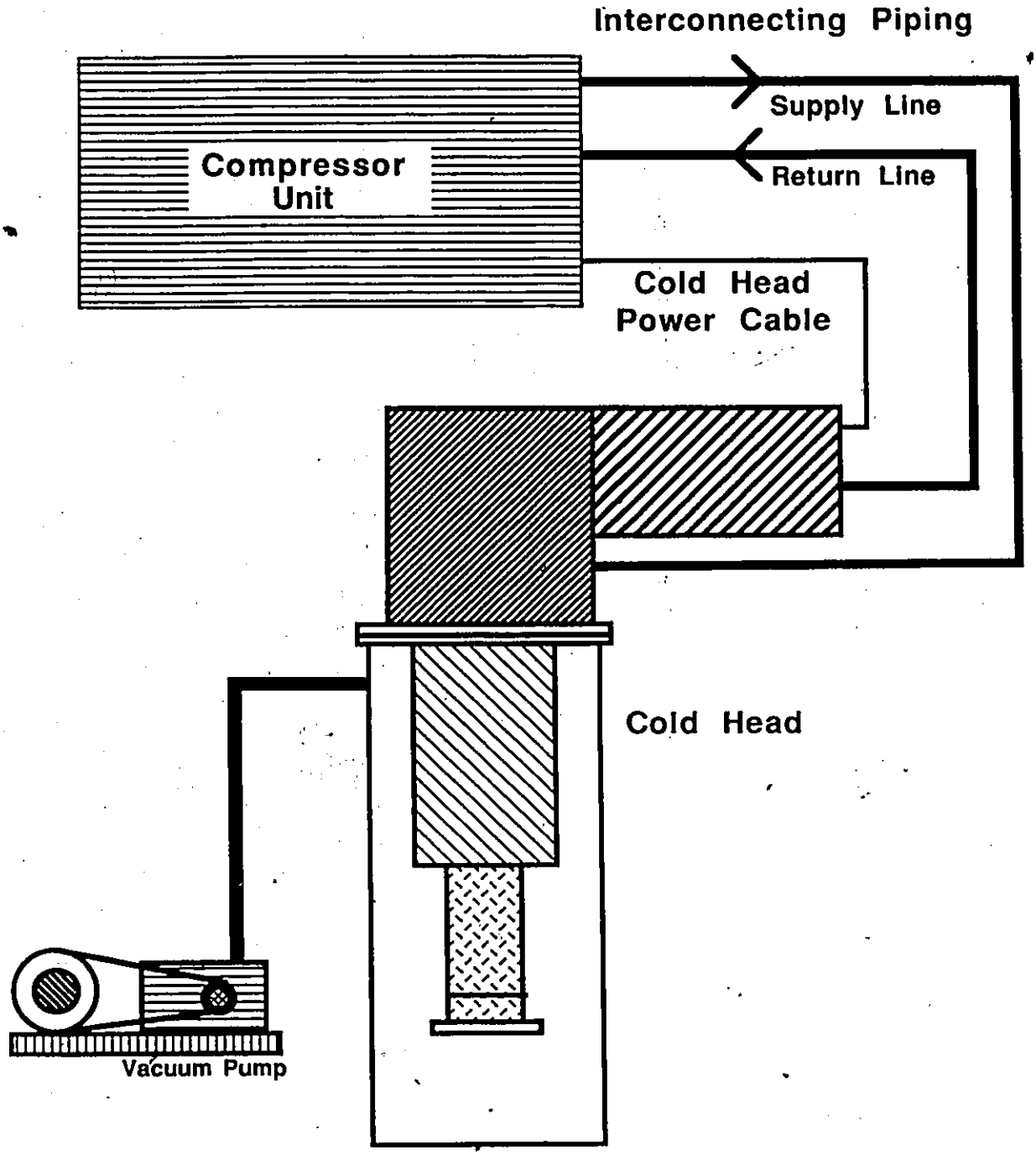

FIGURE 3.4 Schematic of the Cryogenic Apparatus for Measuring the Energy Gap at Low Temperatures.

To control the temperature, a LAKE SHORE CRYOTRONICS model drc-80c Digital Cryogenic Thermometer/Controller, was used. This includes a 0-10 watt and 0-25 watt heater and a calibrated DT-500 series silicon diode thermometer. The temperature could be set for a resolution of 0.1K above 100K and for 0.01K, below. The accuracy of the sensor is stated to be within 0.5K at 4K and at 77K and 1.0K at 273K. The controllability is stated to be within 0.1K or better. This high stability was indeed observed during operation, since any set temperature would remain stable indefinitely. The sensor was mounted on the second stage cold station.

The sample holder, fig 3.6, was firmly attached to the bottom of the second stage. It was made of copper and consisted of two pieces. The main section was designed to attach to the bottom of the cold head in such a way as to provide the maximum possible surface contact. The samples were mounted on a removable copper plate which was connected to the main part of the holder by three brass screws. These screws, being made of a different material, had to be tightened strongly in order to prevent any loosening of the plate at low temperatures.

In order to facilitate mounting and removing samples, heat sink grease, which has a high thermal conductivity, was used to attach the sample to the copper plate. Enough room was available on the holder for up to six different samples at one time.

The entire cold station was enclosed in a vacuum chamber which was maintained at a pressure of 10^{-4}mm of Hg during operation, to provide thermal isolation. The chamber possessed

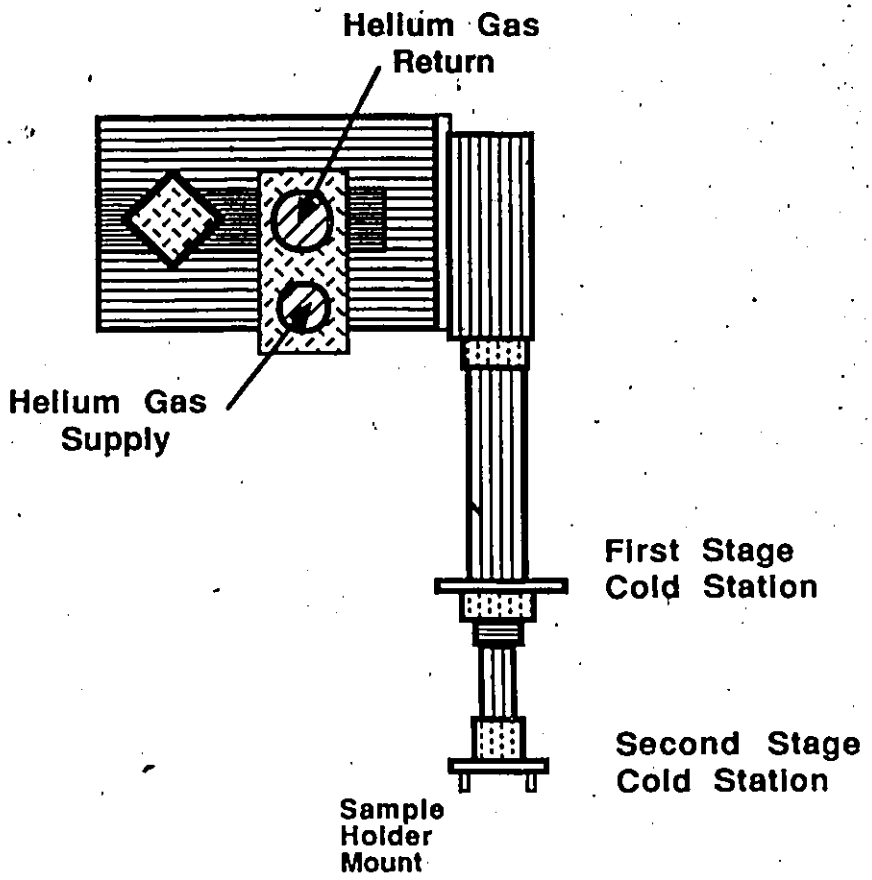

Fig. 3.5 Cold Station of the Cryostat.

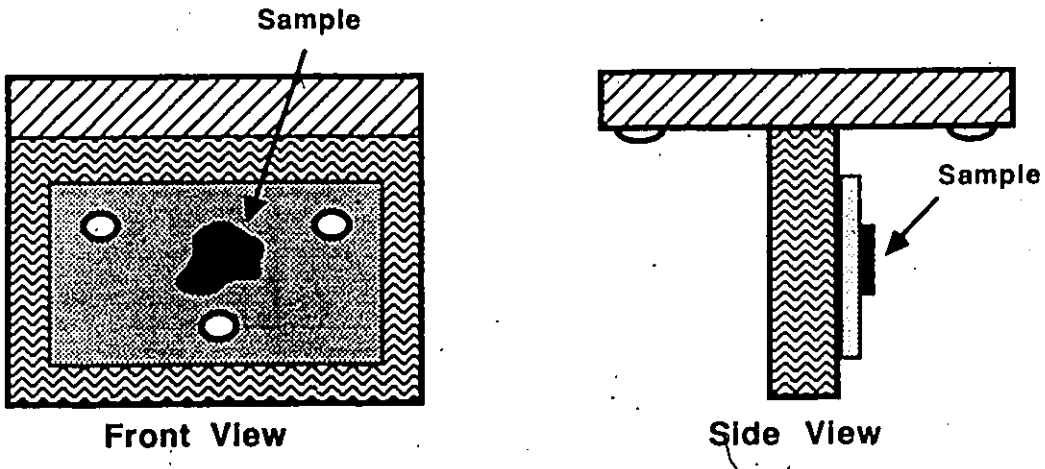

FIG. 3.6 Sample Holder.

four windows for optical measurements of the enclosed sample.

3.4 DETERMINATION OF ENERGY GAP

3.4.1 SAMPLE PREPARATION

The optical measurements were performed on suitable pieces of each sample. These pieces were usually obtained by slicing off a portion between two and three millimeters in thickness. Occasionally fragments, broken from the sample when being handled, were found to be satisfactory. One face of the piece was hand polished using 1.0 micron aluminum powder. This was done to remove any shallow damage in the crystal as well as to make the face as flat as possible. The next step was to etch the piece in a 3% solution of bromine in 99% pure methanol. The etching process involved gently rubbing the face of the sample over the surface of an absorbent paper saturated with the solution. With a good initial surface, no more than a couple of minutes of this was needed to obtain a mirror like finish on the face.

Only the best samples ended up with such good surfaces. Usually, the pieces were pitted, making it impossible to obtain a smooth face, no matter how much polishing was attempted. These particular samples reflected less light but this did not hamper the measurements since the equipment was sensitive enough to handle weaker signals. Measurable signals could be detected, even from samples with very small surface areas due to breakage.

3.4.2 ANALYSIS OF DERIVATIVE CURVES

Once a derivative curve corresponding to an energy band transition was found, the value of that transition had to be determined. From fig. 3.2, one would expect the peak of the reflectance maxima to be given by the point where the derivative curve crosses the base line. Unfortunately, the nature of eq. 3.1, with both an R factor and on I_o factor on the right hand side, makes it difficult, if not impossible, to determine where the base line is. Furthermore, not all of the observed transitions were as symmetrical as what is shown in fig. 3.2, so a method was needed to account for this.

The position of the transition was determined as a fraction of the peak to peak width of the derivative curve. The following procedure, illustrated in figs. 3.7 and 3.8, was used to determine this fraction. First, a "base line" was determined by extrapolating the general trend of the derivative spectrum in the regions away from the transition. Then the distances A and B were measured and substituted into the following equation

$$\frac{D}{C} = \frac{A}{A+B}$$

where the peak to peak width is represented by C and the distance between the first peak and the transition is represented by D.

For a perfectly symmetric curve, B = A, so then D = C/2 and the transition lies right in the centre as in fig. 3.7. If B is small compared to A, the value of D approaches C, or in other words, the position of the transition approaches the second peak in

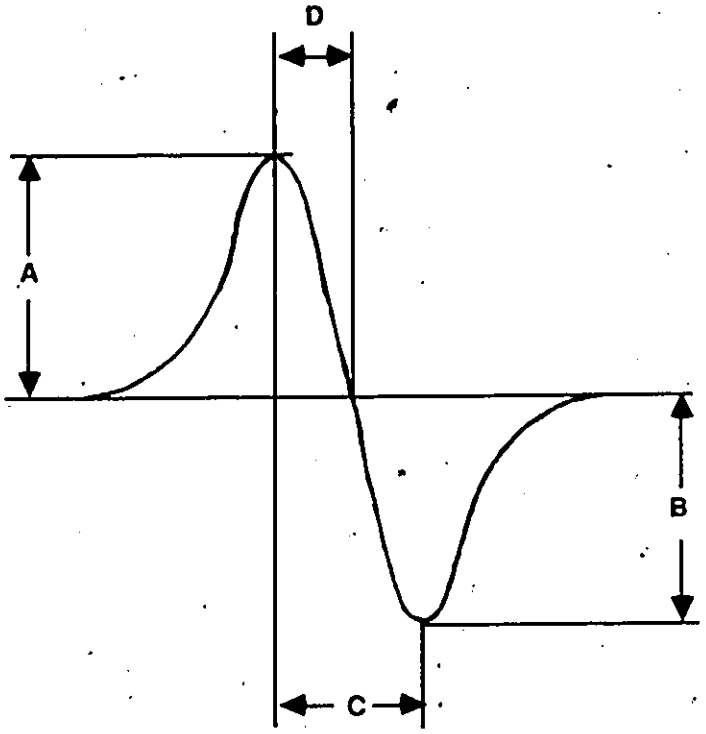

FIGURE 3.7 Symmetric Derivative Curve.

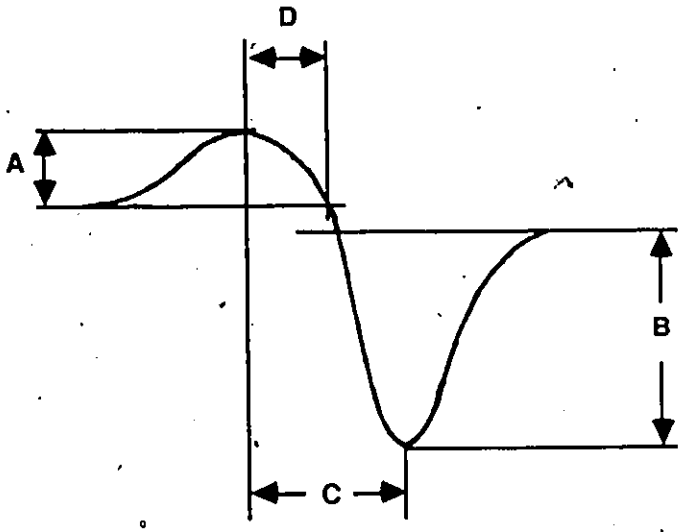

FIGURE 3.8 Asymmetric Derivative Curve.

fig. 3.8. On the other hand, if B is made small then D goes to zero, resulting in the transition being located nearer to the first peak. As can be seen from the figures, this type of calculation can deal successfully with the asymmetry which may be encountered.

In fig. 3.9, a structure in the derivative spectrum for a sample of $Cd_{0.15}Zn_{0.45}Mn_{0.4}Te$ represents a typical result at room temperature. The width between the two peaks is about 9nm. If the method described above gives the energy gap to be at 528nm, then the difference in energy between the two peaks, obtained by using the relation, $E = h\lambda/c$, is about 0.03eV. This is quite small compared to the measured gap of 2.348eV. Any systematic error in this method of pinpointing the transition, would have to be smaller than this. A reasonable uncertainty of about 1nm would give an error of approximately 0.005eV.

3.5 RESULTS OF ENERGY GAP MEASUREMENTS

3.5.1 ROOM TEMPERATURE MEASUREMENTS

A typical room temperature result is presented in fig. 3.9. The diagram shows the raw "sample" signal before any subtraction as well as the "mirror" signal. Several of the samples measured at room temperature had relatively small signals so that it became necessary to perform this type of subtraction in order to estimate the energy gap. But since it was found that the size of the signal increased with decreasing temperature this subtraction became unnecessary at cooler temperatures.

The energy gaps for the alloy system, $Cd_{1-z}Mn_zTe$, has

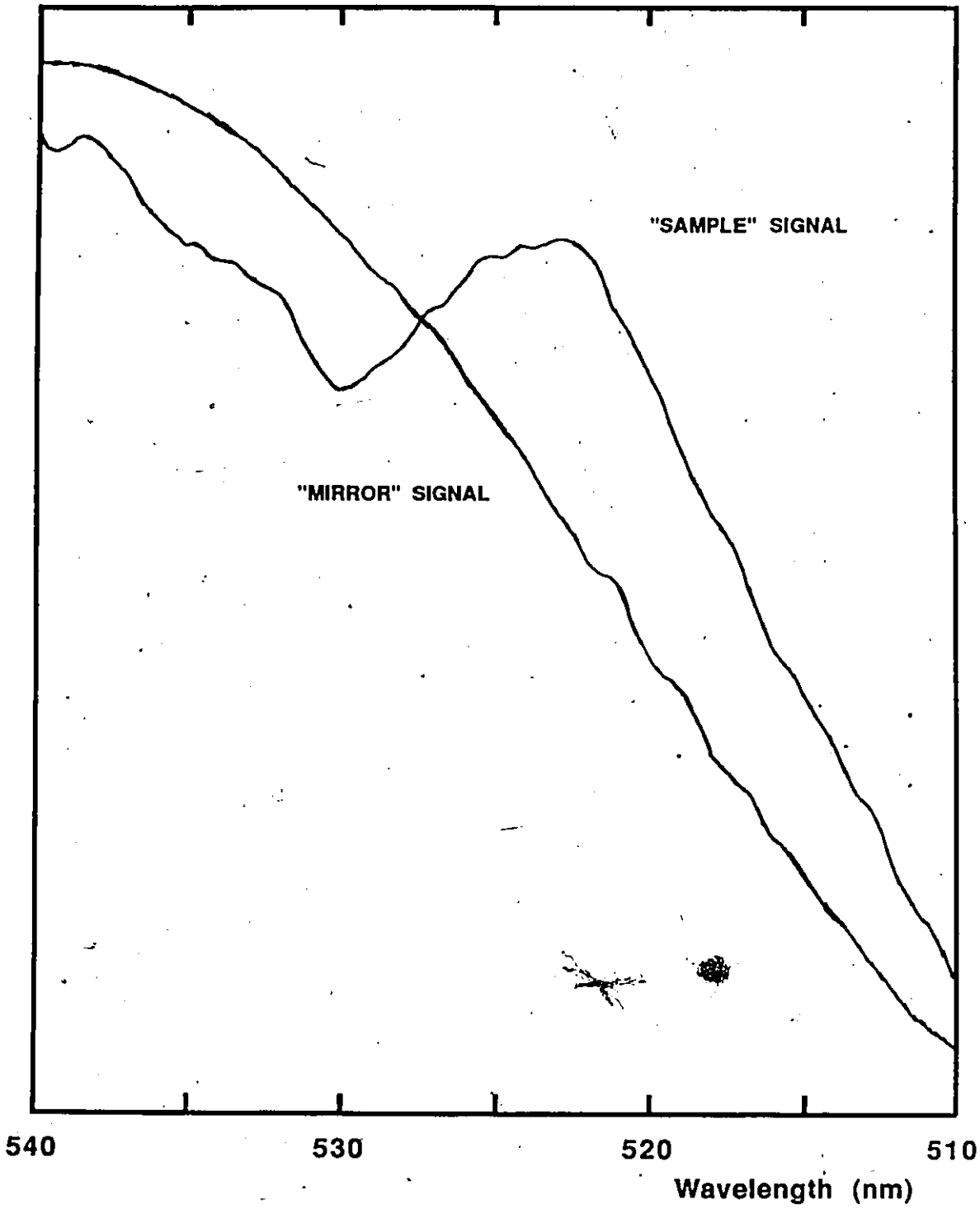

FIGURE. 3.9 Results at room temperature for a sample of $Cd_{0.15}\ Zn_{0.45}\ Mn_{0.4}\ Te$.

been measured by others using a variety of techniques. For example, Bottka et al, (106), have used electroreflectance, while Montegu et al, (108), have used wavelength modulated reflectance in their measurements. As well, absorption was used by Amrani et al, (116) and piezomodulation by Lee and Ramdas, (139). In all these cases, the values obtained for the energy gaps did not differ significantly from the present results or from each other.

Most of the samples for which measurements were attempted, produced satisfactory results. Usually, an anomaly was observed in the wavelength modulated spectrum of the sample. Such a feature would be absent in the derivative spectrum, obtained when an aluminum coated mirror was substituted for the sample inside of the spectrometer. These two spectra would then be subtracted from each other to reveal the derivative signal of the energy gap. The intensity of this signal varied randomly from one sample to another. For some, the signal was too small to be seen and so no anomaly was observed. In a few of these cases, the sought after signal became strong enough to be observed only at lower temperatures. In other cases, only preparing the sample over again produced results which could be measured, indicating that the strength of the energy gap signal varied for different samples of the same composition. Such behaviour can be attributed to the effects of inhomogeneity which depend on the exact conditions under which the sample is prepared.

As with the lattice constants the energy gaps, were plotted as a function of composition. The plots were done in the same way;

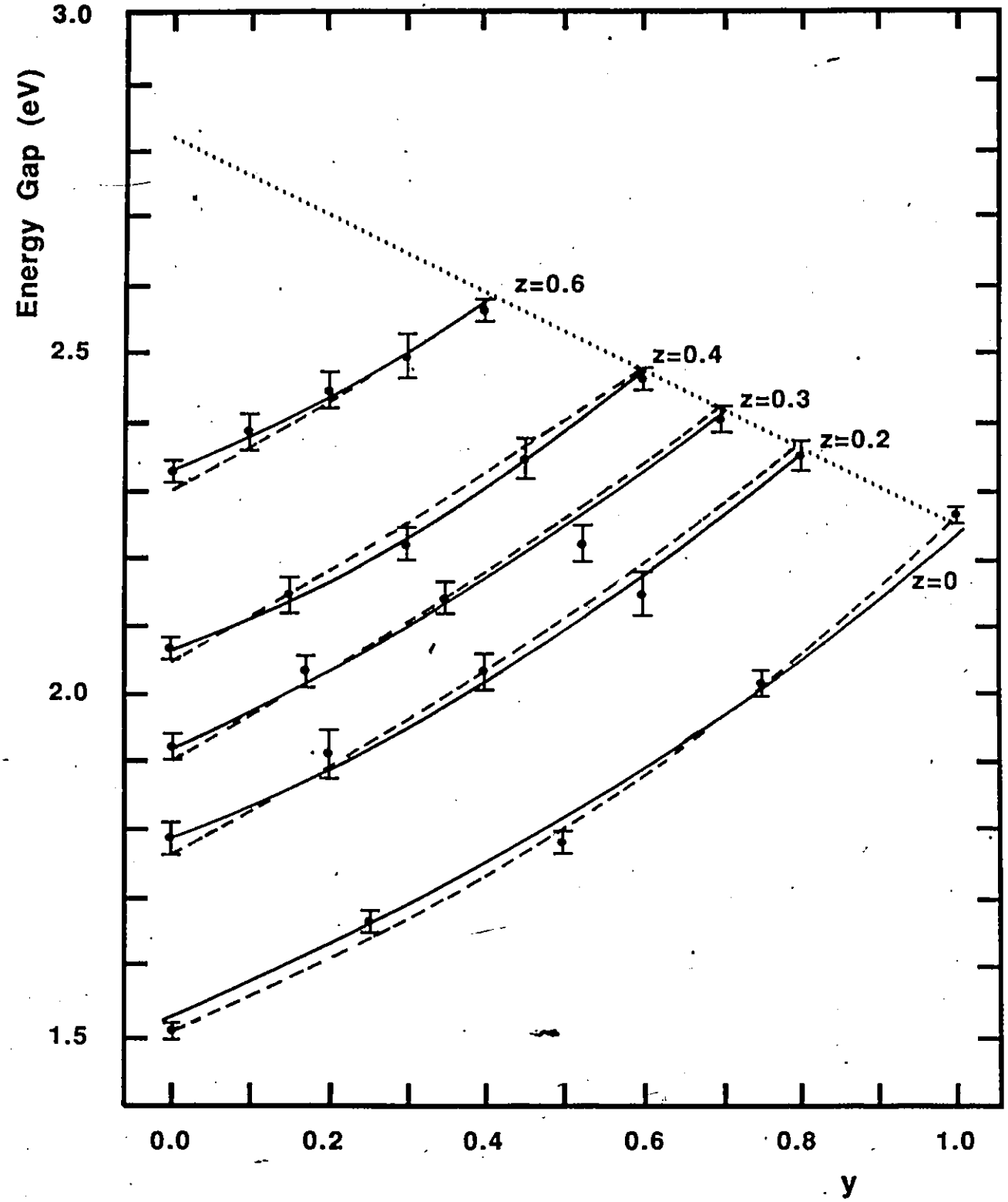

FIGURE 3.10 Energy Gap Variation For Constant z at T=300K. The solid lines were obtained by fitting to eq. 3.8. The broken lines represent an interpolation using eq. 3.10. The dotted line represents the x=0 edge.

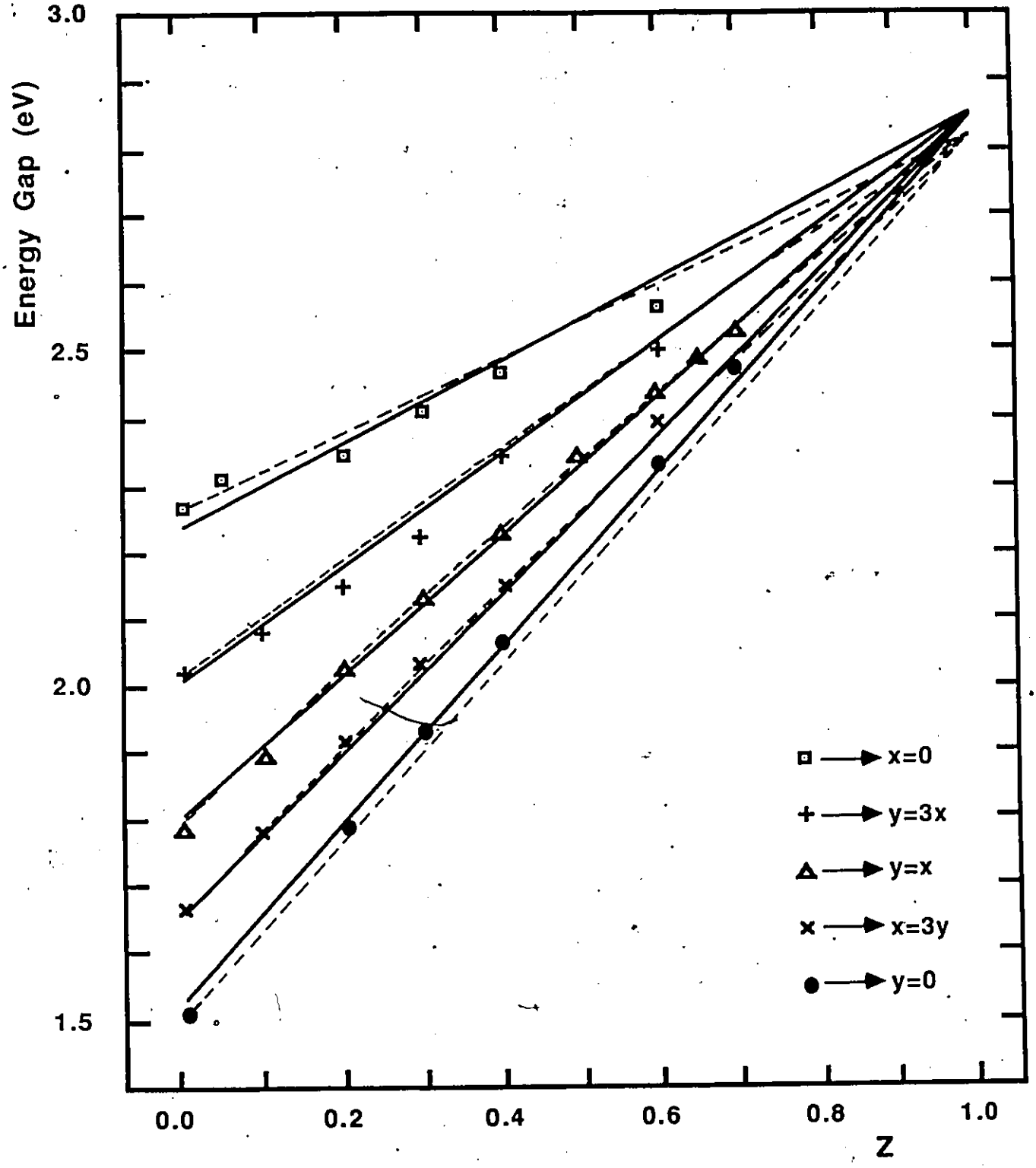

FIGURE 3.11 Energy Gap Variation for x Proportional to y at T=300 K. The solid lines were obtained by fitting to eq. 3.8. The broken lines represent an interpolation using eq. 3.10.

fig. 3.10 illustrates the variation of the energy gap for lines of constant Mn, while fig. 3.11 illustrates the variation for lines of constant Cd:Zn ratio. Fig. 3.11 shows the same linear variation as the lattice constants did in fig. 2.3. The five lines extrapolate to a single point at z=1.0 which would be the energy gap of MnTe, if it existed in the zinc-blende structure. As in the case of the lattice parameters, the same value for this quantity should be obtained from other SMSC alloys which are derived from MnTe and have a zinc-blende phase. In fig. 3.10, the variation with y concentration is non-linear, in contrast to the corresponding lattice parameter results in fig. 2.2. It was found that each curve could be fitted to a second order equation.

In order to plot values of constant energy gap for the ternary diagram, just as was done for the lattice parameters, fig. 2.6, an equation was developed which describes the variation over the entire range of solid solution. The same approach employed for the lattice parameters was used to do this.

The general polynomial equation of section 2.3 may be reduced to a finite number of terms by using the experimental results. Fig. 3.11, tells us that the equation must be a second order relation in y, whereas fig. 3.10, indicates the presence of linear z terms. The development will be accomplished in cartesian coordinates, represented by (Y,Z), and then transformed into triangular coordinates. In cartesian coordinates, the representation wanted is a section of a parabolic surface. For Z=0, the energy gap may be given by

$$E(0)=a+bY+cY^2 \qquad (3.2)$$

What is needed is a method which will linearly reduce this equation to a constant at Z=1. If we take Y as being a function of Z, then a linear scaling factor would be

$$Y(Z)=Y(0)(1-Z) \qquad (3.3)$$

where Y(0) can replace Y in equation 3.2. Similarly, E may be represented by

$$E(Z)=E(0)(1-Z) \qquad (3.4)$$

A more general equation for the whole system would then be

$$E(Z)=a(Z)+b(Z)Y(Z)+c(Z)Y^2(Z) \qquad (3.5)$$

If we now substitute equations 3.3 and 3.4 into equation (3.5), we obtain

$$E(0)(1-Z)=a(Z)+b(Z)(1-Z)Y(0)+c(Z)Y^2(0)(1-Z)^2$$

which when compared to equation 3.2, tells us that $a(Z)=a(1-Z)$ and $c(Z)=c/(1-Z)$. Putting these values back into equation 3.5 gives us

$$E(Z) = (1-Z)a + bY + cY^2/(1-Z) \qquad (3.6)$$

In order to be able to use this equation in the ternary diagram a transformation from cartesian coordinates, (Y,Z), to triangular coordinates, (y,z) became necessary. With the aid of fig. 3.12, the transformation was derived as follows. First, since the z coordinate is the same in both systems, the statement z=Z, may be written immediately. To obtain the relation for Y, the general point, u, from fig. 3.12 was used to geometrically derive the following relations

$$PQ = z\tan(30)$$

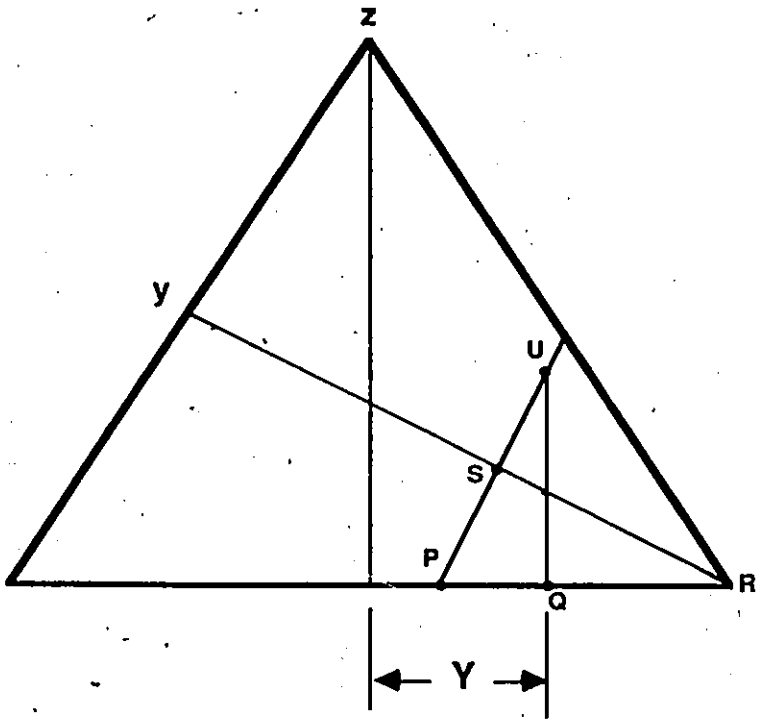

FIGURE 3.12 Transformation From Cartesian Coordinates to Triangular Coordinates.

$$QR = 1/3 - Y$$

$$PR = z\tan(30) + 1/3 - Y$$

$$SR = PR\cos(30)$$

$$y = TS = 1 - SR$$

$$y = 1 - (z\tan(30) + 1/3 - Y)\cos 30$$

$$= 1/2 + 3Y/2 - z/2$$

This may be rearranged to obtain

$$Y = (2/3)y - 1/3 + (1/3)z \qquad (3.7)$$

The final form of the equation then is given by substituting eq. 3.7, into eq. 3.6.

$$E = \frac{C(4y^2+z^2-4y+4yz-2z+1)}{3(1-z)} + \frac{B(2y+z-1)}{3} + A(1-z) + E_o \qquad (3.8)$$

The term E_o, was added to account for the fact that E is not zero at z=1, which was assumed in the derivation. This represents the intersection of the the lines drawn in fig. 3.11.

The constants of eq. 3.8 were obtained by performing a least squares fit to the measured data. The results were as follows

$$A = -1.0421 \text{ eV}$$

$$B = 0.6096 \text{ eV}$$

$$C = 0.2366 \text{ eV}$$

$$E_o = 2.853 \text{ eV}$$

with a standard deviation of 0.021 eV.

A test of the "goodness" of the fit was done using eq. 2.8. For the case of the room temperature energy gaps, the uncertainty in each value, σ_i, was estimated by combining three different contributions. The first is due to the error in the composition

which arises from the process of preparation and was discussed in chapter 2. The second is due to inaccuracies in pinpointing the energy gap in a tracing of the derivative signal and was discussed in section 3.4.2. The final source of uncertainty arises from the errors in calibration discussed in section 3.3.1. As indicated, this last source of error applies only when comparing different samples with each other such as in the present situation. When comparing the energy gap of a sample at different temperatures, the errors associated with this become largely systematic because the conditions of the spectrometer are not changed in a temperature run. The error bars in fig. 3.10 were estimated by combining these three contributions. Using these values in eq. 2.8, the calculation results in χ^2_υ=1.06 which again indicates that eq. 3.8 fits very well to the data, (104).

As with the lattice parameters, the available energy gap data was used to test the Williams equation, 2.6. Unlike the case with the lattice parameters, the relationship between the derived polynomial equation and the interpolated equation, (2.6), was not trivial.

To apply the Williams method to the energy gaps, the three relations, 2.4, 2.5 and 2.6 remained unchanged, with the following exceptions. The values for B_1, B_2 and B_3 became the corresponding energy gaps values for the corners of the ternary diagram in fig. 1.1. The other change occurred for T_{12} of eq. 2.4. This equation represents the z=0 edge of the ternary diagram. As has been shown in fig. 3.10, the energy gap variation was not

linear, so a modification, (3) was used.

$$T_{12} = xB_2 + (1-x)B_1 + C_{12}x(1-x)$$
$$T_{23} = yB_3 + (1-y)B_2 \qquad (3.9)$$
$$T_{31} = zB_1 + (1-z)B_3$$

The C_{12} term in the first equation will be called the bowing parameter and takes care of the non-linear variation. This equation is actually a general second order relation in x, which, as has already been shown, can be fitted very well to the z=0 edge.

Equations 3.9 and 2.6 were substituted into equation 2.5 resulting in the following equation

$$E = \frac{\{B_1+y(B_2-B_1+C_{12})-C_{12}y_2\}yx + yz\{zB_3+(1-z)B_2\} + xz\{xB_1+(1-x)B_3\}}{(xy + yz + xz)} \qquad (3.10)$$

Values for B_1, (CdTe), and B_2, (ZnTe), B_3, (MnTe) and C_{12} were calculated by fitting the energy gaps from the three edges of the composition triangle to eqs. 3.9. The values obtained are as follows

$$B_1 = 1.516 \text{ eV}$$
$$B_2 = 2.267 \text{ eV}$$
$$B_3 = 2.823 \text{ eV}$$
$$C_{12} = -0.3531 \text{ eV}$$

With these values in eq. 3.10, the energy gap can be estimated for any composition. The standard deviation was calculated to be 0.025eV which is not very much larger than that calculated from fitting eq. 3.8. On the other hand, the reduced χ^2 was calculated to be 1.28 which is significantly larger than that for eq. 3.8 but not large enough to suggest that eq. 3.10 is not

appropriate for this data, (104).

A similar analysis was performed by Debska et al, (143), on the energy band gaps of the $Cd_xHg_yMn_zTe$ alloy system. Their measurements restricted to a limited portion of the phase diagram, but they were able to obtain very good agreement between their experimental values and those they interpolating by using eq. 3.10.

Comparisons of the two methods over the entire composition range are shown in figs. 3.10 and 3.11. The solid line is the fitted polynomial equation, while the broken line represents the Williams interpolation. In fig. 3.10, the polynomial equation predicts parabolas for all the constant Mn lines. A check of the Williams equation shows that only the z=0 line is parabolic while the others are rational functions. In fig. 3.11, straight lines are predicted by the polynomial equation, whereas only the y=0 and x=0 lines are predicted to be straight by the Williams equation. Unlike the case for the lattice parameters, there is a distinction between the two equations developed here to describe the energy gap variation. Both result in similar behavior along the edges of the ternary diagram, but are interpolated differently, inside the triangle.

In conclusion then, it was found that the Williams interpolation, which only made use of data from the edges of the composition triangle could be used to predicted values for the "interior" of the triangle but it was not as accurate as a polynomial equation which used all of the data.

The next step in the analysis was to determine the values

of constant energy gap for the system. The preceding analysis resulted in two equations being available to do this with. It was decided to use the polynomial equation because as well as being more accurate, it was simpler to use than eq. 3.10. The results are presented in fig. 3.13.

3.5.2 VARIATION WITH TEMPERATURE

As was indicated earlier, the signal due to the energy gap increased with decreasing temperature to such an extent that it became possible to determine the energy gap without having to subtract the $dI_o/d\lambda$ term. This can be seen clearly in Fig. 3.14 where an example of a good set of signals, obtained for the sample $Cd_{0.175}Zn_{0.175}Mn_{0.65}Te$, is plotted. The intensity of the derivative signal increases by about a factor of five between 300 K and 10 K. Such a dramatic increase in intensity was not observed for all cases. In fig. 3.15, the results for a sample of $Cd_{0.25}Zn_{0.25}Mn_{0.5}Te$ are illustrated. It can be seen that the size of the signal varies very little over the range of temperatures indicated. Some samples, for which a signal was not observed at room temperature, yielded results only at lower temperatures. The extreme example of this is given by the case of $Zn_{0.3}Mn_{0.7}Te$ in fig. 3.16. A very weak structure was observed at the lowest temperature, which shifted towards longer wavelengths as the temperature was increased and eventually disappeared at temperatures higher than 30 K. The larger stationary structure, which occurs at 420nm in this figure, is due to the response of the

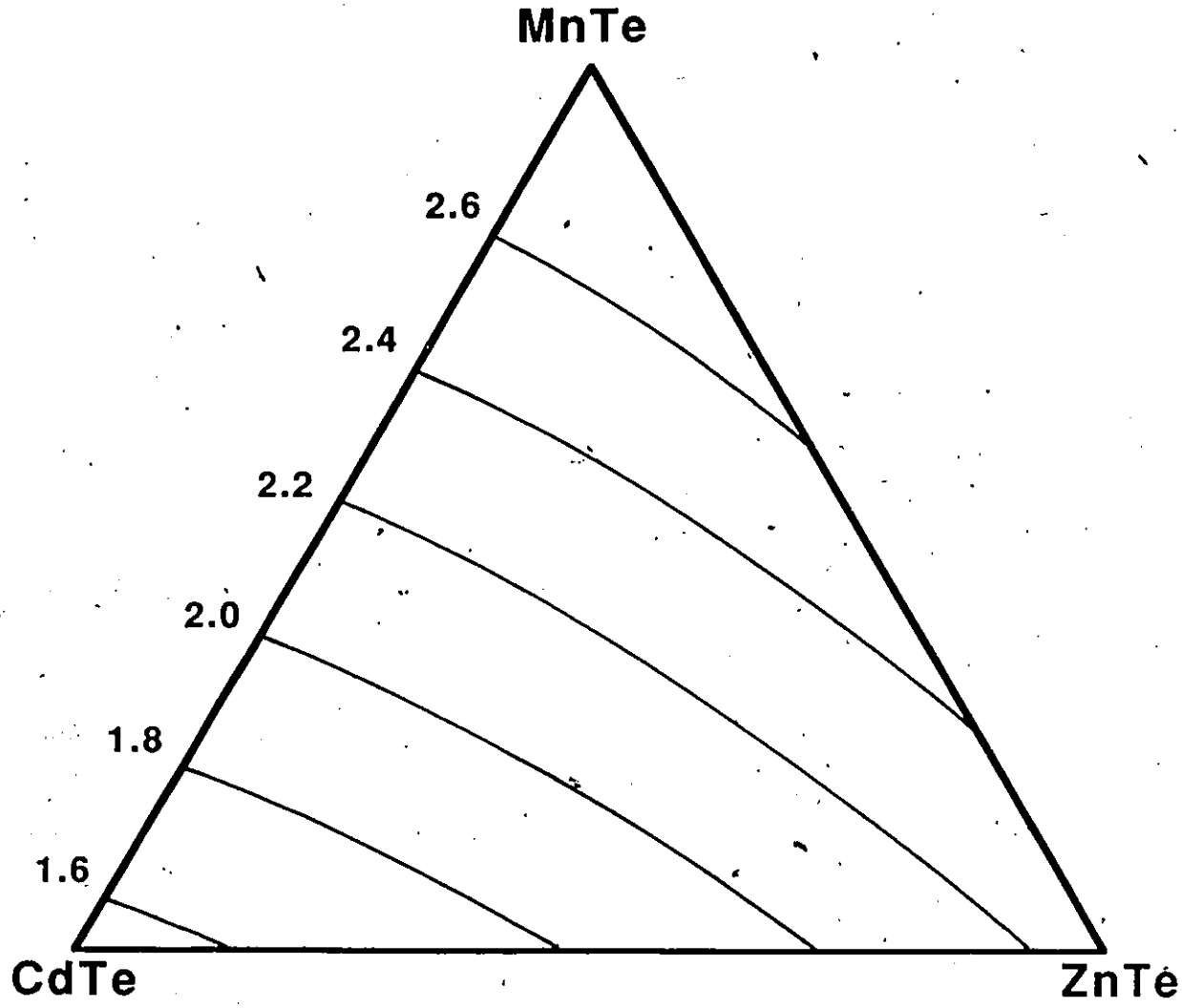

FIGURE. 3.13 Values of Constant Energy Gap.
The values indicated are in units of eV.

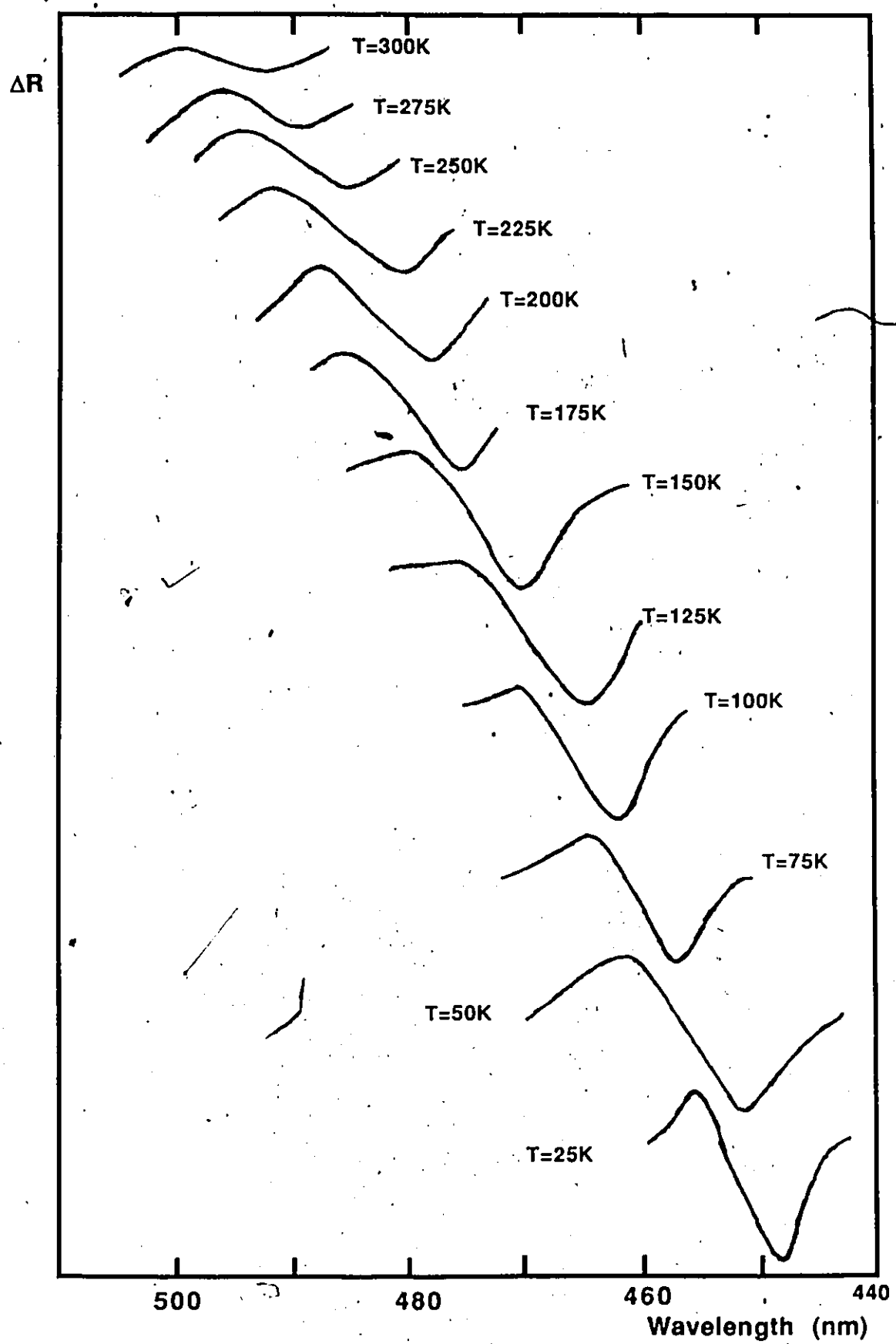

FIGURE 3.14 Energy gap signals measured for a sample of $Cd_{0.175}Zn_{0.175}Mn_{0.65}Te$

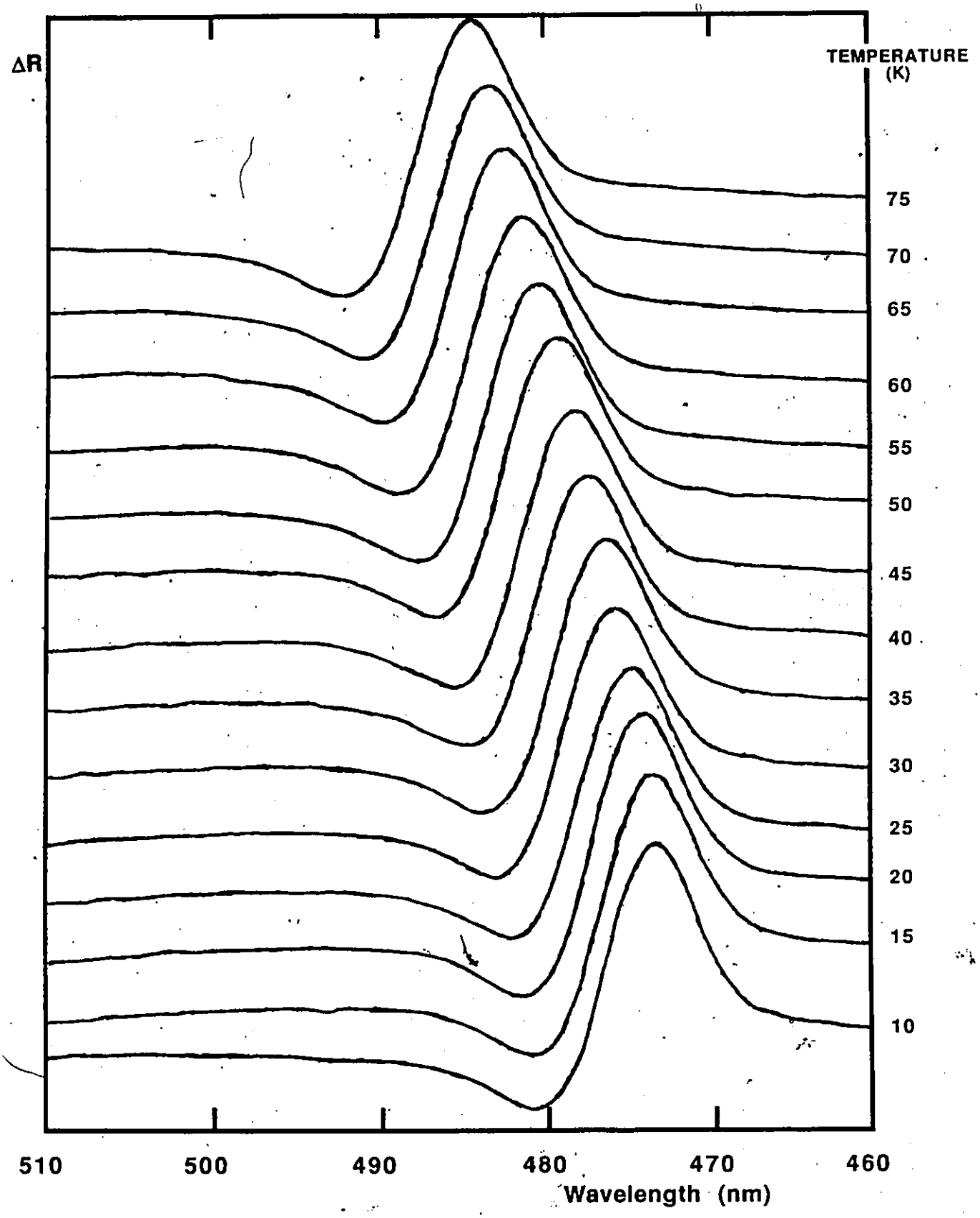

FIGURE 3.15 Energy gap signals measured for a sample of $Cd_{0.25}\,Zn_{0.25}\,Mn_{0.5}\,Te$.

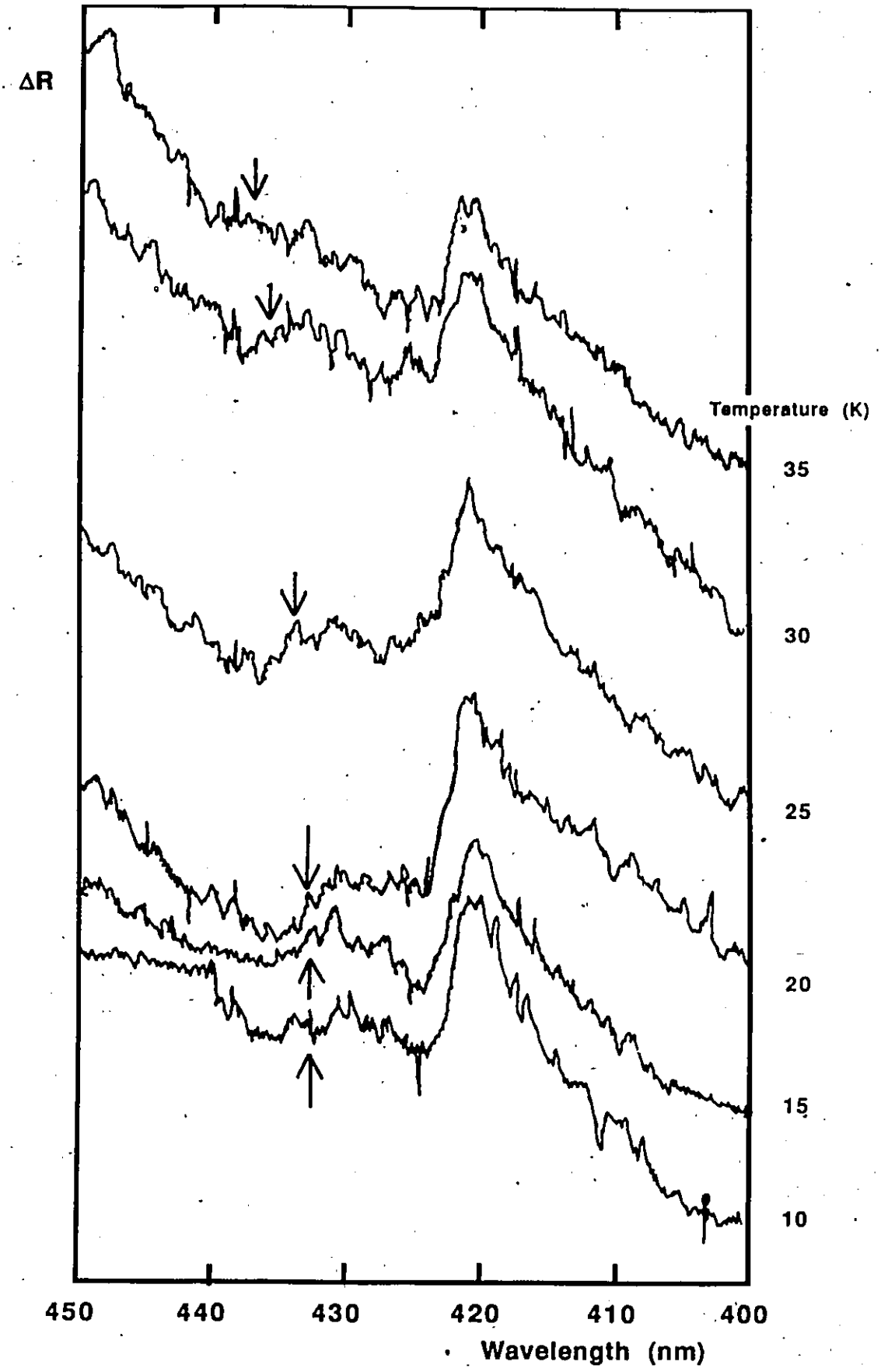

FIGURE. 3.16 Energy gap signals measured for a sample of $Zn_{0.3}Mn_{0.7}Te$. The arrows indicate the positions of the peaks.

optical system, as discussed previously, and should be ignored. These tracings were obtained by combining several different sets of measurements with a signal averager. The relative size of these signals is much smaller than those in figs. 3.14 and 3.15. This can be readily seen by considering the quantity of noise present in each case.

Such dramatic differences in signal intensities appeared in random compositions, indicating that it was not an effect of changing the concentration of the samples. The amount of increase of the signal intensity with a lowering of temperature, was also found to vary independently with composition. This may be seen clearly by considering figs. 3.14 and 3.15. The compositions of the samples in these two diagrams are quite close together, yet the behaviour of the signal intensity is quite different. Such dissimilar behaviours for the variation of the signal intensities are most likely the result of the effects of inhomogeneity in each sample, which depends on the conditions under which it was produced and not on its composition.

Variation of the energy gaps with temperature is presented in figs. 3.17 to 3.21. All samples experienced an increase in the gap with decreasing temperature. This thermal increase was linear for all cases at temperatures above approximately 200 K. Below this point, three different behaviours were observed, over three different composition ranges. For samples with Mn concentrations below 20%, the increase began to level off when the temperature was lowered below approximately 100 K. This behaviour is typical of

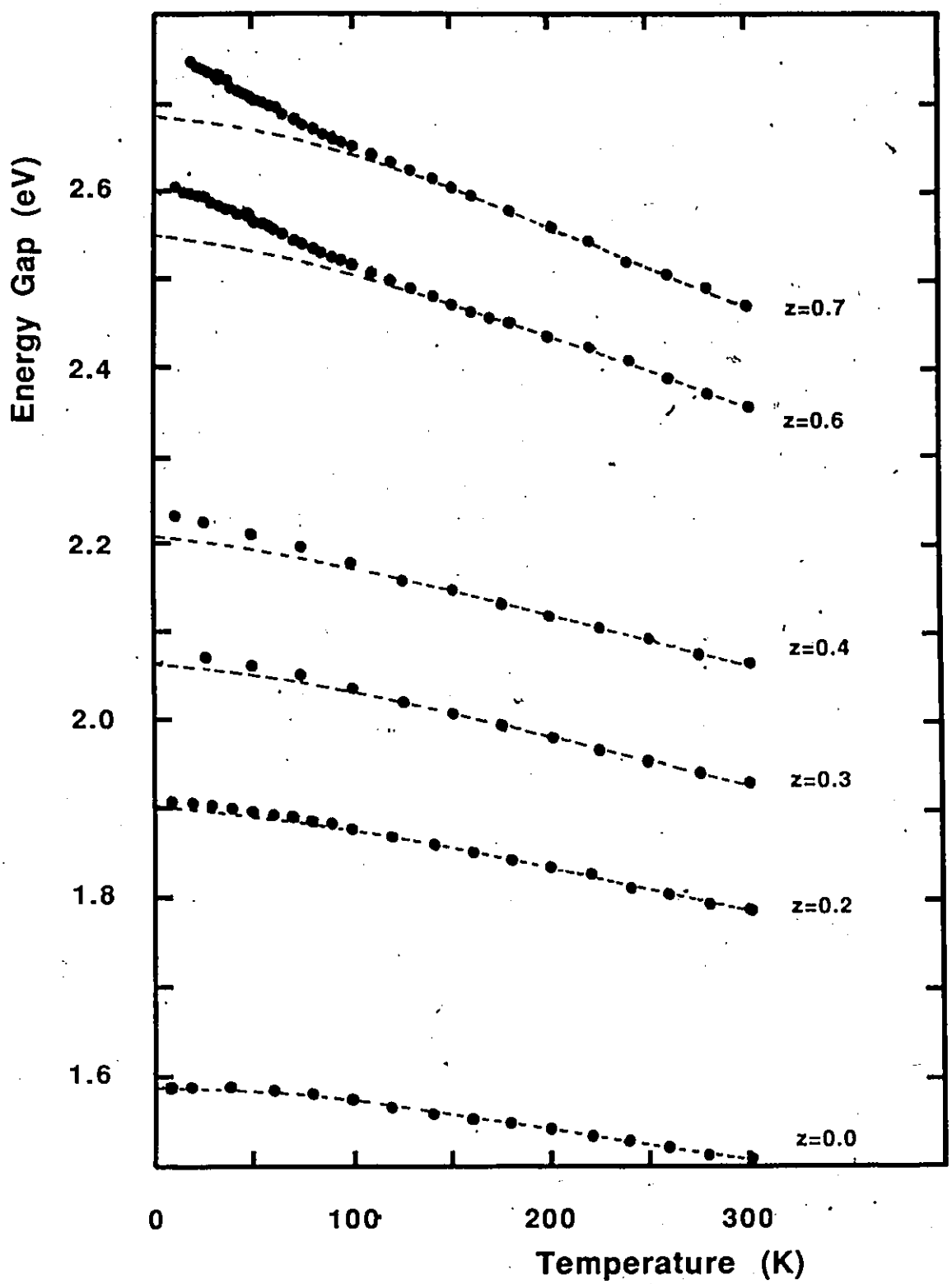

FIGURE 3.17 Energy Gap as a Function of Temperature for y=0 Samples. The broken line for the z=0 sample was obtained by fitting to eq. 3.11. The broken lines for the other samples were obtained by using eq. 3.12.

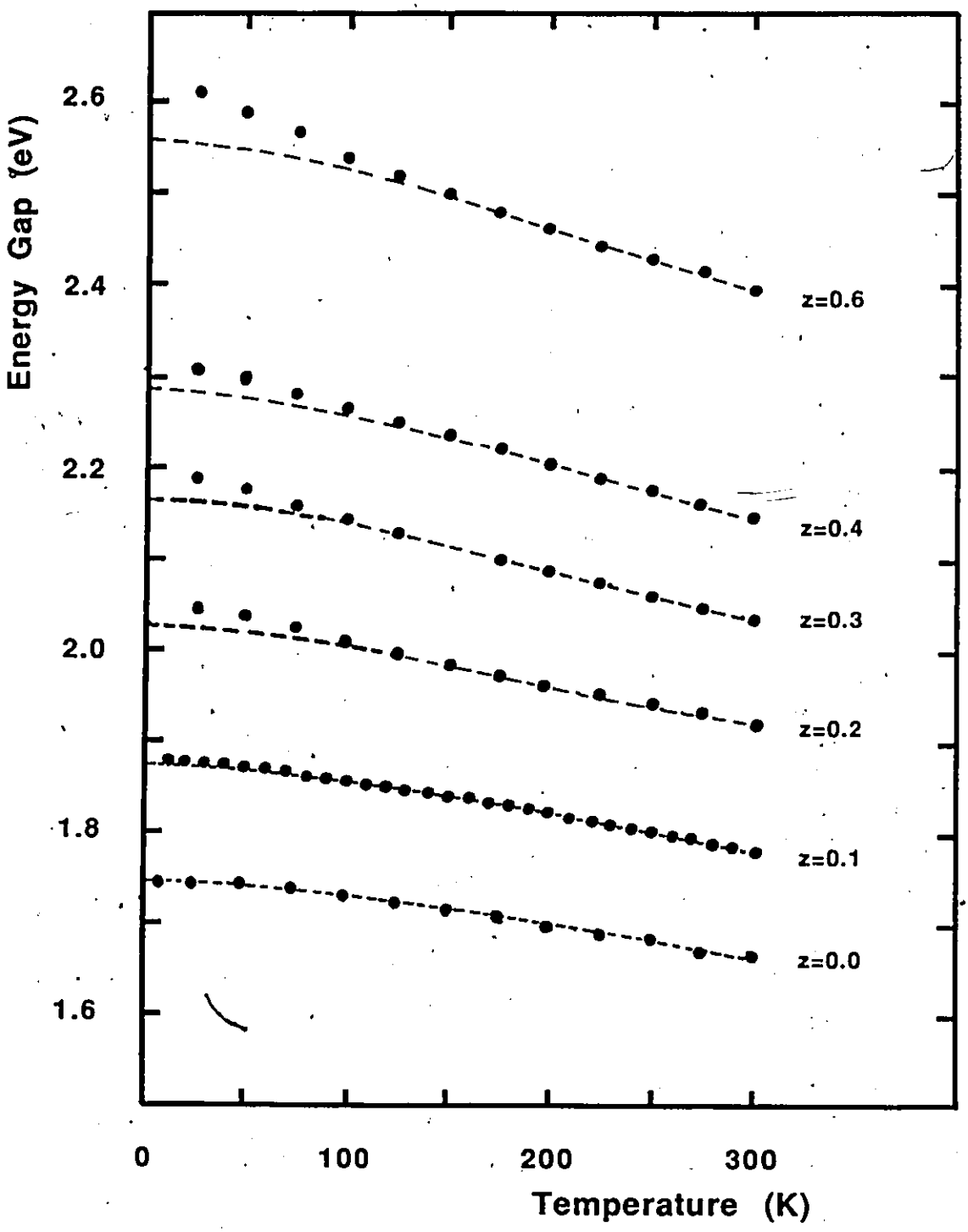

FIGURE 3.18 Energy Gap as a Function of Temperature for x=3y Samples. The broken line for the z=0 sample was obtained by fitting to eq. 3.11. The broken lines for the other samples were obtained by using eq. 3.12.

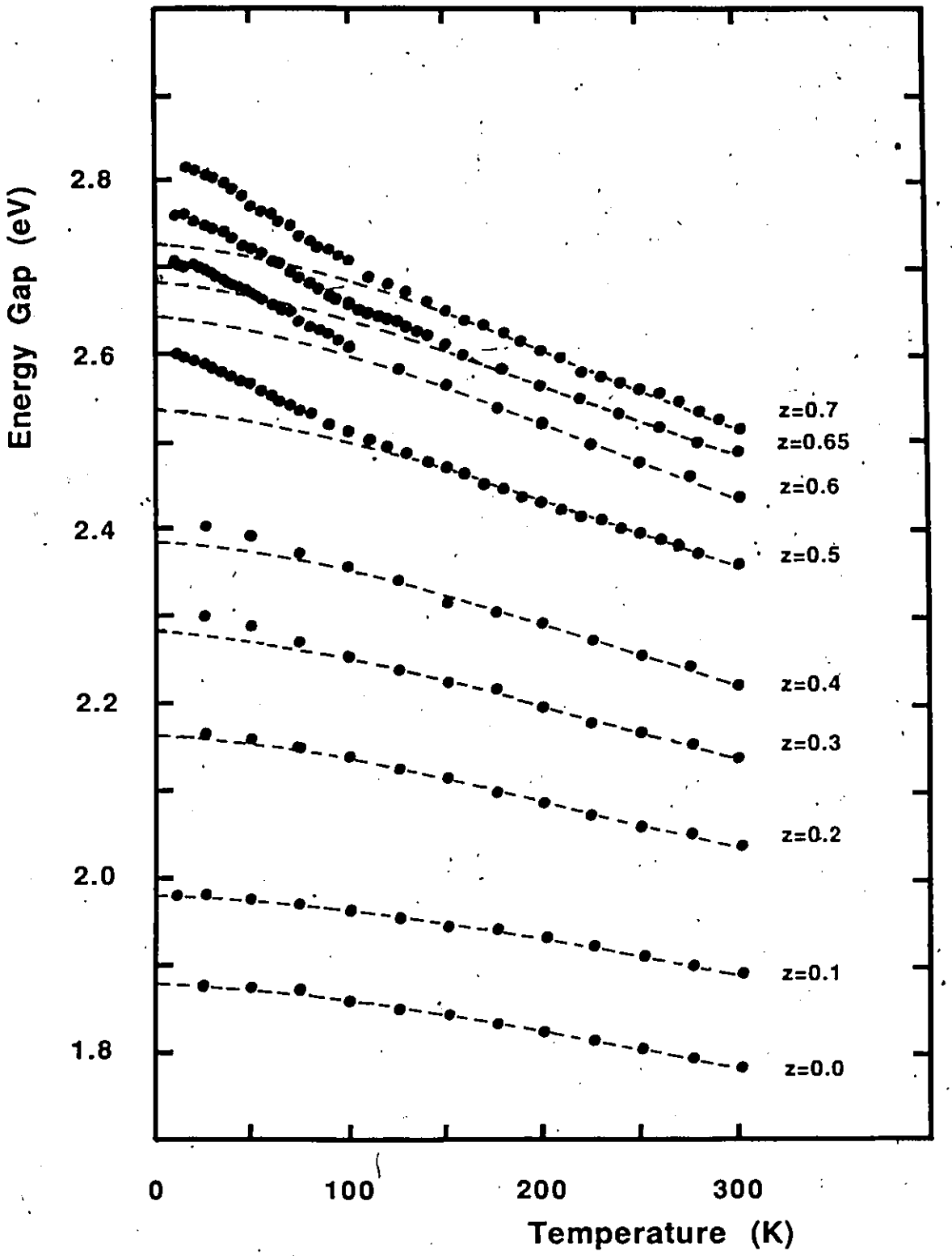

FIGURE 3.19 Energy Gap as a Function of Temperature for y=x Samples. The broken line for the z=0 sample was obtained by fitting to eq. 3.11. The broken lines for the other samples were obtained by using eq. 3.12.

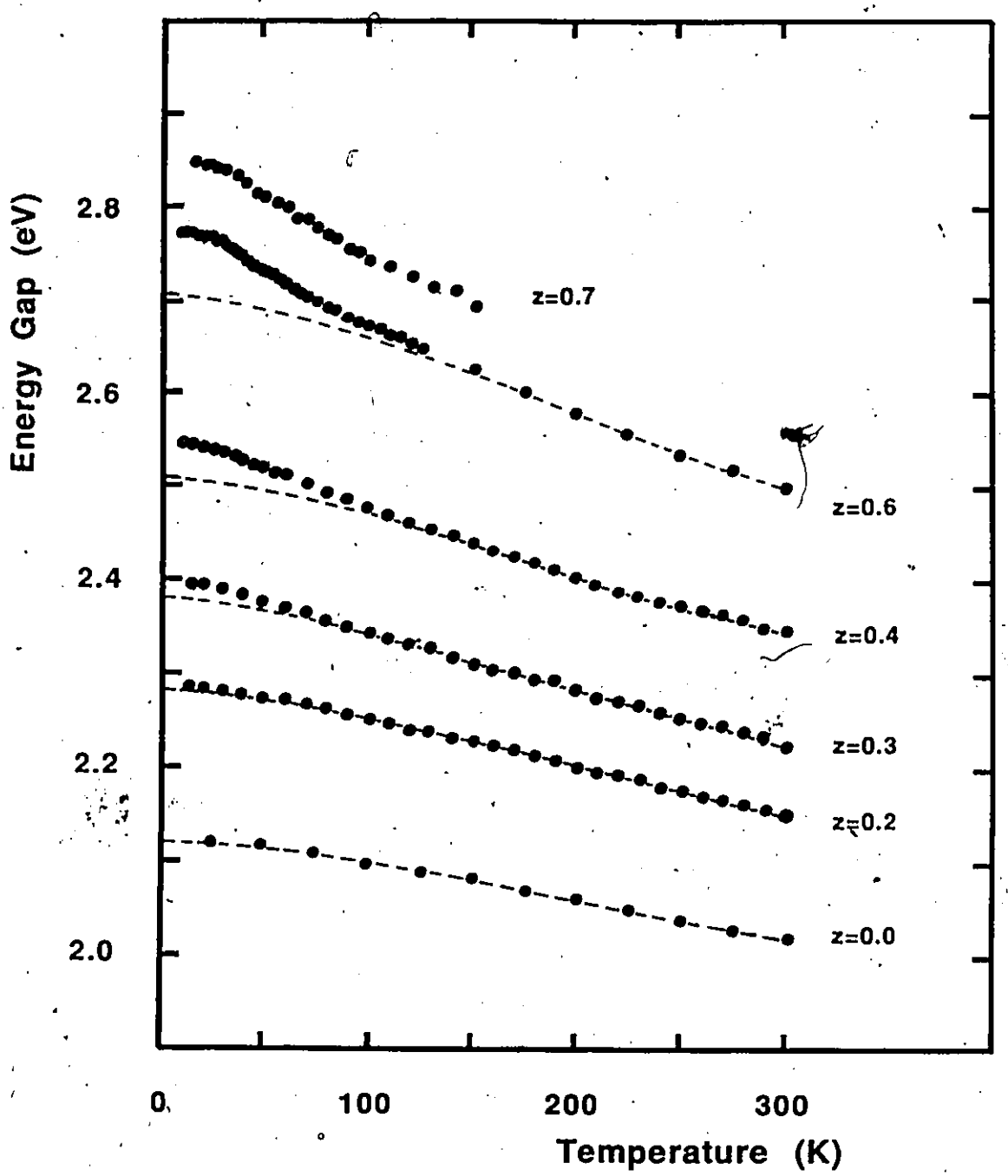

FIGURE 3.20 Energy Gap as a Function of Temperature for y=3x Samples. The broken line for the z=0 sample was obtained by fitting to eq. 3.11. The broken lines for the other samples were obtained by using eq. 3.12.

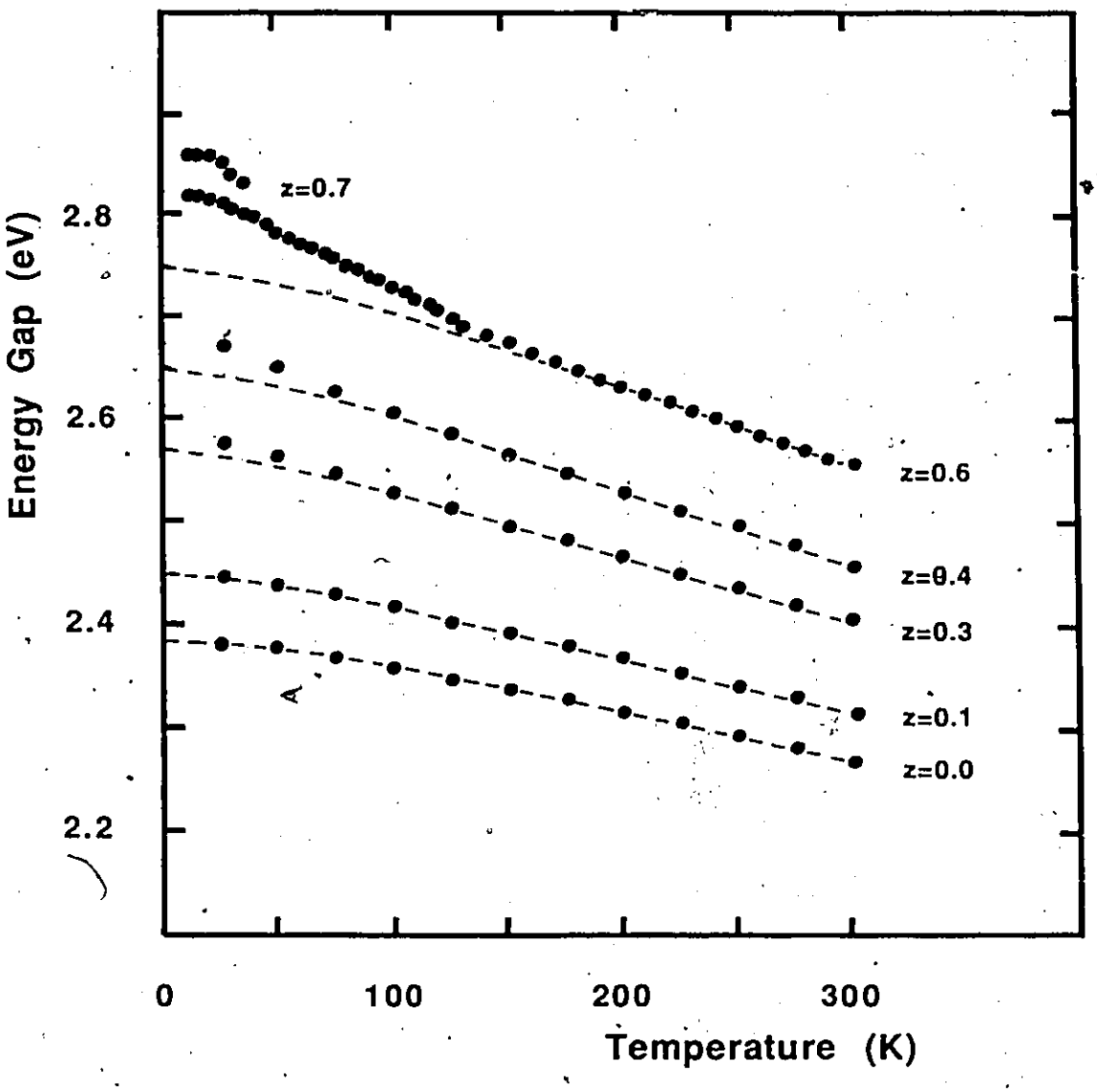

FIGURE 3.21 Energy Gap as a Function of Temperature for x=0 Samples. The broken line for the z=0 sample was obtained by fitting to eq. 3.11. The broken lines for the other samples were obtained by using eq. 3.12.

that observed with conventional nonmagnetic semiconductors with an adamantine or diamond like structure, (33, 34). For samples with Mn concentrations between 20% and 50%, the energy gap increases more rapidly in this range than in the previous case. This results in an almost linear behaviour over most of the temperature range. The rest of the samples also showed an increase but in these cases, it was larger and resulted in an upward curvature in this intermediate temperature range. At the very lowest temperatures, ($T < 20$ K), the curve appeared to level off in all cases. The solid lines in these figures for the z=0 samples are the results of an analysis which will be discussed below. The other solid lines were not produced from a least squares fit analysis but serve merely to guide the eye.

This behaviour suggests that there is an extra increase or a "blue shift" in the energy gap at lower temperatures. The effect increases with Mn concentration and also becomes more pronounced as Zn is increasingly substituted for Cd. Such behaviour is similar to that reported in chapters 4 and 5 where it was found that the magnetic properties generally increased with Mn and with Zn concentrations. In light of this, it may concluded that the increased energy gap is a magnetic effect. The difference between the samples with small y and with large y are seen most clearly for the cases with higher Mn concentration. For the $Cd_{1-z}Mn_zTe$ system in fig. 3.17, the upward curvature of the energy gap is almost totally absent in the large z cases. Measurements of the energy gap as a function of temperature have been made by others on this

edge of the pseudo-ternary diagram using wavelength modulation techniques, (108), as well as electroreflectance, (6, 106), piezomodulation, (139), and absorption, (8, 107). The results in these cases are similar to those reported here but the "blue shift" went largely unnoticed, probably because it is smaller with these Cd samples. However a shift similar to that observed here was discussed in a recent set of measurements by Diouri et al, (141), on the same $Cd_{1-z}Mn_zTe$ system. In those results, the "blue shift" was more distinct for the samples with high z concentration than in the present set of measurements.

It has already been stated that the energy gaps of the samples with low Mn concentration behave like typical diamagnetic semiconductors so these cases will be dealt with first. There are two contributions to the observed shift in the gap. The first is induced by the dilation of the crystal lattice. The second contribution arises from the interaction of phonons with band electrons. A means of accounting for these two factors has been developed by Manoogian and Leclerc (33, 34), and is represented by the following equation

$$E_o(0) - E_o(T) = UT^S + V\theta[\coth(\theta/2T) - 1] \qquad (3.11)$$

where U, V, s, and θ, are parameters independent of temperature. The two terms on the left hand side of the equation represent the energy gap at a temperature 0 K and T, respectively. The effects of the lattice dilation and phonon interaction are represented by the first and second terms of the right hand side of eq. 3.11. The parameter θ was found to correspond very well with the mean

phonon frequency. For this system, θ, may be taken to be approximately 200 K, (35). It was found, by Manoogian and Leclerc and by others, (36, 37), that the value of the parameter s, was always approximately 2/3. Using these two values in eq. 3.11 and obtaining E_o from figs. 3.17 to 3.21, the sets of values for the z=0 samples were fitted to obtain values for U and V which are listed in Table II. Samples with z=0.1 behave in a similar manner to the diamagnetic samples and could also be analyzed using eq. 3.11. These, however, will be considered later in this discussion.

As z is increased above 0.2, the "blue shift" of the energy gap becomes significant. Similar effects have been observed in magnetic semiconductors such as MnO, MnS and CoO, (109), and MnTe, (110). In general, an antiferromagnetic semiconductor possesses a "blue shift", while a ferromagnetic semiconductor experiences a smaller than expected energy gap or a "red shift". With these guidelines in mind, one would tend to infer that the magnetic interaction of these diluted magnetic materials is antiferromagnetic. This will be confirmed by the results of chapter 4. Some materials, such as MnTe, have a kink in the thermal dependence of the absorption edge, which coincides with the Neel temperature measured by magnetic susceptibility. No such kink was observed in the results of figs. 3.17 to 3.21.

Analysis of this magnetic effect on the energy gap required the determination of the magnetic contribution, ΔE. In reference 109, this was accomplished by extrapolating from the high temperature range where such effects would be negligible. A

SAMPLE	U	V	E_o(eV)
CdTe	4.17×10^{-4}	1.57×10^{-4}	1.591
$Cd_{0.75}Zn_{0.25}Te$	1.71×10^{-4}	1.77×10^{-4}	1.750
$CD_{0.5}Zn_{0.5}Te$	2.73×10^{-4}	1.98×10^{-4}	1.877
$Cd_{0.25}Zn_{0.75}Te$	6.01×10^{-4}	1.91×10^{-4}	2.126
ZnTe	7.37×10^{-4}	2.05×10^{-4}	2.390

TABLE II Values of the constants obtained in fitting the thermal dependance of the energy gap of samples on the diamagnetic edge to eq. 3.11, with θ=200K and s=2/3.

similar procedure was performed with the results of these materials using eq. 3.11. The main contribution to the change in E_o is from the second term on the right hand side, (34). Because of this and because of the similarity of the alloys of a given x to y ratio, eq. 3.11 could be modified as follows

$$E_o(0) - E_o(T) = N(z)\{UT^s + V\theta[(\coth(\theta/2T) - 1]\} \quad (3.12)$$

where N(z) is some parameter which depends on z. This equation assumes that the parameters U and V will vary in the same way with z, (38). The values of U and V correspond to the z=0 samples in the five pseudo-binary cases, y=0, x=3y, y=x, y=3x and x=0, and have already been calculated. For the diamagnetic cases, N(z)=1 and eq. 3.12 would reduce to eq. 3.11. For the samples of higher z, only the parameters, N(z) and $E_o(0)$ needed to be determined. Eq. 3.12 was used to fit to the high temperature data and to obtained values for N(z) and $E_o(0)$. This enabled the extrapolation at lower temperatures to be performed which in turn allowed one to estimate ΔE.

The next step in the process is to decide what is the range of temperatures for which the magnetic contribution can be neglected. The analysis which will be carried out on the magnetic contribution, once it is isolated from the total effect, is based on a theoretical study, by Alexander et al, (111). They showed that a shift in the bottom of the conduction band occurs around a magnetic critical point. In these materials, the critical point is either a spin glass or antiferromagnetic transition and will be represented by the symbol T_g. The temperatures where they

occur have been determined through measurements of magnetic susceptibility and are presented in detail in chapter 4. Along with those results, ESR measurements, in chapter 5, show that the magnetic effects due to the proximity of these critical points become important at some temperature below which the linewidths show appreciable broadening. With these considerations, the range of the fit was taken to be from room temperature down to somewhere between 100 K and 200 K, depending on the Mn concentration of the particular sample.

The data for the magnetic samples were fit to eq. 3.12 with the values for the resulting parameters listed in Table III. The broken lines in figs. 3.17 to 3.21 represent the low temperature extrapolations and illustrate the amount of the shift in the energy gap. The difference between the measured values and the broken line was taken as the magnetic contribution to the energy gap, ΔE. For the z=0.1 samples, the broken line fits over the entire temperature range. As well, the value of $E_o(0)$ predicted from eq. 3.12 is identical to that obtained from the graphs. This indicates that the magnetic effect is negligible in these samples.

As indicated previously, the values obtained for ΔE were analyzed using the theory developed by Alexander et al, (111). In their work, the authors considered the effects of spin fluctuations around the critical point on the conduction band. In this case the critical point is the characteristic temperature T_g. A different model has been proposed by Matlak et al, (144), to describe the shift in the absorption edge of an antiferromagnetic

semiconductor. This formulation involves the interaction between the band electrons and an ordered arrangement of antiferromagnetic spins, implying that the shift occurs only below the critical point. Such a model does not seem to apply in the present case because there is no regular arrangement of spins in this material. Also an examination of the T_g values from chapter 4 and the energy gap results in figs. 3.17 to 3.21, indicate that the shift is present at temperatures above the critical point. On the other hand, the model proposed by Alexander et al, deals with spin correlations, which are significant above and below the critical point.

Using spin correlation functions, Alexander et al showed that when the temperature is close to the critical point, the dominant contribution comes from short-range spin correlations and that the long range effects become relatively small. The range of temperature over which this condition holds is called the critical region. When the temperature is sufficiently different from T_g, in the noncritical region, the long range correlations become relatively more important.

On this basis, they showed that the variation of ΔE satisfies the following relation

$$\frac{d}{dt}(\Delta E) \alpha -t^{-\mu}$$

where t is the reduced temperature difference, $\frac{|T-T_g|}{T_g}$, and the form of the exponent μ depends upon the particular conditions being considered. If P is included as a constant of

proportionality, then the expression may be written as

$$-\frac{d}{dt}(\Delta E) = -Pt^{-\mu} \qquad (3.13)$$

Integrating eq. 3.13 gives

$$\Delta E = \frac{-Pt^{1-\mu}}{1-\mu} + K \qquad (3.14)$$

where K is a constant of integration. For a semiconductor with antiferromagnetic interaction between the spins, Alexander et al, (111), showed that in the noncritical region, μ should have a value of 0.5 while Kasuya and Kondo, (112), indicated that in the critical region, μ should have a value close to zero.

If the value of ΔE at T_g is written as ΔE_c, the constant of integration in eq. 3.14 can be eliminated and the equation rearranged to give

$$\ln|\Delta E-\Delta E_c| = \ln\frac{P}{1-\mu} + (1-\mu)\ln(t) \qquad (3.15)$$

By plotting $\ln|\Delta E-\Delta E_c|$ vs $\ln(t)$, the values of ΔE obtained from the application of eq. 3.12 can be analyzed and values for μ_c, the critical exponent, and μ_n, the noncritical exponent, can be determined and compared to the predicted values in references 111 and 112. As well, values for P, which from eq. 3.14 measures the strength of the total spin interaction on the band-gap variation may be calculated. It should be noted that because of the form of eq. 3.14, the behaviour of ΔE for $T < T_g$ would be expected to mirror the behaviour for $T > T_g$. Using the values of T_g from chapter 4, ΔE_c was calculated for each sample and the plots

SAMPLE	E_o(eV)	N(z)	E_c(eV)	μ_c	μ_n	P_c (x100)	P_n (x100)
80 00 20	1.908	1.41	1.913	0.04 ± 0.08	-	0.024 ± 0.07	-
70 00 30	2.068	1.63	2.079	0.24 ± 0.04	-	0.14 ± 0.02	-
60 00 40	2.21	1.72	2.232	0.02 ± 0.03	-	0.34 ± 0.02	-
40 00 60	2.553	2.31	2.588	-0.03 ± 0.03	0.52 ± 0.01	1.74 ± 0.09	1.11 ± 0.03
30 00 70	2.694	2.65	2.725	0.1 ± 0.2	0.58 ± 0.02	2.24 ± 0.1	1.15 ± 0.07
60 20 20	2.031	1.4	2.055	0.12 ± 0.01	-	0.09 ± 0.005	-
52.5 17.5 30	2.164	1.61	2.198	0.08 ± 0.02	-	0.29 ± 0.02	-
45 15 40	2.29	1.76	2.314	0.13 ± 0.02	0.57 ± 0.01	0.54 ± 0.02	0.47 ± 0.02
30 10 60	2.56	2.0	2.612	0.05 ± 0.02	0.52 ± 0.03	2.1 ± 0.09	1.27 ± 0.1
40 40 20	2.163	1.34	2.172	-0.09 ± 0.09	-	0.016 ± 0.006	-
35 35 30	2.285	1.51	2.314	0.13 ± 0.02	-	0.36 ± 0.02	-
30 30 40	2.386	1.69	2.417	0.08 ± 0.01	0.5 ± 0.02	0.69 ± 0.01	0.6 ± 0.04
25 25 50	2.541	1.88	2.596	0.01 ± 0.01	0.45 ± 0.04	1.64 ± 0.03	1.3 ± 0.2
20 20 60	2.646	2.16	2.7	0.02 ± 0.02	0.46 ± 0.02	2.15 ± 0.07	1.52 ± 0.07
17.5 17.5 65	2.685	2.03	2.748	0.09 ± 0.02	0.44 ± 0.05	2.89 ± 0.09	2.1 ± 0.02
15 15 70	2.735	2.22	2.794	0.12 ± 0.02	0.45 ± 0.03	3.6 ± 0.15	2.2 ± 0.2
20 60 20	2.286	1.26	2.293	-0.19 ± 0.14	-	0.019 ± 0.008	-
17.5 52.5 30	2.382	1.45	2.403	-0.1 ± 0.04	-	0.24 ± 0.02	-
15 45 40	2.513	1.59	2.547	-0.16 ± 0.04	0.39 ± 0.03	0.65 ± 0.04	0.7 ± 0.07
10 30 60	2.711	1.98	2.757	0.08 ± 0.03	0.59 ± 0.02	2.2 ± 0.1	1.26 ± 0.07
00 70 30	2.572	1.38	2.591	0.06 ± 0.03	-	0.33 ± 0.02	-
00 60 40	2.652	1.61	2.687	0.07 ± 0.02	0.54 ± 0.02	0.86 ± 0.04	0.77 ± 0.06
00 40 60	2.754	1.63	2.81	0.03 ± 0.02	0.59 ± 0.04	1.89 ± 0.05	1.5 ± 0.2

TABLE III Results of the analysis of the magnetic contribution to the energy gap. E_o and N(z) are as defined in eq. 3.12, while E_c, μ and P are as defined in eq. 3.15. The subscripts on μ and P differentiate between the values obtained from the critical and non-critical range. Each sample is identified by the percentage concentration of Cd, Zn and Mn, in that order.

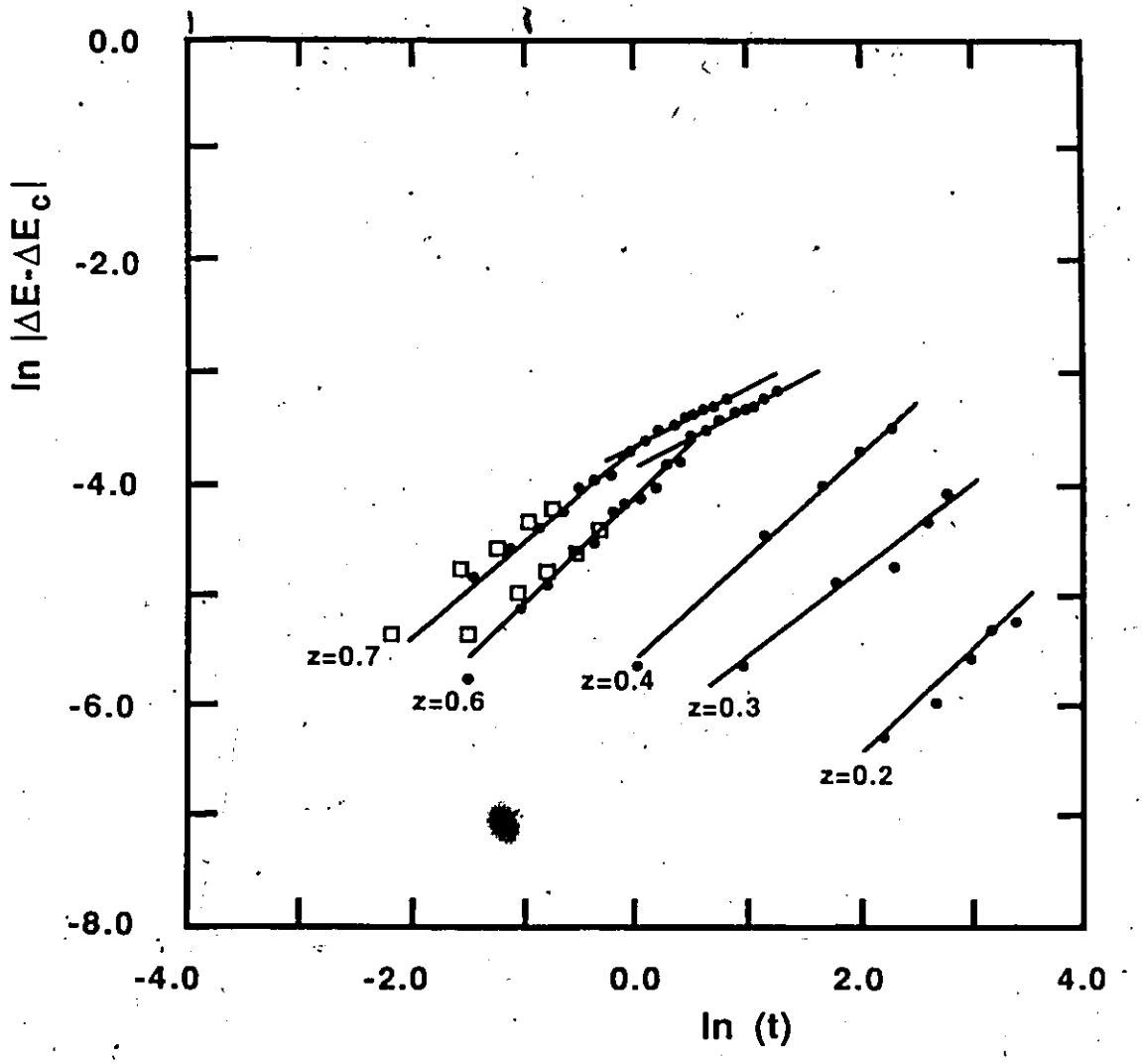

FIGURE. 3.22 Analysis of ΔE for $y \doteq 0$ using eq. 3.15. The solid dots represent values for which $T > T_g$ while the squares represent values for which $T < T_g$.

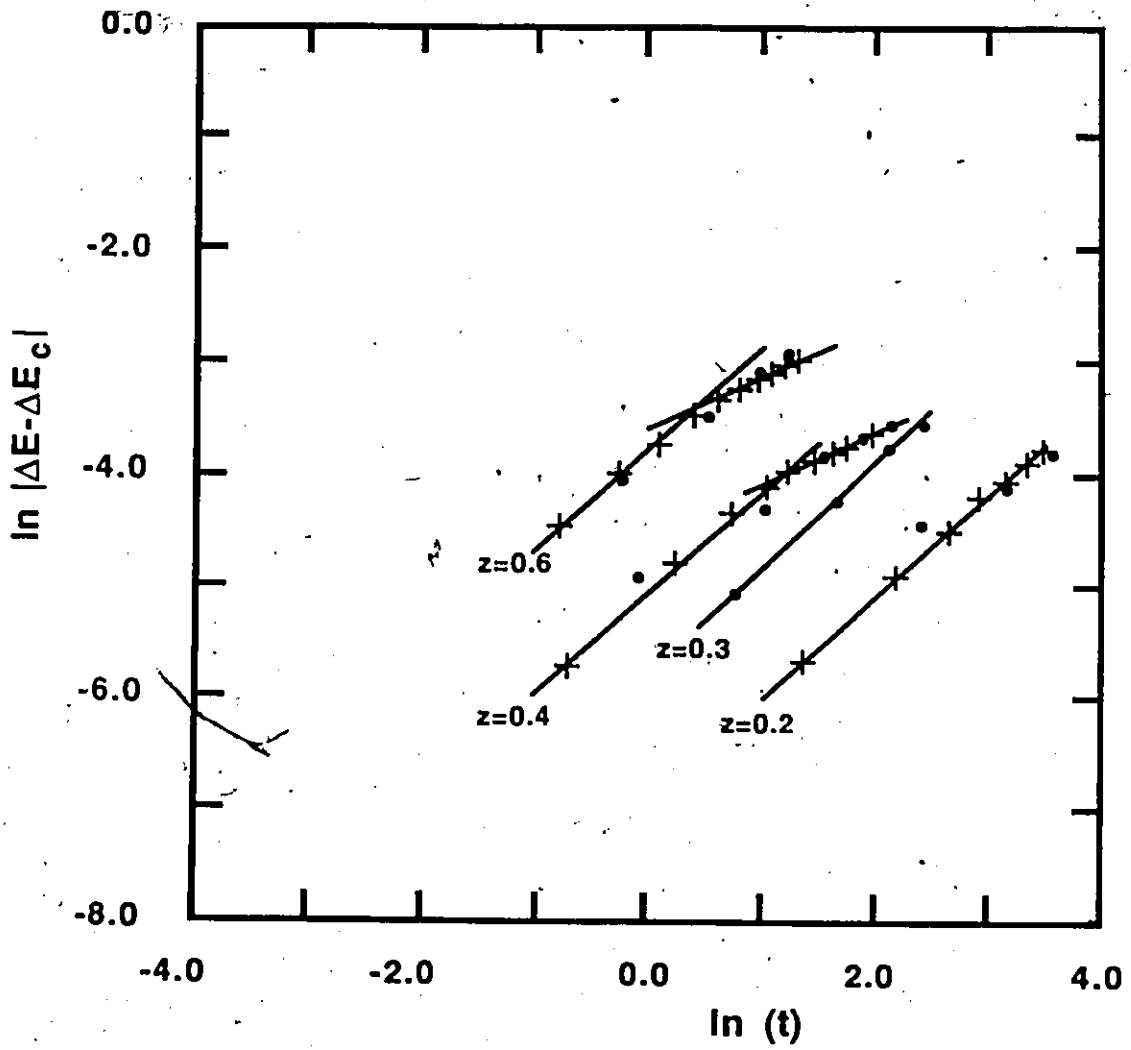

FIGURE. 3.23 Analysis of ΔE for x=3y using eq. 3.15. The solid dots represent actual experimental values while the crosses represent interpolated values. For all cases, $T>T_g$.

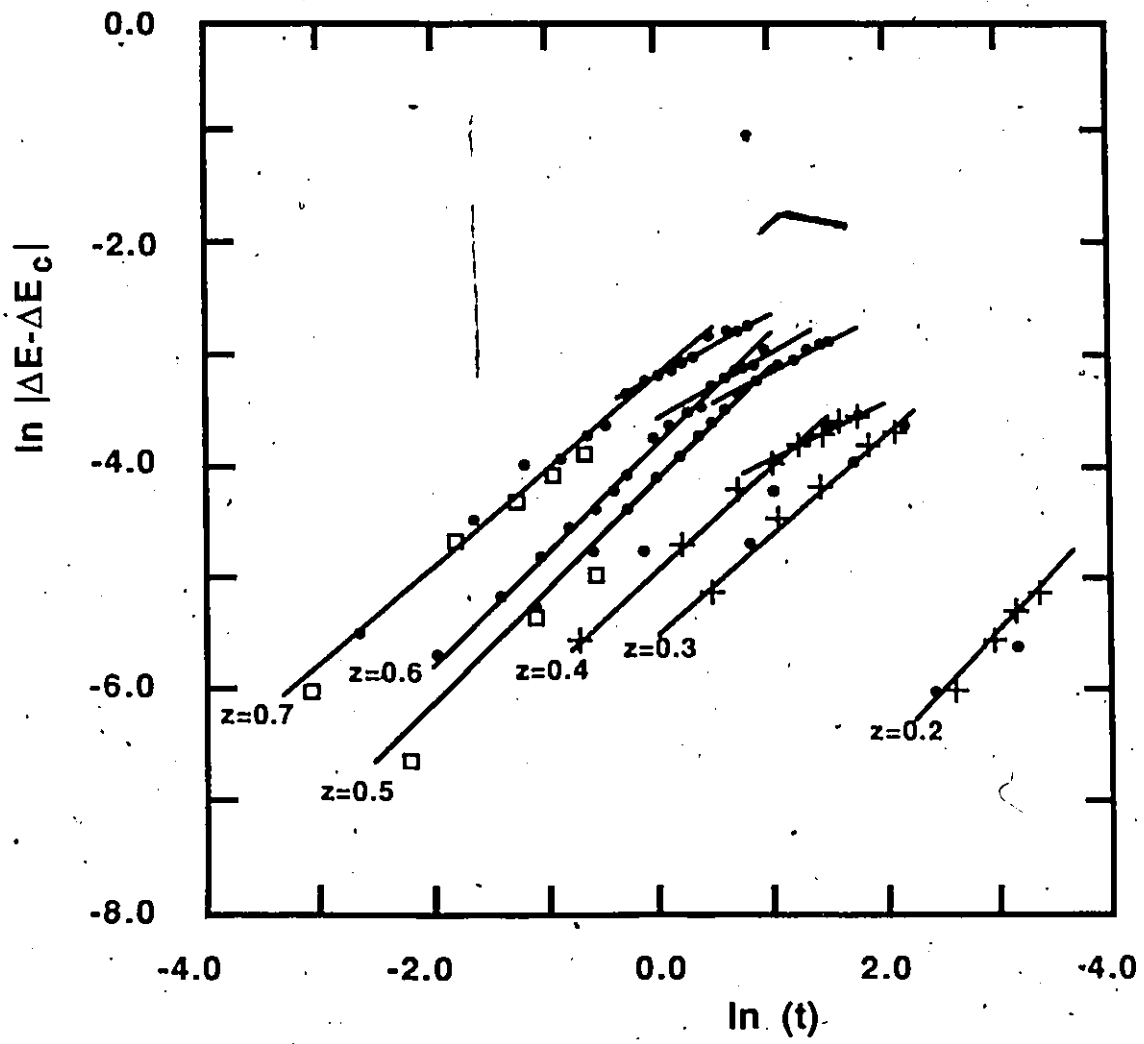

FIGURE. 3.24 Analysis of ΔE for y=x using eq. 3.15. The solid dots represent actual experimental values while the crosses represent interpolated values. The squares are experimental values with $T<T_g$.

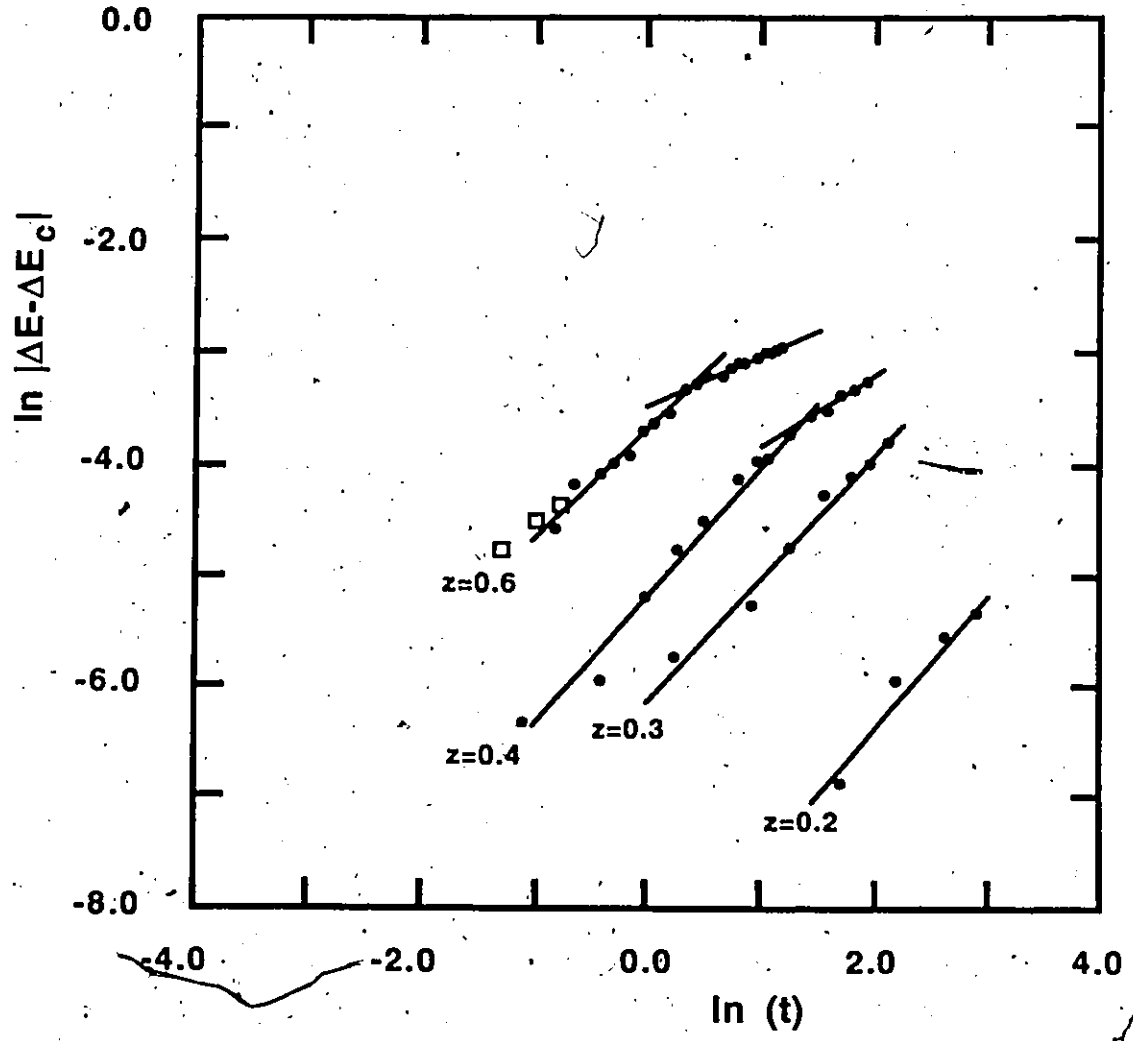

FIGURE. 3.25 Analysis of ΔE for y=3x using eq. 3.15. The solid dots represent values for which $T>T_g$ while the squares represent values for which $T<T_g$.

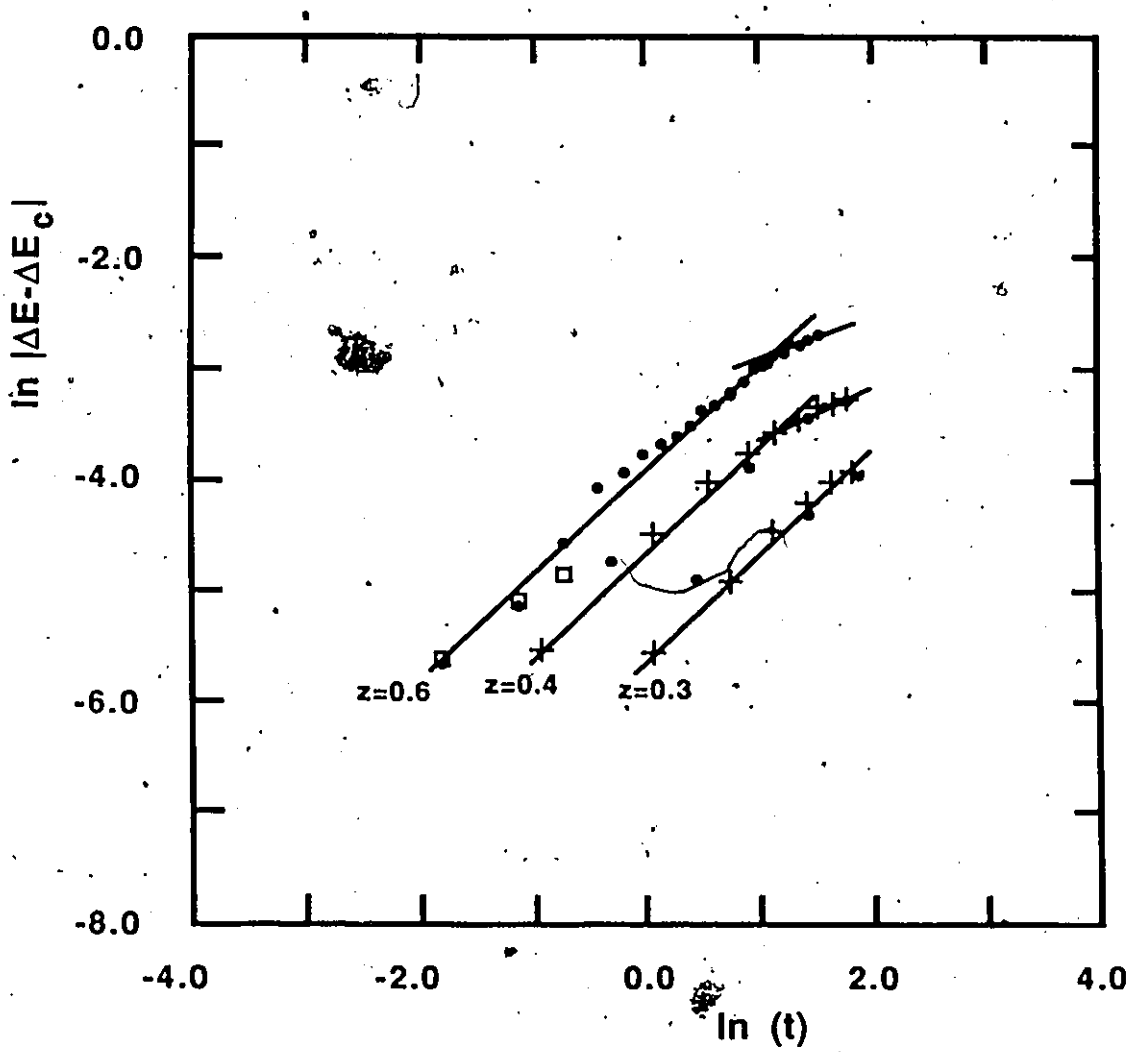

FIGURE 3.26 Analysis of ΔE for x=0 using eq. 3.15. The solid dots represent actual experimental values while the crosses represent interpolated values. The squares are experimental values with $T<T_g$.

based on eq. 3.15 were made and are presented in figs. 3.22 to 3.26.

In these figures, it can be seen that for the cases of high z, each set of points divides into two parts and that, to a reasonable approximation, they may both be fitted to two different straight lines. These two sections presumably represent the critical and noncritical behaviours. Samples with smaller values of z, only had a single linear part indicating that only critical behaviour is observed and that the long range spin correlations never become significant. In some cases, T_g was large enough so that several measurements could be made at temperatures below the critical point. These values are represented by the squares in the figures. They show that the behaviour of ΔE below T_g is similar to that above, as would be expected from eq. 3.14. For each sample, values of P and μ were determined both in the critical range, μ_c and P_c, and, when available, in the noncritical range, μ_n and P_n. These values are summarized in Table III.

For the critical range, the values of μ_c are very close to zero with a mean value of 0.04 and a standard deviation of 0.1. This is in good agreement with the value quoted by Kasuya and Kondo, (112). In the noncritical region, the μ_n values were all found to be close to 0.5 with a mean value of 0.51 and a standard deviation of 0.07. Again, this agrees well with the prediction of Alexander et al, (111).

In figs. 3.27 and 3.28, the values of P_c and P_n are plotted as a function of Mn concentration. It can be seen that in

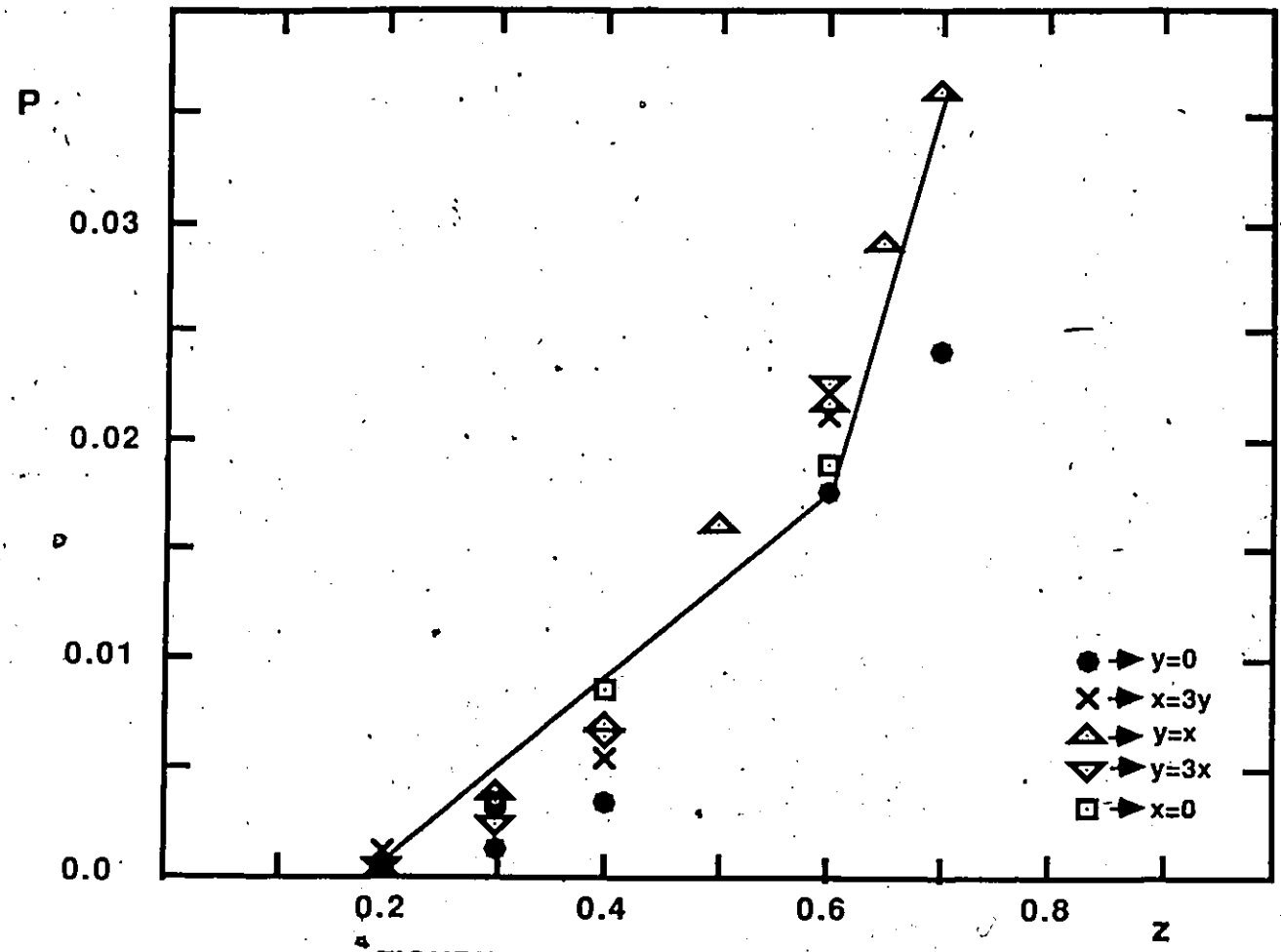

FIGURE 3.27 P_c versus z.

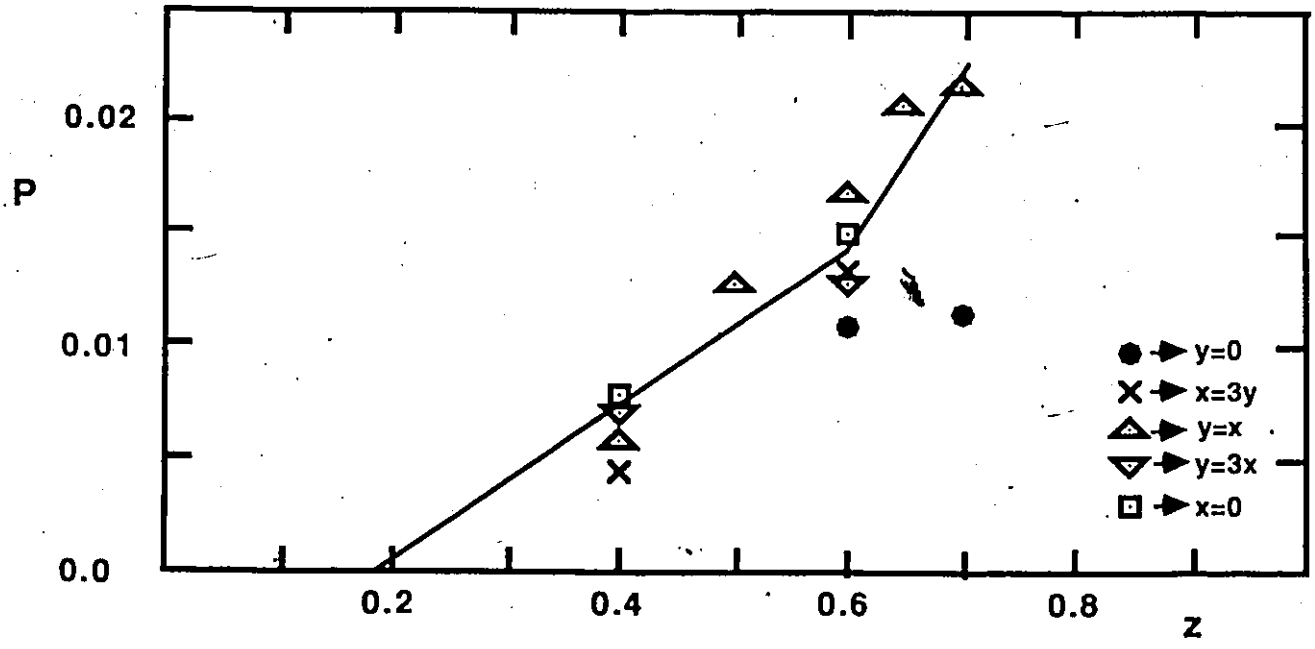

FIGURE 3.28 P_n versus z.

both of these cases, the amount of scatter nearly obscures a small increase in P when the Mn concentration is held constant and the Zn concentration is increased. For samples with $z<0.6$, the points on both graphs decreases with decreasing z and can be made to extrapolate to $z=0.18$ at $P=0$. This last quantity coincides with the nearest neighbour percolation limit determined by magnetic susceptibility results in chapter 4. Below this concentration, the nearest neighbour interaction becomes negligible and the remaining longer range interactions result in a weaker T_g occurring at temperatures below 1 K. It is then not surprising that samples with z below this percolation limit do not have a significant shift in the energy gap. For $z>0.6$ there were fewer values of P available, but in both figures, the values of P increased more rapidly with z than for the more diluted cases. In this range, the magnetic susceptibility results of chapter 4, and the neutron diffraction measurements of Holden et al, (50) and Giebultowicz et al, (51) show that the material behaves like an antiferromagnetic so a change in behaviour is not unexpected. Overall, figs. 3.27 and 3.28 resemble the magnetic phase diagram presented in fig. 4.12.

Estimates of the temperature at which there is a change from critical to noncritical behaviour, T', can be made from figs. 3.22 to 3.26. These values are plotted as a function of z in fig. 3.29 along with some values of T_g from susceptibility measurements. The values of T' appear to give a straight line which can be extrapolated to the origin. Alexander et al do not

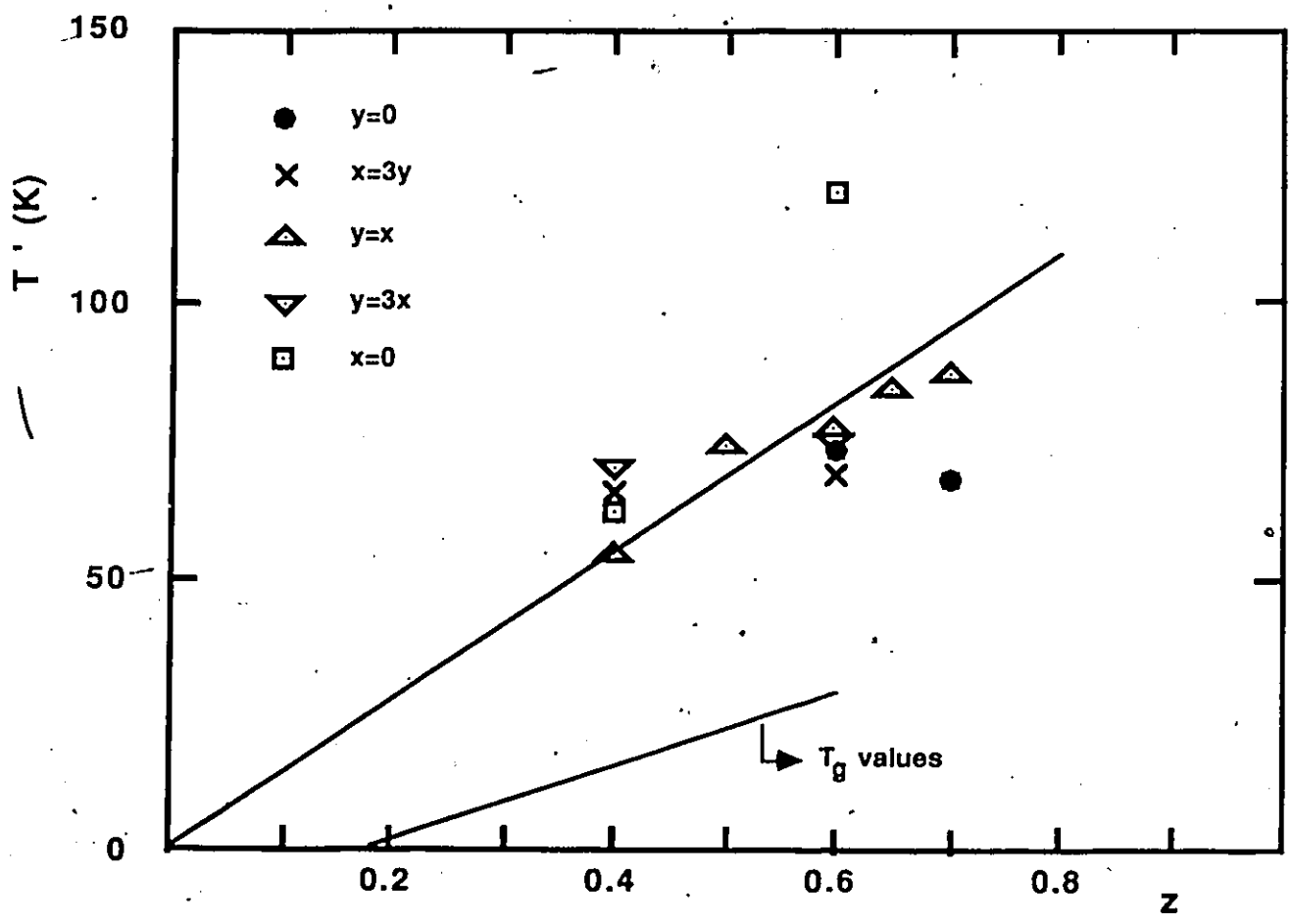

FIGURE 3.29 Temperature at which a Critical-Noncritical transition occurs.

give a value for the limit of the critical range, but it can be seen from fig. 3.29 that in general, $T' \geq 2T_g$. Also, since both T' and T_g give straight lines, it is possible to write

$$T' = aT_g + b \qquad (3.16)$$

and within the scatter of these results, a=2 and b=25 K.

The preceding analysis, which is based on extrapolating the magnetic behaviour by using eq. 3.11, has yielded good results. In order to test the sensitivity of the results to the type of equation used to describe the high temperature variation of the energy gap, a similar analysis was performed for a few samples using an equation proposed by Varshni, (145).

$$E_o(T) = E_o(0) - \alpha T^2/(T+\beta) \qquad (3.17)$$

where α and β are constants independent of temperature. A least squares fit to the energy gap data for CdTe resulted in values for the constants which did not differ to greatly from those of Sundersheshu and Kendelewicz, (107). A fit to the high temperature values for $Cd_{0.4}Mn_{0.6}Te$ and $Cd_{0.3}Mn_{0.7}Te$ yielded a deviation at low temperatures similar to that found when using eq. 3.11. The resulting values for α were found to increase systematically with Mn composition and are presented in Table IV. Values for ΔE were calculated and then analysed using eq. 3.15 and the results are also listed in Table IV. For $Cd_{0.3}Mn_{0.7}Te$ the critical and non-critical values for μ and P turned out to agree very well with those listed in Table III. For $Cd_{0.4}Mn_{0.6}Te$, μ_c and μ_n differed from the corresponding values in Table III, although they still agreed with the expected values. An investigation of some other

SAMPLE	E_o(ev)	$\alpha x10^{-4}$	β	μ_c	μ_n	P_c	P_n
CdTe	1.589	-3.91	120	--	--	--	--
$Cd_{0.4}Mn_{0.6}Te$	2.546	-8.8	120	0.07±0.03	0.45±0.02	1.6±0.1	1.15±0.03
$Cd_{0.3}Mn_{0.7}Te$	2.69	-10.4	120	0.08±0.01	0.60±0.01	2.1±0.1	1.02±0.07

TABLE IV Results of the application of eq. 3.17 to the energy gap variation of some of the samples. E_o, α, and β, are as defined in eq. 3.17, while μ and P are as defined in eq. 3.15. The subscripts on μ and P differentiate between the values obtained from the critical and non-critical range.

samples indicated that the size of the magnetic contribution to the energy gap predicted by eq. 3.17 was always the same as that predicted by using eq. 3.11.

It is often of interest to know the value of E_o near T=0. These may be determined from figs. 3.17 to 3.21 and are plotted as a function of z in fig. 3.30. Although each set of points may show a slight curvature, within the limits of experimental scatter, it is possible to draw five straight lines through the data. As with the room temperature results, the five lines intersect at one point for z=1. This value of 3.22 eV corresponds to $E_o(0)$ for MnTe in the zinc blende form. For comparison, the room temperature results for x=0 and y=0 as estimated by eq. 3.8, were plotted as two sets of broken lines. The difference between $E_o(0)$ and $E_o(300)$ is seen clearly with a large increase occurring in the slope of the lines when the temperature is lowered from T=300 K to T=0 K. The magnitude of this effect may be demonstrated by considering the results for two samples on the x=0 edge. For z=0, the value of $E_o(0)-E_o(300)$ is 0.11 eV, while for z=0.6, the value is 0.29 eV.

In this section, it has been shown that there is a strong magnetic influence on the energy gaps of this material at low temperatures. This effect increases with Mn concentration, as would be expected. The results also show that the magnetic influence increases with y composition at constant z. This might also be expected since the same behaviour was observed for the T_g values. It will be shown in the next chapter that such an

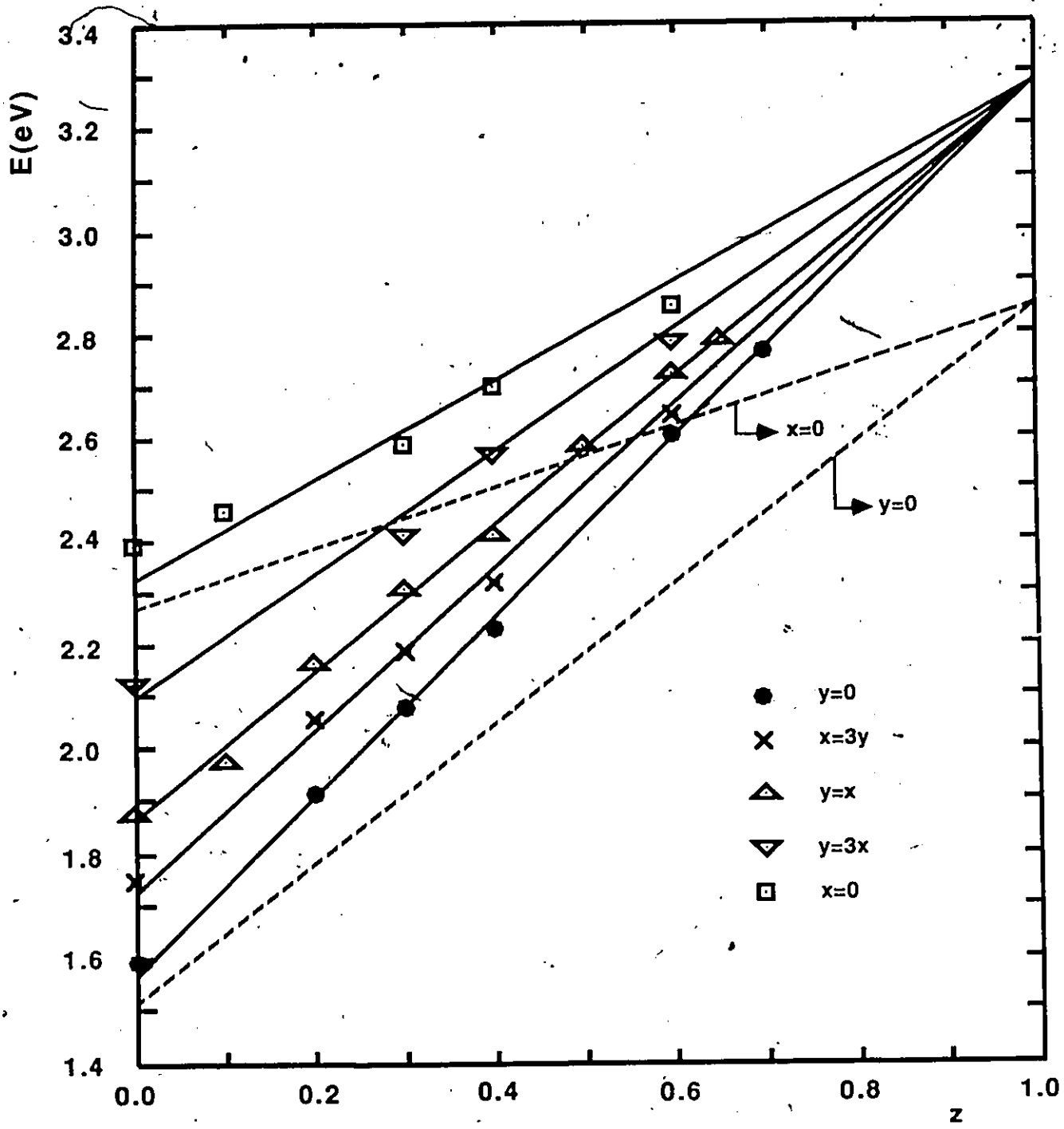

FIGURE 3.30 Plot of the energy gap, extrapolated to T=0 K, versus Mn composition. The solid lines are drawn so as to intersect at one point for z=0. The broken lines represent the room temperature values obtained from Fig. 3.11.

increase can be attributed to the decrease in lattice parameter which was reported in the previous chapter.

CHAPTER 4

MAGNETIC SUSCEPTIBILITY MEASUREMENTS

4.1 INTRODUCTION

An electron bound to a nucleus possesses a magnetic moment due to its spin and orbital angular momenta. The magnetic moments associated with these angular momenta are given by

$$\mu_s = -g\mu_B s$$

$$\mu_l = -g\mu_B l$$

where s and l are the spin and orbital quantum numbers, μ_B is the Bohr magneton and g is the spectroscopic splitting factor, which has a value very close to 2.0 for a free electron. For atoms with more than one electron, it is necessary to consider the combination of all the spin and orbital momenta. The method used is called Russell-Saunders coupling and consists of a vector addition of all the l and s quantum numbers to form resultant L and S values. These are then subsequently combined to form the total angular momentum quantum number J. The total magnetic moment for a free atom is then

$$\mu_J = -g\mu_B J. \qquad (4.1)$$

The g factor is now given by the Landé equation;

$$g = 1 + \frac{J(J+1) + S(S+1) - L(L+1)}{2J(J+1)} \qquad (4.2)$$

The vector addition of the quantum numbers results in only partially filled electronic levels possessing a non-zero resultant momentum. Because of this only atoms such as Mn, can have a net magnetic moment. The five unpaired 3d electrons of Mn results in a

value of spin momentum, S, equal to 5/2. In a solid, the angular momentum, L, may be quenched by the crystal field (19, 43). Consequently, it may not contribute to the total magnetic moment. Substituting S=J=5/2 and L=0 into equation 4.2 gives g=2 for Mn.

According to their magnetic properties, materials may be classified into three general categories; diamagnetic, paramagnetic and exchange coupled magnetic systems. The response of these materials to an applied magnetic field, especially as a function of temperature, provides one method of distinguishing between them. For diamagnetic materials, this magnetic susceptibility, which is defined as $\chi=M/H$, turns out to be negative and independent of temperature. Paramagnetic systems have a positive susceptibility and at high temperatures and in small magnetic fields, follow the Curie Law, (19);

$$\chi = \frac{Ng^2\mu_B^2 J(J+1)}{3k_B T} = \frac{C}{T} \qquad (4.3)$$

where C is the Curie constant, N is the number of magnetic atoms, k_B is the Boltzman constant and T is the temperature in Kelvin. The spectroscopic splitting factor, g, is given by equation 4.2.

Exchange coupled systems possess the common feature of having interactions between the atomic magnetic moments that result in some kind of alignment or correlation among these various moments or spins in the lattice. This category includes such substances as ferromagnetic, antiferromagnetic and ferrimagnetic materials. In these systems, the coupling occurs through an exchange interaction which is a quantum mechanical phenomenon with

no classical analog. It arises from the Pauli Exclusion Principle and from the indistinguishability of electrons and depends on the overlap of the electronic wave functions, (49). There are essentially two forms of exchange, direct and indirect. Direct exchange occurs through the direct overlap of the electronic wave functions. Indirect exchange occurs through an intermediary such as through the outer p electrons of a diamagnetic ion. An example of this superexchange, would be the interaction which occurs in MnO. Here the Mn magnetic ions are coupled together through an oxygen ion. Another type of indirect exchange would be the RKKY interaction which was mentioned in chapter 1. In this case, the coupling occurs through the conduction electrons.

The exchange interaction tends to orient a pair of spins in a particular manner and competes with thermal processes which tend to disrupt the correlation. A ferromagnet has its spins arranged in a parallel manner. Above a certain characteristic temperature, the thermal agitation overcomes the exchange forces and the alignment is lost. In this state, the material behaves like a paramagnet. At temperatures far above this point and in small magnetic fields, the susceptibility may be described by the Curie-Weiss law, (19);

$$\chi = \frac{C}{T-\theta} \qquad (4.4)$$

Here θ is the ferromagnetic ordering temperature and is positive, and C is the Curie constant as defined in eq. 4.3.

An antiferromagnet, on the other hand, has its spin

arranged in an antiparallel manner. This may be demonstrated most simply by a body centered cubic lattice. Such a lattice can be divided into two sublattices, one represented by the body center site and the other by the corner sites. Each sublattice consists of an internal parallel alignment but is directed oppositely to the other. Again the alignment is lost above a characteristic temperature, known as the Neel point, T_N, and the material assumes a paramagnetic like state. At high temperatures above T_N and in a small magnetic field, the susceptibility is also described by eq. 4.4, (19), but with the Curie-Weiss temperature, θ, negative. An example of the temperature varying susceptibility is shown in fig. 6.1.

Note that if θ in eq. 4.4 is zero, it reduces to eq. 4.3. Therefore in all three of the cases discussed, the susceptibility at temperatures above any ordering point and in a small magnetic field is described by eq. 4.4, with θ indicating the type and strength of the exchange interaction. A negative value denotes negative exchange and antiferromagnetic behaviour while a positive value means that the exchange is positive and the interaction is ferromagnetic. Paramagnetic materials do not possess a significant exchange interaction, consequently, θ is zero.

A spin glass system is different from the types discussed above in that the coupling doesn't produce a long range order. The spins end up being frozen in random directions. Above a characteristic temperature, the thermal processes overcome the freezing and paramagnetic behaviour occurs. The magnetic

susceptibility variation with temperature is similar in appearance to an antiferromagnet, fig. 6.1, with the freezing temperature, T_g, occurring at the cusp.

This freezing of spins may be understood by considering the concept of frustration, (39, 66). Frustration occurs when there is a competition in the interactions between spins. For example, a magnetic moment sitting in a crystal lattice may experience an exchange force with its nearest neighbours which tend to align it in a particular direction. At the same time, it may experience a force with its next nearest neighbours which tend to align it in a different direction. If the two forces are comparable in strength, then the resulting orientation will be an equilibrium position quite different from the orientation due to the effects of either the nearest or next nearest neighbour. Extending this to an entire lattice would result in a set of spins which are frozen in random orientations.

In metallic spin glasses, Mn ions are coupled indirectly through the conduction electrons. This process is known as the RKKY (Ruderman-Kittel-Kasuya-Yosida) interaction, (39). The exchange oscillates between positive and negative values as it decays with distance. This results in competing antiferromagnetic and ferromagnetic interactions from magnetic moments of differing distances which in turn leads directly to frustration. On the other hand, in some SMSC's, the carrier concentration is not high enough to support a significant RKKY effect. This is especially true for the $Cd_xZn_yMn_zTe$ system since it has such a large energy

gap. In addition to this, the exchange coupling is believed to be solely antiferromagnetic, (67), so there is no competing ferromagnetism to cause frustration.

The ordering of spins with only antiferromagnetic interactions is affected by the type of lattice involved. The simplest arrangement occurs with a body centered cubic lattice, where all nearest neighbours are aligned antiparallel to each other while the next nearest neighbours are aligned parallel. With an FCC lattice, the ordering is not as straight forward. One possible arrangement is illustrated in fig. 4.1, (67). If one considers nearest neighbours only, one can see that the orientation of any one spin is influenced by competing forces. Thus it is not difficult to imagine that the spin alignment can be frustrated with a diluted lattice. With his calculations, De Seze, (23), has predicted that such behaviour does occur under these conditions. This lattice effect is believed to be the source of the spin glass properties in these materials.

Clustering of magnetic moments may play another major role in these magnetic alloys. The importance of clusters has long been recognized in metallic spin glass systems because of its success in explaining some anomalous effects. As a result, a lot of effort has gone into developing cluster theories of spin glasses, (see for example refs. 21, 26, 42, 61 and 62). In a diluted magnetic material, the magnetic ions would be distributed randomly among the available lattice sites. Such a random distribution would mean that some proportion of the ions are grouped together into clusters

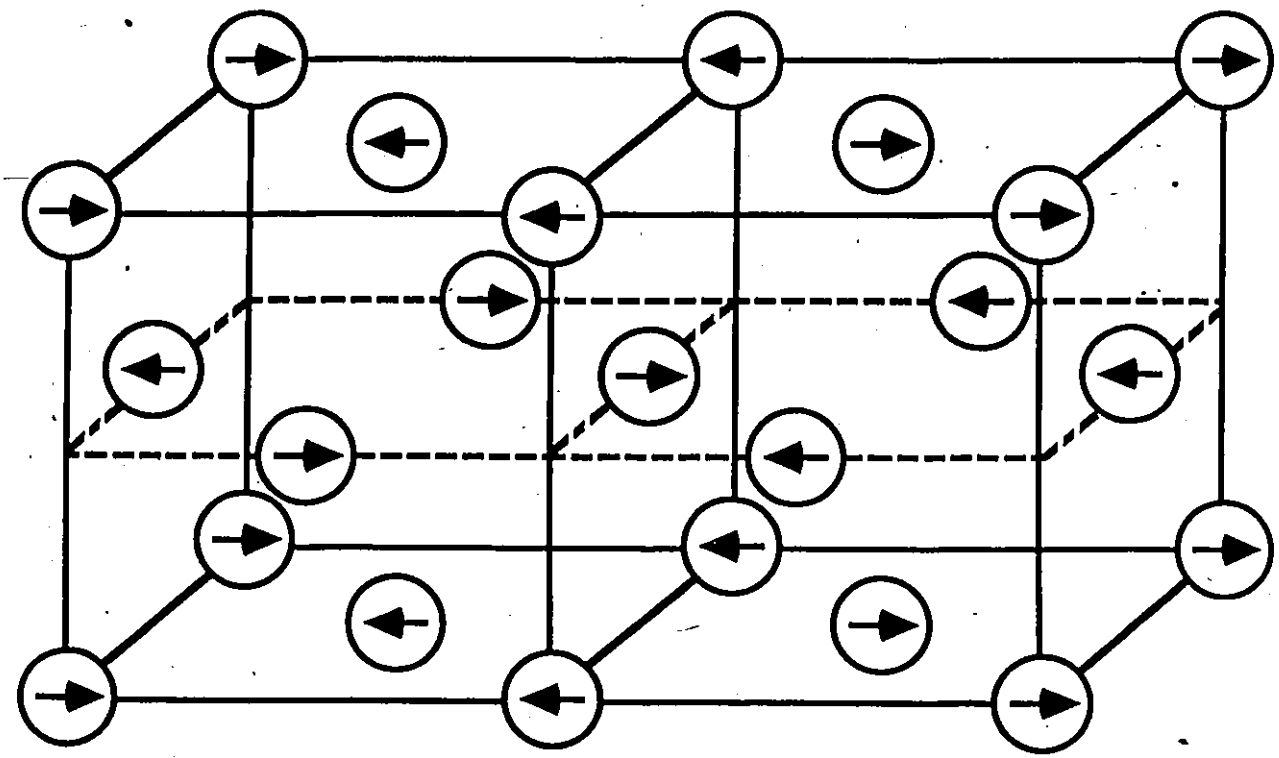

FIGURE 4.1 Arrangement of spins in a type III antiferromagnet.

of various sizes. The proportion of ions and the average size of the clusters would depend on the concentration of ions. They may also be affected by chemical clustering, a term which is meant to account for all effects which might cause the distribution of ions to be nonrandom. These physical clusters remain unchanged over the range of temperatures in which the magnetic susceptibility is measured.

At low temperatures, the interactions between the magnetic ions will become important and magnetic clusters may form. A magnetic cluster consists of a group of magnetic ions which are completely aligned or frozen. In the extreme case each magnetic cluster becomes an independent entity which is free to rotate as a whole in the presence of other well defined magnetic clusters. The size of these clusters will depend on the distribution of the physical clusters and is probably affected by the temperature.

In SMSC, effects of clustering have been postulated from measurements of magnetization, (62, 63). In ref. 62, the authors discuss magnetization scaling laws in terms of an effective concentration which is related to the clustering. They conclude that these systems, ($Cd_{1-z}Mn_zTe$ and $Cd_{1-z}Mn_zSe$), are made of antiferroclusters whose size increases with Mn concentration and that they would be described more accurately by the term cluster-glass. This of course implies that the clusters are well defined entities and that the important interaction which leads to the long range freezing is that which occurs between these hard clusters and not between the individual spins. However, the

results to be presented in section 4.4 suggest that the presence of clusters is not all that significant to the freezing process for $Cd_{1-z}Mn_zTe$.

Along with the magnetization results mentioned above, specific heat measurements on SMSC with small concentrations of the magnetic component, (18, 64, 65), have tended to show that the cluster distribution was not random and that there might be significant amounts of chemical clustering, but this conclusion has been questioned, (140). More evidence of chemical clustering in $Cd_{1-z}Mn_zTe$ crystals was deduced by Escorne and Mauger, (63), from their measurements of susceptibility and magnetization. However, recent work by Ayadi et al, and Oseroff et al, (119), have shown that this last effect might in fact be a result of inhomogeneous crystals.

4.2 MEASUREMENT OF SUSCEPTIBILITY

The susceptibility of a magnetic material is found by measuring its magnetization when under the influence of an applied field. This was accomplished by using a SQUID magnetometer. The high sensitivity of the SQUID enabled measurements to be carried out on samples of small masses. Other methods of measurement, such as using mutual inductance or a torsion balance, require a large mass, typically about four to five grams. However, with the SQUID, the magnetization of samples as small as 0.02gms could be measured, so the apparatus did not have to be designed to accommodate large samples.

One other advantage that a SQUID magnetometer has over other types of magnetometers, is that only a small applied magnetic field is needed to detect the magnetization. Previous measurements on the systems, $Cd_{1-z}Mn_zTe$ and $Cd_{1-z}Mn_zSe$, (25), as a function of magnetic field intensity, indicated that the value of the spin glass transition temperature was affected by the different applied fields. These results showed a decrease of three to four degrees in some samples, in fields of 30 kgauss.

The major disadvantage with the SQUID is the fact that the detection system needs to be in a superconducting state. This requires the detecting coils to sit in liquid helium throughout the experiment. At the same time, the sample, which must be in close proximity to the coils, has to have a variable temperature environment. This makes it very difficult to reach a high sample temperature without boiling off a large quantity of helium.

The word SQUID is an acronym for Superconducting QUantum Interference Device. This instrument may be used to measure very small magnetic fields with an extremely high degree of accuracy. It is based on two physical principals; the quantization of flux inside a superconducting loop and the Josephson effect, (88). Basically, the SQUID can be thought of as a flux counter which counts the "quanta" of flux through the coil. This "quantum" is equal to h/2e, Planck's constant divided by twice the electronic charge. This value is of the order of 2×10^{-7} Gcm^2. The particular device used in these measurements could measure small fractions of a quantum resulting in an instrument sensitivity of about a

thousandth of one flux quantum.

The experimental setup used to measure the susceptibility is illustrated in fig. 4.2. The cryostat is a typical double dewar system with liquid helium in the inner dewar and liquid nitrogen in the outer. A lead shield inside the helium bath surrounded the inner part of the system and so reduced any penetration from external stray fields. A solenoid and a niobium cylinder were placed inside this shield in the helium bath. The solenoid provided a magnetic field which was trapped by the superconducting niobium when liquid helium was transferred into the dewar. A field ranging between 25 to 30 gauss was applied through the solenoid. The niobium cylinder also provided additional magnetic shielding.

A SHE model 330 SQUID was used. The magnetization was detected by a pair of oppositely wound superconducting pick up coils. The change in flux in these coils was measured by the SQUID in a flux transformer. The pick up coils provided two consecutive measurements of the magnetization of the sample as it successively passed through each of the sets of coils. Since they were oppositely wound, the two signals possessed opposite polarity. The coils, as mentioned previously, were also in contact with the liquid He, in order to keep them below their superconducting transition temperature.

A sample was placed on the end of a long plastic rod which extended outside the cryostat and was attached to a reversible motor. This enabled different samples to be inserted and extracted without opening up the whole system as well as providing a means

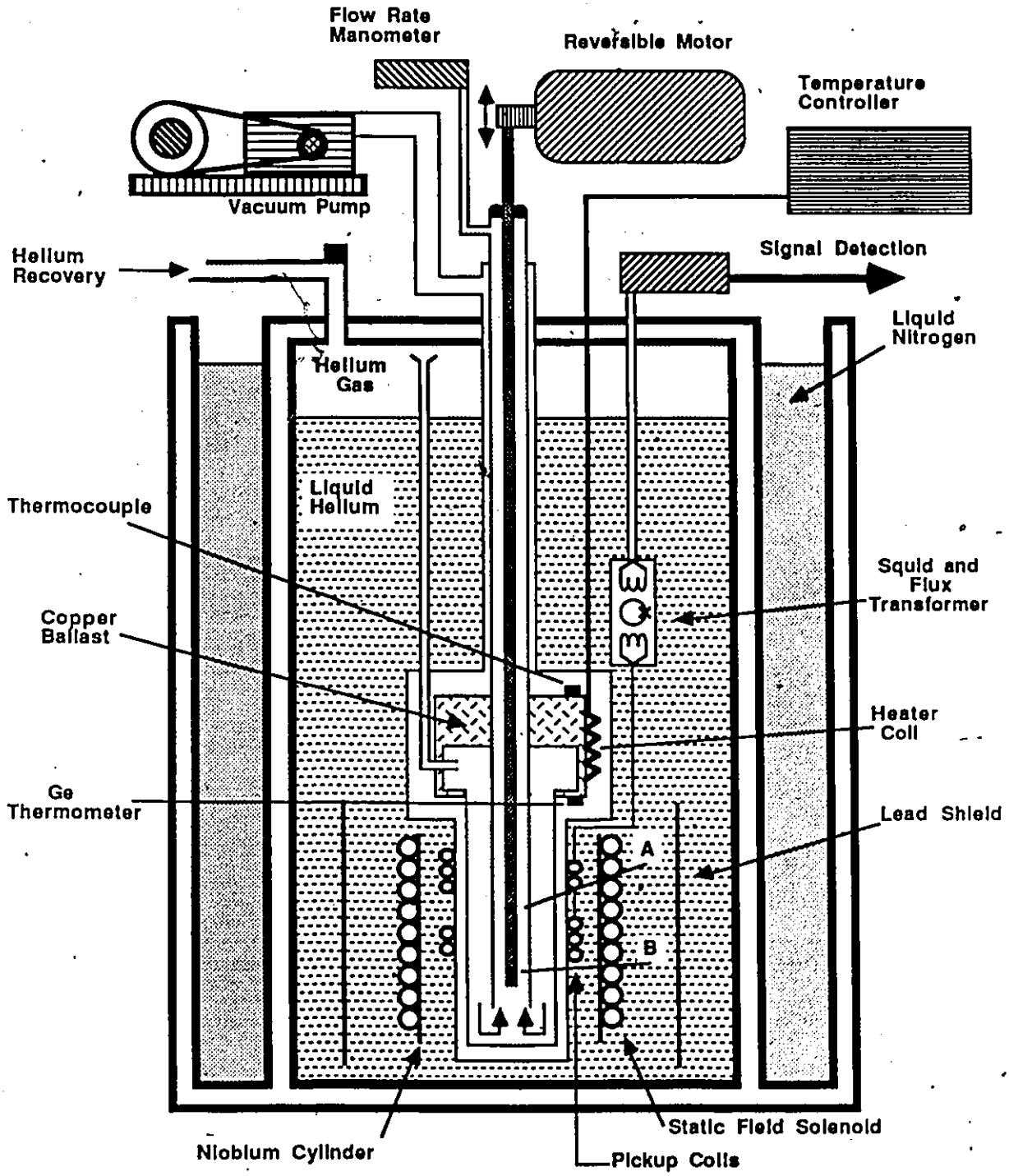

FIGURE 4.2 Magnetic Susceptibility Apparatus. A sample is placed in postion B. A second sample or a paramagnetic salt is placed in position A.

for driving the sample through the pickup coils. To prevent the magnetization of the sample holder from interfering with the measurement of the sample, a very pure copper container was attached to the end of the plastic rod to hold the sample. This consisted of a small capsule, for holding the sample, which could be screwed to the bottom of a short rod of copper. This arrangement did succeed in eliminating signals due to the sample holder, but it did prove to be difficult to clean all the remnants of one sample from the capsule when preparing for the next one.

To control the temperature of the system, He gas was circulated around the sample. The gas from over the helium bath was allowed to enter a tube, which passes into the inner container, under its own pressure. The tube was wrapped several times around a copper ballast. A heating coil was also attached to the copper block. The He gas was heated as it passed through this point. From there the gas entered a double concentric tube system which directed it around the sample and out of the dewar. The pressure of the gas could be controlled by a pinch clamp on the exit tube and was usually maintained at about 2.0mm of mercury.

A great deal of effort went into obtaining accurate determinations of the temperature of the sample without interfering with the magnetic measurement. Any temperature indicator would have to be far enough away from the sample so that it would not add any magnetic flux to the measurement. But since the heating of the sample is accomplished through a gas flow, too large a separation may result in the temperature sensor and the sample being at

different temperatures. Three different thermometers were used, each one placed in a different location. A chromel:gold 0.07% iron thermocouple was positioned on top of the copper block. A calibrated Ge resistance thermometer was placed near the bottom of the block. Finally, a magnetic thermometer was placed on the sample holder about 10 cm above the sample. The thermocouple was connected to the temperature controller and so was used as a reference for controlling the temperature. The Ge thermometer was used to calibrate the magnetic thermometer at 4.2K. The magnetic thermometer consisted of a paramagnetic salt whose susceptibility was known to obey the Curie law.

Numerous measurements were made using these three thermometers. After examining and comparing the temperature data, it was concluded that there was less than a one degree disagreement between them. Consequently, subsequent measurements were performed without the magnetic thermometer, substituting in its position another sample. This enabled two samples to be measured simultaneously.

To determine values of the Curie-Weiss constant, (eq. 4.3), the absolute magnetic susceptibility had to be determined. The measuring system was calibrated by Dr. Gilles Lamarche using small lead spheres. The relation obtained is as follows;

$$\chi = \frac{(1.25\times10^{-5})V}{(i/2+0.23)M} \quad \text{emu/gm} \qquad (4.5)$$

The units of this equation are electro magnetic units per gram of sample. The SQUID voltage is represented by V and the mass of the

sample in grams, by M. The applied magnetic field is allowed for by the i/2 term with i representing the current through the solenoid in mA. The largest amount of error in determining the absolute susceptibility rested in the determination of the the applied field and sample mass. Together, they resulted in a total uncertainty of about 2%. Using these units for susceptibility requires an adjustment to eq. 4.3;

$$\chi = \frac{zN_A g^2 \mu_B^2 J(J+1)}{3k_B W(T+\theta)} \quad \text{emu/gm} \qquad (4.6)$$

where N_A is Avogadro's number and z is the Mn concentration. W is the molecular mass of each sample and is given by;

$$W = (xM_{Cd} + yM_{Zn} + zM_{Mn}) + M_{Te}$$

where M_{Cd} is the molecular mass of Cd, etc. If eq. 4.6 is multiplied by W, then the susceptibility will be expressed in units of emu/mole. The units of χ which will be used to present the data in the next sections are in emu/(mole of Mn) and were obtained by further dividing eq. 4.6 by z.

4.3 Results and Discussion of Susceptibility Measurements

4.3.1 Spin Freezing

Measurements were carried out over the entire range of solid solution and for temperatures between 4.2 K and 280 K. Examples of the low temperature susceptibility are presented in figures 4.3 through 4.7. Samples with z concentration between 0.25 and 0.6 were found to exhibit a sharp cusp at a characteristic temperature, T_g. In their work on $Cd_{1-z}Mn_zTe$, Galazka et al,

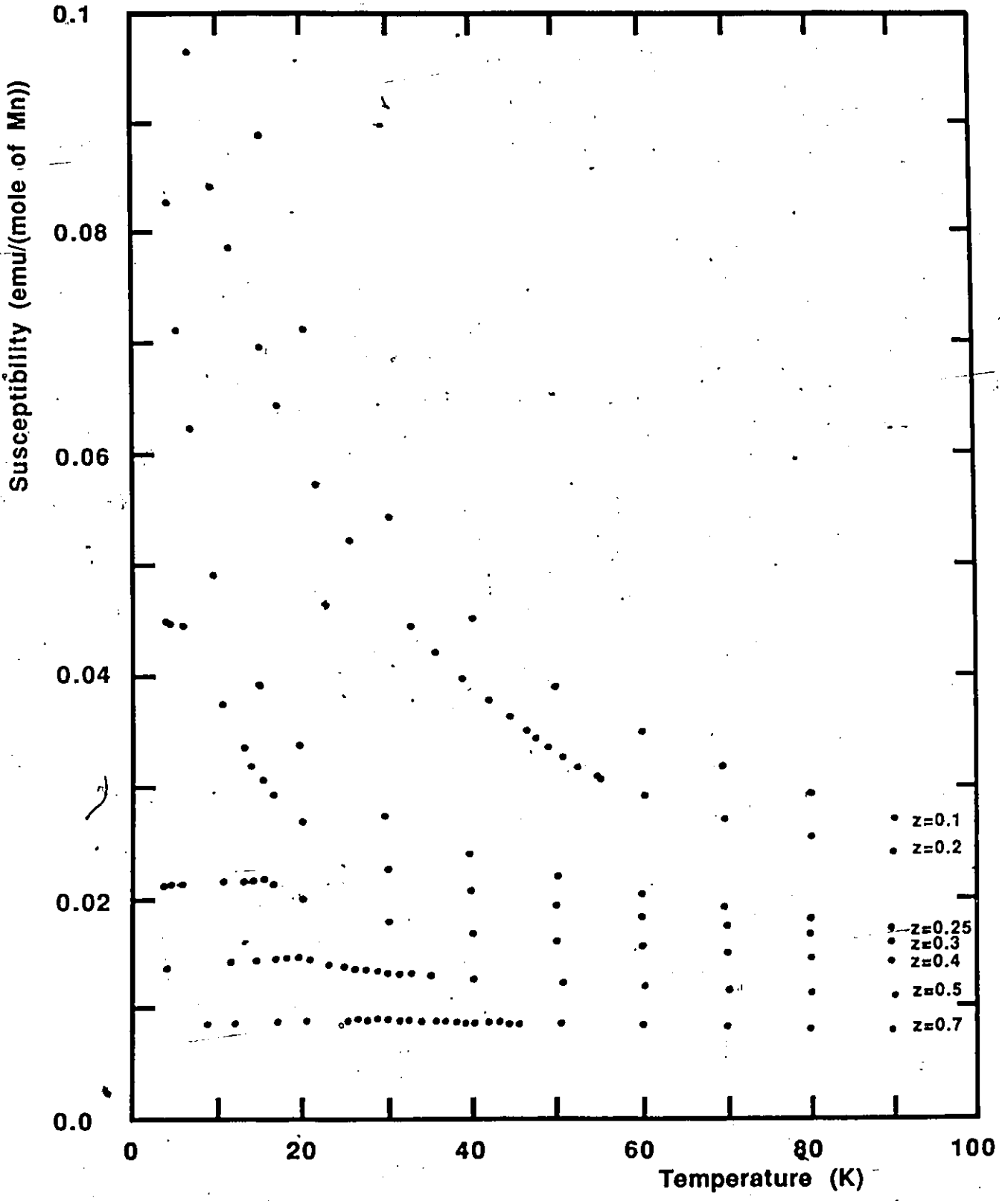

FIGURE 4.3 Results of measurements of magnetic susceptibility for some samples with y=0.

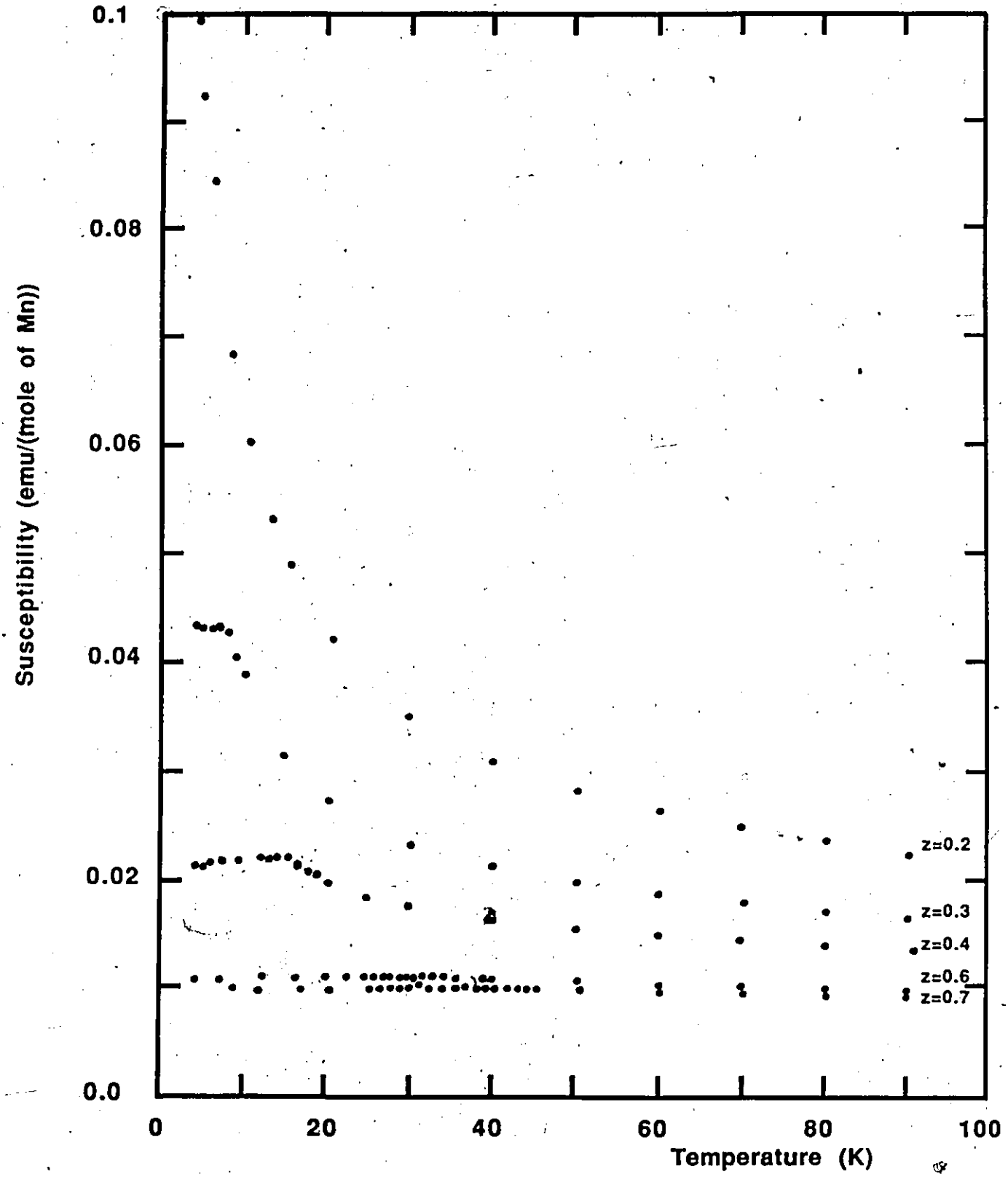

FIGURE 4.4 Results of measurements of magnetic susceptibility for some samples with x=3y.

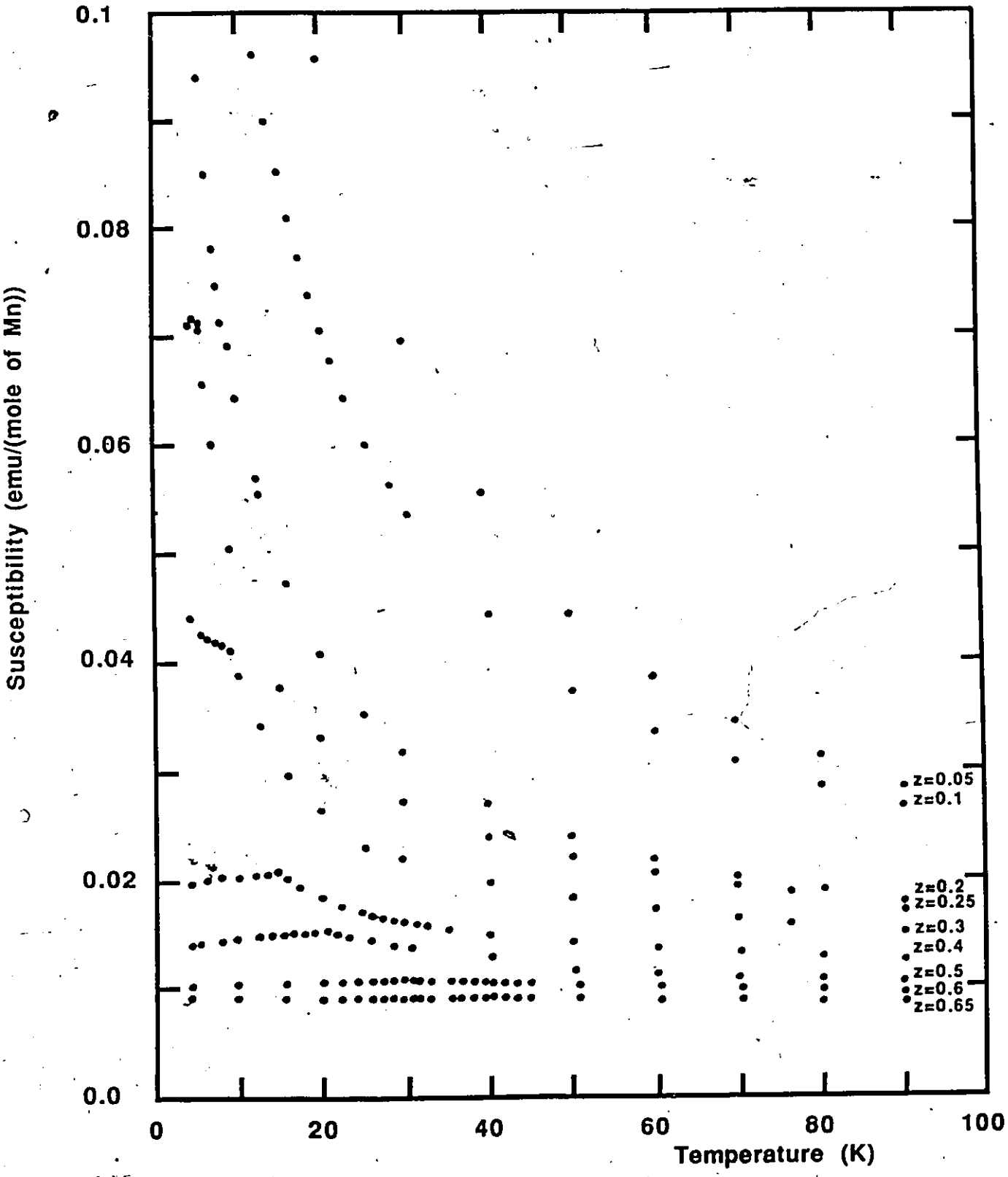

FIGURE 4.5 Results of measurements of magnetic susceptibility for some samples with y=x.

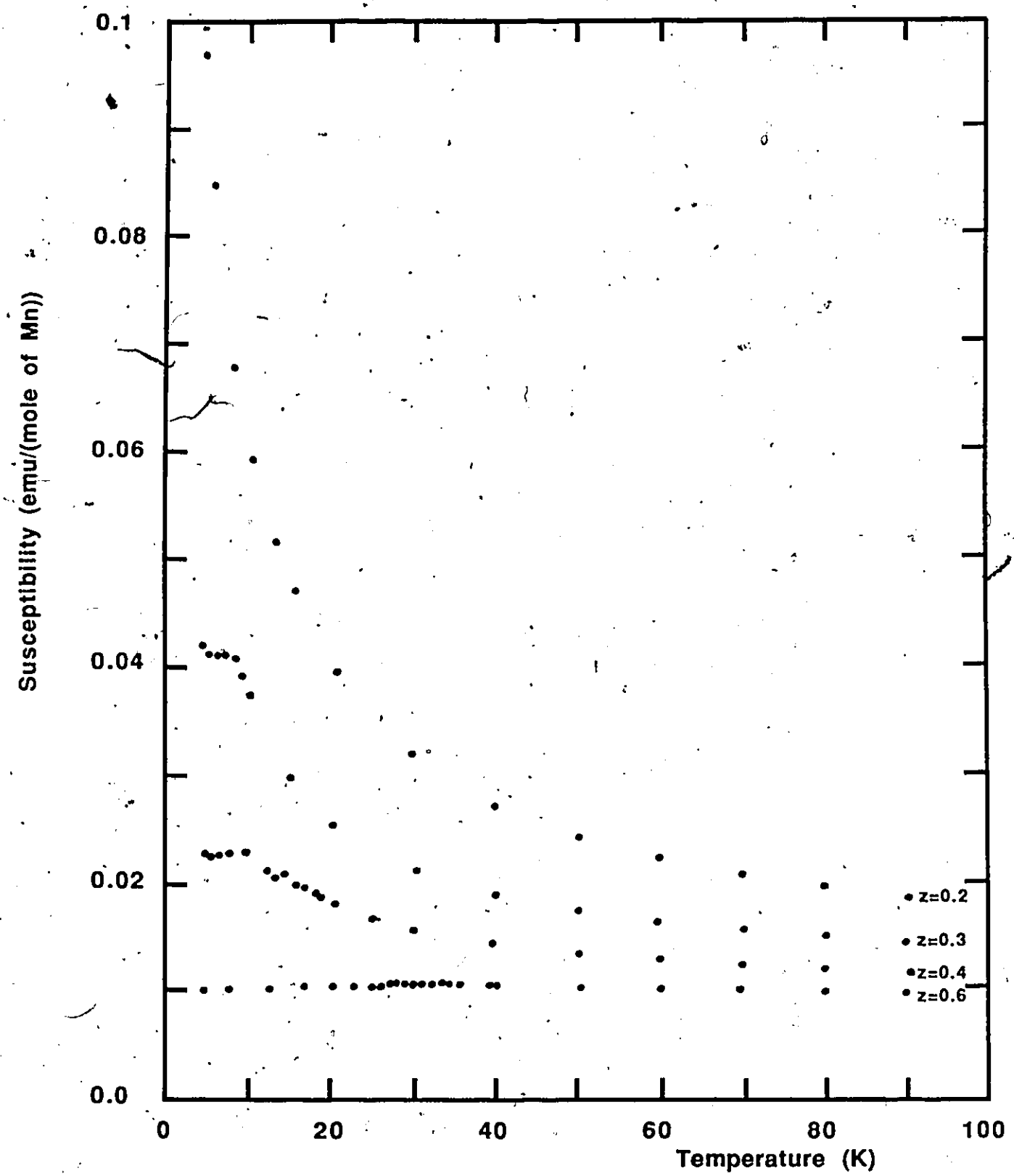

FIGURE 4.6 Results of measurements of magnetic susceptibility for some samples with y=3x.

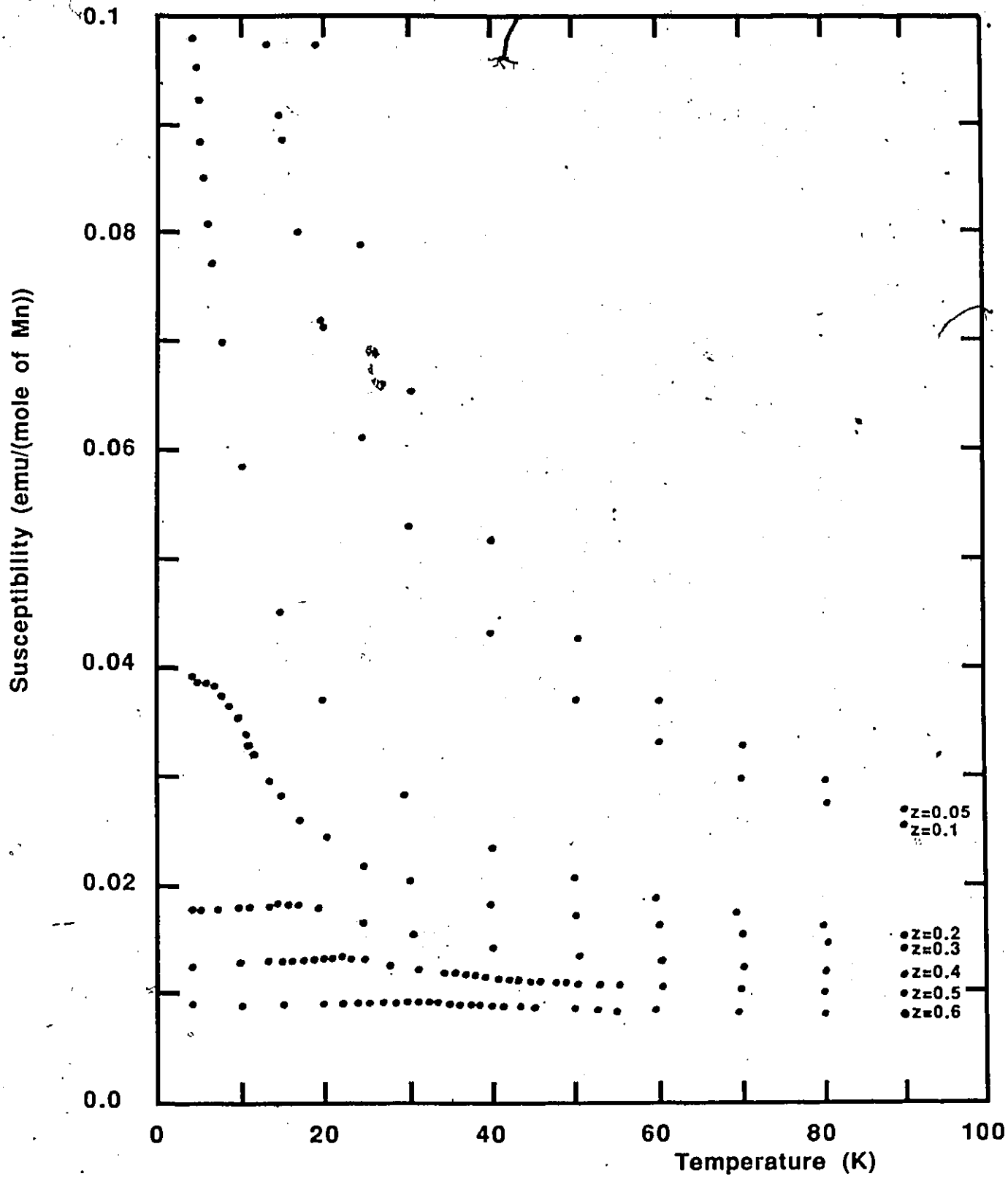

FIGURE 4.7 Results of measurements of magnetic susceptibility for some samples with x=0.

(18), concluded that this cusp is due to spin glass freezing. This was based on several pieces of evidence including their measurements of specific heat, which show no features at all at the temperature where the cusp occurs. As well, neutron diffraction results, by Holden et al on $Zn_{1-z}Mn_zTe$, (50) and by Giebultowicz et al on $Cd_{1-z}Mn_zTe$, (51), indicate that there is no ordered spin arrangement below these critical temperatures. These are the same phenomena observed in the metallic spin glasses, (39).

The results illustrated in figs. 4.3 to 4.7 were obtained by cooling the sample to as low a temperature as possible before applying the magnetic field. The cusp is seen most clearly under these conditions of zero field cooling, (ZFC). If a field is applied before the sample's temperature is lowered below its freezing point, (FC), then the cusp is somewhat obscured, as illustrated in fig. 4.8. The striking difference between the ZFC susceptibility and the FC susceptibility below T_g may be observed as an irreversible behaviour when measurements are carried out as follows. First, the sample is cooled in zero field down to 4.2 K. As the temperature is raised, the susceptibility is observed to increase with a sharp maximum occurring at the spin glass transition point, as indicated in fig. 4.8. As the temperature is further increased, χ, is seen to decrease. Now, if the measurements are made as the temperature is decreased, the susceptibility is found to coincide with the original values above T_g. Below this point, the values are larger than the original ZFC measurements. This type of behaviour is also similar to that

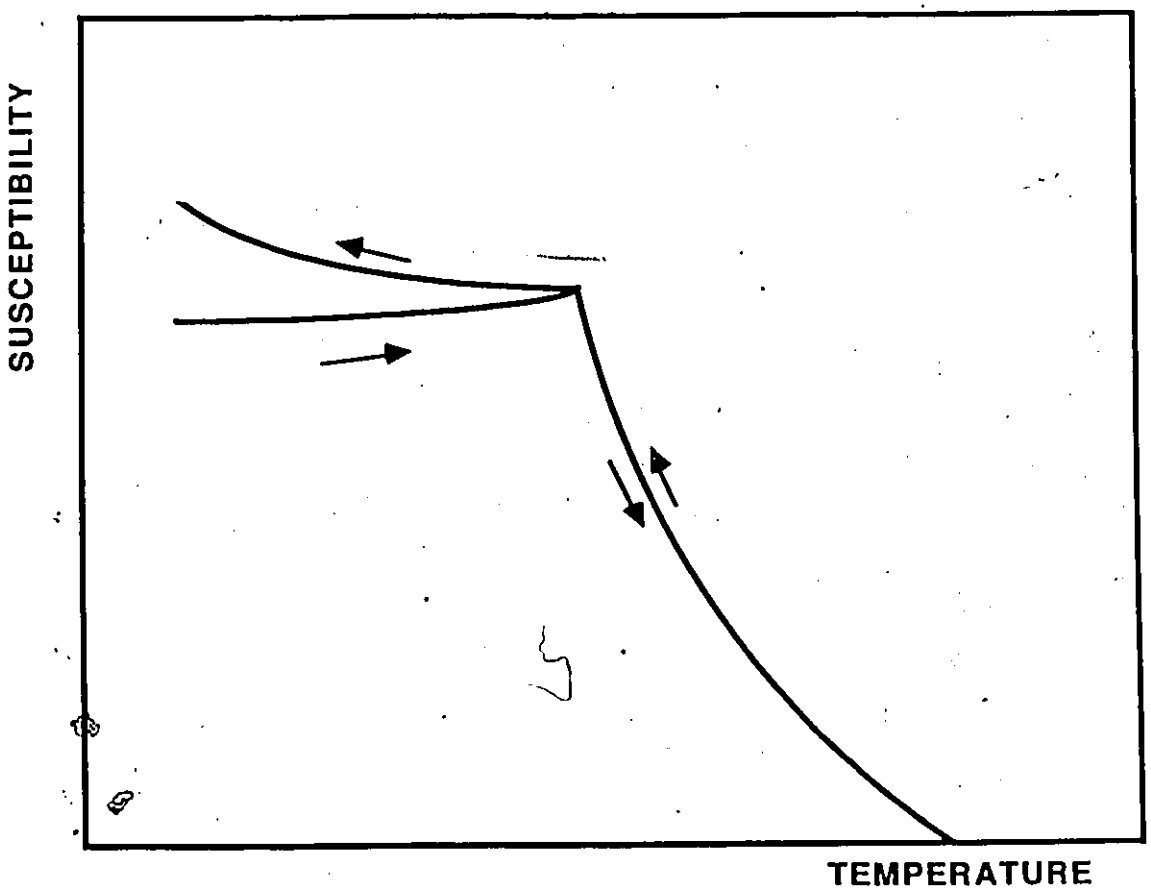

FIGURE 4.8 Irreversible Effects in Spin Glasses. The arrows indicate the sequence of measurements which produced this result after the sample is initially cooled in zero field.

of the metallic spin glasses and indicates that at higher temperatures, an alignment of the spins by a magnetic field is, to a certain extent, retained by the spin system below the freezing point, (52). The observation of these irreversible effects further supports the identification of the cusp with a spin glass transition.

For $z<0.25$, no cusp was observed and the material behaved like a paramagnet down to 4.2 K, the lowest temperature which could be reached. At the other extreme, $z>0.6$, the sharp cusp was reduced to a more or less rounded maximum. Specific heat measurements made on a sample of $Cd_{0.3}Mn_{0.7}Te$, by Galazka et al, (18), reveals a maximum which coincides with the susceptibility maximum. As well, the previously cited neutron diffraction results, (50, 51), on samples of $Cd_{1-z}Mn_zTe$ and $Zn_{1-z}Mn_zTe$ with $z>0.6$ show structures due to type III antiferromagnetic ordering on a face centered cubic lattice. This type of ordering is illustrated in fig. 4.1.

Such diverse behaviour has led researchers to use a magnetic phase diagram to illustrate the properties of these systems. The diagram is obtained by plotting values of T_g against Mn concentration, as shown in fig. 4.9. However, it should be noted that the use of the term "phase" should not necessarily imply that the transition into a spin glass state is a true phase change. It should also be noted that the term "T_g" will be used to label the transition temperature for the samples with $z>0.6$ as well as for those which behave like a spin glass.

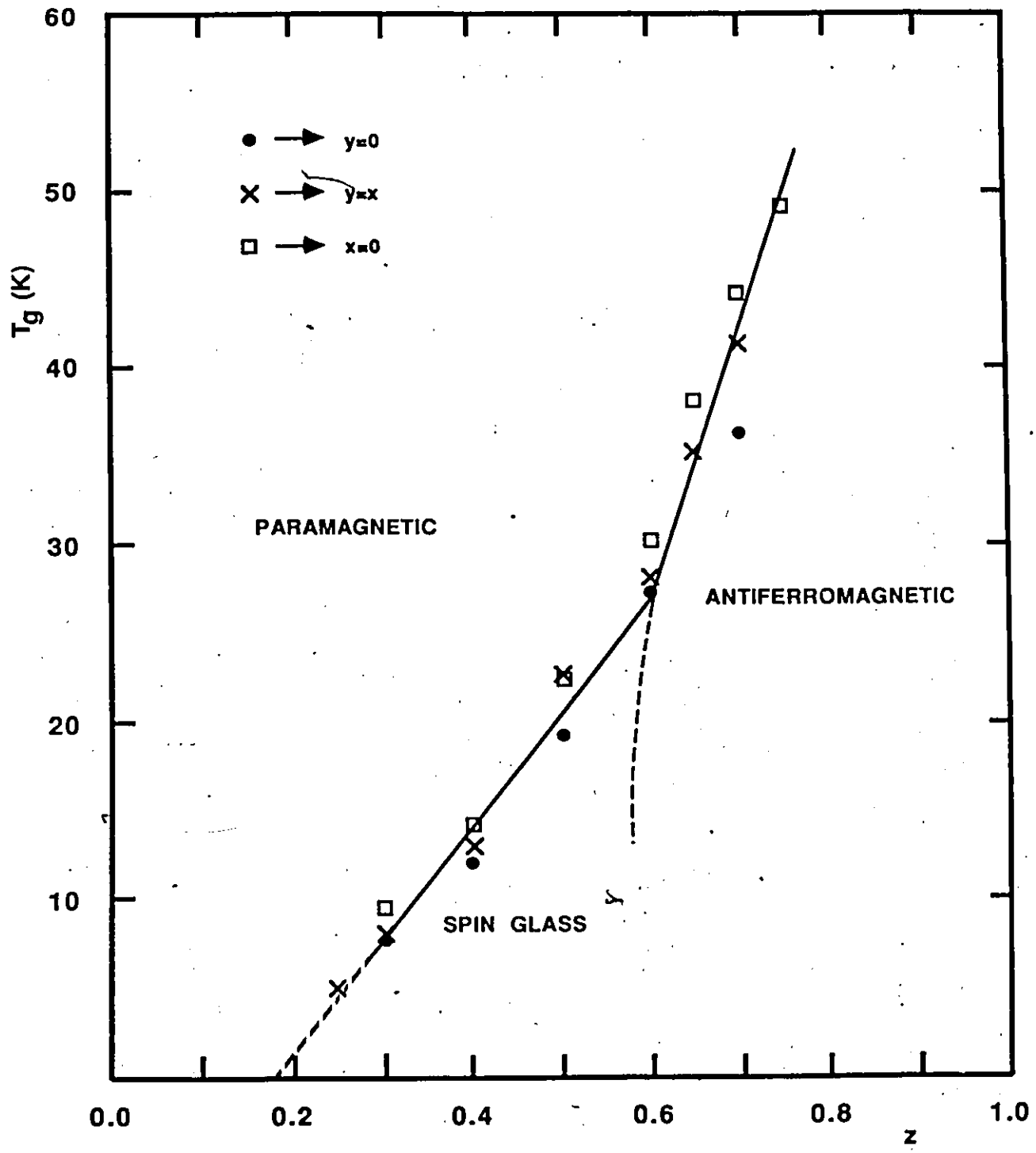

FIGURE 4.9 Plot of T_g versus z composition for samples with three different x:y ratios. The lines serve merely to guide the eye.

Values of T_g, obtained in the present work, are plotted as a function of composition in figs. 4.9 and 4.10. These show fairly good agreement with values obtained by other researchers, on $Cd_{1-z}Mn_zTe$, (18, 54) and $Zn_{1-z}Mn_zTe$, (53). It can be seen that T_g increases more or less linearly with z for $z<0.6$ and extrapolates to about $z=0.18$ at $T_g=0$. Since T_g values for samples of constant z occur very close to each other, only the values for $y=0$ and for $x=0$ are shown in fig. 4.9. The values for all the samples which were investigated, may be more clearly presented by plotting as a function of y composition, as shown in fig. 4.10. A small but definite increase of T_g with Zn concentration is observed in this diagram. This small increase can at least be partly explained by the results of chapter 2. In that section, it was found that the lattice parameter decreased with y, (fig. 2.5), consequently, the distance between Mn ions becomes smaller towards the Zn side of the pseudo-ternary diagram. In general, exchange interactions tend to increase with a decrease in separation between the magnetic ions. This would mean that the spins would freeze at a higher temperature.

Linear extrapolations of the T_g values for the different x:y ratios are shown in fig 4.10. For each case, the extrapolation at 0 K corresponds to a z value very close to 0.18, which is the same as that obtained from fig. 4.9. This value agrees quite well with the nearest neighbour percolation limit for an FCC lattice as calculated by various authors using a variety of techniques, (9, 24, 56, 57, 58). The percolation limit represents the Mn

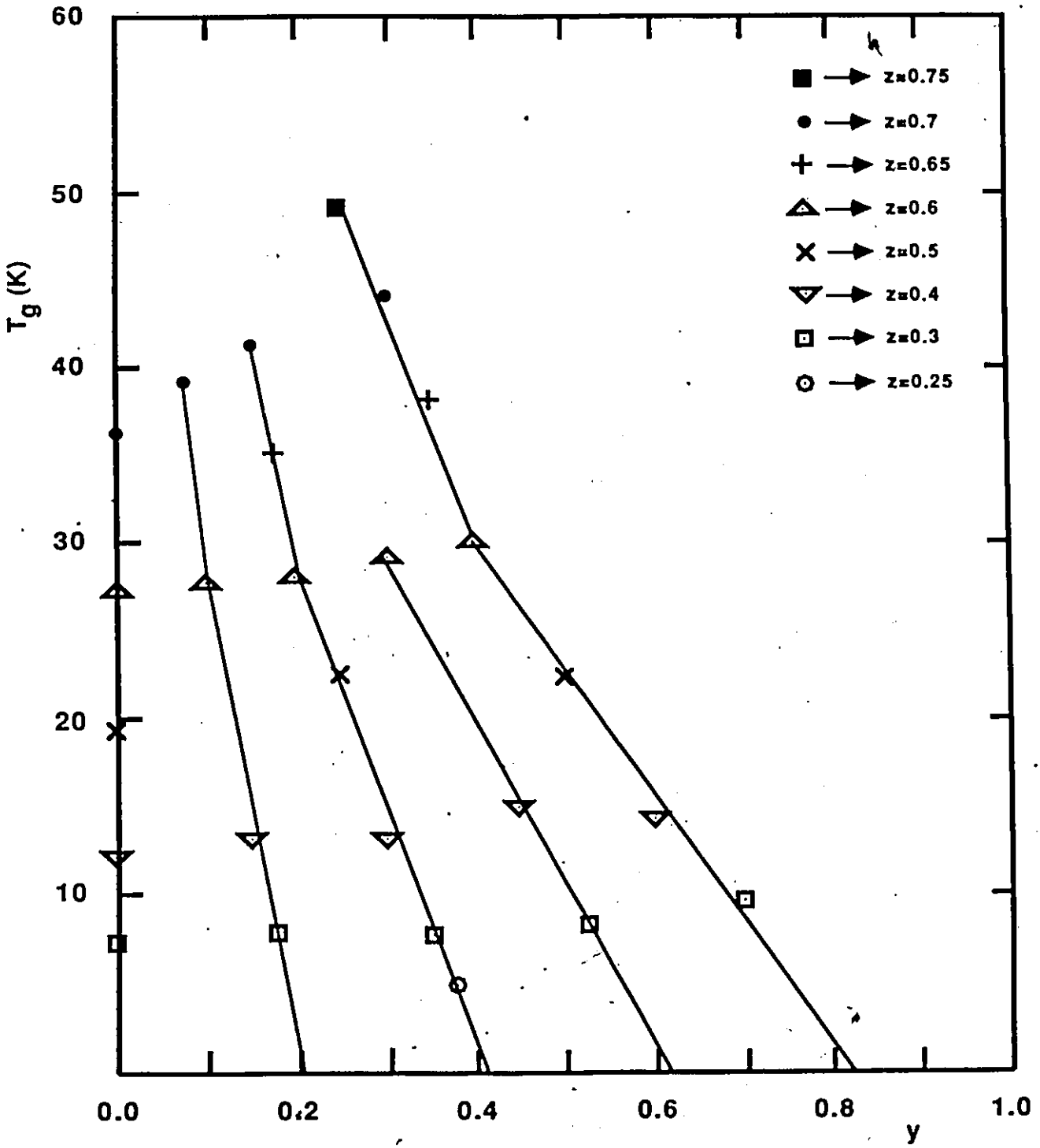

FIGURE 4.10 Plot of T_g versus y composition for all samples. The lines serve merely to guide the eye.

concentration below which the remaining Mn ions are too few to support a long range order or freezing through nearest neighbour interactions only. This concept may be readily illustrated in two dimensions by using fig. 4.11. The percolation limit of an infinite square lattice is calculated to be 59%, (59). In Fig. 4.11(a) a randomly generated square lattice with 64% of the sites occupied and with nearest neighbours connected by solid lines, was generated by a computer. It can be seen that most of the occupied sites are connected together into one large group with a few small isolated clusters interspersed amidst it. There also appears to be larger isolated clusters near the boundaries but one should keep in mind that these figures are only finite windows onto the infinite lattice and that these apparently isolated clusters would probably connect up with the main cluster outside this window. In fig. 4.11(b), a square lattice with 54% occupation, which is below the percolation limit, is presented. In this case, there is no single large cluster, only several small clusters which are definitely isolated from each other. This is the essential idea behind percolation. Below the percolation point, the system is made up of many non-interacting or isolated clusters. As the concentration increases, the size of the clusters grow until they begin to overlap and eventually form an infinite size cluster at the percolation threshold.

According to figs. 4.9 and 4.10, values of T_g for z=0.2 should occur at temperatures below 4.2K. This would explain why they were not observed since the measuring system does not go below

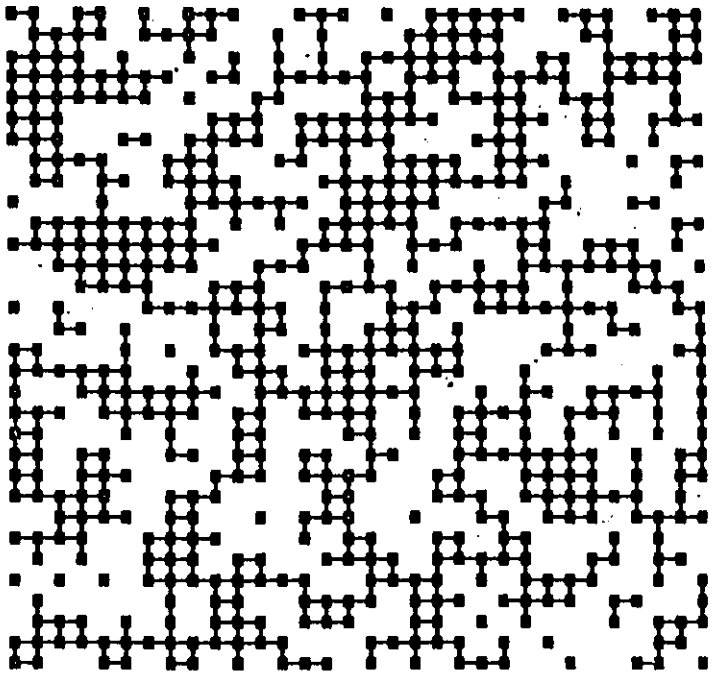

FIGURE 4.11(a) Square Lattice with 64% Occupation.

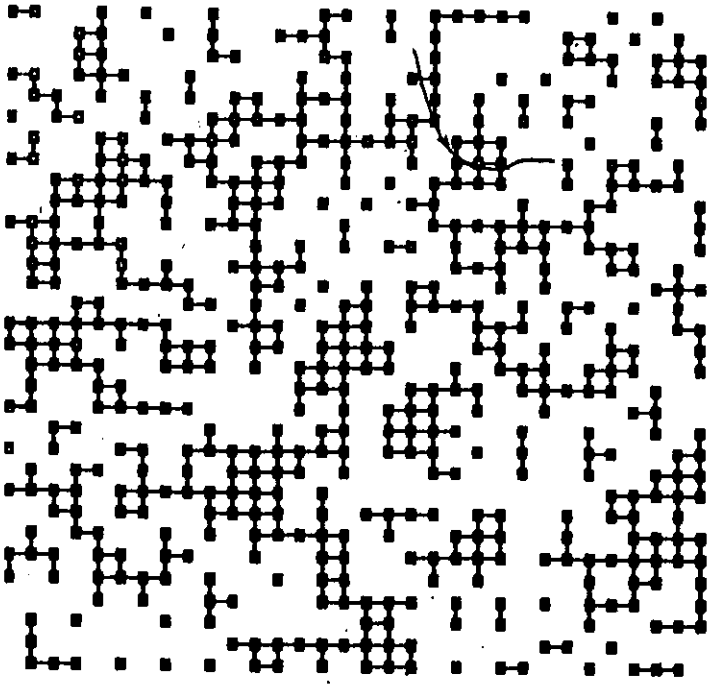

FIGURE 4.11(b) Square Lattice with 54% Occupation.

liquid helium temperatures. However, according to the same figures, T_g for sample $Zn_{0.75}Mn_{0.25}Te$, which was not observed, should lie in the observable range. In fact, one would expect its critical temperature to be larger than that for a sample of $Cd_{0.375}Zn_{0.25}Mn_{0.375}Te$, which was clearly observed. There are several possible explanations for this failure. One reason might be due to errors in stoichiometry as described in section 2.1.

Another possibility may arise from the fact that the ZFC susceptibility of the low z samples tends to rise again as the temperature is reduced below T_g, as can be seen for the z=0.3 samples in figs. 4.3 to 4.7. The same phenomenon was observed for $Cd_{1-z}Mn_zTe$ crystals of $z \leq 0.3$ by other researchers, (18, 63 and 81) and has been attributed to contributions from small isolated clusters. This upturn in χ may partly obscure the cusp for sample $Zn_{0.75}Mn_{0.25}Te$ if it were to occur very close to it. The masking of the cusp would be enhanced by the possible presence of chemical clusters. In the results of refs. 63 and 81, the authors claim not to have observed a cusp for a sample of $Cd_{0.8}Mn_{0.2}Te$, in contrast to the results reported in refs. 18 and 54. This has been attributed to chemical clustering and recent measurements by Ayadi et al, (118), and by Oseroff and Gandra, (119), have shown that the presence of this type clustering may be reduced by preparing materials with high homogeneity. For the present work, one would suppose that the annealing procedure in the preparation of the samples would tend to produce homogeneous samples, so this last effect might not be important.

Another reason for the failure to observe a cusp for sample $Zn_{0.75}Mn_{0.25}Te$ may be due to a partial failure in the ZFC process. To make measurements by ZFC, the sample is slowly lowered through the cryostat with the helium flow set at a high level to cool the sample below its transition temperature before it reaches the region of the cryostat where the field is present. For the cases of small z, T_g is expected to occur very near the lowest temperature which could be attained. It then becomes very possible for the sample to arrive in the vicinity of the magnetic field before it has been cooled below its transition temperature. As was explained earlier, this would result in the FC susceptibility being measured, rather than the ZFC. Consequently, the cusp would not be as sharp as the other spin glass samples.

Below the percolation limit, $z \leq 0.18$, no ordering or freezing of spins can occur from nearest neighbour interactions. However, if the range of the exchange interaction extends out to the next nearest neighbours and beyond, one might expect that, at a low enough temperature, these interactions would produce a long range spin glass freezing. In reference 58, the critical concentration of an FCC lattice was found to be 0.136 for second nearest neighbours and 0.061 for third nearest neighbours. In order to see if there is such a transition, measurements would have to be performed at much lower temperatures than could be attained by the current set up. Novak et al, (55, 69), observed spin glass transitions in samples of $Cd_{1-z}Mn_zTe$ for which z was smaller than the nearest neighbour percolation limit, at temperatures down to

below 1 K. Although samples in this range of composition have usually been classified as having a paramagnetic behaviour, it seems that this designation may have to be revised.

As well as predicting a percolation limit, some of the references cited earlier predict an antiferromagnetic state for an FCC lattice with a concentration higher than z=0.4, (24), and z=0.5, (57). That such a state exists has been verified by the measurements of specific heat, (18) and neutron diffraction, (50, 51), which were mentioned earlier. The transition from spin glass to antiferromagnetism is observed in figs. 4.9 and 4.10 as a change of behaviour in how T_g increases with concentration, around the point where z=0.6. Unlike the case of the percolation limit, the antiferromagnetic transition does not agree with the predictions. However, it is interesting to note that the linear variation of T_g for z>0.6, in fig. 4.9, extrapolates to a value which falls inside the range of these predictions.

A more exact determination of the position of the transition cannot be obtained from these diagrams since it is impossible to decide in which state the z=0.6 samples belong. Neutron diffraction measurements, by Holden et al on $Zn_{1-z}Mn_zTe$, (50), and by Giebultowicz et al on $Cd_{1-z}Mn_zTe$, (51), indicated that samples with z=0.6 became antiferromagnetic. It was also determined that this was not a normal antiferromagnetic phase since the diffraction lines corresponding to magnetic ordering were found to be broadened. Instead, it was reasoned that the magnetic state was composed of large, well ordered antiferromagnetic clusters

which were spread over several lattice constants and therefore contained several hundred lattice sites. The transition from antiferromagnetic to spin glass behaviour was deduced from the variation of the intensity of the diffraction lines with composition and was found to occur at z=0.58. However, evidence of the magnetic ordering lines in a sample of $Cd_{0.45}Mn_{0.55}Te$ indicate that this is not necessarily a sharp and distinct transition.

In figs. 4.3 through 4.7, the examples shown for $z \geq 0.6$ are not very clear due to the scale and the fact that the susceptibility does not change by very much over the entire temperature range. Replotting them on a reduced scale in fig. 4.12 shows that the maxima are broad and quite different from the behaviour observed for normal antiferromagnets. It is interesting to note that for samples in the spin glass state, for which a pointed cusp was observed, the specific heat measurements show no corresponding features, which would imply that this is not a true phase transition, despite the sharpness of the susceptibility cusp. On the other hand, as was pointed out earlier, specific heat measurements by Galazka et al, (18), on a sample of $Cd_{0.3}Mn_{0.7}Te$, which lies within the antiferromagnetic composition range, do show such a feature. This indicates that some sort of phase transition does occur for this sample, even though the susceptibility maximum is not as sharp as for the samples which lie in the spin glass composition range.

An attempt to explain some of the strange features observed

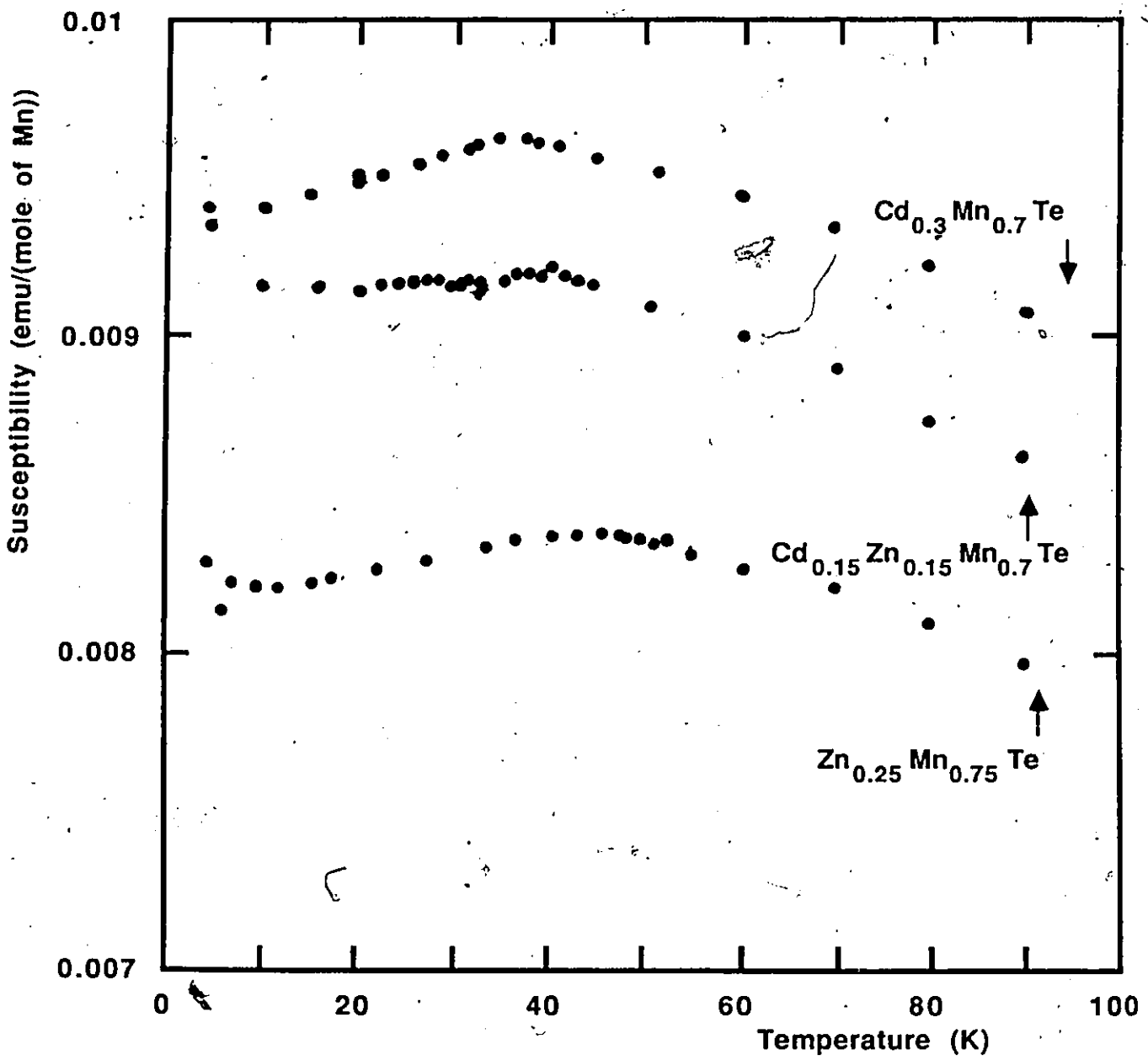

FIGURE 4.12 Examples of susceptibility results for some samples with $z>0.6$.

in the antiferromagnetic range has been made by Giebultowicz et al, (17), using a simple cluster model which assumes that the transition to the magnetic state occurs at different temperatures for different clusters. This would, in a qualitative way, account for the rounded behaviour in the susceptibility and in the specific heat. The distribution of these temperatures was derived from specific heat results and then used to predict the susceptibility and neutron diffraction results. Except for the case of susceptibility, the predictions turned out to be quite close to the actual results. The predicted position of the susceptibility maximum agreed very well with the measured value, but the variation was different above and especially below the transition temperature.

Another interesting feature which was observed in the present work is the variation of the susceptibility at the peak with composition, $\chi(T_g)$, which shows a change of behaviour when going from the spin glass to antiferromagnetic range. This was observed most clearly when plotted in units of emu/mole as illustrated in fig. 4.13. This diagram shows that $\chi(T_g)$ decreases rapidly in the spin glass region, then goes through a minimum between z=0.55 and 0.6, and finally increases gradually in the antiferromagnetic region. The position of the minimum appears to correspond to the z composition at which the transition between spin glass and antiferromagnetic behaviour occurs, as determined from neutron diffraction. This diagram illustrates a further difference in behaviour between the samples from these two regions.

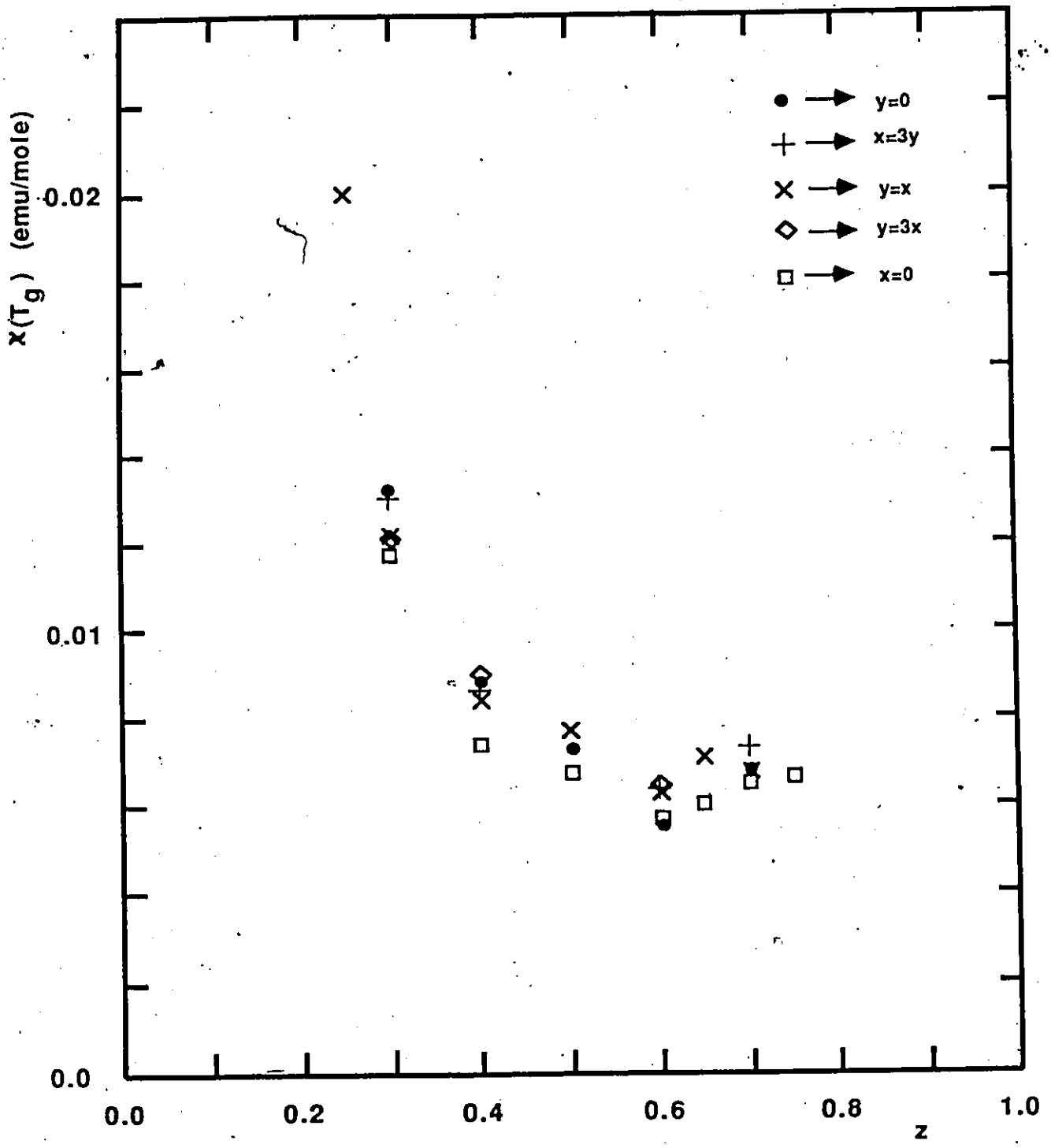

FIGURE 4.13 Plot of Susceptibility at T_g versus z Composition. The susceptibility is in units of emu/mole.

4.3.2 Evaluation of Curie-Weiss Parameters

If the susceptibility obeys the Curie law, (eq. 4.3), or the Curie-Weiss law, (eq. 4.4), then plots of $1/\chi$ against temperature should produce straight lines. The intercept of the lines on the temperature axis will give an indication of the type of interaction which is occurring between the spins. A positive value for the value of θ indicates ferromagnetism while a negative intercept would suggest antiferromagnetism. Paramagnetism is denoted by an intercept at the origin.

Plots of $1/\chi$ versus temperature are presented in figs. 4.14 to 4.18. In all cases, it can be seen, that at high temperatures, the behaviour is very linear and extrapolates down to negative temperatures. Thus, these materials follow the Curie-Weiss law and the main interaction is antiferromagnetic. At lower temperatures, and above the onset of any type of long range spin freezing, there are significant deviations from Curie-Weiss behaviour. This effect will be dealt with in the next section. There have also been reports, (54, 70), of ferromagnetic behaviour for samples with less than 5% Mn. In these cases, the extrapolated $1/\chi$ line gave a positive intercept on the temperature axis. Such an effect has been attributed to a different exchange mechanism, such as RKKY, becoming significant in extremely diluted materials. This ferromagnetic behaviour has so far not been widely corroborated.

From eq. 4.4, one can see that the Curie-Weiss constant, C, is obtained from the slope of the straight line while the

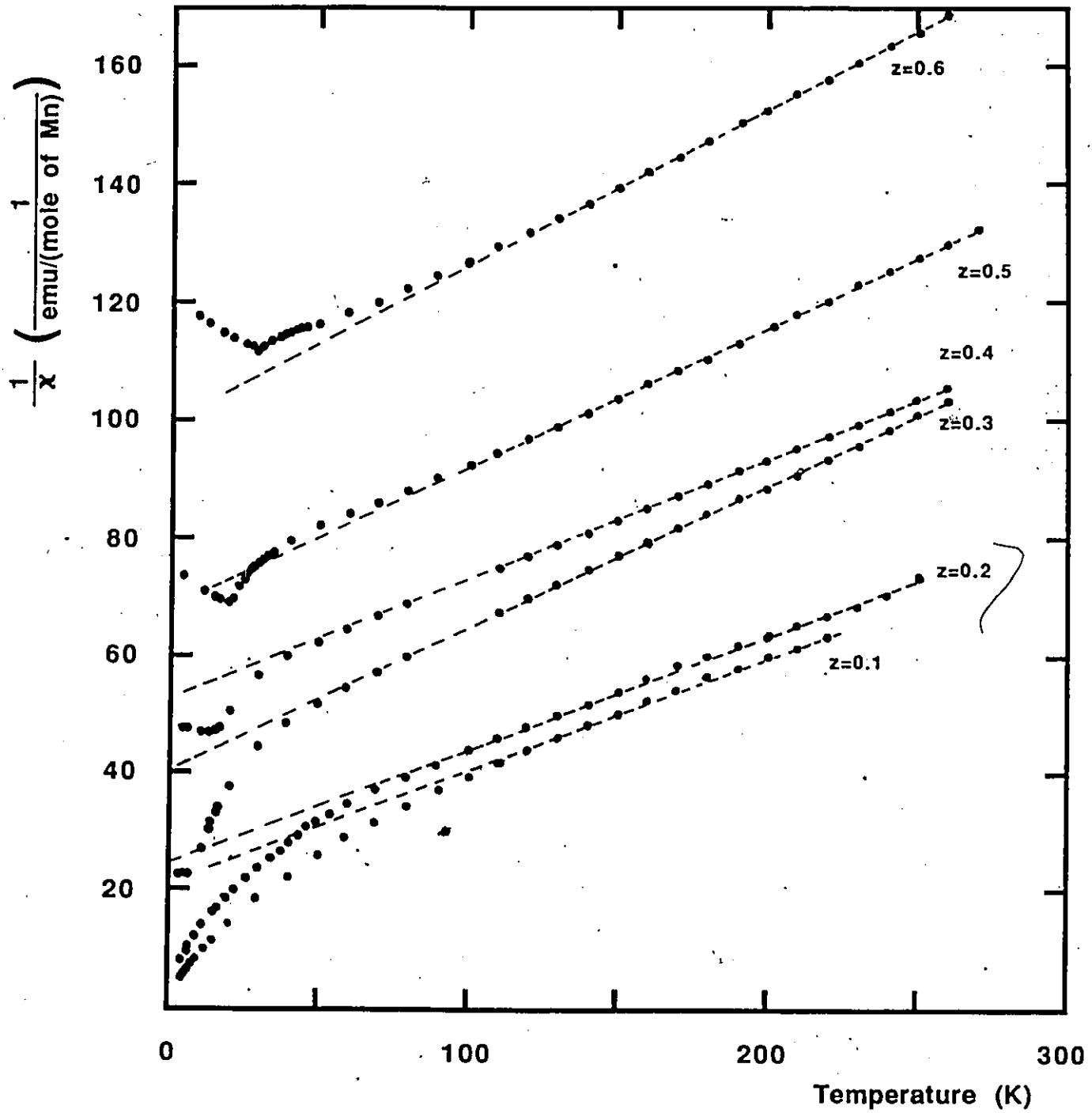

FIGURE 4.14 Plots of $1/\chi$ for some samples with y=0.

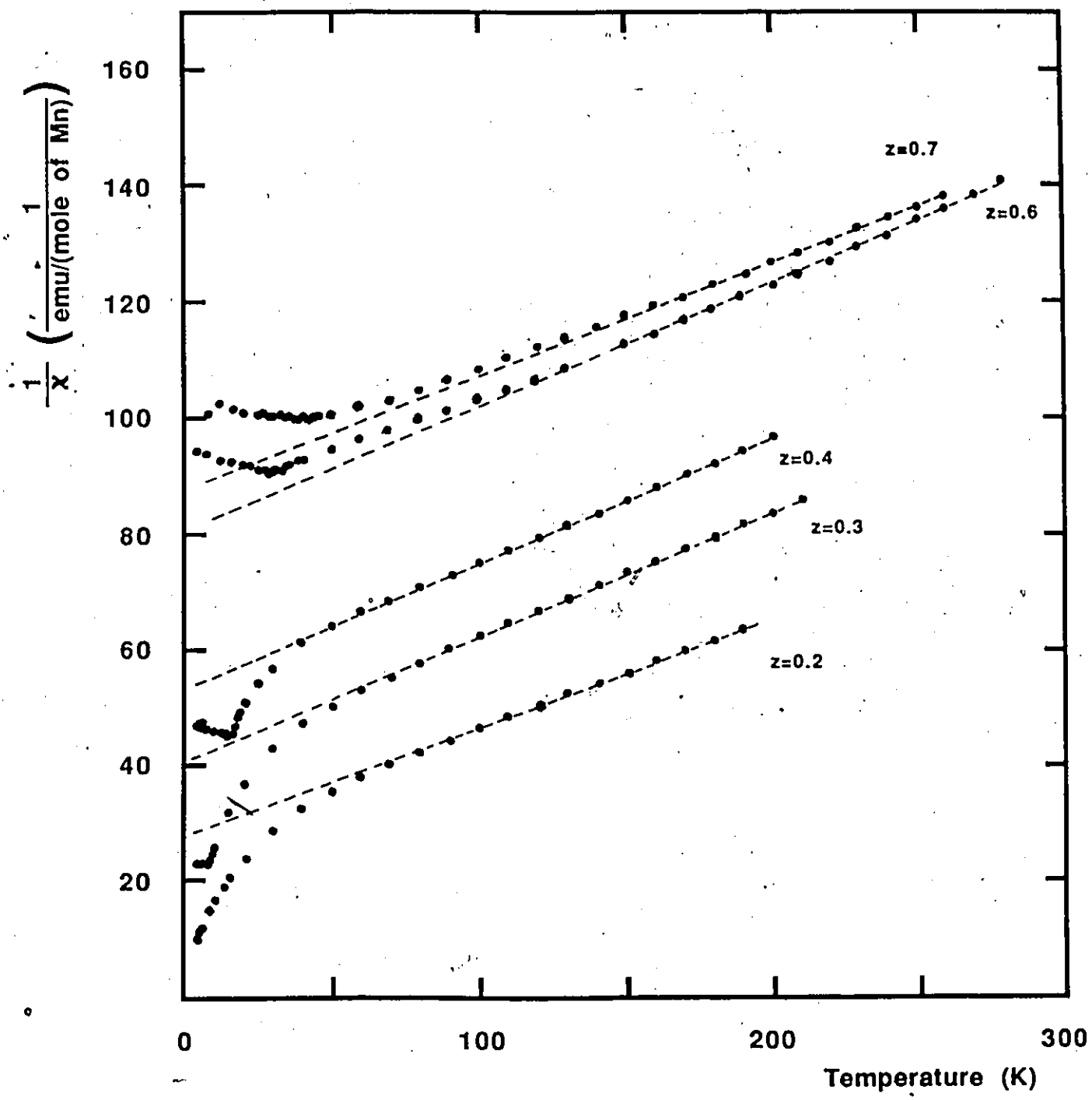

FIGURE 4.15 Plots of 1/ χ for some samples with x=3y.

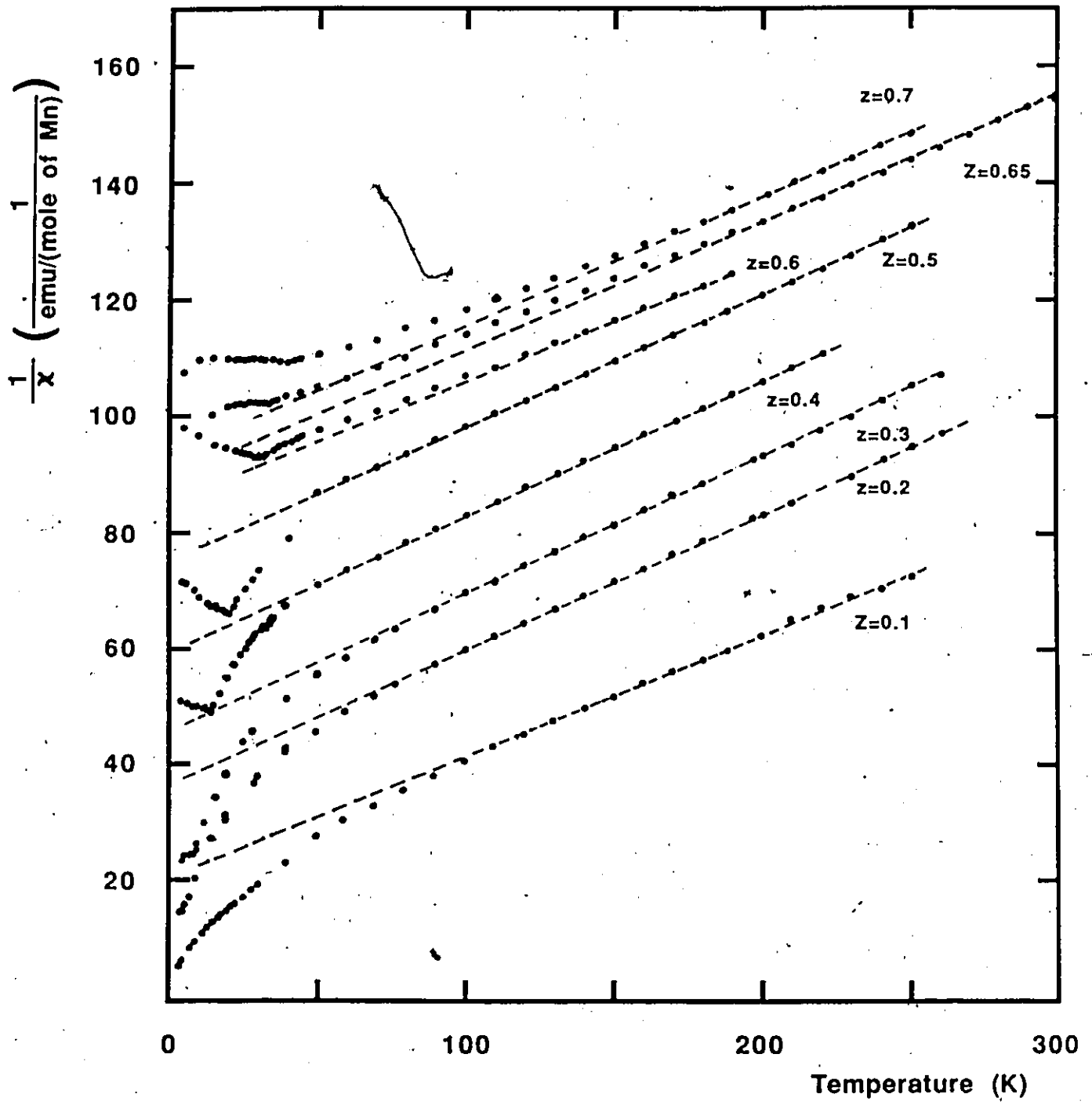

FIGURE 4.16 Plots of 1/ χ for some samples with y=x.

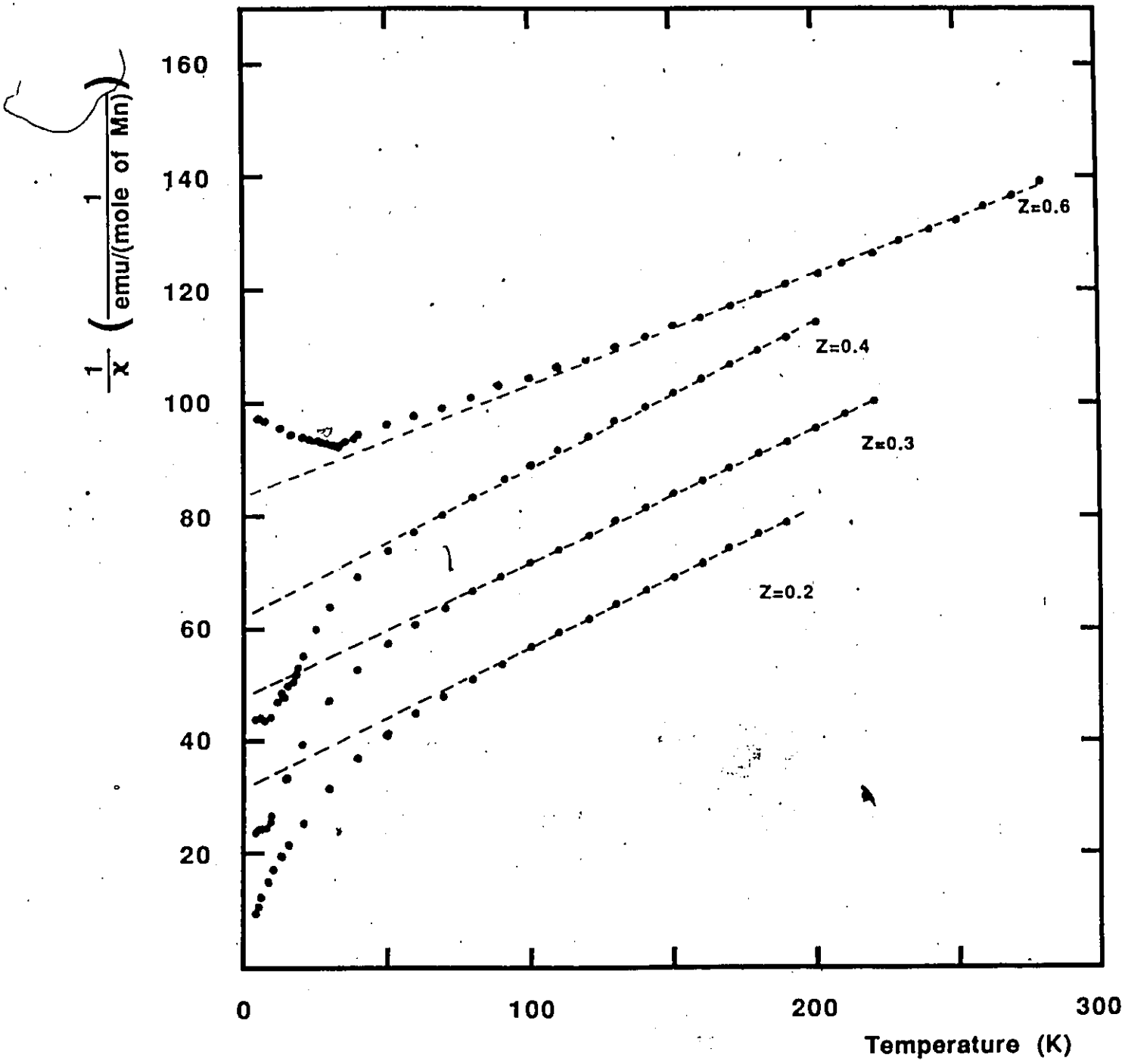

FIGURE 4.17 Plots of $1/\chi$ for some samples with y=3x.

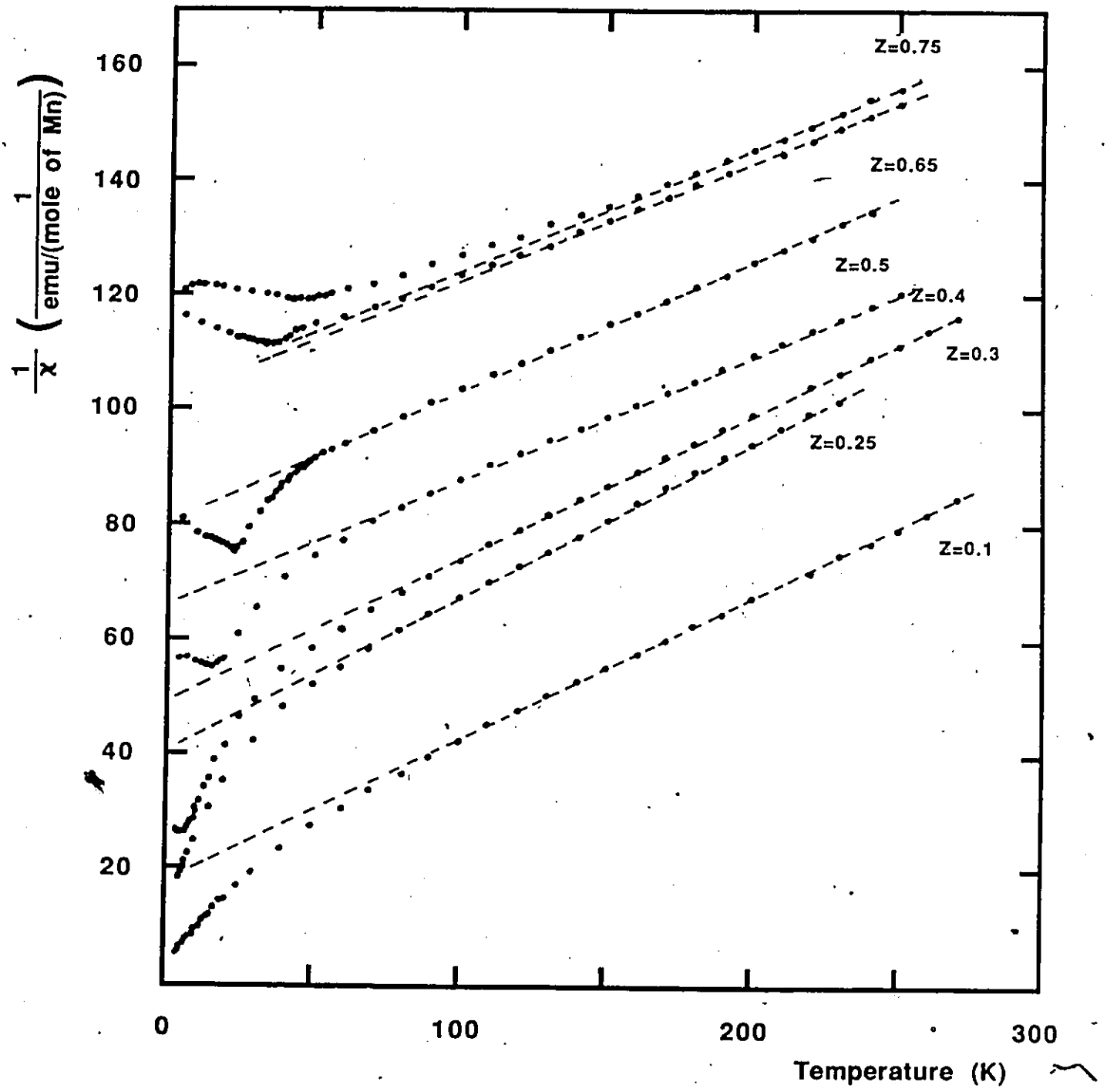

FIGURE 4.18 Plots of $1/\chi$ for some samples with x=0.

Curie-Weiss temperature, θ, is given by the intercept on the temperature axis. These quantities are plotted as a function of z in figs. 4.19 to 4.23.

Consider at first only the θ graphs. The broken lines represent the results of calculations carried out in section 4.4 and should be ignored for the time being. The error bars were estimated by considering the uncertainty in the composition, as discussed in chapter 2, and the uncertainty in determining the intercept from the extrapolation. The Curie-Weiss temperature appears to vary more or less smoothly for all values of z with no apparent change of behaviour in the antiferromagnetic range. At the low concentration range and keeping in mind the observation of ferromagnetic behaviour which was mentioned previously, one might expect to see a projection of the θ variation with z to change sign near z=0.05. Unfortunately, there is too much scatter in the plotted values to either confirm or deny this. An accurate projection is also hampered by the fact that for the low z samples, (z<0.2), the susceptibility signal drops to such a small level at high temperatures that its accuracy is much less than that for other samples: The design of the sample holder did not permit an accurate set of measurements on a sample with a mass very much greater than 0.05 gms so that the signal strength could not be improved.

It was pointed out in section 4.3.1 that T_g increased with Zn concentration probably as a result of the decrease in lattice parameter giving rise to an increase in the exchange

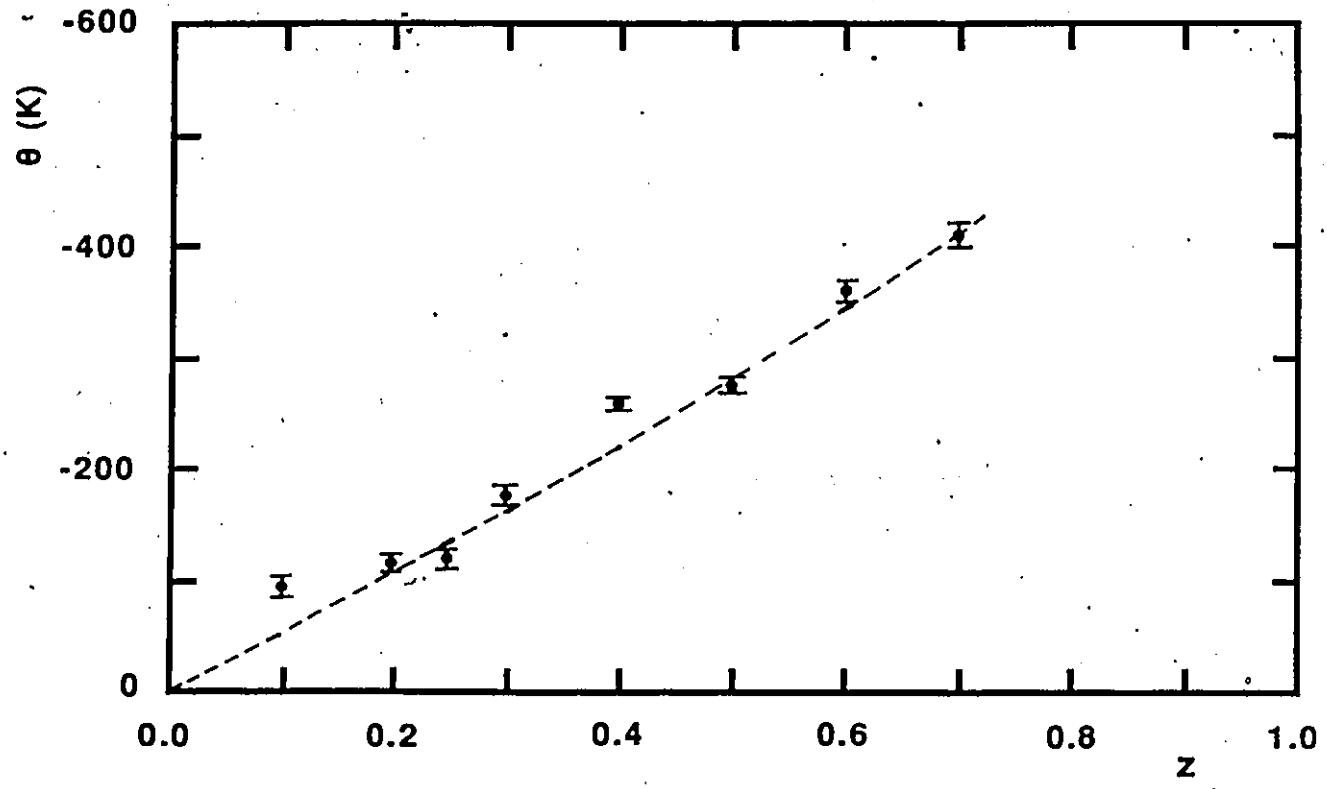

FIGURE 4.19(a) Values of the Curie-Weiss Temperature for y=0 samples. The broken line represents the results of eq. 4.16.

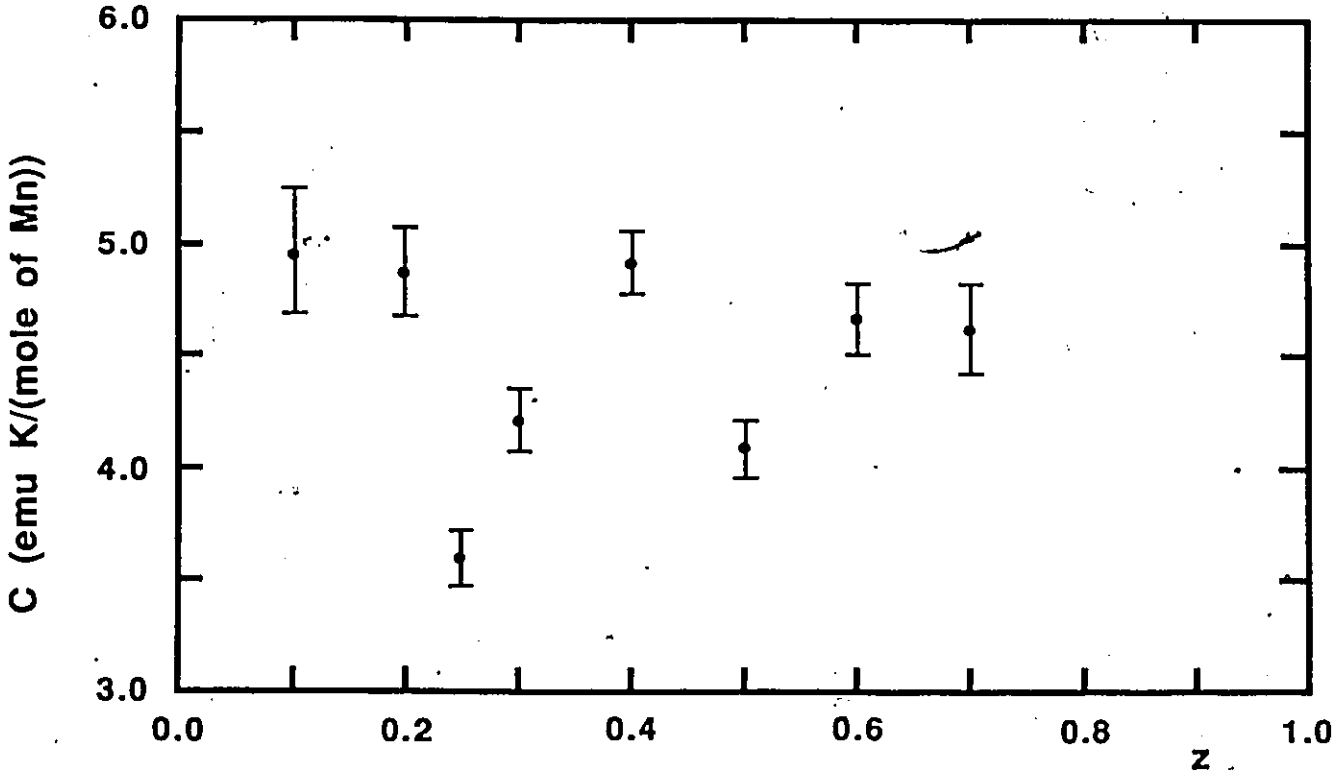

FIGURE 4.19(b) Values of the Curie-Weiss Constant for y=0 samples.

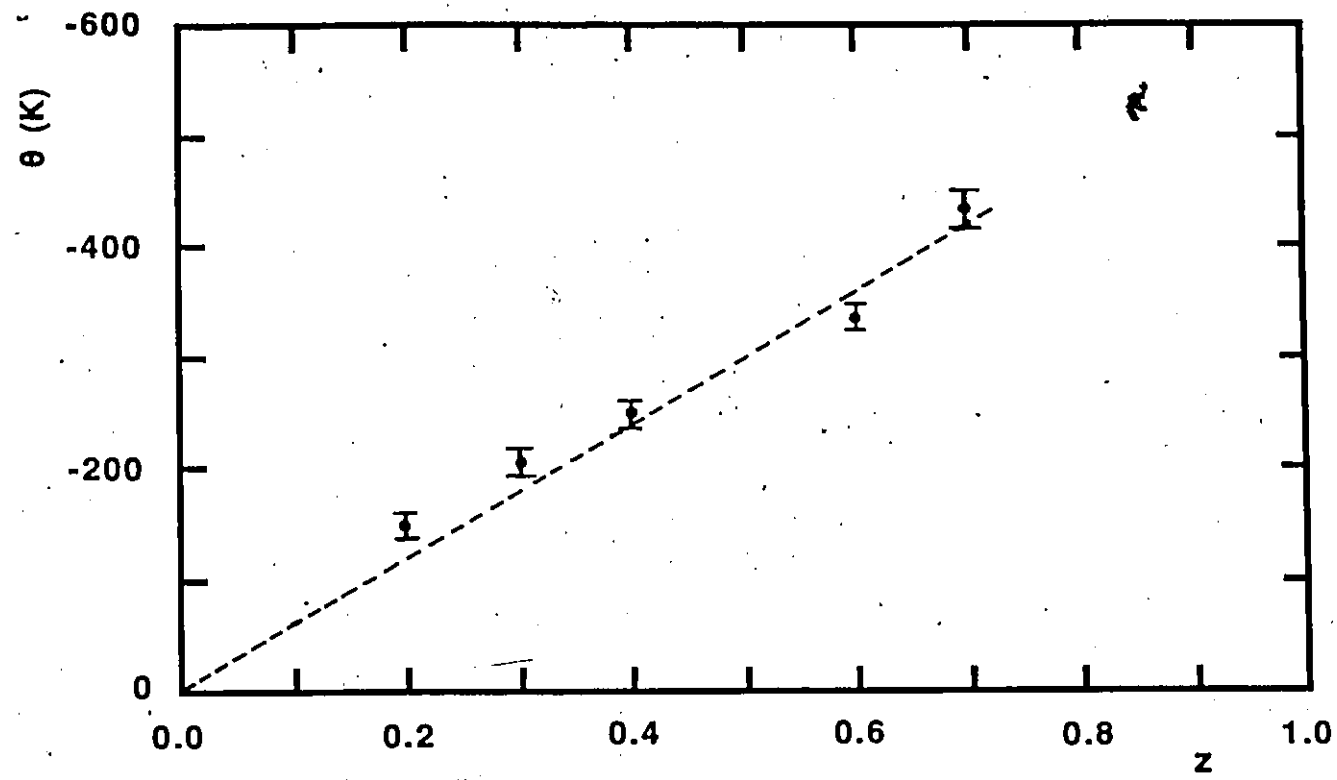

FIGURE 4.20(a) Values of the Curie-Weiss Temperature for x=3y samples. The broken line represents the results of eq. 4.16.

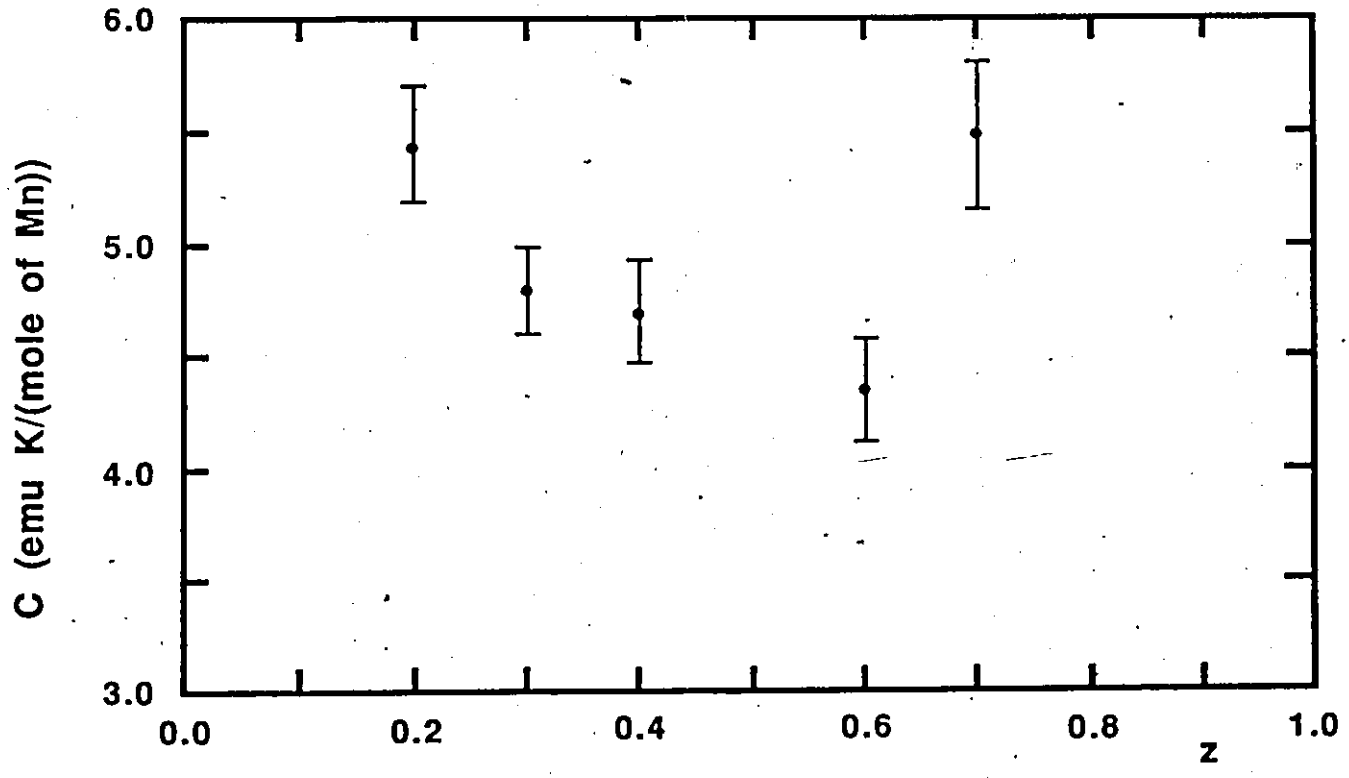

FIGURE 4.20(b) Values of the Curie-Weiss Constant for x=3y samples.

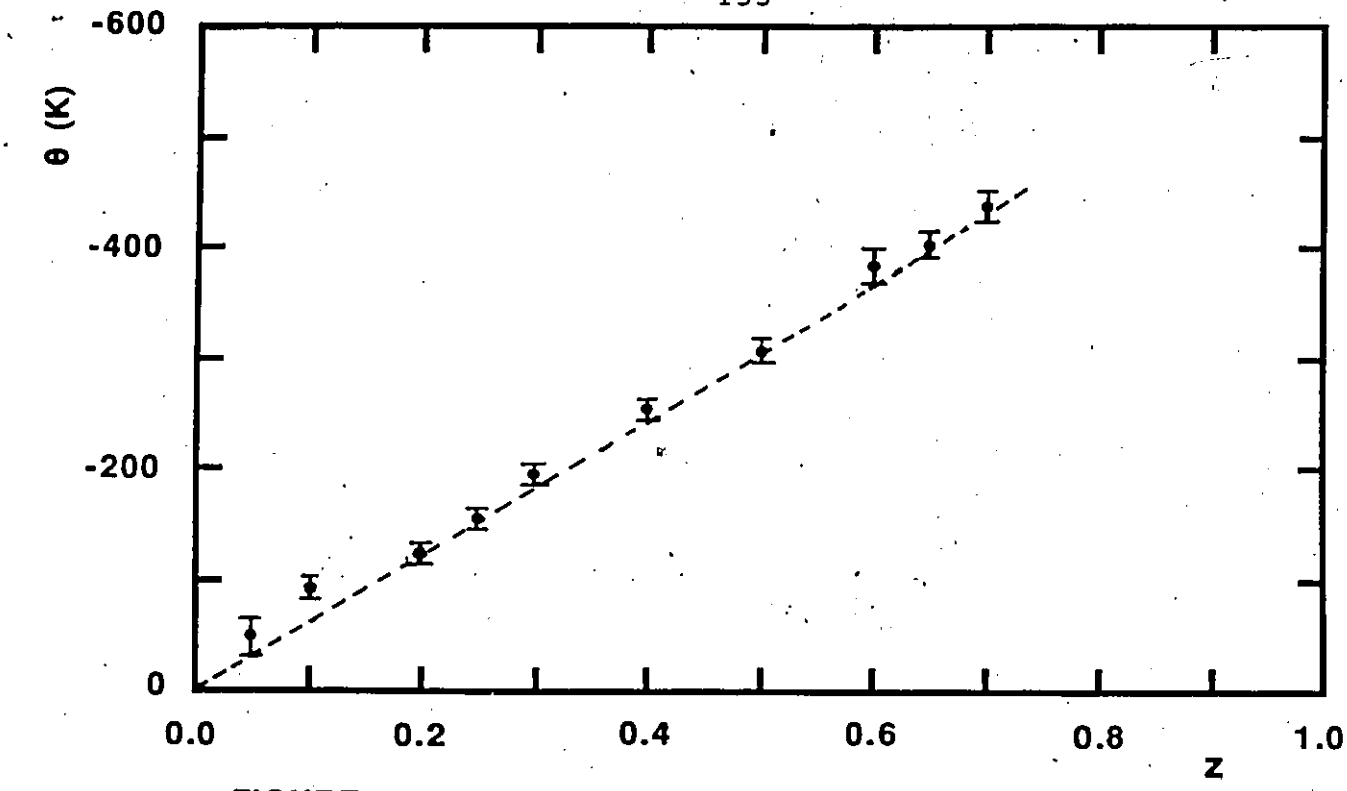

FIGURE 4.21(a) Values of the Curie-Weiss Temperature for y=x samples. The broken line represents the results of eq. 4.16.

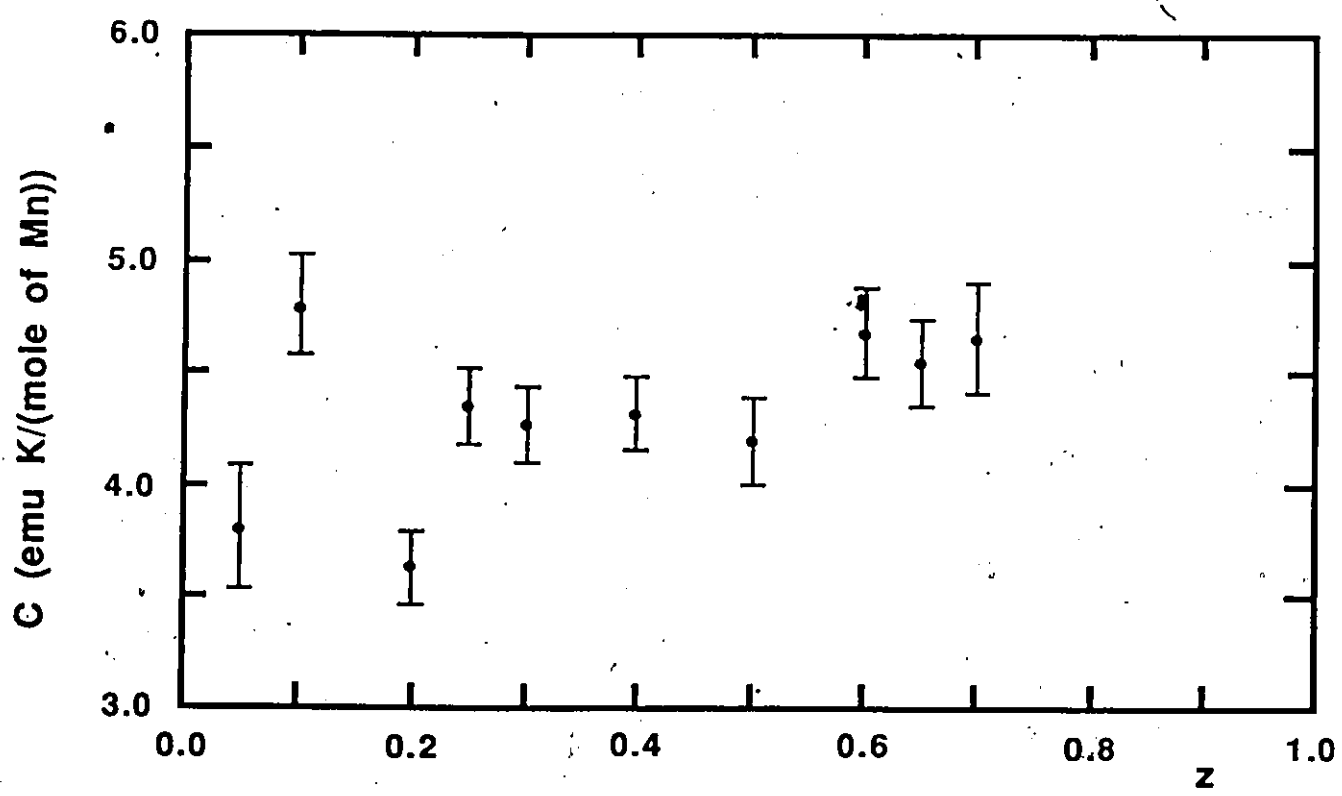

FIGURE 4.21(b) Values of the Curie-Weiss Constant for y=x samples.

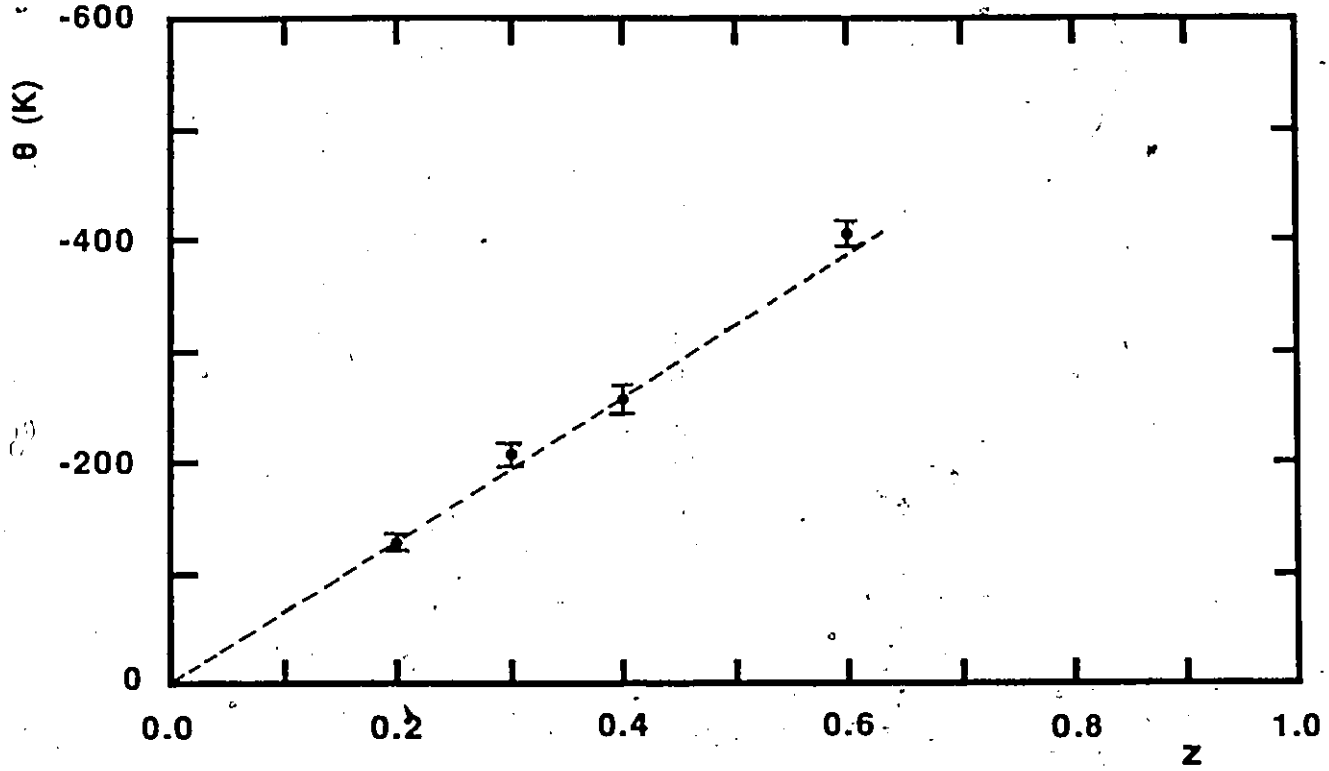

FIGURE 4.22(a) Values of the Curie-Weiss Temperature for y=3x samples. The broken line represents the results of eq. 4.16.

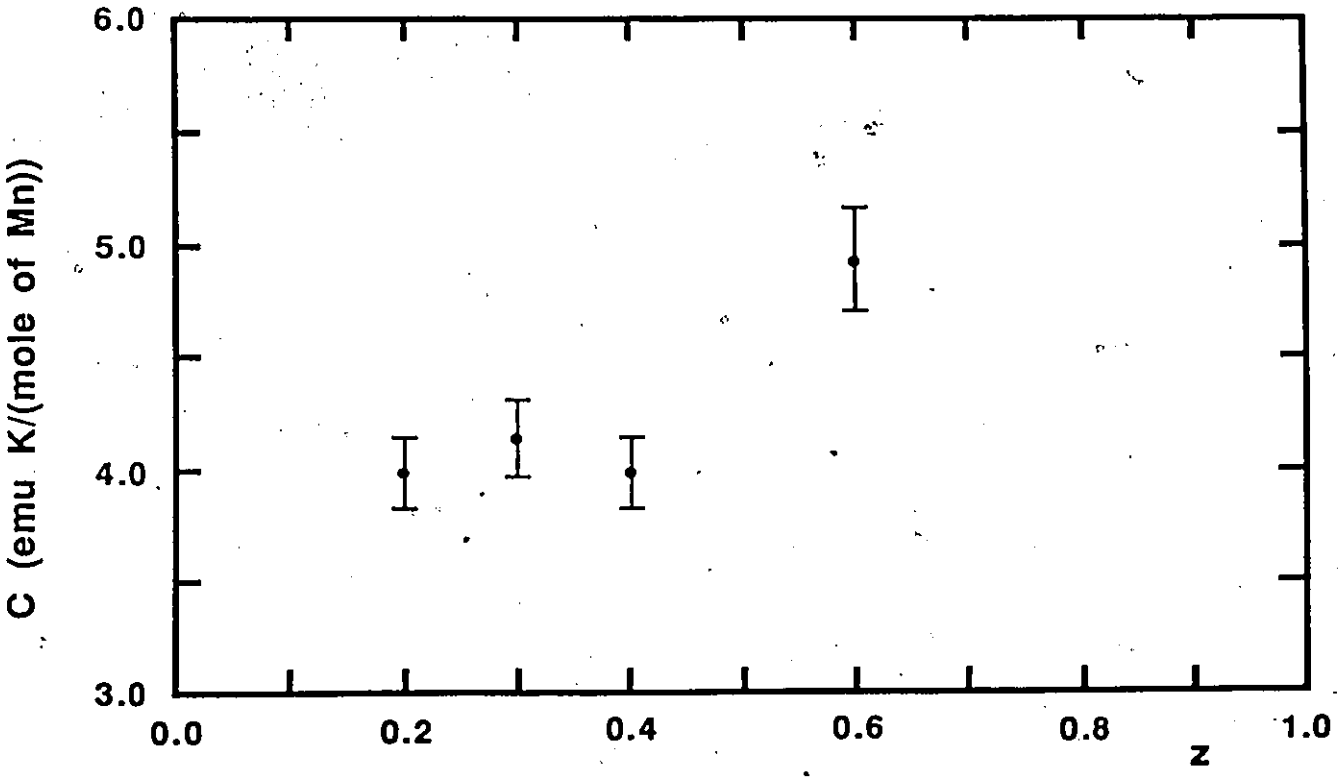

FIGURE 4.22(b) Values of the Curie-Weiss Constant for y=3x samples.

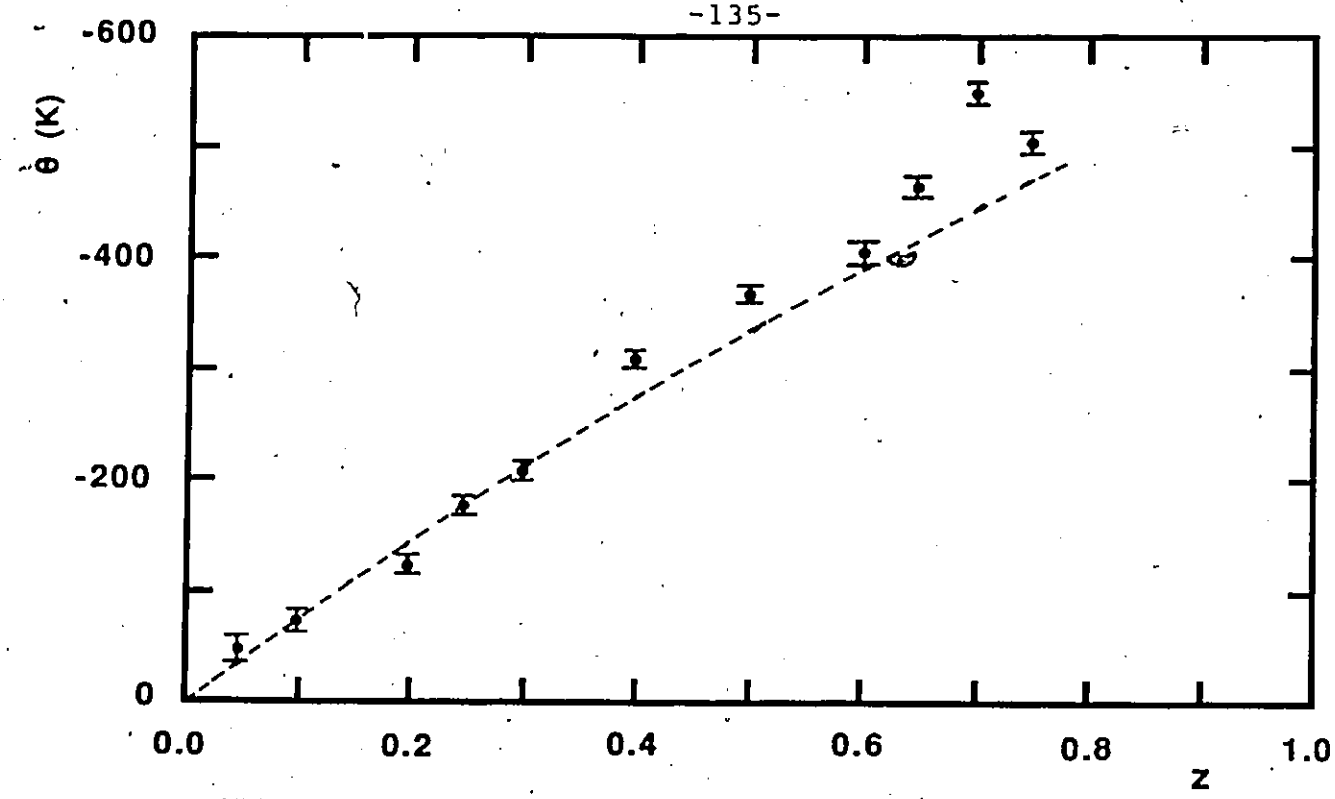

FIGURE 4.23(a) Values of the Curie-Weiss Temperature for x=0 samples. The broken line represents the results of eq. 4.16.

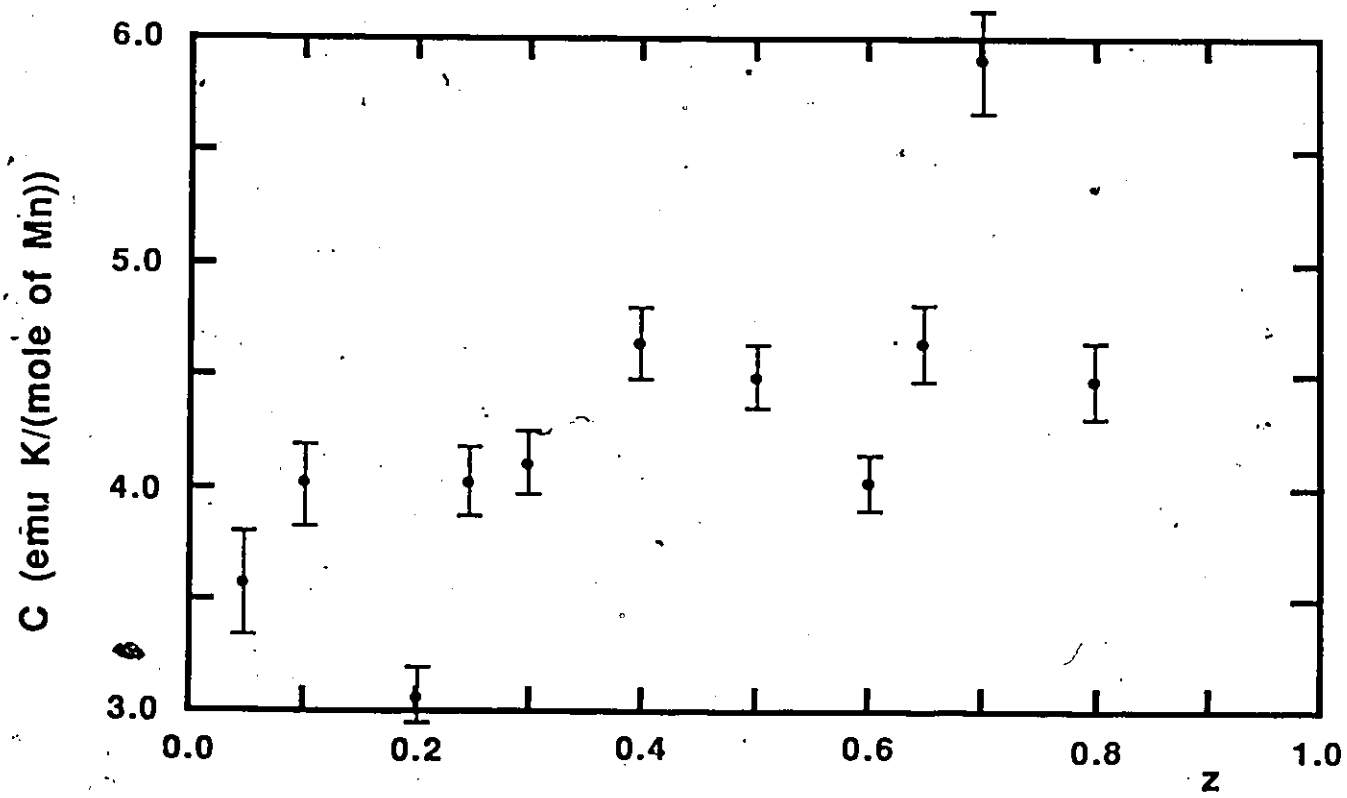

FIGURE 4.23(b) Values of the Curie-Weiss Constant for x=0 samples.

energy. Since θ also depends on the exchange, its magnitude should also increase with y. In fig. 4.24, the values for y=0 and x=0 are plotted on the same axes. In fig. 4.25, the values are plotted as a function of y. In both cases, the increase of θ with Zn concentration is clear.

According to eq. 4.6, the Curie-Weiss constant in units of emu/(mole of Mn), will vary with composition only if g or S varies with composition. For Mn, g is expected to be very close to 2.0. Confirmation of this will be given in chapter 5. Thus only S can vary with composition. The plots of C vs z concentration in figs. 4.19(b) to 4.23(b) indicate that any variation of C would be quite small. The error bars in these diagrams were estimated by combining the uncertainties in determining the absolute susceptibility, discussed at the end of section 4.2, with errors in composition and in the determination of the slopes. A small increase in C with z can be observed for the cases in which x=0 and y=3x but this is not confirmed by the other results. Averaging the values gives a mean C of 4.4 emu/(mole of Mn) with a standard deviation 0.5. Using this in eq. 4.6 along with g=2 results in an S value of 2.51 ± 0.09. This agrees very well with the value of 5/2, for isolated Mn ions. Any variation of S with composition would have to be much smaller than the quoted error value.

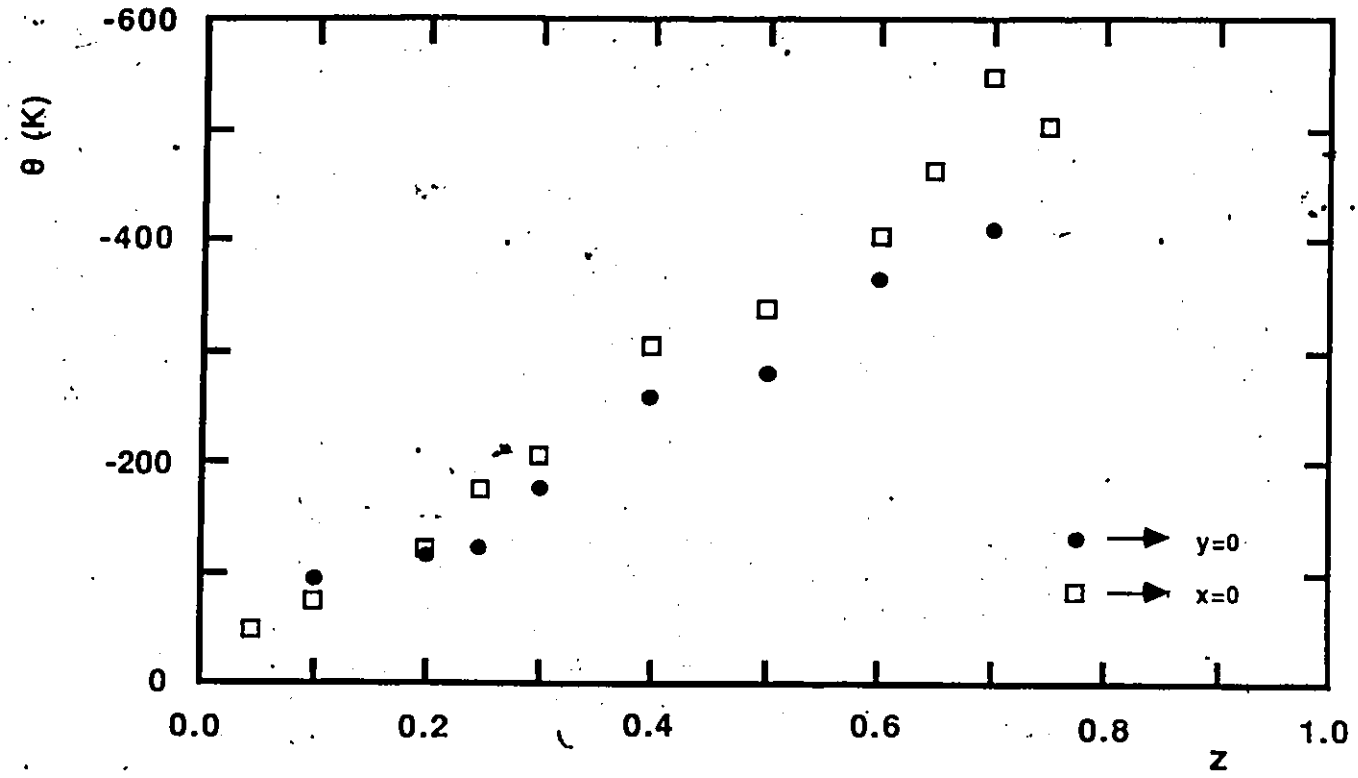

FIGURE 4.24(a) Curie-Weiss Temperature versus z composition for samples with y=0 and x=0.

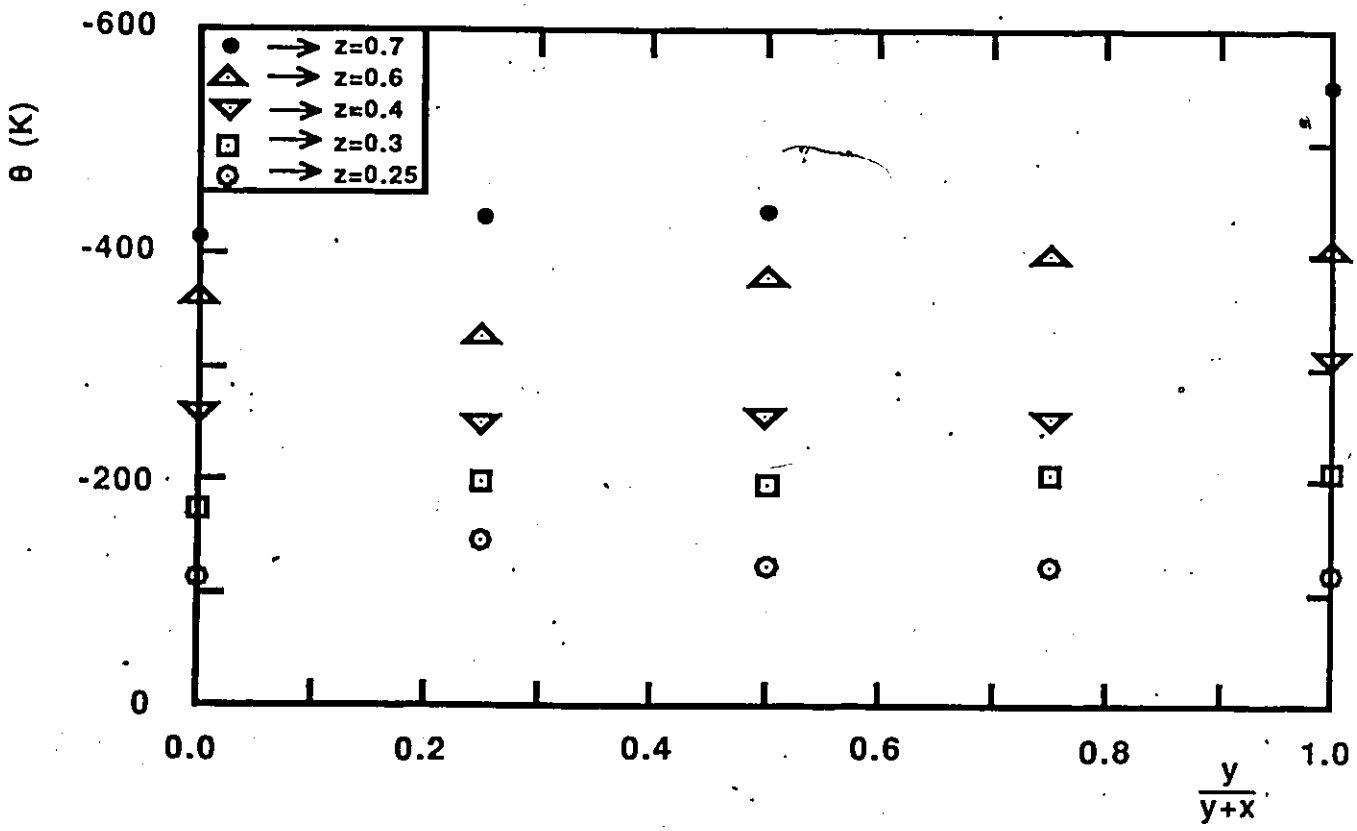

FIGURE 4.24(b) Curie-Weiss Temperature versus y/(y+x).

4.3.3 Non Curie-Weiss Behaviour

It has been pointed out that at lower temperatures, the $1/\chi$ plots of figs. 4.14 to 4.18 show deviations from Curie-Weiss behaviour. For the $z<0.6$ cases, an enhanced susceptibility was observed which resulted in a downward deviation of the $1/\chi$ curves. This effect has been also been observed, by other researchers, in $Cd_{1-z}Mn_zTe$, (54), and in $Zn_{1-z}Mn_zTe$, (53), as well as in other pseudo-binary SMSC's such as $Hg_{1-z}Mn_zTe$, (65) and $Cd_{1-z}Mn_zSe$, (54).

On the other hand, samples with higher Mn concentrations were found to exhibit a reduced susceptibility which resulted in an upturn of the $1/\chi$ curves in figs. 4.14 to 4.18. This effect may also be observed in the $1/\chi$ plots of Oseroff, (54), for $Cd_{1-z}Mn_zTe$. A similar behaviour is also observed by Heikens et al in $Mg_{1-z}Mn_zS$, (121), and by Fiorani et al in $ZnCr_{2x}Ga_{2-2x}O_4$, (122), for samples with a higher concentration of magnetic atoms.

One sample, $Cd_{0.5}Mn_{0.5}Te$, in fig. 4.14 seems to exhibit both of the above behaviours. At high temperatures, the susceptibility typically follows the Curie-Weiss law. At lower temperatures, the $1/\chi$ plot first deviates upward, as in the cases of high Mn concentration. As the temperature is lowered further, the $1/\chi$ curve then turns down with the resulting behaviour resembling that of the samples with lower concentration. This gives the appearance of a competition between two effects. Similar behaviour can be seen in some of the plots of $1/\chi$ published in both reference 54 and 122.

One way to examine this phenomenon more closely is to calculate the deviation from Curie-Weiss behaviour at T_g. This may be accomplished by using the following quantity;

$$\Delta\chi(T_g)=\chi_{ext}(T_g)-\chi_{meas}(T_g)$$

where the first term on the right hand side represents the susceptibility at T_g extrapolated from the high temperature Curie-Weiss behaviour and the second term represents the actual measured value at T_g. The results were plotted in fig. 4.25. For $z<0.6$, $\Delta\chi(T_g)$ decreases rapidly as the Mn concentration is increased, just as $\chi(T_g)$ did in fig. 4.13. For $z>0.6$ the variation levels out and takes on negative values. A smooth curve is drawn through all the points. It is interesting to note that the curve crosses the z axis and changes sign at about $z=0.58$ which coincides with the onset of the antiferromagnetic phase as determined by neutron diffraction, (50, 51). The point where it changes sign also coincides with the minimum of the $\chi(T_g)$ variation plotted in fig. 4.13. However, it should be mentioned that this should not be considered as a well defined point, since using Oseroff's results for a sample of $Cd_{0.47}Mn_{0.53}Te$, (54), would give a negative value for $\Delta\chi(T_g)$. This would seem to indicate that the concentration where $\Delta\chi(T_g)$ changes sign is more ambiguous than what might be indicated by fig. 4.25.

The $Mg_{1-z}Mn_zS$ alloy system crystallizes into a NaCl structure over its entire composition range, (121). Therefore the Mn ions will be distributed over the sites of an FCC sublattice which is the same as the situation that occurs in $Cd_xZn_yMn_zTe$.

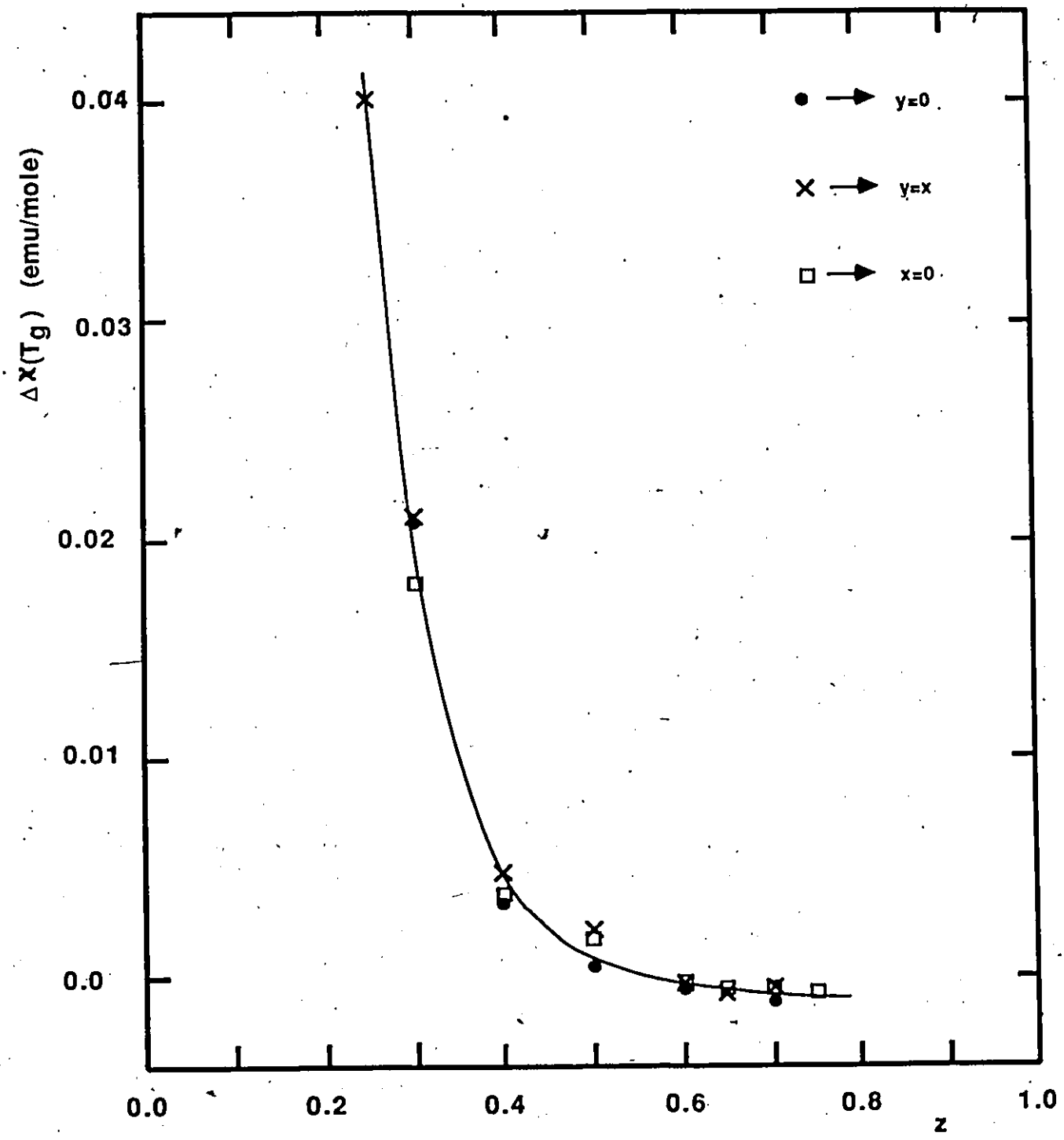

FIGURE 4.25 $\Delta\chi(T_g)$ versus Temperature.
The solid line serves merely to guide the eye.

In the case of this sulfide alloy, the results indicate that a change from enhanced to reduced Curie-Weiss behaviour occurs for $0.53<z<0.676$. This agrees with the results obtained in the present work.

The onset of this non-Curie-Weiss behaviour was estimated within an uncertainty of apporoximately 10K and is plotted as a function of z in fig. 4.26. For the case of sample $Cd_{0.5}Mn_{0.5}Te$, two different temperatures could be obtained, one for the initial onset and one where the $1/\chi$ curve drops below the extrapolated Curie-Weiss line. For $z<0.6$, this temperature decreases with increasing z, whereas for $z>0.6$, it increases very rapidly. A very sharp discontinuity seems to occur just below $z=0.6$ which coincides with the transition concentrations of figs. 4.13 and 4.25 as well as with the spin glass to antiferromagnetic transition. However, once again one should not place to great an emphasis on the apparent sharpness of this discontinuity since it can be blunted somewhat by including the temperature of the initial onset of the non-Curie-Weiss behaviour for sample $Cd_{0.5}Mn_{0.5}Te$.

To summarize these results one may replace the magnetic phase diagram presented in fig. 4.9 by a magnetic state diagram, shown in fig. 4.27. For samples with $0.05<z<0.5$, a spin glass behaviour is observed at the lowest temperatures. At higher temperatures, enhanced paramagnetism is observed followed by true paramagnetism at even higher temperatures. Samples with $z\geq0.6$, behave like a antiferromagnet at the lowest temperatures. At higher temperatures, they exhibit a reduced paramagnetism, and then

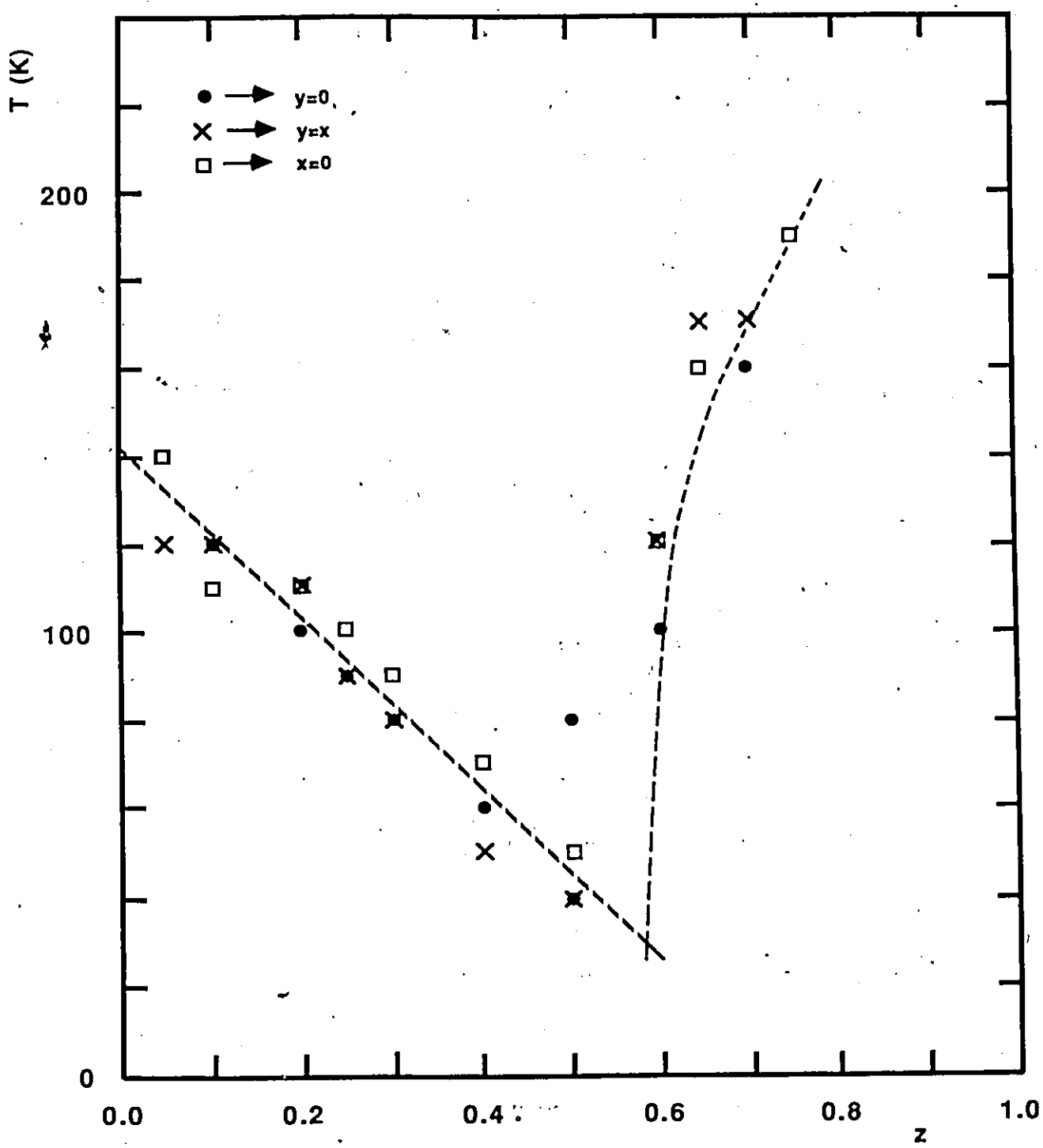

FIGURE 4.26 Temperature of the Onset of Non-Curie-Weiss behaviour versus z Composition. The values indicated could be determined to an accuracy of approximately ±10 K.

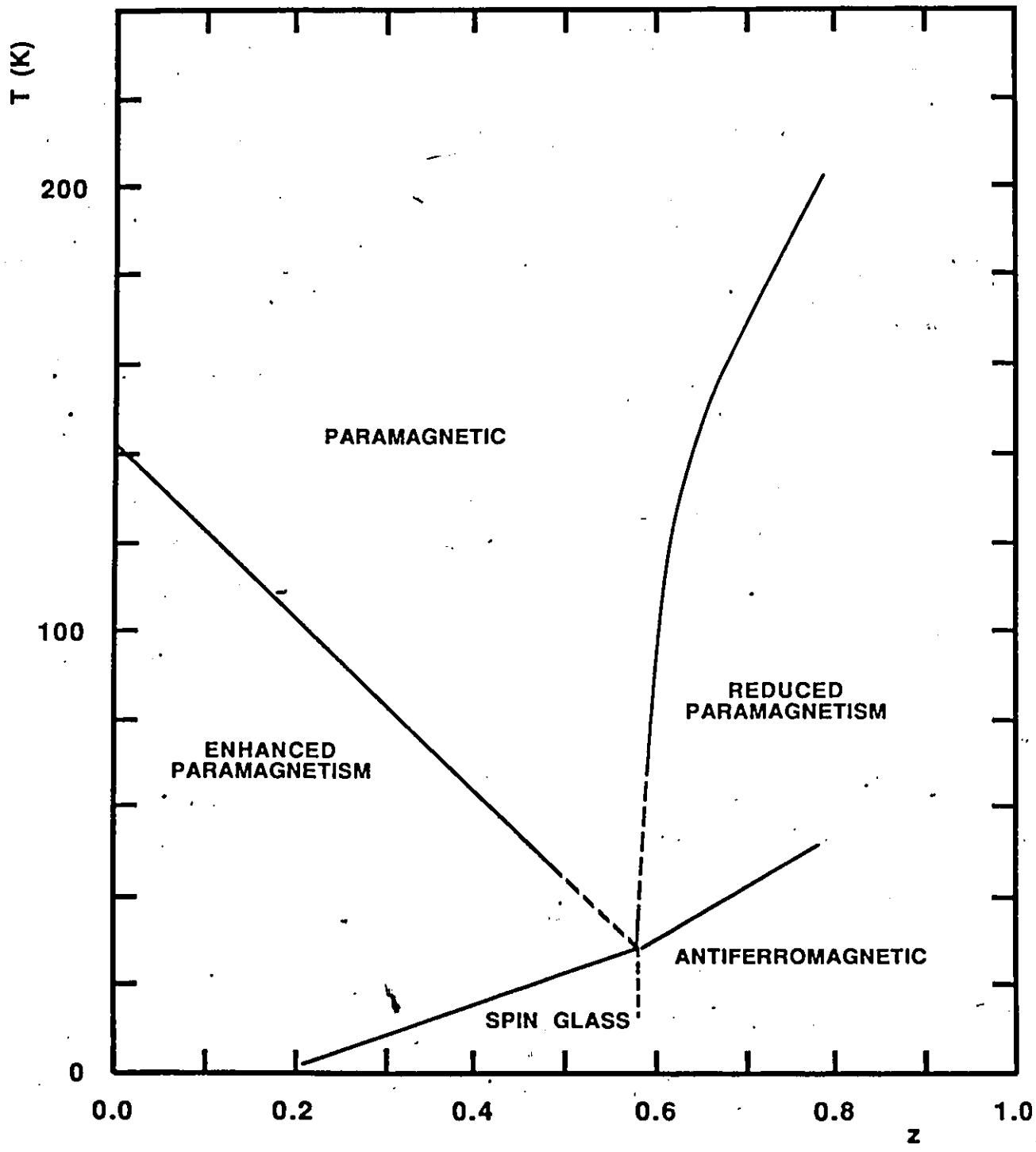

FIGURE 4.27 Magnetic State Diagram. The lines separating the different magnetic states appear to meet at the point represented by T~28K and z~0.58.

true paramagnetism at even higher temperatures. Somewhere in between these two composition ranges, $0.5<z<0.6$, a transition from spin glass to antiferromagnetic behaviour, as well as a transition from enhanced to reduced paramagnetism, occurs.

One possible explanation for the non-Curie-Weiss behaviour may be arrived at by considering the effects of the clustering of Mn ions, (68). It was explained in section 4.1 that in any diluted magnetic material the magnetic ions will group into some form of clusters, whether or not a completely random distribution exists. At high temperatures, the exchange coupling is completely overwhelmed by the thermal effects and so the magnetic moments due, to the ions within any of these physical clusters, will be independent of each other. In this case, all spins will respond to a magnetic field according to the Curie-Weiss law. At low temperatures, the thermal energy is decreased and the exchange interaction between the closest Mn ions will cause some sort of short range coordination. Since the interaction is antiferromagnetic, one might expect a more or less antiparallel alignment of spins within these magnetic clusters, as was demonstrated by neutron diffraction measurements for samples with high Mn concentration, (50, 51). With this type of alignment, pairs of spins would tend to cancel each other out and so, would contribute very little to the resulting susceptibility. Since the total number of free spins is reduced, the susceptibility would be reduced. However, there will be an imperfect cancellation among the spins on the surface of the magnetic cluster, resulting in it

behaving like a large particle with a magnetic moment. The susceptibility due to these clusters would depend on the strength of the interaction between them. Since this would be smaller than that between two spins, χ, would tend to be larger, because the Curie-Weiss temperature in eq. 4.6 would then be smaller. This effect is known as superparamagnetism or super-antiferromagnetism (20), and, since it depends on the proportion of spins which are situated on the surface of a cluster, would be greatest when the size of the clusters are small. Therefore, samples with smaller z concentrations would exhibit a stronger enhanced paramagnetism as indicated by fig. 4.25. It would also be expected that the temperature where the effects of superparamagnetism become significant would also increase with decreasing z, as indicated in fig. 4.26.

When the magnetic clusters are large, there are fewer uncompensated spins in the sample since the volume of a cluster grows faster than its surface. This would result in a greatly reduced superparamagnetism. It was pointed out earlier that the loss of free spins to clusters results in a smaller susceptibility. If the superparamagnetism is not strong enough to overcome this, then the total susceptibility would decrease. Such a circumstance would occur for samples with the large z, since the higher the concentration, the larger the clusters and consequently, the effects of superparamagnetism would be smaller and the reduction due to the loss of free spins, would be greater. Also, according to Giebultowicz et al, (17), the Mn ions of the samples which lie

in the antiferromagnetic range group into large antiferro clusters which have a wide range of Neel temperatures. This might explain why the transition from enhanced to reduced paramagnetism seems to correspond to the transition from spin glass to antiferromagnetic behaviour.

Another explanation for this non-Curie-Weiss behaviour is contained in a paper by A.W. Simpson, (120), on amorphous antiferromagnetism. He points out that in a diluted magnetic alloy, isolated paramagnetic atoms may exist. Since there would be basically no interaction between these atoms, their susceptibility would be very large at low temperatures, i.e. θ, in eq. 4.6 would go to zero. These isolated atoms would be more numerous when the Mn concentration is small and will decrease with increasing z. This would lead to the same conclusions as outlined above.

Both of the mechanisms which have been discussed can equally well explain the non-Curie-Weiss behaviour as shown in figs. 4.25 and 4.26. The first mechanism depends on clustering are and would produce the greatest effect with hard clusters. The second mechanism may also be affected by clustering. It can also be used to explain the upturn of the susceptibility of the z=0.3 samples at low temperatures, which had been previously discussed in section 4.3.1. It is likely that these mechanisms are both present simultaneously since they both arise from the dilution of a magnetic crystal.

4.4 The Exchange Interaction

As indicated previously, an exchange interaction is responsible for the coupling of the magnetic ions in these materials. In metallic spin glasses, the exchange occurs via an indirect coupling through conduction electrons, (39). This is known as the RKKY exchange and has the following form;

$$J(r) \approx \frac{\cos 2k_F r}{(k_F r)^3}$$

where k_F is a wave vector. This leads to the scaling laws of Tholence and Tournier, (71), which have proven to be quite successful in explaining some of the relationships which occur between the magnetic properties and the concentration of the magnetic ions.

For many SMSC's, the absence of conduction electrons in suitable numbers usually results in a negligible RKKY contribution to the exchange interaction. The coupling would then have to originate through a different process.

It is believed that the direct exchange mechanism may be excluded for this material, (72), for two main reasons. The localization of the 3d electrons together with the large distance between Mn ions would result in very little direct overlap of the wavefunctions. As well as this, it can be seen from fig. 2.2 that there is a Te ion partly between the Mn ions, which would tend to block the direct interaction. However in recent years, Oelhafen et al, (73), have concluded from their measurements that the Mn 3d

electrons in $Cd_{1-z}Mn_zTe$ are in fact delocalized. This might throw into doubt the validity of the first of the above reasons.

A possible candidate for the exchange mechanism in SMSC might be superexchange, (74). This is responsible for the coupling in many classic antiferromagnetic materials such as MnO. In this case, the Mn 3d electrons indirectly interact with each other through the intervening oxygen 2p electrons. However, there are problems with this. The classic theory of superexchange involves the use of strongly localized wave functions of the anion valence electrons. In SMSC's the anion valence electrons are delocalized and are more correctly described by a band model. It would then appear that the normal superexchange interaction is not adequate for these materials.

In attempting to determine the mechanism which is responsible for the spin coupling in these materials, one can consider the behaviour of the T_g's as a function of composition. It was indicated in section 4.3.1 that the T_g values of figs. 4.9 and 4.10 extrapolate to the theoretical nearest neighbour percolation limit. This implies that the interaction between nearest neighbours dominates in the concentration range $0.2<z<0.6$. It was also indicated that values of T_g were observed for samples of $Cd_{1-z}Mn_zTe$ with z smaller than the percolation limit of 0.18 by Novak et al, (55). This suggests one of two possibilities. The first is that a different exchange mechanism is acting at these lower concentrations. The second is that there is only one mechanism present and the strength of this interaction decreases

rapidly with distance.

With this last possibility in mind, it is useful to consider the variation of T_g values in terms of the relation initially proposed by Escorne et al, (63, 81), which assumes that the exchange between two Mn ions can be written as;

$$J(r) = J_o \exp(-\alpha r) \qquad (4.8)$$

where r is the distance between ions. The nearest neighbour spacing on an FCC cation sublattice is $a/\sqrt{2}$, where "a" is the lattice parameter. For a concentration z of Mn ions arranged at random on such a sublattice, the mean spacing between magnetic ions is $(a/\sqrt{2})z^{-1/3}$. Therefore, the mean exchange between Mn ions is given by;

$$J = J_o \exp(-\alpha a z^{-1/3}/\sqrt{2})$$

Since two spins become frozen with respect to each other when the thermal energy between them becomes smaller than the exchange, it is assumed that $k_B T_g = -AJ$, where A is a constant independent of z. This then leads to the following relation;

$$\ln T_g = \ln(-AJ_o/k_B) - \alpha(a/\sqrt{2})z^{-1/3} \qquad (4.9)$$

If the two assumptions made above are satisfied and α is a constant, then a plot of $\ln T_g$ vs $(a/\sqrt{2})z^{-1/3}$ should give a straight line.

Such a plot was produced using values of T_g from figs. 4.9 and 4.10 along with values of "a" from chapter 2 and is presented in fig. 4.28. For the range of values corresponding to $z<0.6$, a linear behaviour is observed. The small increase of T_g with y for a constant value of z, which was mentioned in

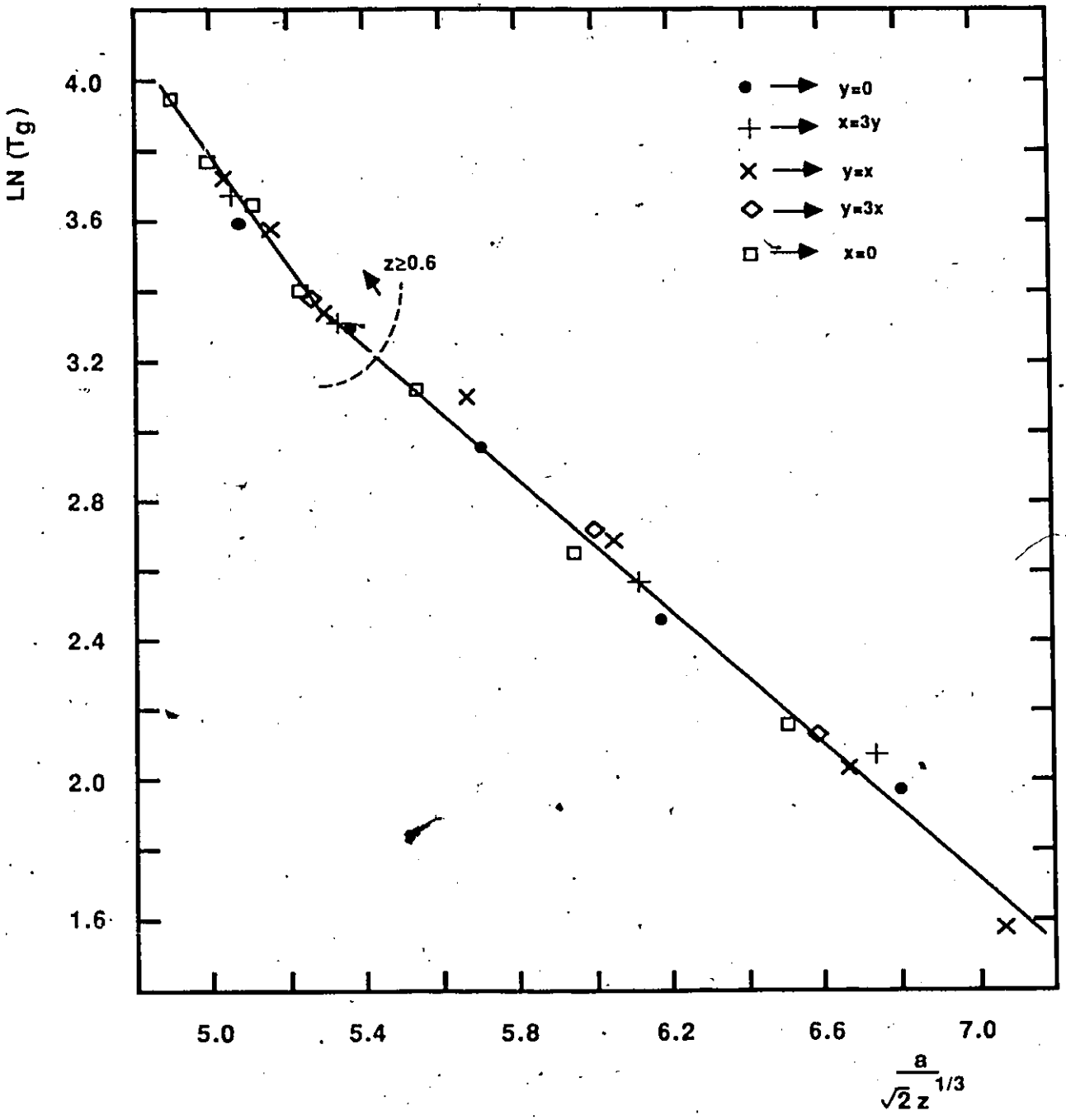

FIGURE 4.28 Analysis of T_g values using eq. 4.9.

increase of T_g with y for a constant value of z, which was mentioned in section 4.3.1, appears to be completely compensated by the change in lattice parameter so that groups of values with the same z concentration are spread apart just enough for them to all fall on a single line.

In the antiferromagnetic range of z, the values plotted in fig. 4.28 break away from this linear behaviour with a change of slope similar to the situation in fig. 4.9 and 4.10. The point where this change occurs is obscure but considering the results of section 4.3, one might expect the change to occur over a small concentration range somewhere between z=0.5 and z=0.6. Such a change in behaviour at first suggests a change in the exchange energy. This may signify that a different exchange mechanism may become important in this composition range and the onset of antiferromagnetic behaviour is not only a consequence of filling up the FCC cation sublattice.

Fig. 4.28 indicates that in this material, the exchange interaction may be represented by eq. 4.8 with α, a constant. It was found that the simple exponential relation could be replaced by a slightly more complex one, without changing the features observed in fig. 4.28. The more complex representation is as follows;

$$J(r) = \frac{J_o \exp(-\alpha r)}{r^t} \qquad (4.10)$$

where t is an integer between zero and three. To illustrate this, the example of t=2 will be developed. With $r=(a/\sqrt{2})z^{-1/3}$, eq. 4.9 must be replaced by;

$$\ln\left\{\frac{a^2 T_g}{2z^{2/3}}\right\} = \ln\left\{-\frac{AJ_o}{k}\right\} - \frac{\alpha a'}{\sqrt{2}z^{1/3}} \qquad (4.11)$$

A plot of the data based on eq. 4.11 is presented in fig. 4.29. It can be seen that the form of the diagram is exactly the same as that of fig. 4.28, with both demonstrating that α is a constant for all samples with $z<0.6$. Similar results were obtained for $t=1$ and $t=3$ in eq. 4.10.

In the spin glass range, the linear behaviour allows us to calculate a value for α of 7.8 ± 0.3 nm^{-1} from fig. 4.28. Using eq. 4.10 with this value and with $t=0$, one may calculate the ratio of the nearest neighbour exchange, J_1, which occurs at a separation of $a/\sqrt{2}$, to next nearest neighbour exchange, J_2, which occurs at a separation of "a". Using typical values for "a", J_1/J_2 is estimated to be approximately 5.0. This is different from the value of 8.3 arrived at by Escorne et al, (81), using a similar analysis on their results for samples of $Cd_{1-z}Mn_zTe$. The disagreement can be accounted for by the fact that their values for T_g were several degrees smaller than those for equivalent samples in this work as well as in ref. 18 and 54. However, the conclusion that J_2 is small but not negligible, which was arrived at by Escorne et al, is still supported by this.

For fig. 4.29, α is calculated to be 6.0 ± 0.2 with a value for J_1/J_2 slightly larger than six. Therefore, the exchange interaction decreases more rapidly when $t=2$, as might be expected.

The possible exchange mechanisms which may possess the behaviour indicated by eq. 4.10 will now be considered: The first

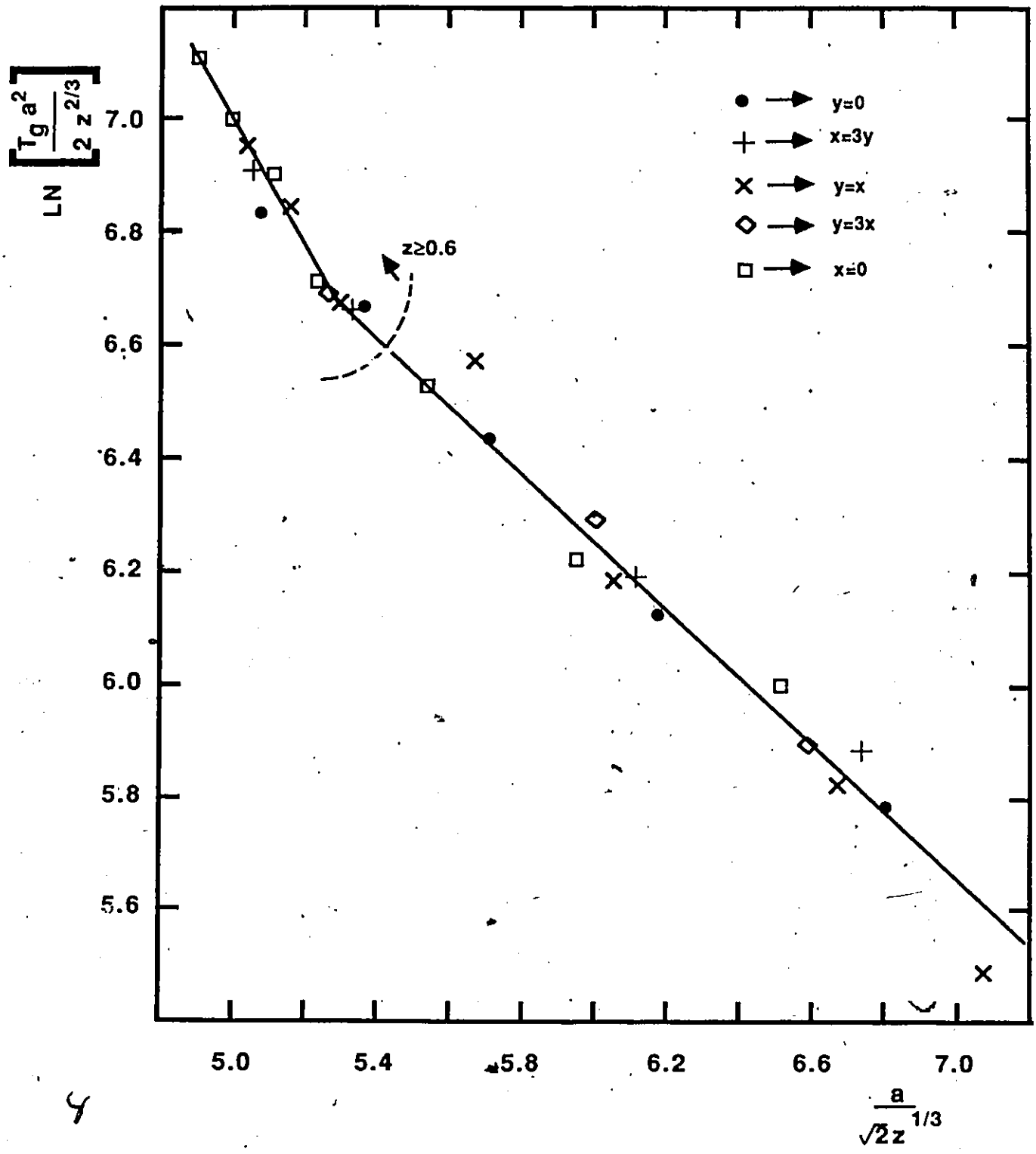

FIGURE 4.29 Analysis of T_g values using eq. 4.11.

mechanism is based on the Bloembergen-Rowland interaction, (29), and has inspired a great deal of interest, (72, 75-79). The exchange occurs through a virtual electronic transition from the valence band to the conduction band. The model appears to be successful for the case of zero gap $Hg_{1-z}Mn_zTe$, (80), which would have an enhanced probability of occurrence for this type of virtual transitions. Under certain conditions of lattice size and energy gap width, Bloembergen and Rowland, (29), indicate that the variation of the exchange with r is very similar to eq. 4.10. However, in this case the exponent is given by;

$$\alpha = \left\{ \frac{2m_c E_g}{\hbar^2} \right\}^{1/2} \qquad (4.12)$$

The quantity m_c is the conduction band effective mass and E_g is the energy gap.

The difficulty with this mechanism arises from the fact that α depends on the energy gap, which was shown to vary from about 1.5eV to approximately 2.8eV in chapter 3. One can see that if α were to remain constant, the effective mass must be inversely proportional to the energy gap. However in ref. 11, the authors indicate that the effective mass increases with the energy gap indicating that α could not be constant with composition. One might have to conclude that this form of the virtual interband exchange interaction is not dominant in these crystals. However, it should be pointed out that eq. 4.12 was arrived at by considering only a finite part of the conduction band. Ginter et al, (72), have shown that if the entire conduction band is taken

into account, the form of the exchange is changed, although it is still strongly dependent on the energy gap. They go on to say that the final result for this type of indirect exchange is very sensitive to the shape of the bands and may require numerical calculations of the band structure. It is unknown at present whether this would be sufficient to result in an expression for which is independent of the energy gap.

An alternative mechanism has been suggested by Gulacsi et al, (82), as a possibility for insulating spin glass systems. In this case, the indirect coupling is mediated by phonons resulting in the following form;

$$J(r) = g\frac{\cos(kr)}{r^s}\exp(-r/l) \qquad (4.13)$$

where g and k are constants and s is either equal to three or to five depending on the range of k. The exponential part of 4.13 is included as a modification to account for the finite mean free path, l, of the phonons due to lattice imperfections. Depending on the value of k, the cosine term in this equation may introduce a complication which would make it unable to explain the results of figs. 4.28 and 4.29. As well, the exponent in this case, depends on the mean free path, which is unlikely to remain constant when the composition is varied. This is because the change in lattice parameter, measured in chapter 2, suggests that the cations, Cd, Zn and Mn, have different sizes. Therefore it would seem that this mechanism is also not appropriate for this material.

Another possibility is similar in concept to the virtual

interband transition model. It involves a virtual transition from the valence band into a Mn 3d state, (83, 84, 85, 142). Basically this involves going from a ground state consisting of a full valence band and a $3d^5$ level, to an excited one consisting of a valence band with a hole and a $3d^6$ level. The left over empty state makes it possible for the coupling of the spins to occur through the valence band. This type of transition conforms better with the results because for these materials, the valence band is insensitive to changes in composition. Thus one would expect that the energy difference between the two states does not change very much with concentration. This is important because the form of this interaction depends on this quantity just as eq. 4.12 depends on the energy gap. The exchange is given by, (85);

$$J(r) = \frac{J_o \exp(-\alpha r)}{r^2} \qquad (4.14)$$

where in this case α is given by;

$$\alpha = 2\left\{\frac{2\epsilon m_v}{\hbar^2}\right\}^{1/2} \qquad (4.15)$$

where ϵ is the energy difference between the ground state and the excited state and m_v is the valence band effective mass. It can be seen that eq. 4.14 has the same form of eq. 4.10 with t=2. Also, since there is nothing in eq. 4.15 which would indicate that the exponent must vary with composition, it would seem that this exchange mechanism meets the necessary requirements.

Previously, it was pointed out that values of T_g were determined for samples of $Cd_{1-z}Mn_zTe$ with z smaller than the

nearest neighbour percolation limit, by Novak et al, (55). With these values, fig. 4.29 was redrawn in fig. 4.30 with a different scale, which allowed for the inclusion of the new data. Five points were obtained by estimating the position of the susceptibility peaks from the diagrams in Novak et al. The three highest concentrations, z=0.15, 0.125, 0.1, were all found to lie reasonably close to the fitted line extrapolated from higher values of z. So there is very good agreement with this form of the exchange down to z=0.1. The results for z=0.05 and 0.01 were significantly different from the predictions with both falling well above the line. It was pointed out by Novak et al that the interaction between dipoles may be significant at these low concentrations. It is possible that the higher values of T_g for these samples may be due to this. An alternative explanation may be that in this composition range, z<0.05, some researchers have reported observing some ferromagnetic behaviour, (54, 70), so a different exchange mechanism may become important. However, as was pointed out in section 4.3.1, one should not attach to great an importance to this. In spite of these two points, the use of eqs. 4.14 and 4.15 appears to be further justified and so all of the subsequent analysis will be done assuming that the exchange is given by these equations.

The analysis of the T_g values has already been done and is presented in fig. 4.29. It was indicated previously that α, obtained from the slope had a value of 6.0 ± 0.2 nm^{-1}. Using eq. 4.15, one can calculate ϵ, which is the energy difference in the

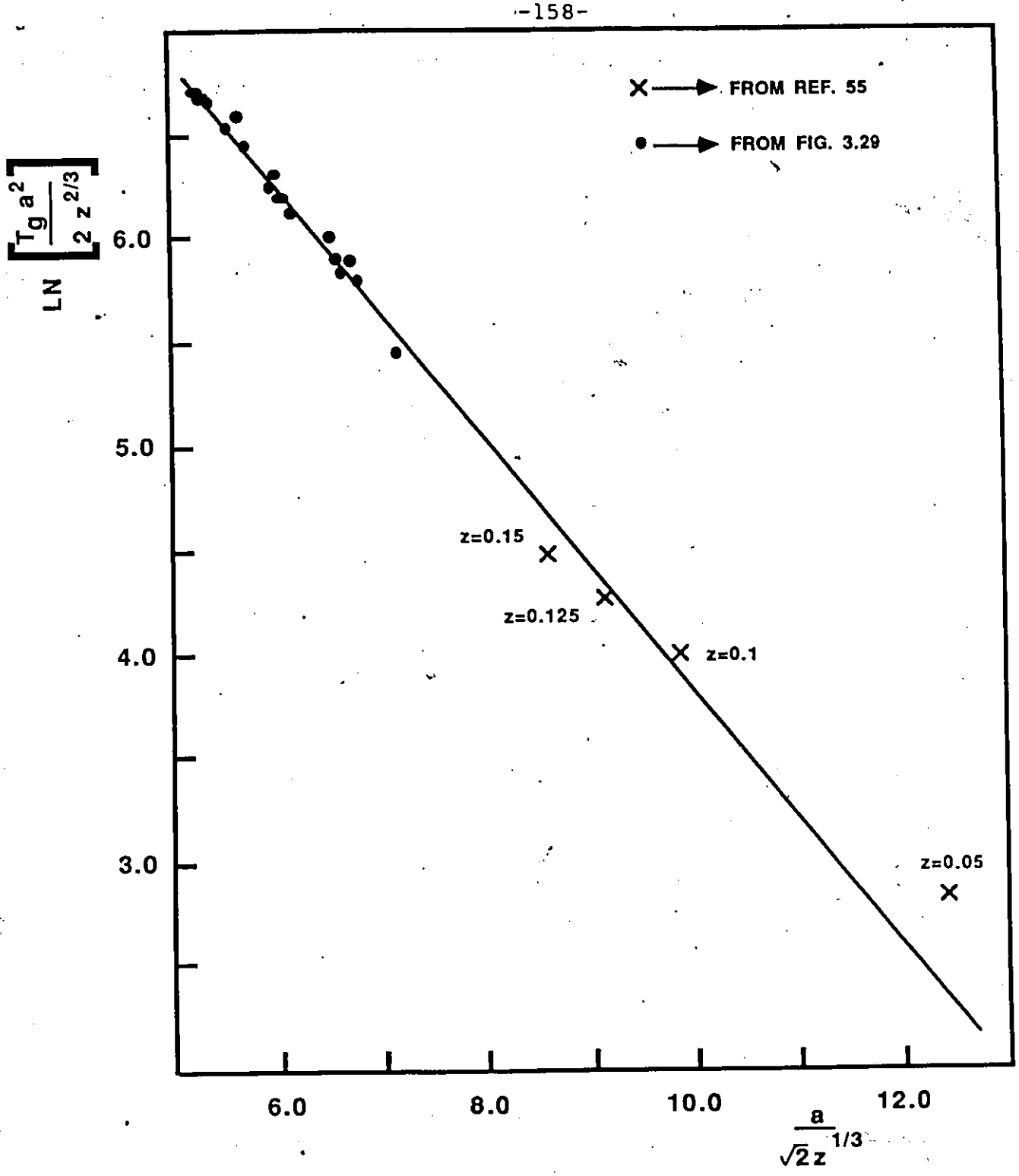

FIGURE 4.30 Analysis of T_g Values Using Eq. 4.11. Included in this plot is data for z<0.2 from ref. 55. The value for z=0.01 from this reference falls well outside the range displayed here.

virtual transition. A reasonable estimate for the effective mass is given by the heavy hole mass for CdTe which is close to the free electron mass, (123). Thus, the value of ϵ is calculated to be 0.34 ± 0.05 eV. This is smaller than the energy gap of any composition, as was shown in chapter 3, indicating that this mechanism would be favored over the Bloembergen-Rowland interaction.

The intercept of fig. 4.29 gives, $\ln(AJ_o/k_B)=9.83\pm0.13$. It was indicated by Anderson, (22), that for regular antiferromagnetic materials, A may be equated to S(S+1). Using S=5/2, as determined in section 4.3.2, J_o may be estimated. For the present case, the value which was calculated was $J_o/k_B=-21\pm3$ K nm^2. This result enables the independent calculation of the nearest neighbour and next nearest neighbour exchange energy which can be compared to particular values quoted in the literature. The results for a typical value of "a" are as follows;

$$\frac{J_1}{k_B} = -7.0\pm0.3 \text{ K}$$

$$\frac{J_2}{k_B} = -1.135\pm0.03 \text{ K}$$

The values reported in the literature were all for samples of $Cd_{1-z}Mn_zTe$ of various concentrations. Although the exchange energy varies with composition, the range of concentration which is possible does not allow it to vary by much more than the uncertainties which are indicated above. Consequently this effect

will be neglected in the comparisons.

For the nearest neighbour exchange energy, Galazka, (67), quotes a value of 0.55K from specific heat measurements, and between 6K and 8K from ESR and high temperature susceptibility results. Ching & Huber, (100) quote a value of -1.1 K while Shapiro et al, (86), obtain a value of -10 K while a theoretical calculation by Larson et al, (142), resulted in a value of -12 K. Both Shapiro and Galazka suggest that the smaller values may in fact be the next nearest neighbour exchange. This hypothesis is supported by the results obtained in this work and quoted above. The comparison also supports the use of the exchange mechanism represented by eqs. 4.14 and 4.15.

Further support for this mechanism comes from the results of other members of the research group. The alloy systems $Cd_xZn_yMn_zSe$, (92), and $Cd_{1-z}Mn_zSe_{1-y}Te_y$, (91), both have a zinc blende crystal phase over part of their range of concentration, as well as an hexagonal wurzite phase, over a different range. For the zinc blende phase a plot similar to fig. 4.29 shows the same linear dependence as in the present case. In fact, the values lie on the same line as in fig. 4.29 so that the exchange constants obtained from them are identical. For the wurzite phase, a different slope and intercept was obtained, (91, 92). Values for the nearest neighbour exchange energies of those alloys also agreed with those quoted in the literature.

The next step in this analysis is to now take this model of the exchange interaction and use it to predict values of

Curie-Weiss θ. This was accomplished by using an equation for antiferromagnetic materials, (87);

$$\theta = \frac{2zS(S+1)}{3k_B}\sum n_i J_i \qquad (4.16)$$

where the sum is taken over the i'th nearest neighbours, n_i is the coordination number for the i'th neighbours and $J_i = \exp(-\alpha r_i)/r_i^2$. This equation is exact for high temperatures. Values for n_i and for r are given in Table V for the first seven terms. One can see that the first term accounts for about 80% of the magnitude with the significance of the subsequent terms dropping rapidly with the index i. Consequently only the first four terms were used in the calculation. The results of these calculations are represented by the broken lines in figs. 4.19 to 4.23. One can see that there is a remarkable agreement between these predicted values and the measured results. This is a further indication of the validity of eq. 4.14. With the exception of the samples on the Zn edge, the agreement extends into the antiferromagnetic range. This might indicate that even if a different mechanism becomes important in this range, much of the behaviour can still be attributed to the original exchange.

The agreement may be examined more closely by the use of residual analysis. The residual for each value of θ is defined as follows;

$$R = \frac{\theta_p - \theta_m}{\sigma} \qquad (4.17)$$

where θ_p and θ_m are the predicted and measured values

i	POSITION	r_i	n_i	% of First Term
1	(1/2,1/2,0)	$a/\sqrt{2}$	12	-
2	(0,0,1)	a	6	8.1
3	(1,1/2,1/2)	$\sqrt{3/2}a$	24	9.2
4	(1,1,0)	$\sqrt{2}a$	12	1.67
5	(3/2,1/2,0)	$\sqrt{10}/2a$	24	1.41
6	(1,1,1)	$\sqrt{3}a$	8	0.22
7	(0,0,2)	2a	12	0.03

TABLE V Values of the distance and the coordination number for the i'th neighbours of a face centered cubic lattice. The distances are given in terms of the lattice parameters. The size of each term relative to the nearest neighbour term is shown in the final column.

of θ respectively and σ is the standard deviation, which is estimated to be approximately 27K. Values of R were plotted against composition in fig. 4.31. This type of plot enhances the differences between the predicted and measured values and highlights any trends. In this case, the points in fig. 4.31 are scattered around a negative value of R, signifying that the predictions are generally smaller than the measurements. The only trend that is observed is a slight reduction in R for the high z values, especially for x=0. The average value of R is about -0.4 resulting in the average predicted θ's to be about 10K too small.

The results discussed in this section indicate that a good explanation of the experimental data can be given in terms of the exchange mechanism represented by eqs. 4.14 and 4.15. The value of the energy separation, ϵ, was found to be smaller than the smallest energy gap in the alloy system. This served as further indication of the validity of this mechanism over the Bloembergen-Rowland interaction. It was found that there was good agreement between the values of J_1/k_B and J_2/k_B and those reported in the literature. As well, the results could be used to give a very good prediction of the values of θ, over most of the composition range, without any adjustable parameters. It is interesting to note that many of these results were obtained by using techniques and equations which were developed for ordinary antiferromagnetic materials. This may indicate that the similarity between spin glass freezing in these alloys and normal antiferromagnetic ordering is greater than what might be expected.

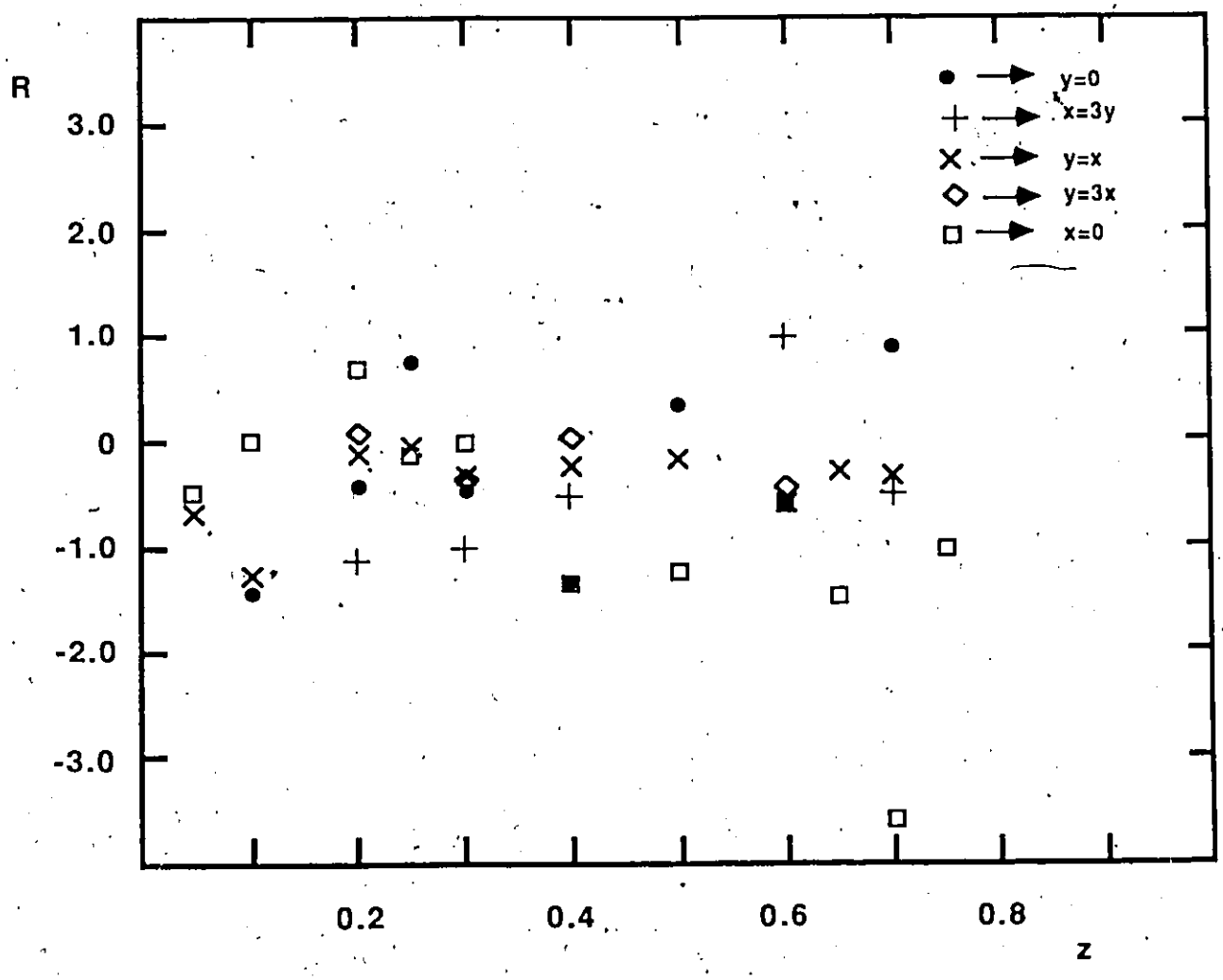

FIGURE 4.31 Residual Analysis of θ. results.

CHAPTER 5

ELECTRON SPIN RESONANCE MEASUREMENTS

5.1 Introduction

A free magnetic ion which possesses a resultant angular momentum quantum number J would give 2J+1 different degenerate levels. In the effect known as Zeeman splitting, the degeneracy is removed by the application of a static magnetic field H. The resulting energy levels are described by $E=g\mu_B M_J H$, where M_J is the magnetic quantum number, g is defined as in eq. 4.2 and μ_B is the Bohr magneton, (89). For the alloy system being investigated, J=S, and g is expected to be very close to 2.0. Without any other considerations, the form of the splitting would be as illustrated in fig. 5.1(a).

In electron spin resonance, (ESR), transitions between these levels are induced by an alternating electromagnetic field and the resulting absorption is measured. The quantum mechanical selection rules are such that only transitions between adjacent levels are allowed, so that in the example shown in fig. 5.1(a), a single resonance is observed, given by;

$$\hbar\omega = g\mu_B H \qquad (5.1)$$

It can be seen that the resonance may be observed by either fixing the frequency, ω and varying H or vice versa. In normal ESR the former method is used, with the frequency fixed at some point in the microwave range.

It should be mentioned that the condition represented by eq. 5.1 may be modified by fine and hyperfine splitting. In the

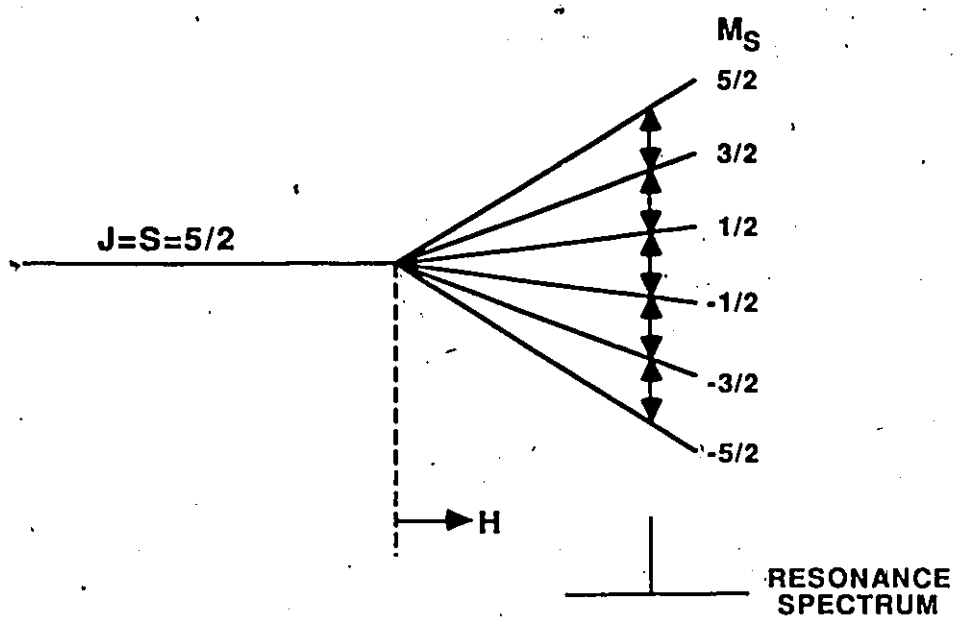

FIGURE 5.1(a) Zeeman Splitting of a $3d^5$ level. In this example there is only one resonance line.

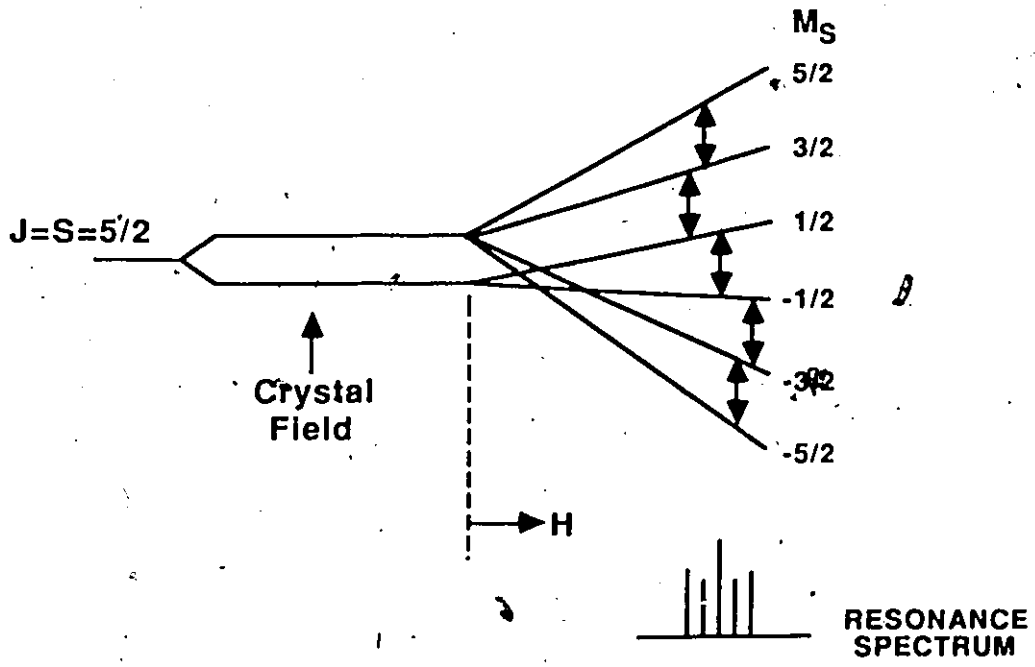

FIGURE 5.1(b) Zeeman Splitting of a $3d^5$ level with Fine Splitting. The single resonance line is split into five by the presence of a crystal field.

former case, some of the degenerate levels are split initially by the crystalline field as indicated in fig. 5.1(b). When a magnetic field is applied, multiple resonance points would occur, resulting in the observation of more than one line. Evidence of these effects was observed by Lambe and Kikuchi, (124), for a sample of $Cd_{1-z}Mn_zTe$ with z=0.01. With hyperfine splitting, the nuclear magnetic moments are coupled to the electron moments to produce an extra splitting of each level. In these materials, structures in the ESR spectrum due to this have been observed in diluted samples, ($z<0.05$), of $Cd_{1-z}Mn_zTe$ by, for example, Oseroff et al, (28). Neither of these effects were observed in crystals with larger Mn concentrations. At higher temperatures, the spectra of samples with higher z, were found to consist of a single resonance line in the present work, as well as in the work of other researchers, (28, 98).

In general the absorption does not occur at a sharply defined magnetic field. Instead it is spread out over a range of H. The size of the spread may be related to several different effects, including various types of relaxation phenomena, such as spin-spin and exchange interactions, (89). Another factor which may affect this linewidth, referred to as ΔH, is inhomogeneous broadening and is caused by an overlapping of any fine or hyperfine structure, as well as by the presence of inhomogeneous fields in the crystal, (89). The main objective in performing these ESR measurements was to determine ΔH as a function of temperature and composition and to investigate the cause of the broadening.

5.2 ESR Measurements

The resonance absorption for different compositions was observed over a wide temperature range, (10 to 500 K). Both the linewidth and the g factor were determined from each absorption curve. The actual measurements were performed by others in the ESR lab. Since the responsibility for the instruments rested in their hands, the apparatus will not be described in detail.

The apparatus consisted of a microwave source, which supplied radiation at X-band frequency, (~9.4 GHz), and a waveguide system, which directed the microwaves into and out of a resonant cavity. Samples placed in the cavity would absorb the radiation when the resonance condition, (eq. 5.1), was satisfied. This was detected as a reduction in the intensity of the microwaves leaving the cavity.

An electromagnet supplied the constant field which was applied to the resonant cavity. The field intensity could be adjusted from zero to about seven kilogauss, allowing for a maximum linewidth measurement of approximately 5.0 Kgauss. Determining the width of a broad absorption line is simplified by measuring its derivative, so the static field was modulated by a small oscillating field. This is similar to the wavelength modulated reflectance measurements described in chapter 3 and illustrated in fig. 3.2. The linewidth was taken as the peak to peak distance of this derivative curve.

5.3 Results of ESR Measurements

At the highest attainable temperature, 500 K, all of the samples produced a single symmetric line with a g value very close to 2.0. Plots of ΔH versus temperature, for a wide range of concentrations are presented in figs. 5.2 to 5.6. In all cases, the linewidth increased with decreasing temperatures. In figs. 5.7 and 5.8, ΔH for two fixed temperatures is plotted as a function of $y/(y+x)$. A more or less uniform increase is observed for any set of values with constant Mn concentration, as Zn is progressively substituted for Cd in the lattice. For small z values, the increase is not very great but it becomes much larger at higher z concentrations. It has already been suggested by Kremer and Furdyna, (90), that such an increase may be related to a decrease in the lattice parameter and hence to an increase in the exchange interaction. This is similar to the case of the magnetic susceptibility measurements of chapter 4, where it was found that both the θ and T_g increases with Zn were directly attributed to the difference in lattice spacing. However, the linewidth increase appears to be larger than the relative increases shown in figs. 4.10 and 4.24, suggesting that perhaps another effect may be involved as well.

For the most part, the shape of the resonance lines remained symmetrical at the higher temperatures. But at lower temperatures, where ΔH started to increase appreciably, the lineshape was observed to broaden asymmetrically. When this occurs, the low field peak of the derivative line remained

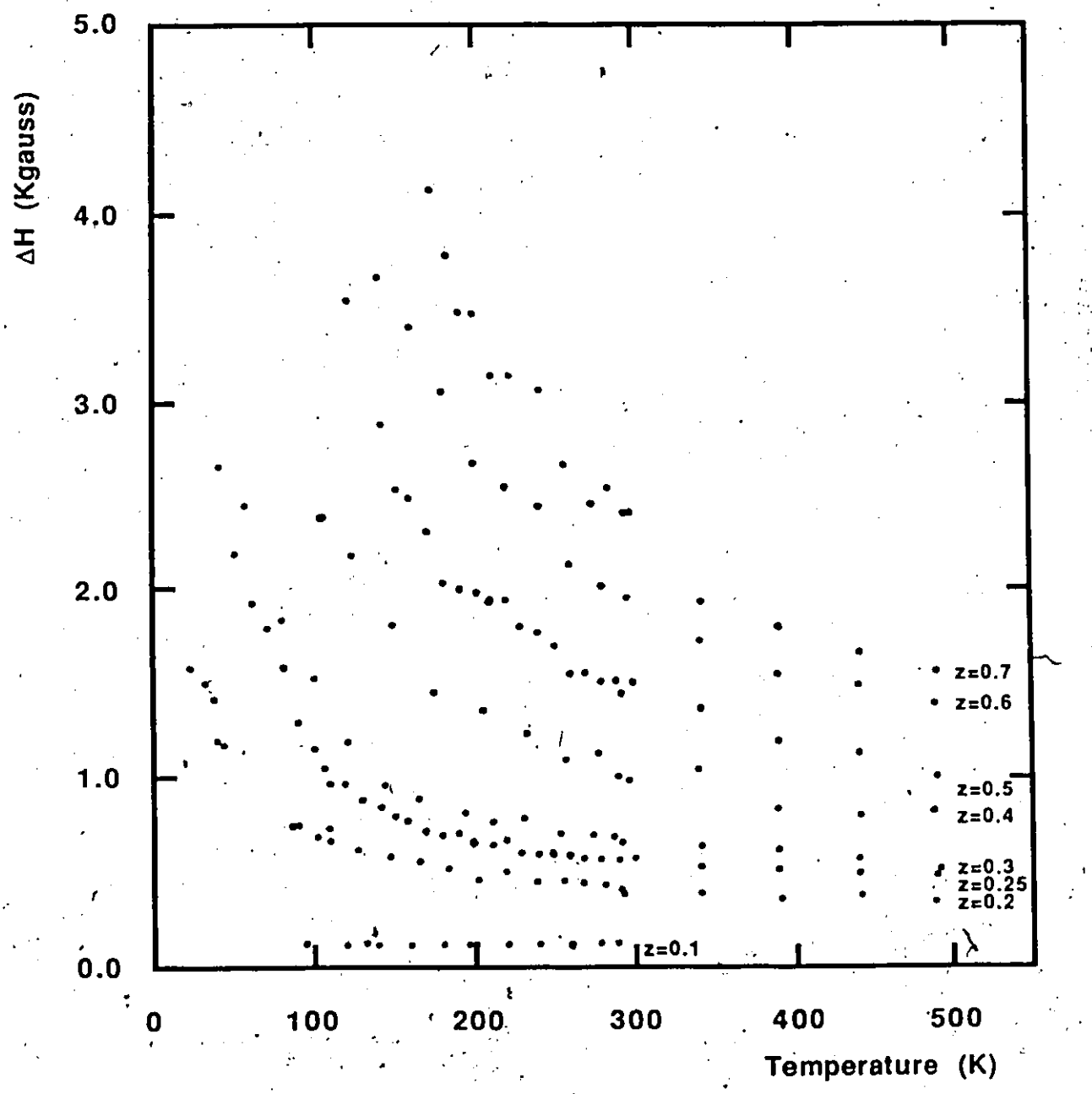

FIGURE. 5.2 Linewidth versus Temperature for y=0 samples.

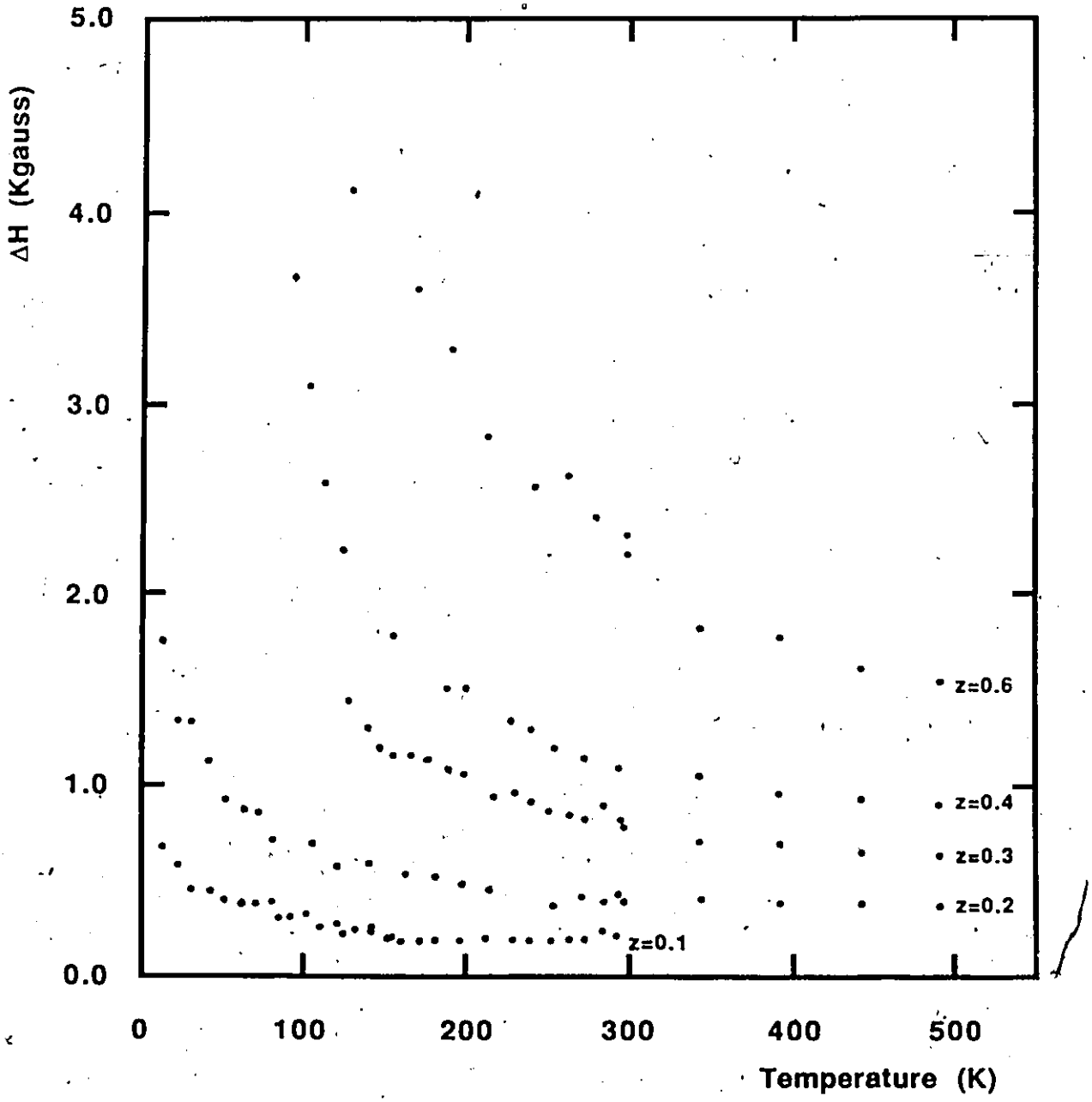

FIGURE. 5.3 Linewidth versus Temperature for x=3y samples.

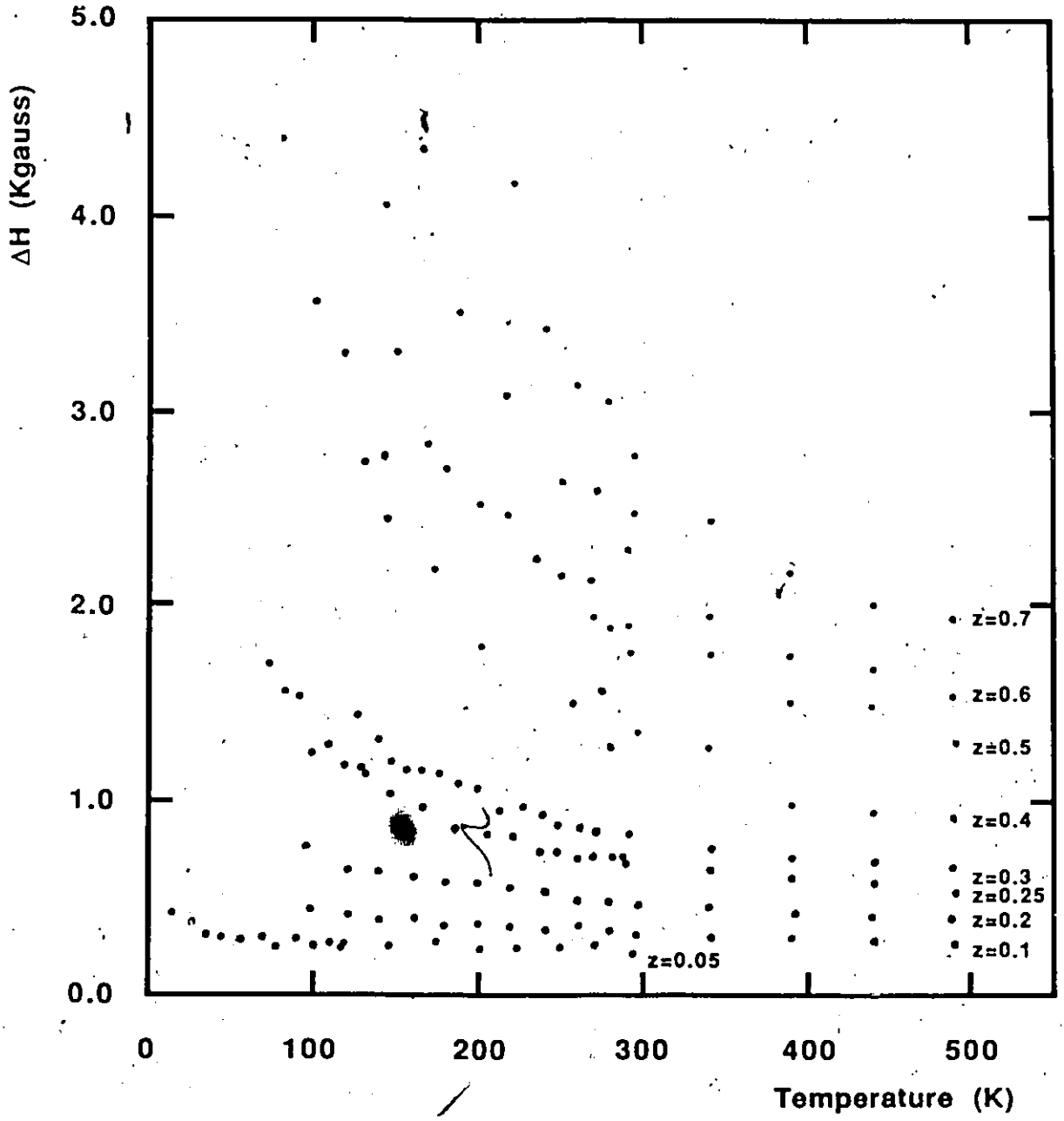

FIGURE. 5.4 Linewidth versus Temperature for y=x samples.

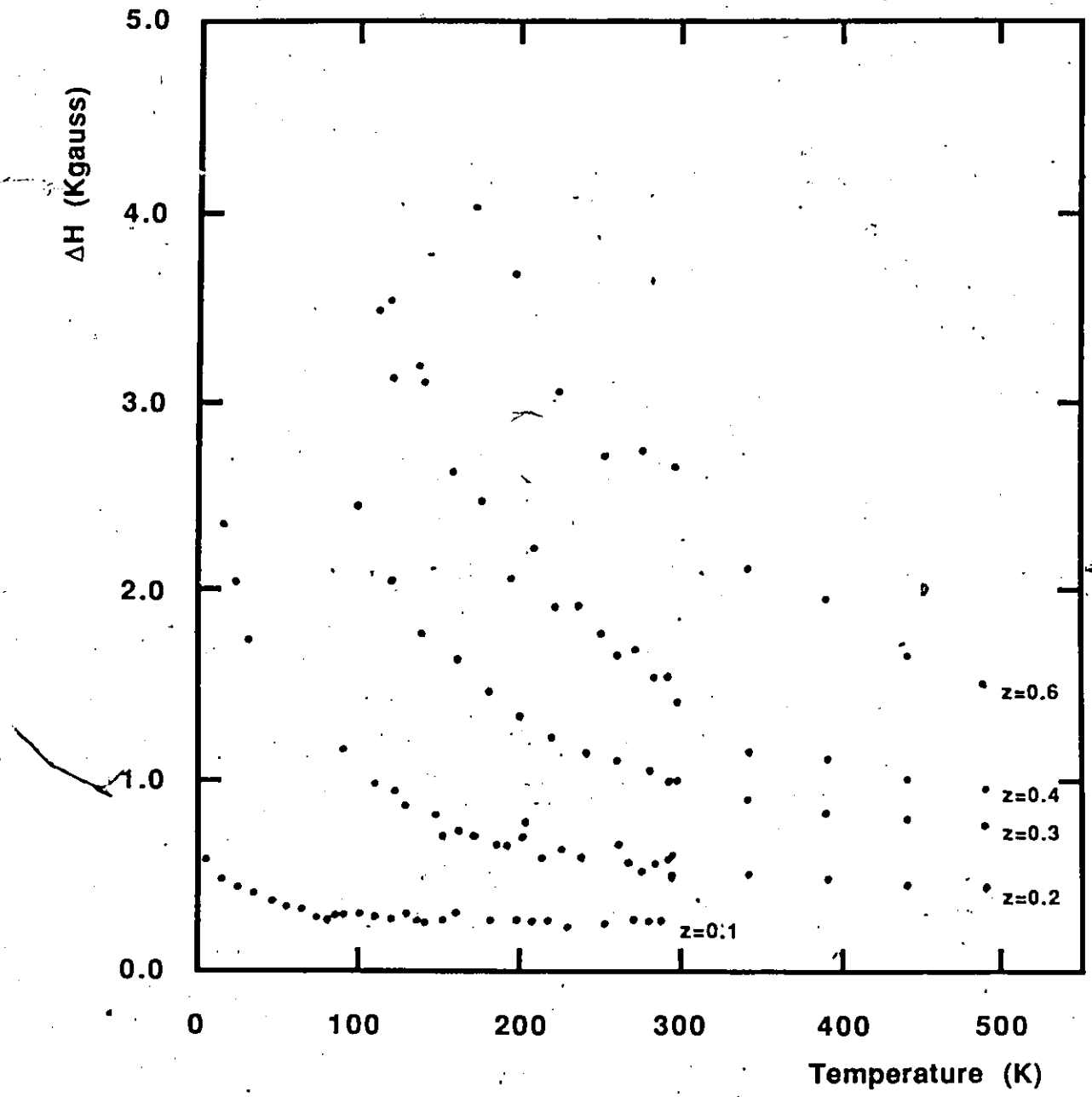

FIGURE. 5.5 Linewidth versus Temperature for y=3x samples.

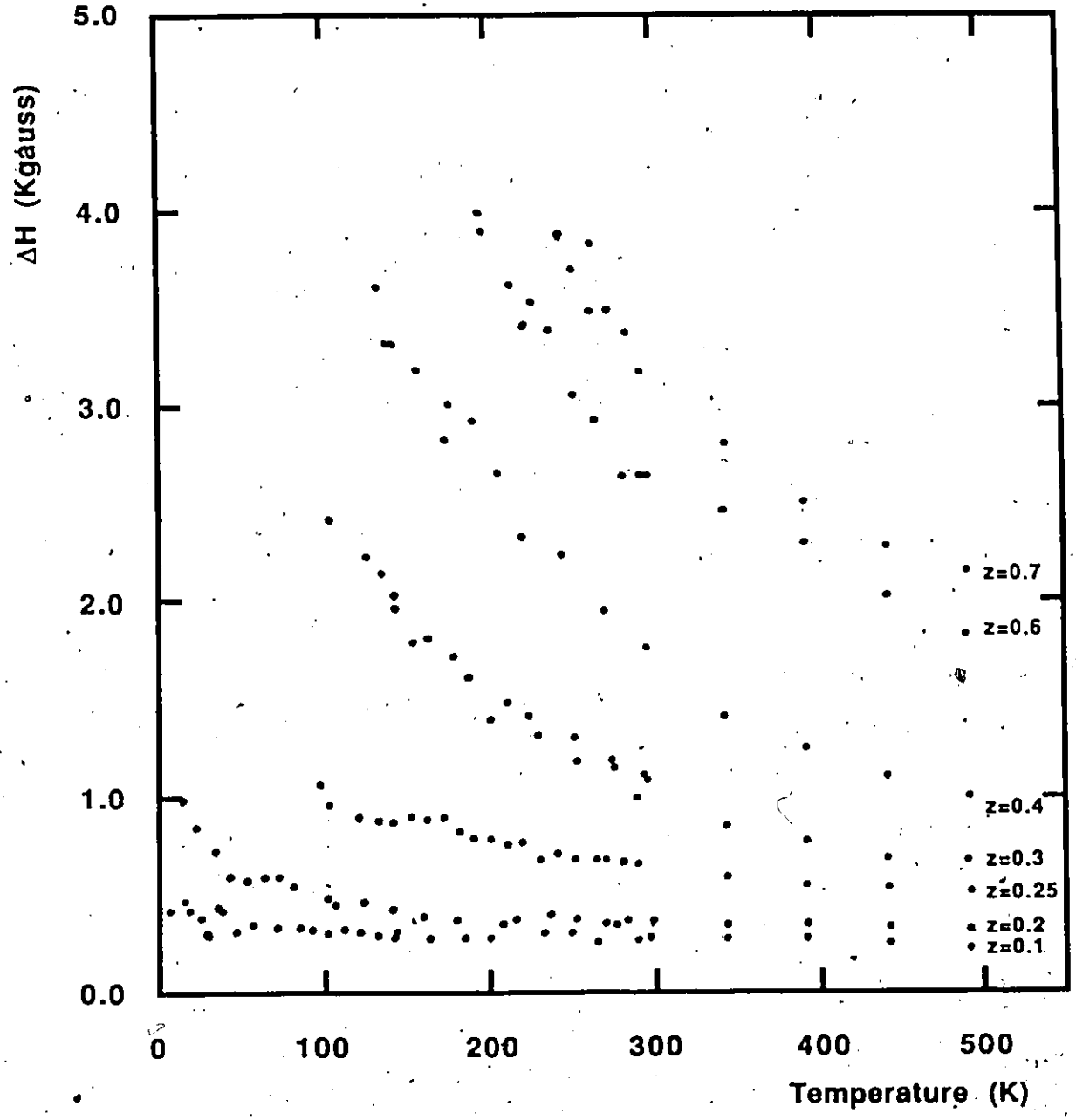

FIGURE. 5.6 Linewidth versus Temperature for x=0 samples.

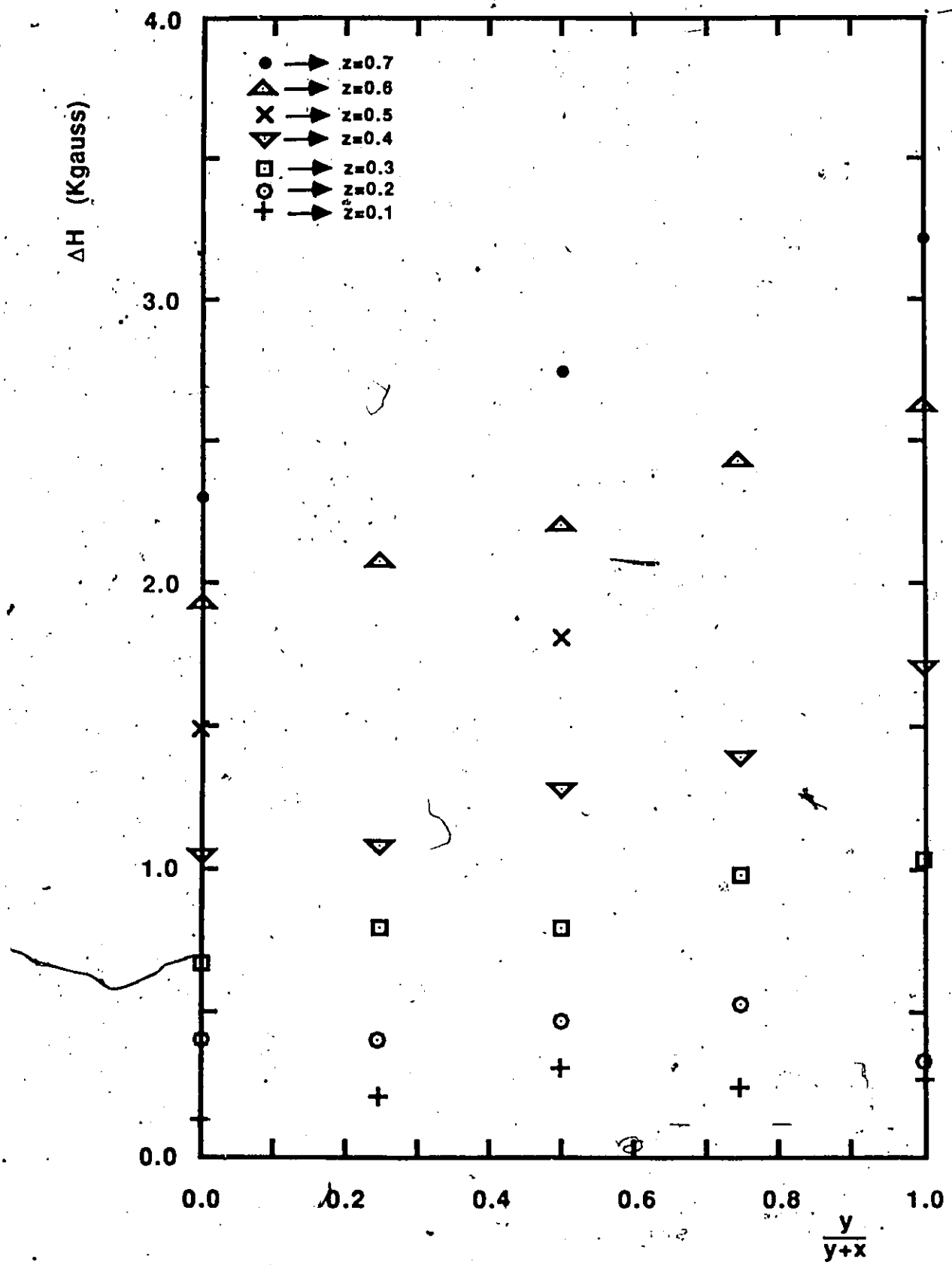

FIGURE 5.7 ESR Linewidth at T=300 K.

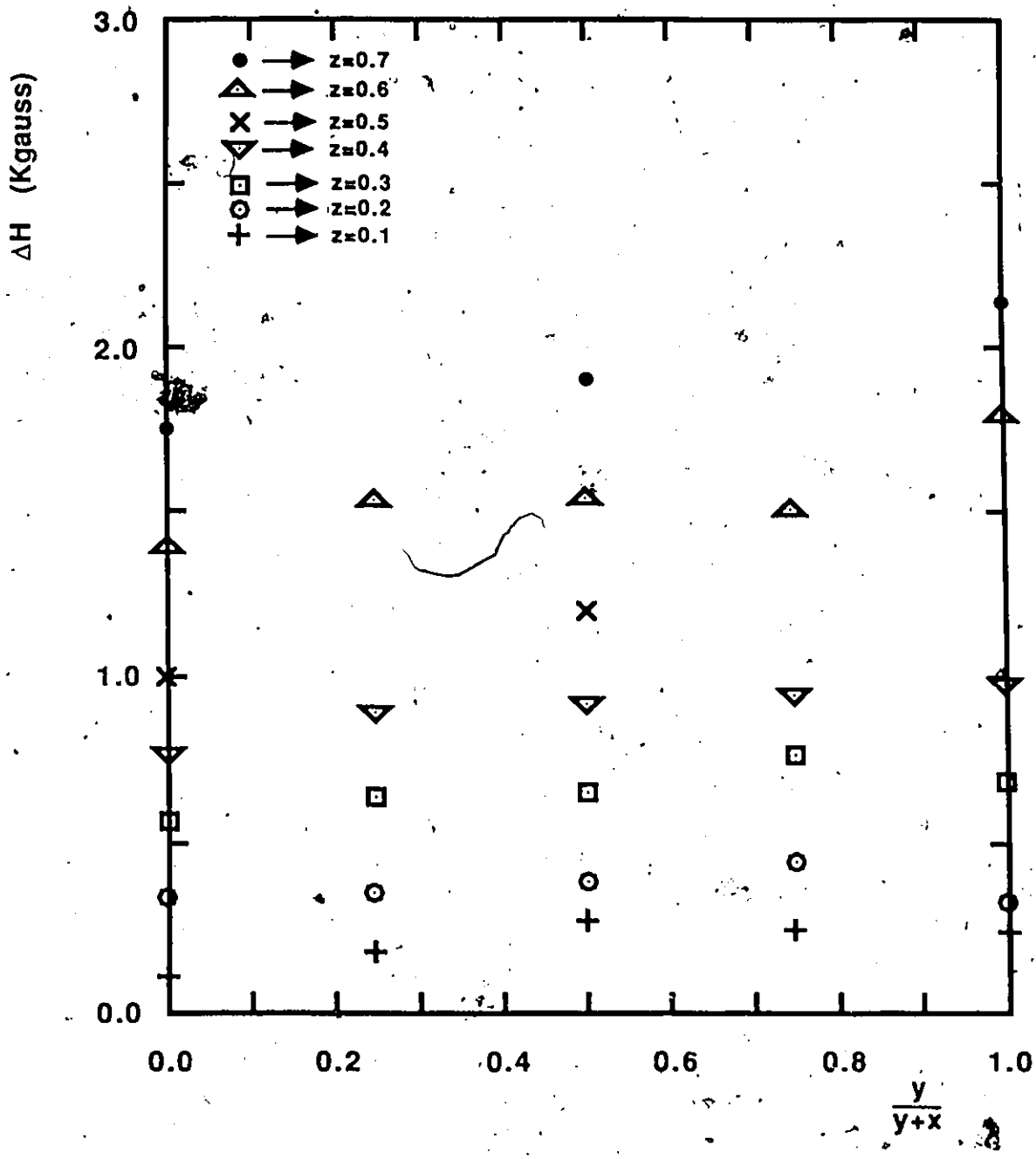

FIGURE 5.8 ESR Linewidth at T=500 K.

essentially the same while the high field peak becomes greatly broadened and flattened out. An example of this is illustrated in fig. 5.9 where it can be seen that in some cases, the line eventually splits into two parts, which continue to separate as the temperature is decreased further. At this point the intensities of the lines decreased quickly and almost fell to zero. This phenomenon of asymmetric broadening was not observed very well for samples with $z<0.2$ since it would have occurred close to the 10 K lower temperature limit of the apparatus.

It should be mentioned that this feature was not unique to this material, since the other alloy systems being investigated in the research group, $Cd_{1-z}Mn_zTe_{1-y}Se_y$, (91) and $Cd_xZn_yMn_zSe$, (92) also showed the same effects. The splitting of the line at low temperatures is similar to the behaviour reported by Searl et al, (93, 94, 95), on polycrystalline materials with uniaxial g-value anisotropy. The two structures can be interpreted as representing $g_{\parallel}$ and $g_{\perp}$. Since all materials in this system, as well as the others mentioned above, are polycrystalline samples, such an effect remains a possibility. Other researchers working on single crystals, (25, 28, 54, 98, 125), have not reported this behaviour indicating that it may be present only in polycrystalline samples. However, Sayad and Bhagat, (125), have observed asymmetrical ESR lines, but only at lower temperatures than those reported here.

For each sample, the highest temperature at which the anisotropy can be detected, T_A, was determined and then plotted in figs. 5.10 and 5.11. The uncertainty in these values ranged

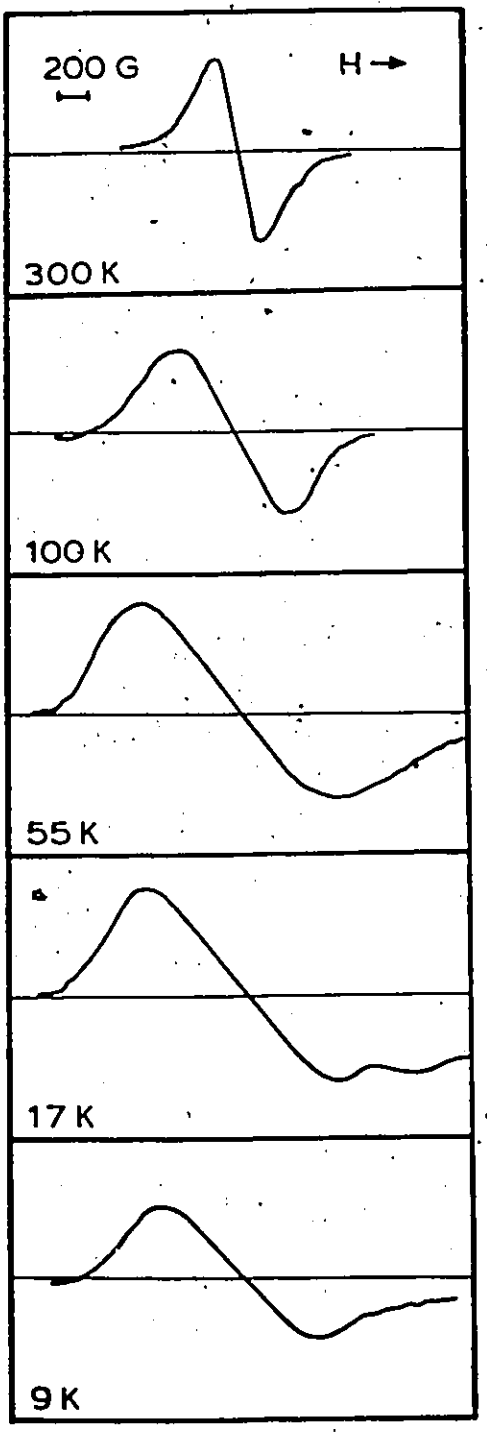

FIGURE 5.9 An example of asymmetric broadening of the ESR Linewidth. At the lowest temperatures, the resonance line splits into two.

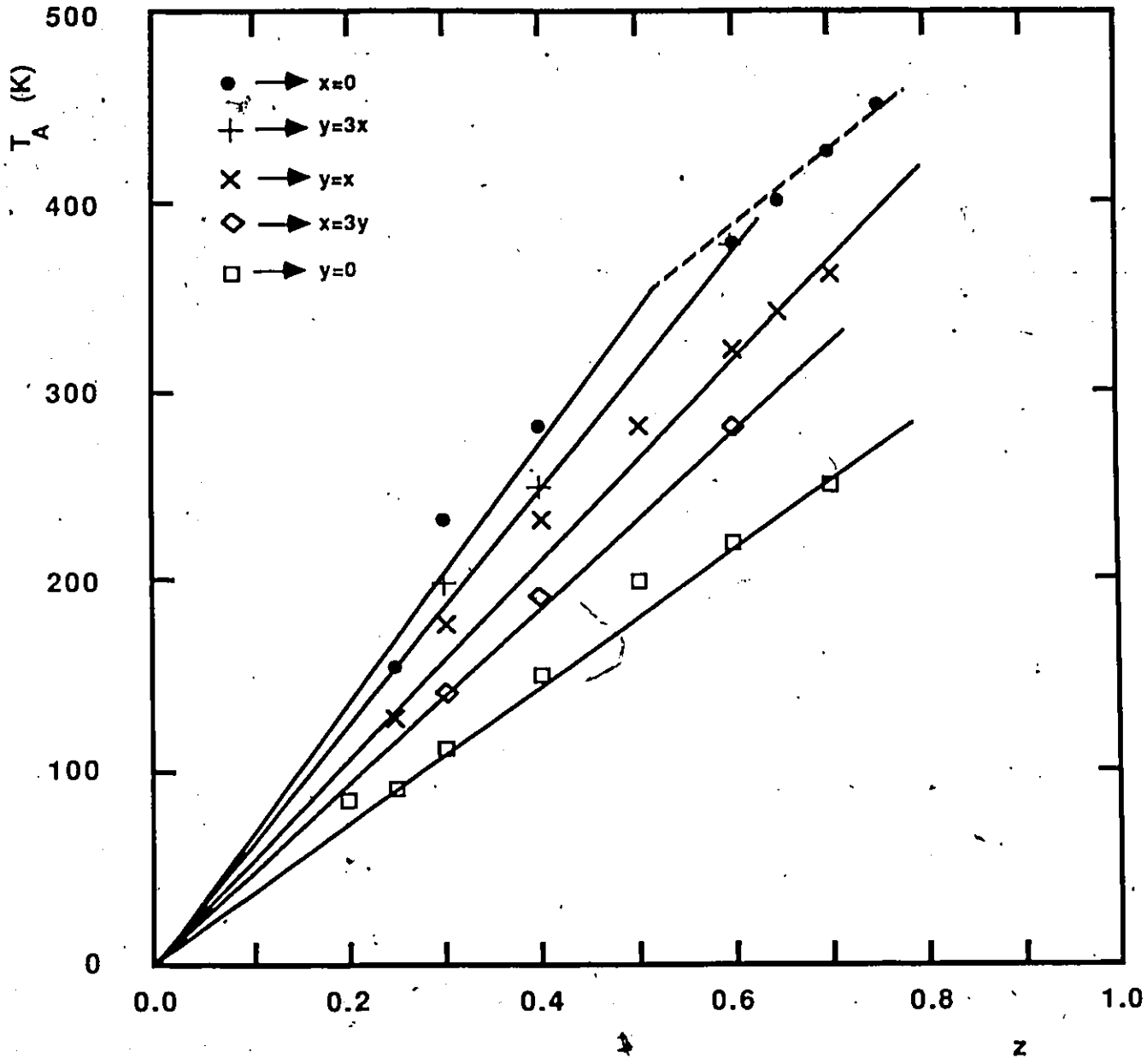

FIGURE 5.10 Temperature at which the ESR linewidth becomes asymmetric as a function of z concentration. The uncertainties in these values range between 10 and 30 degrees. The lines in this diagram serve merely to guide the eye.

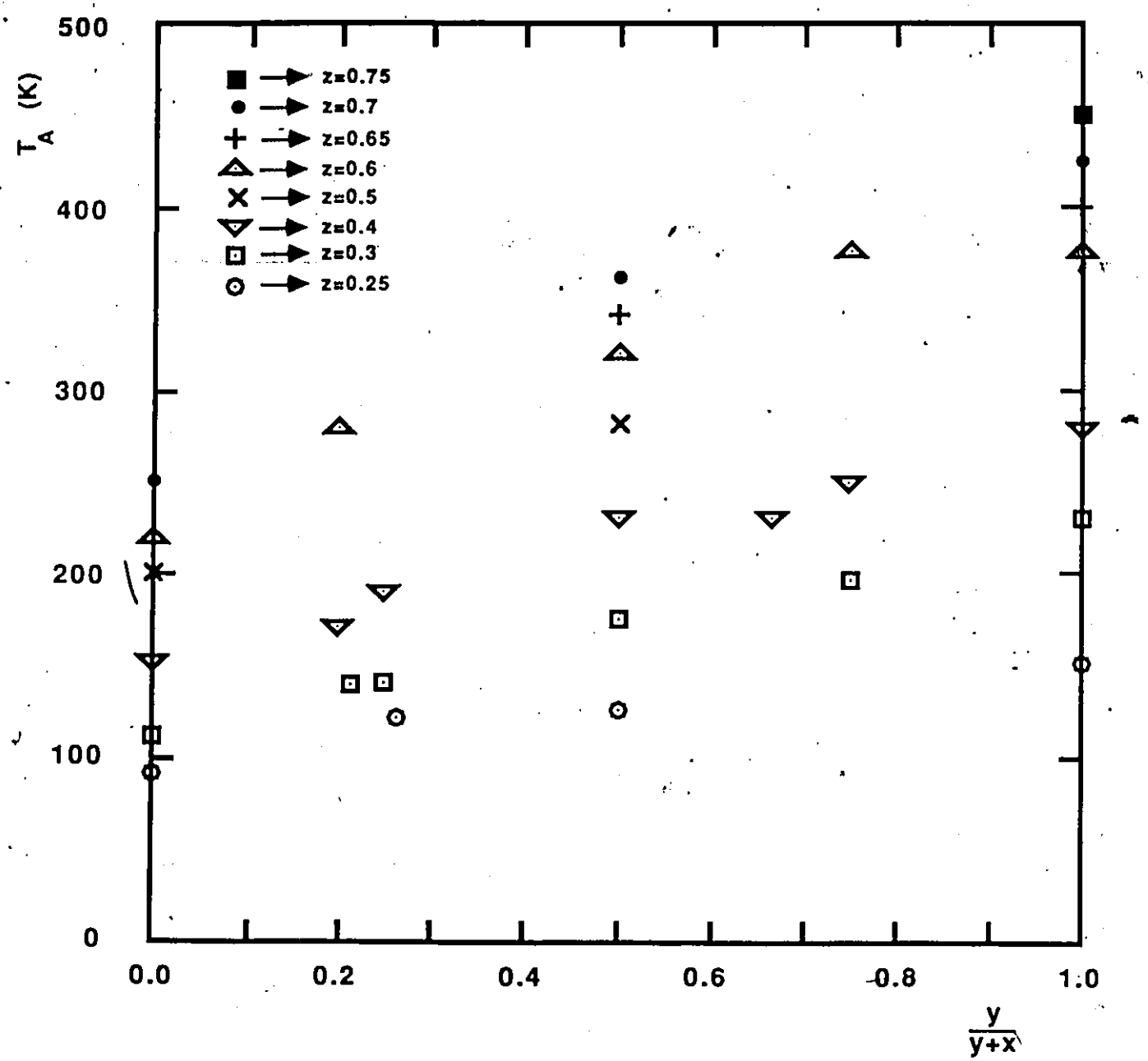

FIGURE 5.11 Temperature at which the ESR linewidth becomes asymmetric as a function of y/(y+x). The uncertainties in these values range between 10 and 30 degrees.

between 10 and 50 K. As might be expected, T_A increases with Mn as well as with Zn concentration. One would be tempted to ascribe the results of fig. 5.11 to the decreasing lattice parameter, as has been suggested for figs. 5.7 and 5.8. However, as was discussed earlier, a large change might suggest that another effect may be present as well. The magnitude of the increase in T_A is illustrated by the fact that all the values could be plotted in fig. 5.10 without too great an overlap. This is in contrast to the T_g and θ results in figs. 4.9 and 4.24, where there was room for only a few of the results.

The g values were found to retain a constant value of approximately 2.0 for all temperatures and compositions where the linewidth remained symmetric. A large asymmetry would tend to shift the measured g value to a smaller quantity. This may not be a true shift in g but only an effect of the broadening of the high field peak of the derivative ESR line. An example of this so called shift is illustrated in fig. 5.12 where it can see that the g value decreases when the temperature falls below T_A. Another example of the effect of asymmetry is seen in fig. 5.13 where the g values at room temperature for $Zn_{1-z}Mn_zTe$ samples were plotted as a function of z. For $z<0.5$, the g values are close to 2.0, while for $z>0.5$, they are smaller and seem to decrease with further increase of z. According to fig. 5.10, T_A for these higher Mn content samples occurs at a temperature higher than room. It should be mentioned that Oseroff et al, (25), as well as Kremer and Furdyna, (105), have observed a sharp increase in g for some $Cd_{1-z}Mn_zTe$ crystals, at low temperatures. This is definitely not

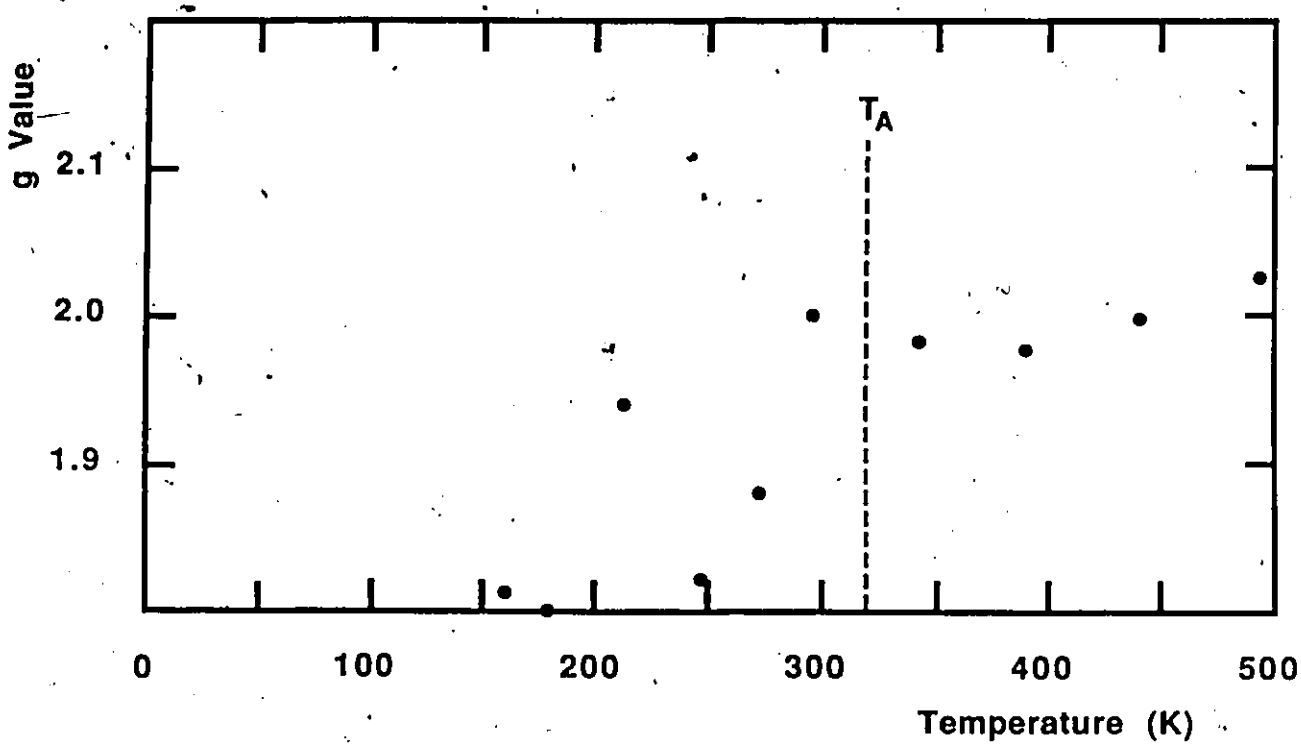

FIGURE 5.12 Plot of the g Value versus Temperature for a sample of $Cd_{0.2}Zn_{0.2}Mn_{0.6}Te$.

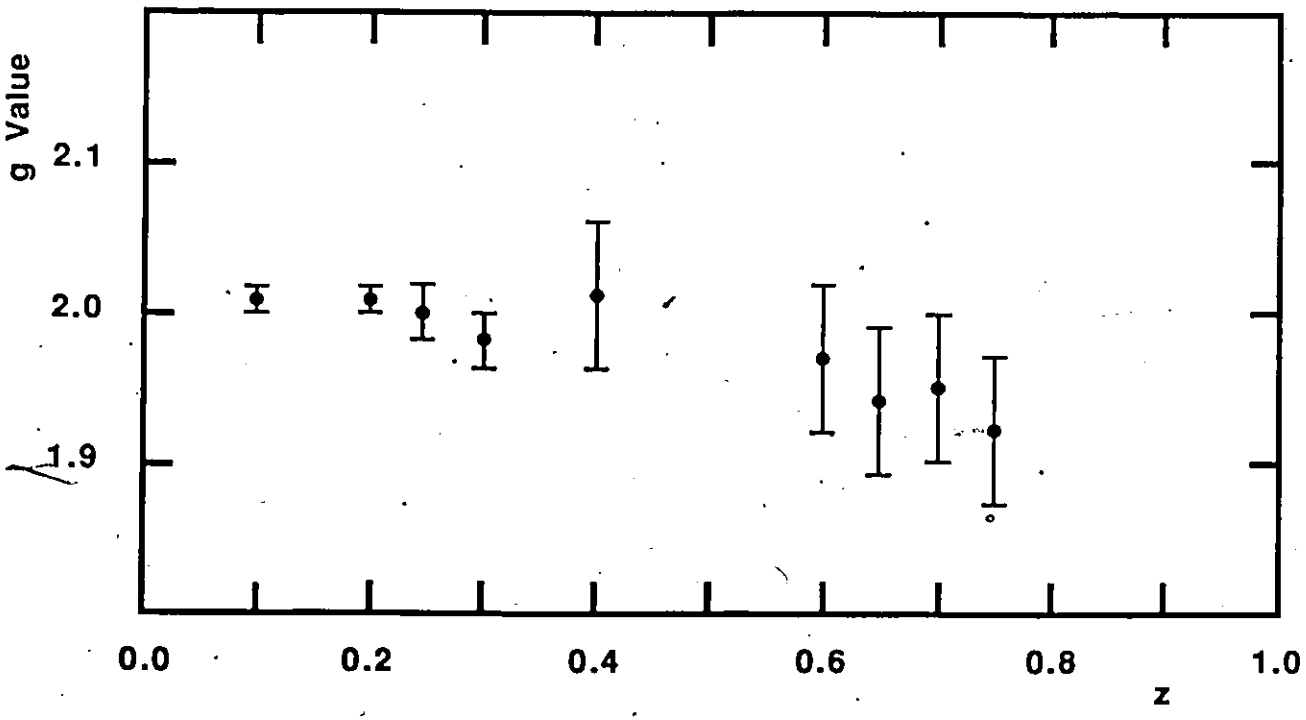

FIGURE 5.13 Plot of g Value versus z Concentration for x=0 samples.

the same phenomenon observed here since the shift is in the opposite direction. The asymmetric behaviour at low temperatures prevented us from verifying this behaviour.

One last observation should be mentioned about this asymmetrical broadening. In fig. 5.14, the linewidth at T_A is plotted as a function of y/(y+x). Despite the scatter, it can be seen that there is very little change as the Zn concentration is increased indicating that the asymmetry always sets in when the linewidth reaches a certain broadness. This characteristic broadness increases with Mn composition and is plotted in fig. 5.15, which shows that it varies more or less smoothly and extrapolates to the origin.

5.4 Analysis of ESR Linewidth

In metallic spin glasses, the ESR linewidth is affected by the presence of conduction electrons, (126). It has been suggested by Aliev and Tagirov, (127), that similar behaviour might be expected from SMSC alloys such as $Hg_{1-z}Mn_zSe$ and $Hg_{1-z}Mn_zTe$ since they have a large carrier concentration. However as pointed out previously, the $Cd_xZn_yMn_zTe$ alloy system has a very small carrier concentration so that this effect should not be significant.

Having established, in chapter 4, that the exchange interaction is essentially antiferromagnetic in character, it becomes useful to consider the variation in linewidth of a typical antiferromagnetic insulator such as MnF_2, (17). This is

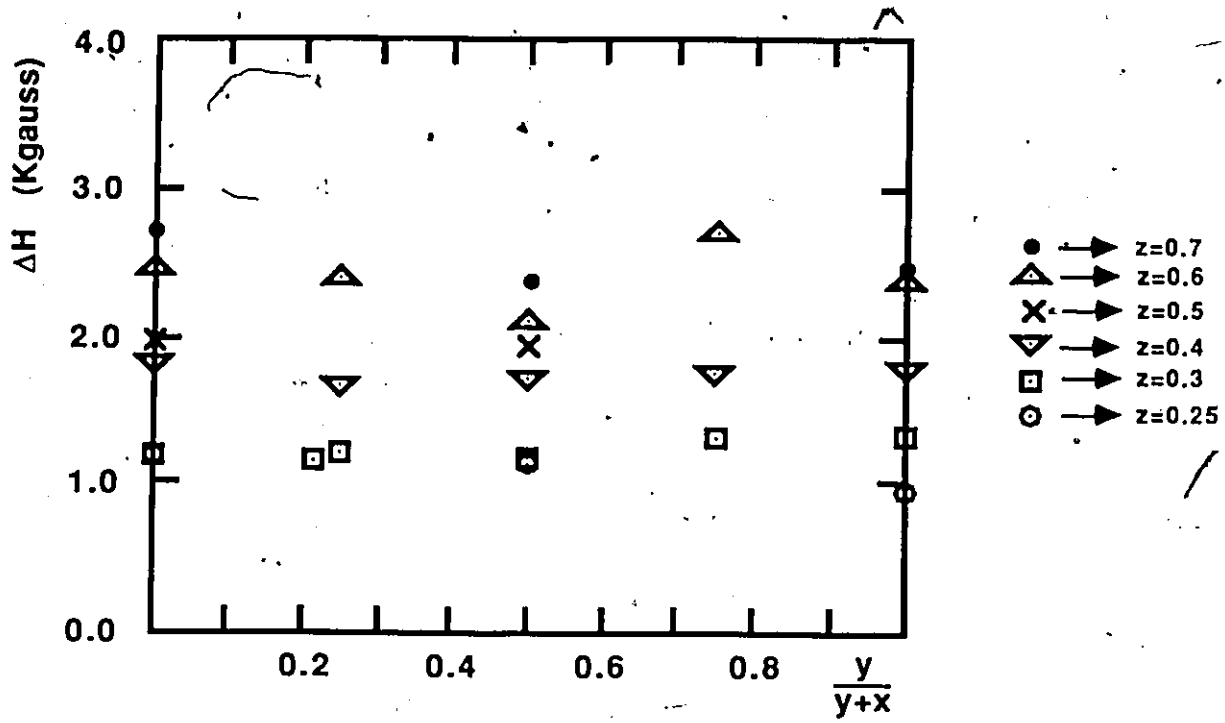

FIGURE 5.14 Linewidth at T_A versus y/(y+x) for several different z compositions.

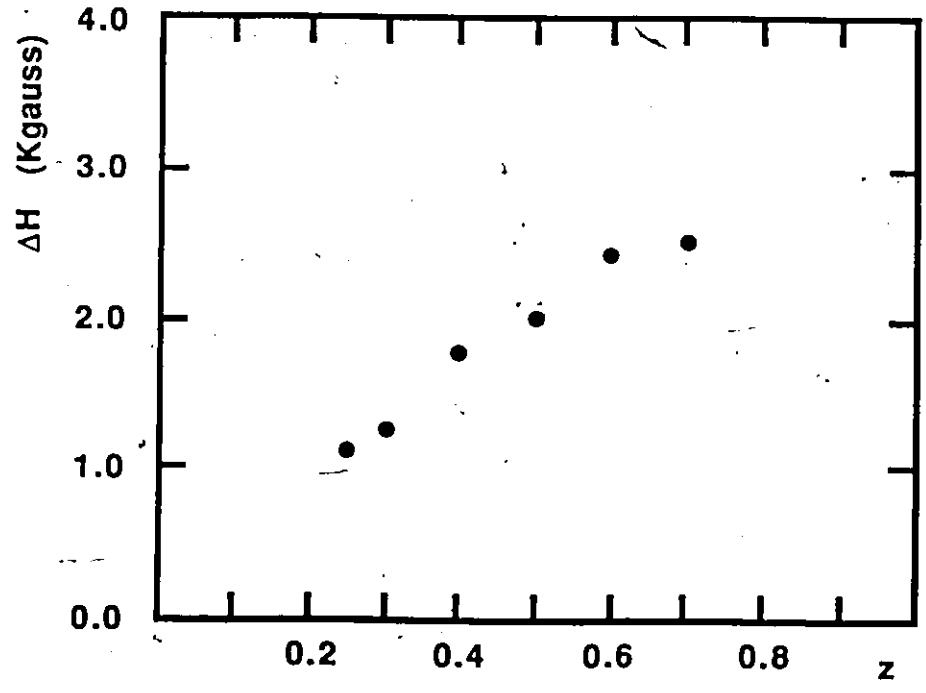

FIGURE 5.15 Linewidth at T_A versus z Composition. The values for each z composition were obtained by calculating the average of the points in Fig. 5.13.

illustrated in fig. 6.1 where it can be seen that as the temperature is lowered, ΔH increases slowly at first and then quite rapidly near the Neel temperature. Below this point, the effects of the crystal anisotropy field and the Weiss exchange field causes the resonance condition to change resulting in a shift in the position of the resonance line, (44). In many cases, the shift is so large that the resonance point falls outside the range of measurements.

The present set of measurements, illustrated in figs. 5.2 to 5.6, as well as for those of other researchers working on different SMSC alloy systems, (54, 91, 92), are restricted to temperatures above the critical point. In these cases, it was found that the temperature variation of the linewidth resembled that of the antiferromagnetic material discussed above with the point where ΔH begins to increase more rapidly occurring at progressively higher temperatures when the Mn concentration was increased.

This behaviour for $Cd_{1-z}Mn_zTe$ and for $Cd_{1-z}Mn_zSe$ has been analyzed as a critical phenomenon near the spin glass temperature by Oseroff et al, (25, 28, 54, 96), using the following expression;

$$\Delta H = A \left\{ \frac{T_g}{T-T_g} \right\}^{\alpha} + B \left\{ 1 + \frac{\theta}{T} \right\} \qquad (5.2)$$

where A and B are constants independent of temperature, T_g and θ are the quantities discussed in chapter 4, and α is the critical exponent. This equation is based on a theory developed by

Huber, (27), for antiferromagnetic materials. The first term on the right hand side accounts for the dynamical contribution to the linewidth and is valid for T very close to the critical temperature. The second term is a modification introduced by Dormann and Jaccarino, (97), to account for a gradual increase in linewidth observed for antiferromagnetics at temperatures much greater than the critical point. It is referred to as the paramagnetic contribution.

The main problem with eq. 5.2 is that in all cases, the onset of the large increase in ΔH, occurred at temperatures far above the critical point, T_g. In fact, the linewidth disappears well before this temperature is reached. Some samples with a high Mn concentration showed the pronounced increase at all temperatures. Presumably, this is only due to the limitations of the measuring equipment and so the more gradual increase would appear at temperatures higher than 500 K. Nevertheless, these results indicate that linewidth begins to increase rapidly at $T > 10T_g$ which is very unusual for a critical type phenomenon. This would suggest that a broader effect is responsible for the increase in linewidth, one which is significant over a large range of temperature. Further confirmation of this is provided by a simple manipulation of eq. 5.2. Multiplying both sides of the equation by T yields;

$$T\Delta H = F(T) + B(\theta+T) \qquad (5.3)$$

where F(T) is some unspecified function. It can be seen that the second term in this equation is linear in T and so plots of $T\Delta H$ vs

T should yield straight lines for the high temperature range, where the paramagnetic term is valid. The intercepts on the temperature axis would correspond to the Curie-Weiss temperatures determined in chapter 4. Examples of this are shown in figs. 5.16-5.18. There is much more scatter in these plots than in the $1/\chi$ plots, (figs. 4.14 to 4.18). However, many of the samples do show this linear behaviour at high temperatures. The extrapolation of the high temperature linear behaviour to the temperature axis produces a value which agrees very well with the Curie-Weiss θ in figs. 4.19(a) to 4.21(a). The range of temperature where the points vary in this linear manner is reduced as both the Mn and the Zn concentration is increased. Samples with high z and samples for which x=0 did not show this linear behaviour and were not included in the plots. In the cases which are presented, deviations from linearity would be due to the emerging significance of F(T) in eq. 5.3. Examining the results for the cases with the lowest Mn concentration suggests that most of the linewidth variation is due to the paramagnetic term. At higher values of z and y, the F(T) term becomes more important at decreasingly lower temperatures. So, it can be seen in figs. 5.16-5.18 that the paramagnetic term is significant and that in many samples, F(T) is important over a large range of temperatures. This verifies the earlier statement of the broadening not being a critical type phenomenon.

A different approach to analyzing the temperature behaviour of the linewidth has been proposed by Bhagat et al, (99), and applied to the $Cd_{1-z}Mn_zTe$ system by Webb et al, (98), and by Sayad

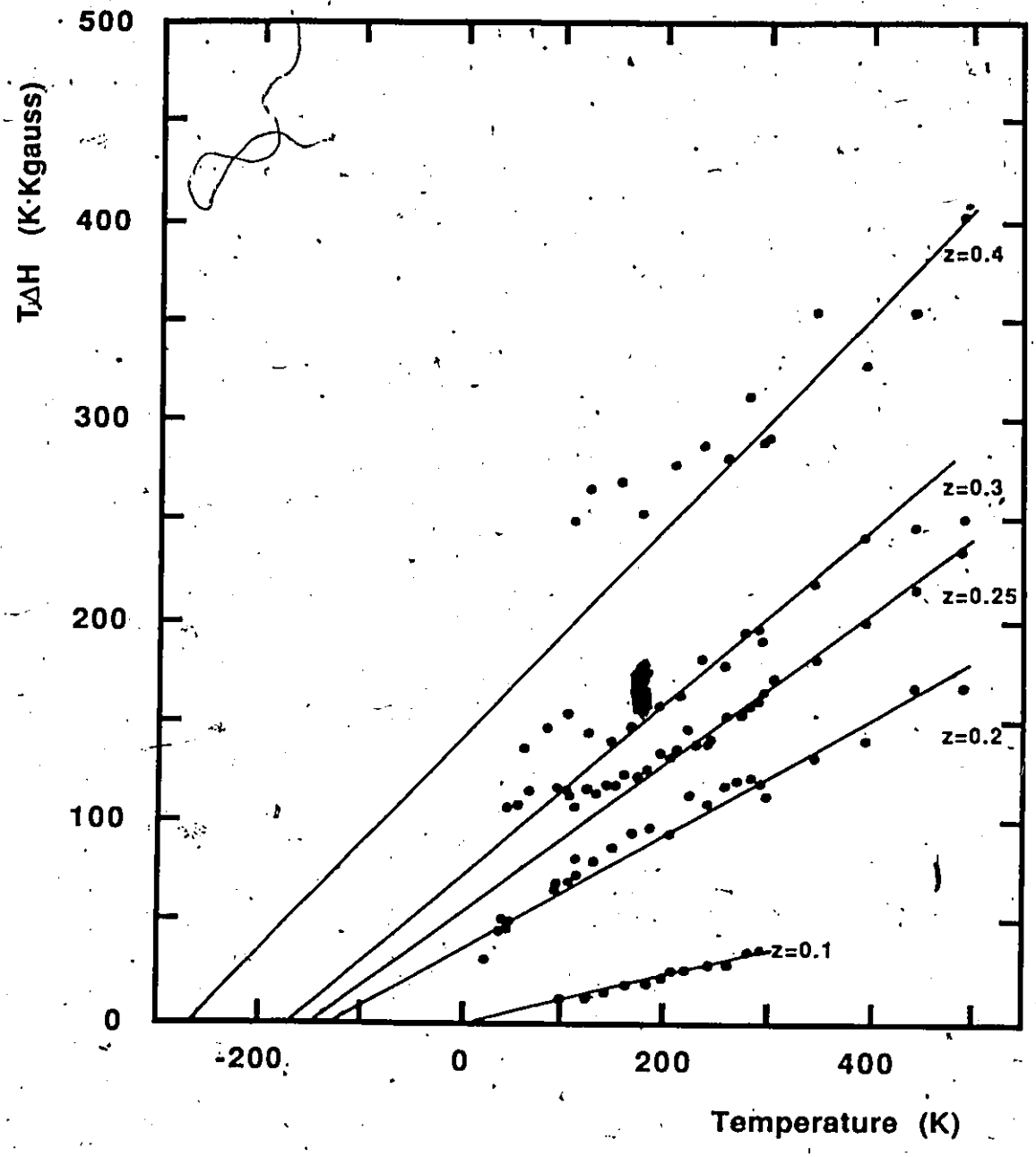

FIGURE 5.16 Plots of TΔH versus T for some y=0 samples. For each example shown, the solid lines extrapolate to the Curie-Weiss temperature as determined in chapter 4.

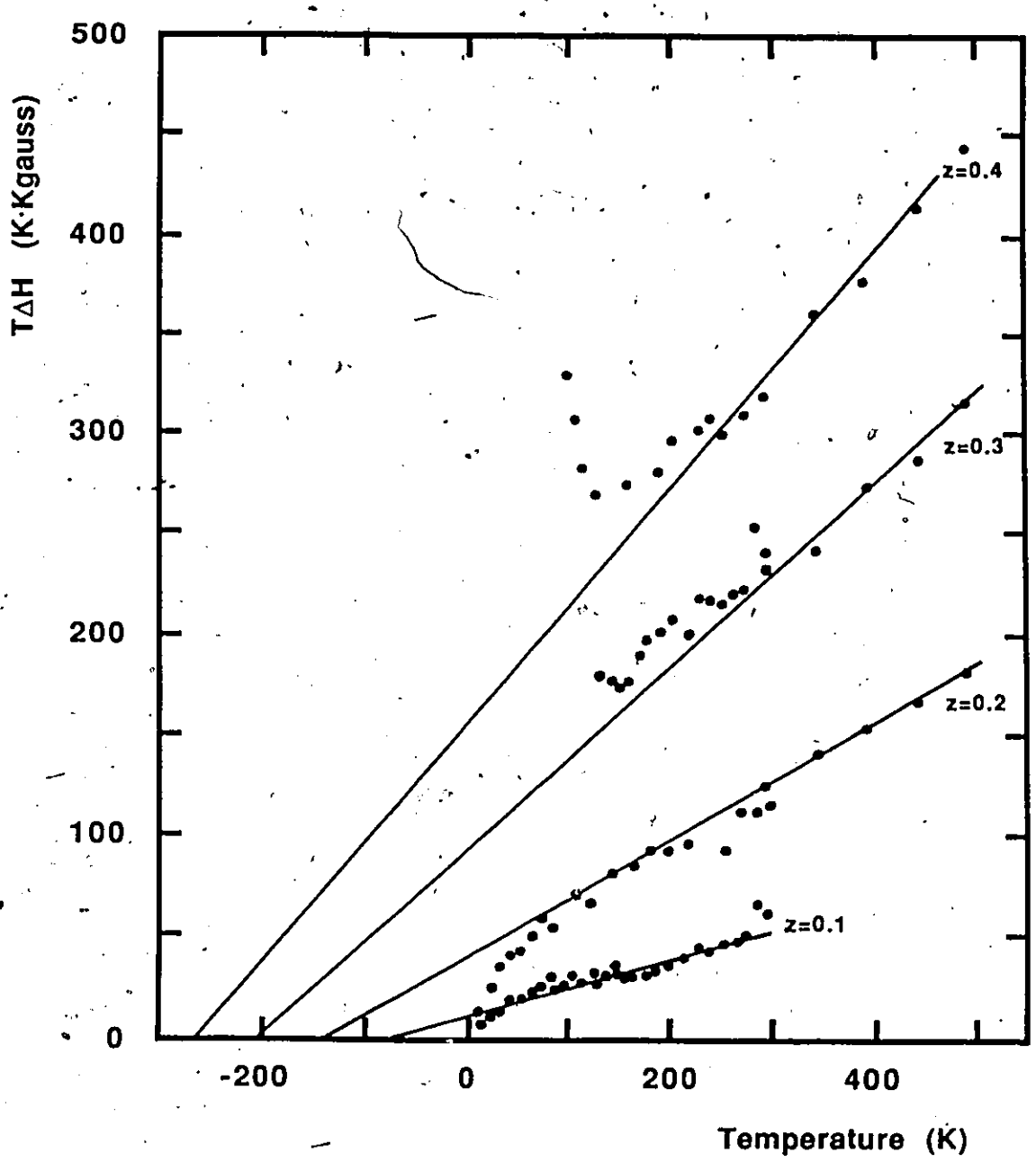

FIGURE 5.17 Plots of TΔH versus T for some x=3y samples. For each example shown, the solid lines extrapolate to the Curie-Weiss temperature as determined in chapter 4.

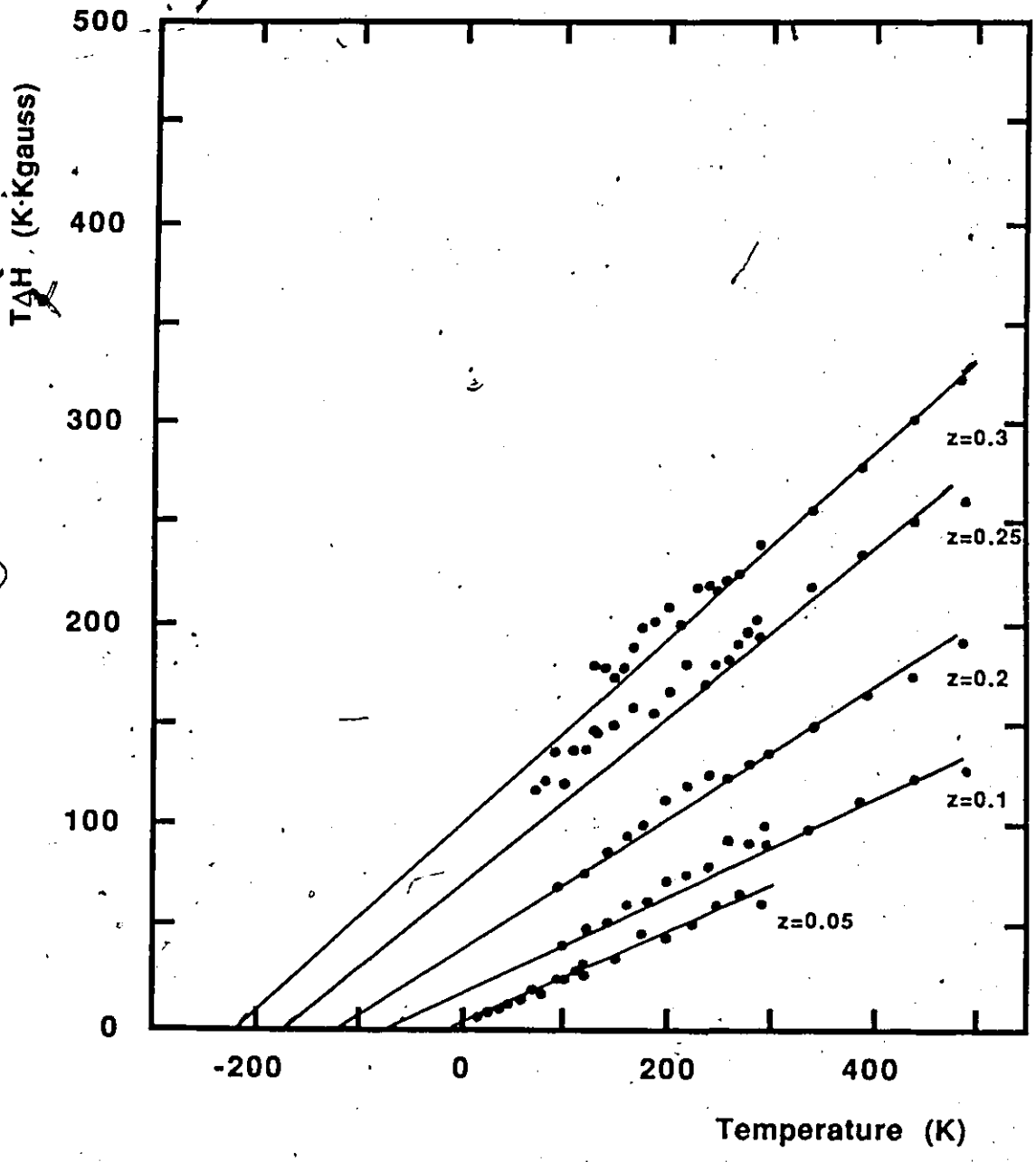

FIGURE 5.18 Plots of TΔH versus T for some y=x samples. For each example shown, the solid lines extrapolate to the Curie-Weiss temperature as determined in chapter 4.

et al, (125). The broadening mechanism considered in their work is attributed to an inhomogeneous distribution of local fields. Calculations of the distribution of local fields in an FCC lattice have been made by Ching and Huber, (100). They show that for a fully occupied lattice, each spin experiences the same local field. However, diluting the lattice, even by a small amount, produces a shift and a broadening of this distribution. The authors, of reference 100, also note that there is no abrupt change in the behaviour of the local fields for the concentrations corresponding to the nearest neighbour percolation limit or to the antiferromagnetic to spin glass transition. This may be compared to the results of the ESR linewidth measurements, (figs 5.2 to 5.10) where a similar situation seems to hold. The consequences of a local field distribution are that the spins do not all experience the same H and so possess different resonance points. The situation is then as shown in fig. 5.19 where there is a distribution of resonance lines about a central point, (101). These individual resonances are smeared into one broad envelope.

At the highest temperatures, all the spins are fluctuating fast enough for this effect to be averaged out. As the freezing temperature is approached, the spins slow down and can become correlated for short periods of time, allowing the local moments to become significant. As the correlation increases, the broadening increases. Through numerical calculations, Bhagat et al, (99), have concluded that the linewidth variation may be empirically described by the following equation;

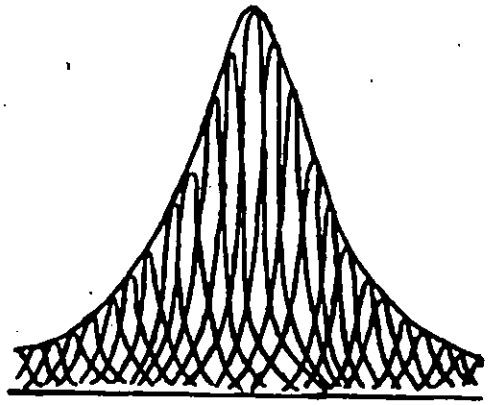

FIGURE 5.19 Inhomogeneous Broadening.

$$\Delta H = \Gamma_1 \exp\left\{-\frac{T}{T_o}\right\} + \Gamma_o \qquad (5.4)$$

The high temperature linewidth is represented by Γ_o. The quantity T_o is a measure of the potential barrier separating two neighbouring ground states of the disordered spin system. Γ_1 essentially measures the width of the distribution of the local fields seen by the Mn ions, which is a measure of the degree of random behaviour in the alloy.

In reference 98, the authors show that plots of the log of the "extra" linewidth, $\Delta H - \Gamma_o$, against temperature are linear over a wide range of temperatures. Values for Γ_o were obtained from the linewidth at the highest available temperature, 300 K. Included in their analysis was data taken from an early paper on $Cd_xZn_yMn_zTe$ published by this research group, (102). Since this publication, the measurements have been extended beyond room temperature, up to 500 K. With this greater range, the analysis done in reference 98 on the results of a sample of $Cd_{0.7}Mn_{0.3}Te$ can be repeated. In fig. 5.20, the same type of plot is presented with Γ_o obtained from the linewidth at room temperature, at 500 K and at some temperatures intermediate to these. This was done to show that any of these values for Γ_o are equally viable. These different lines will of course give very different values for T_o and Γ_1 casting doubt over this procedure for using eq. 5.5 since the results seem to depend on how high a temperature is reached.

It should also be noted that the results of figs. 5.16 to

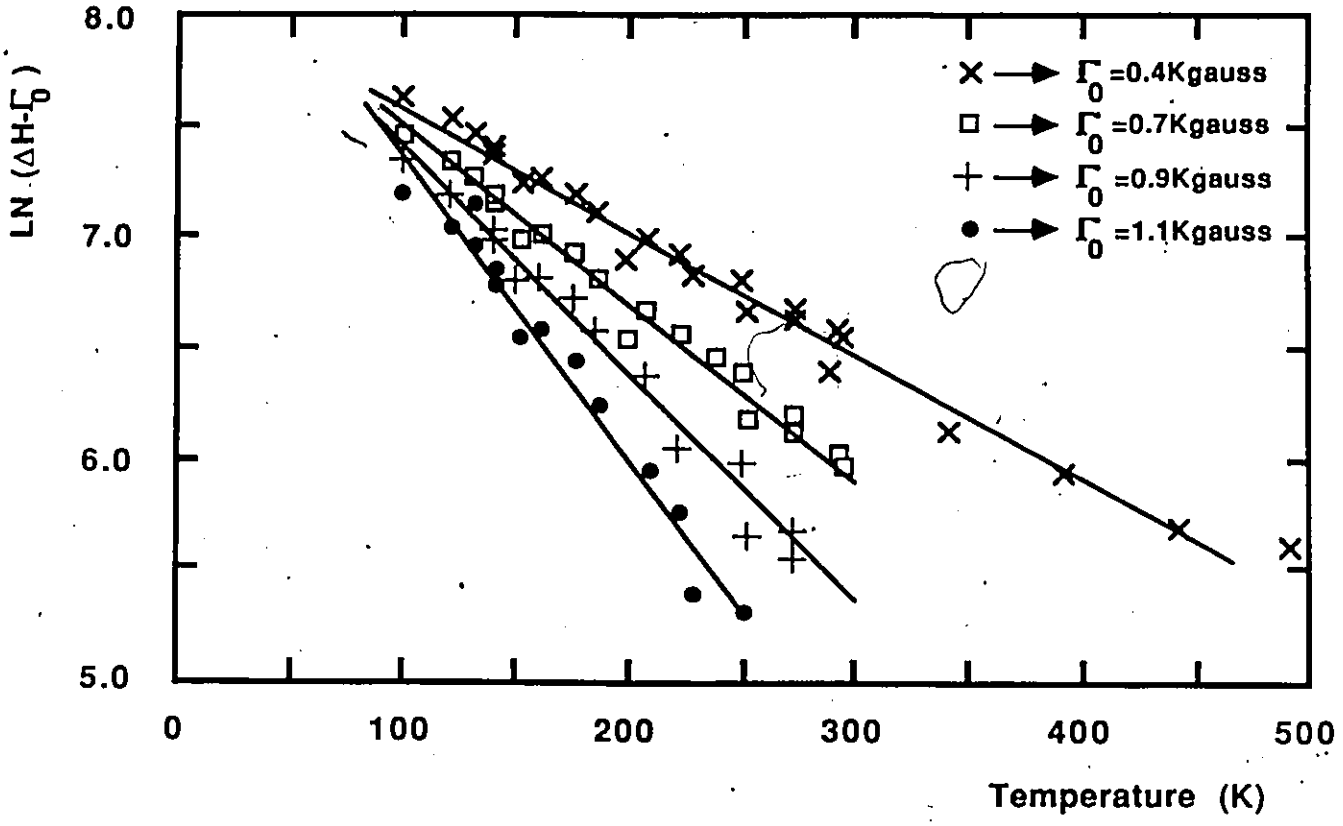

FIGURE 5.20 Plots of the Log of the "Extra" Linewidth as a Function of Temperature for different values of Γ_0 . For this sample of $Zn_{0.7}Mn_{0.3}Te$, the resulting values for T_0 and Γ_1 ranged from 3.4 to 5.9 Kgauss and from 182 to 74 K respectively.

5.18 indicate that the high temperature linewidth variation may be described by the paramagnetic term in eq. 5.2. This would mean that eq. 5.4 would have to be modified as follows;

$$\Delta H = \Gamma \exp\left\{-\frac{T}{T_o}\right\} + B\left\{1 - \frac{\theta}{T}\right\} \qquad (5.5)$$

where the paramagnetic term has been substituted for Γ_o. The data was analyzed with this equation by a numerical search in parameter space for the optimum values of the constants, Γ, T_o, and B, which would minimize the χ^2_υ function, (103). Basically, the parameters were adjusted so that the total deviation between the measured values and the values predicted by eq. 5.5, is as small as possible. However, because of its form, the paramagnetic term was found to overestimate its contribution so that the rapid increase in linewidth appeared to be dominated by this term rather than the exponential. As the temperature is lowered the number of free spins decreases because of the freezing process. Since the paramagnetic contribution is due to these free spins, eq. 5.5 should be modified so that it reflects this loss of spins. The final equation is then;

$$\Delta H = \Gamma \exp\left\{-\frac{T}{T_o}\right\} + B\left\{1 - \frac{\theta}{T}\right\}\left\{1 - \exp\left\{-\frac{T}{T_o}\right\}\right\} \qquad (5.6)$$

Using θ values measured by susceptibility in chapter 4, the parameters were determined for all the measured samples and plotted as a function of z in figs. 5.21 to 5.25. The range of the fit for each sample was chosen to avoid including the greatly asymmetrically broadened lines discussed in the previous section.

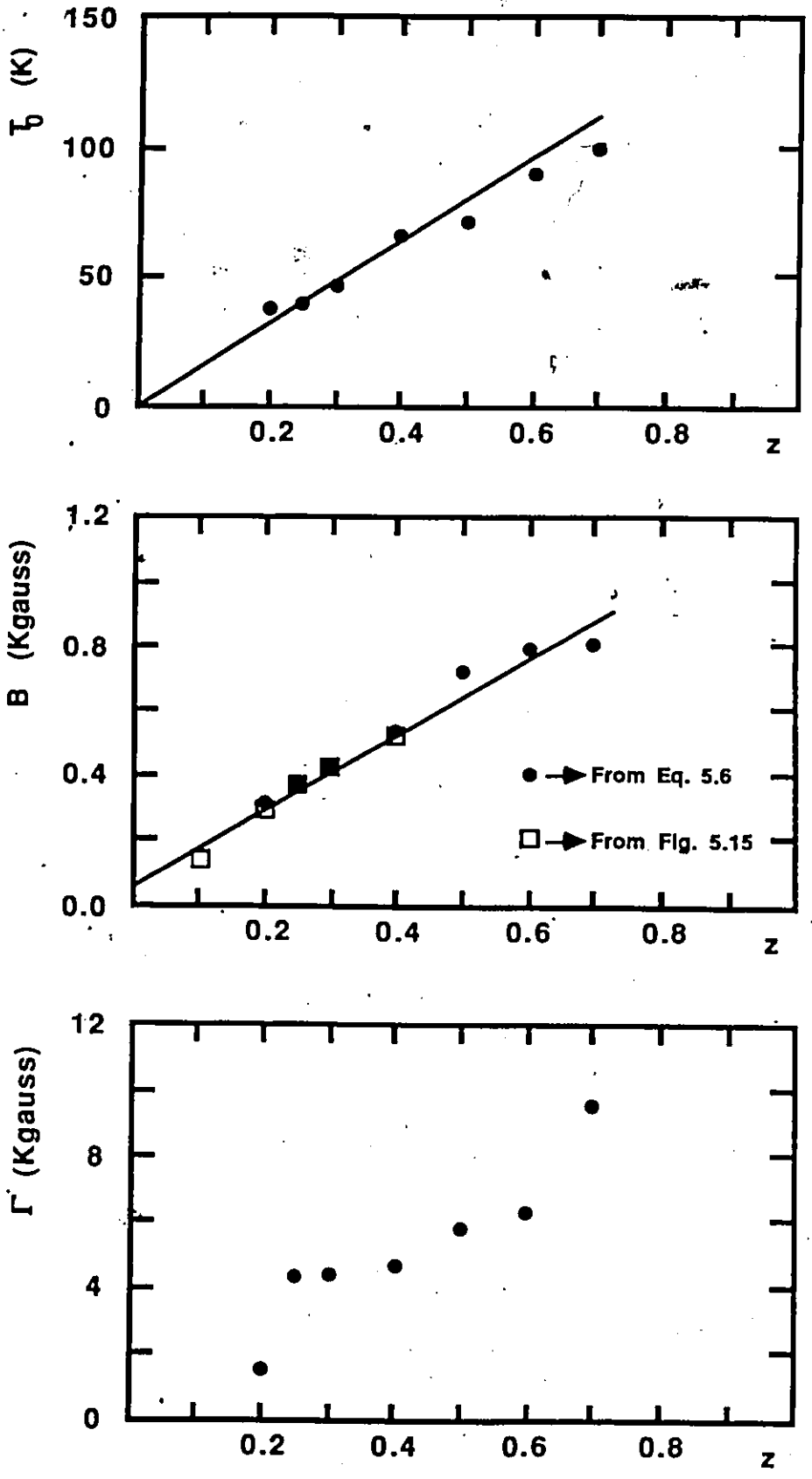

FIGURE 5.21 Values of T_0 , B and Γ versus z Concentration for y=0 Samples.

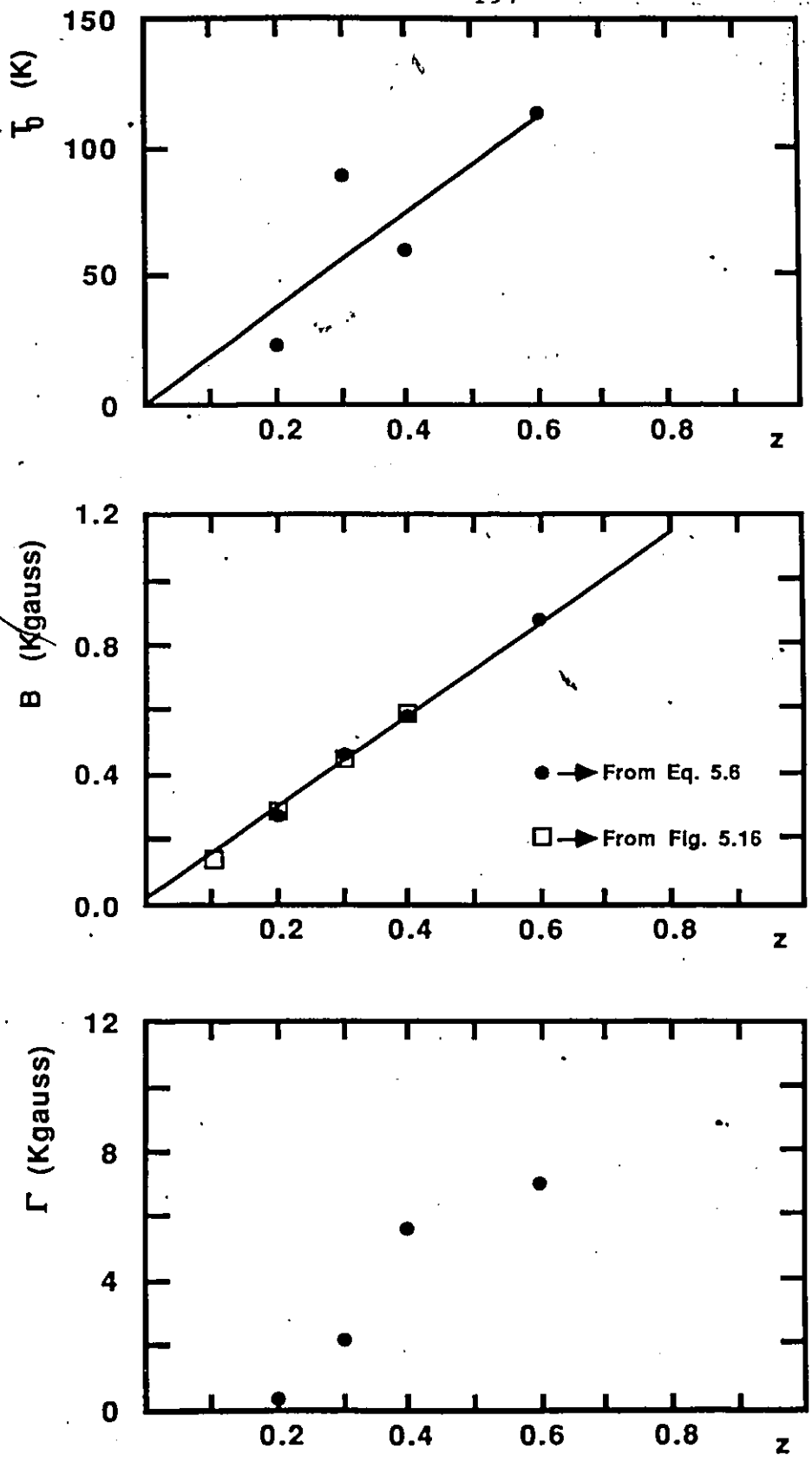

FIGURE 5.22 Values of T_0 , B and Γ versus z Concentration for x=3y Samples.

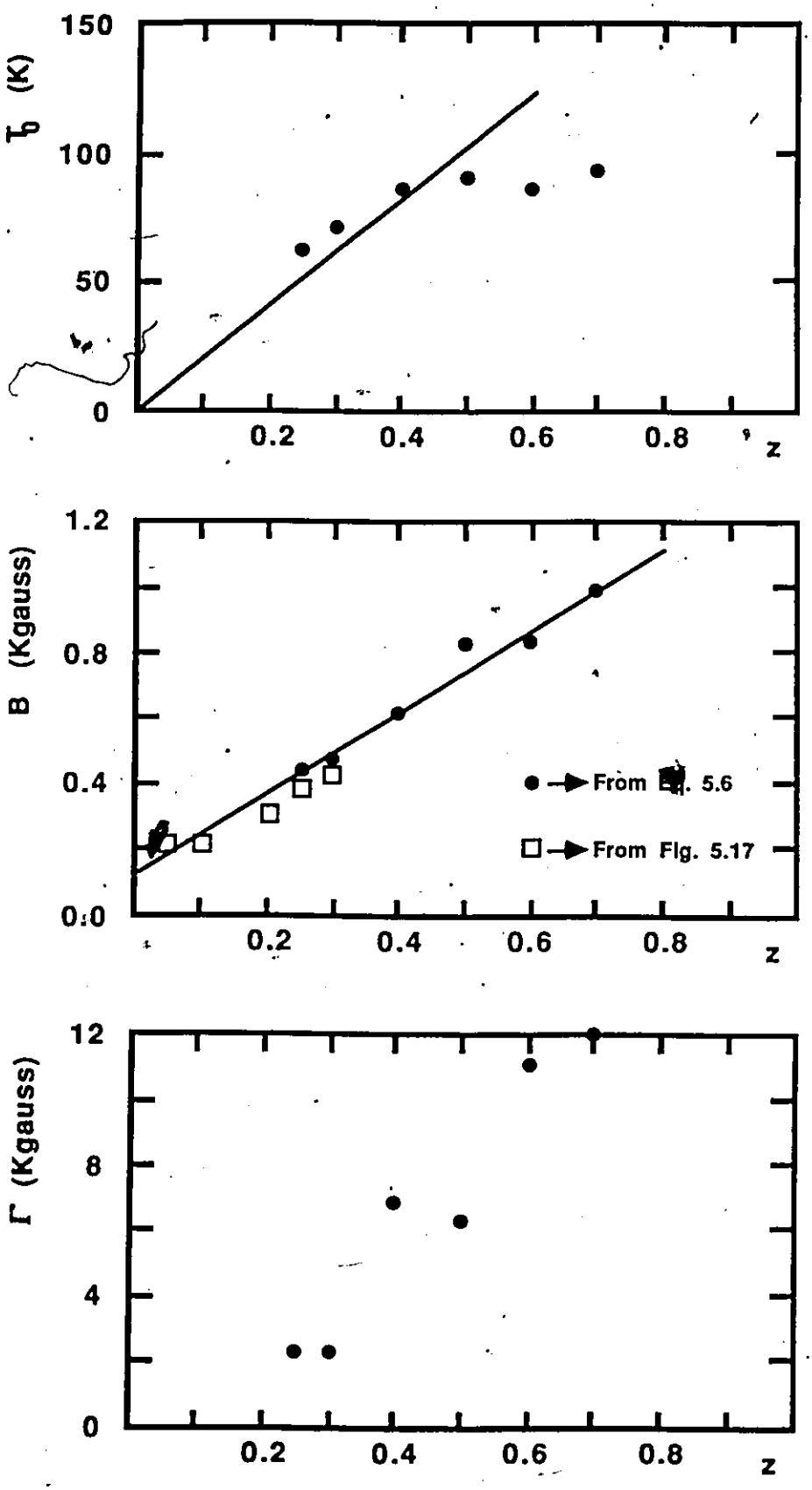

FIGURE 5.23 Values of T_0 , B and Γ versus z Concentration for y=x Samples.

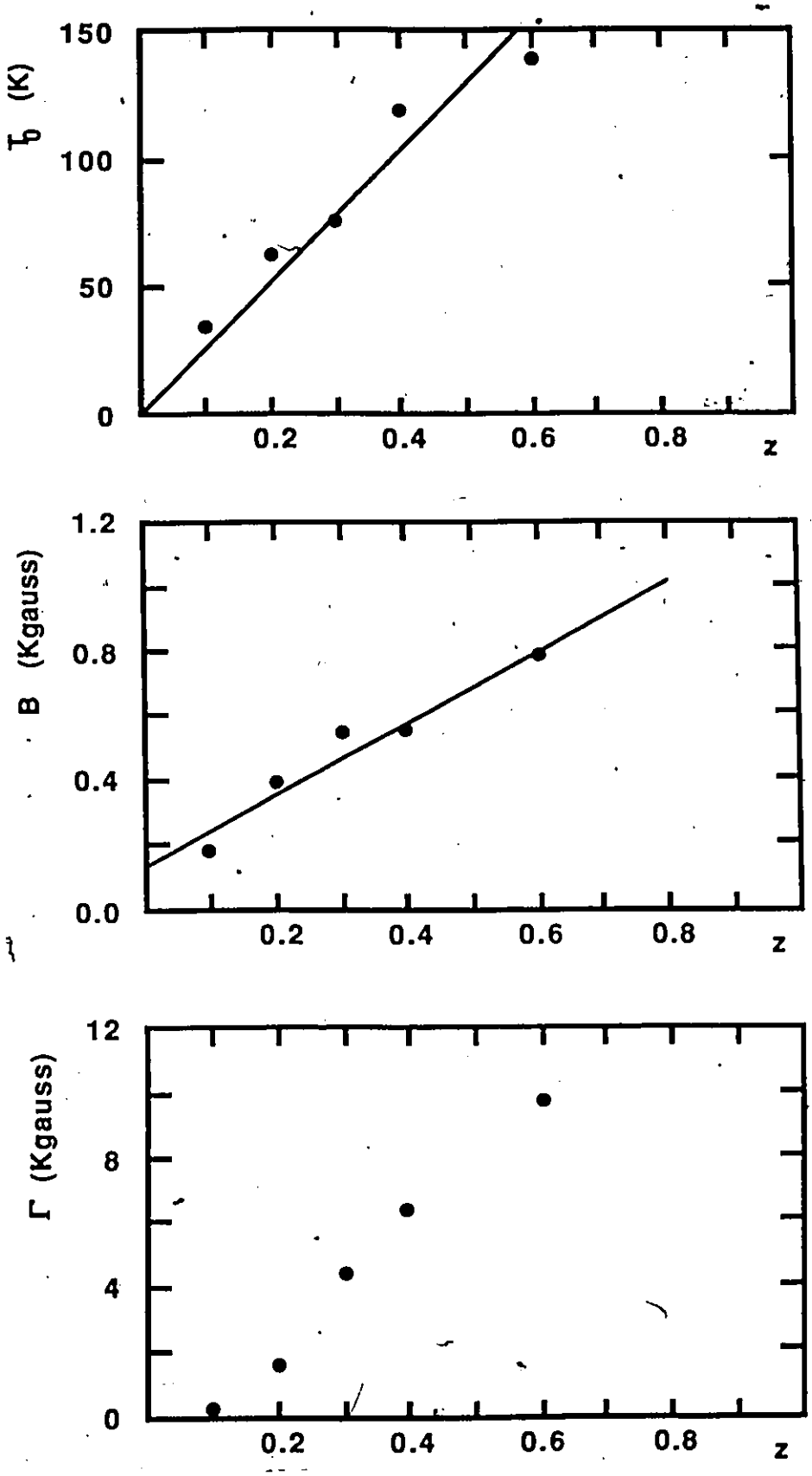

FIGURE 5.24 Values of T_0 , B and Γ versus z Concentration for y=3x Samples.

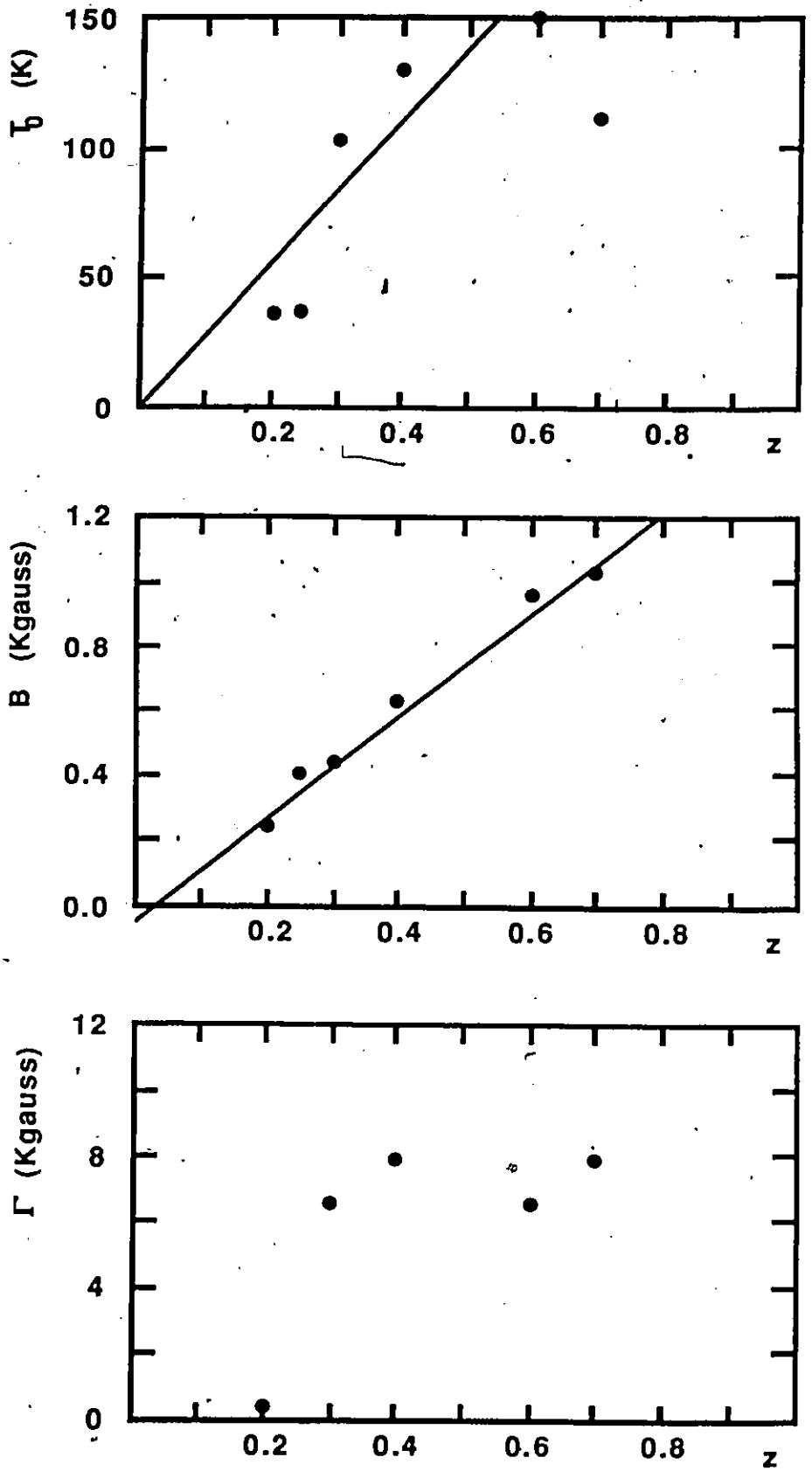

FIGURE 5.25 Values of T_0 , B and Γ versus z Concentration for x=0 Samples.

The final values obtained for the χ^2_υ function ranged between 0.9 and 1.5 which is indicative of a reasonable fit, (104).

The most consistent results were those of the y=0 samples in fig. 5.21. There was more scatter in the values obtained for the other samples. This was likely due to the fact that the larger values of T_A would restrict the available range which could be fitted, more than for the cases with smaller values of T_A. This may be further illustrated by considering the results of the selenide alloy systems, $Cd_xZn_yMn_zSe$ and $Cd_{1-z}Mn_zTe_{1-y}Se_y$ investigated by this research group, (91, 92). In these cases, the temperature where the linewidth became asymmetric occurred at lower values, and the scatter in the constants obtained by the fit was greatly reduced.

The variation of T_o with z shown in fig. 5.21(a) is linear and extrapolates to 0 K for z=0. The other plots of T_o, in figs. 5.22(a) to 5.25(a), display a similar behaviour. However, as was pointed out previously, there is more scatter present and a few points, at high z values, do not follow the straight lines. The variation of T_o with Zn concentration may be examined more clearly by calculating the slope, dT_o/dz, for each set of x:y ratios and plotting the result as a function of y/(y+x), as shown in fig 5.26(a). It can be seen that dT_o/dz increases smoothly with y concentration indicating that T_o increases when Cd is replaced by Zn in the lattice. This is not unexpected since the other magnetic properties, which have already been discussed, behave in the same fashion.

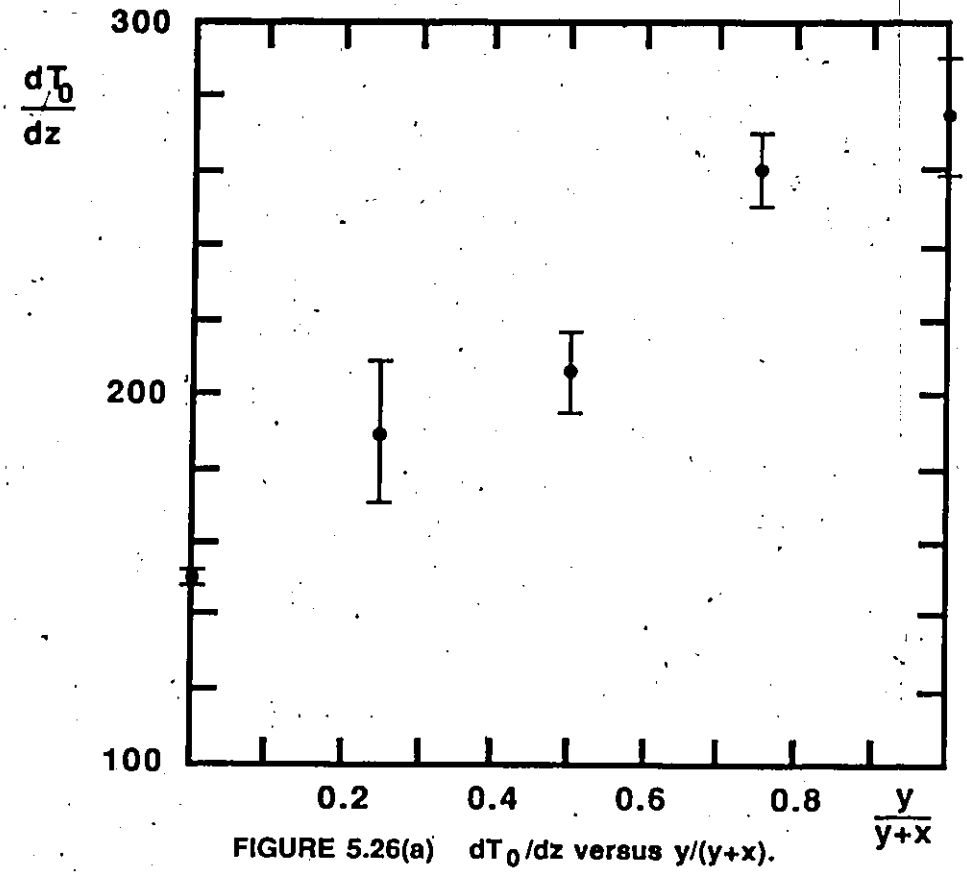

FIGURE 5.26(a) dT_0/dz versus $y/(y+x)$.

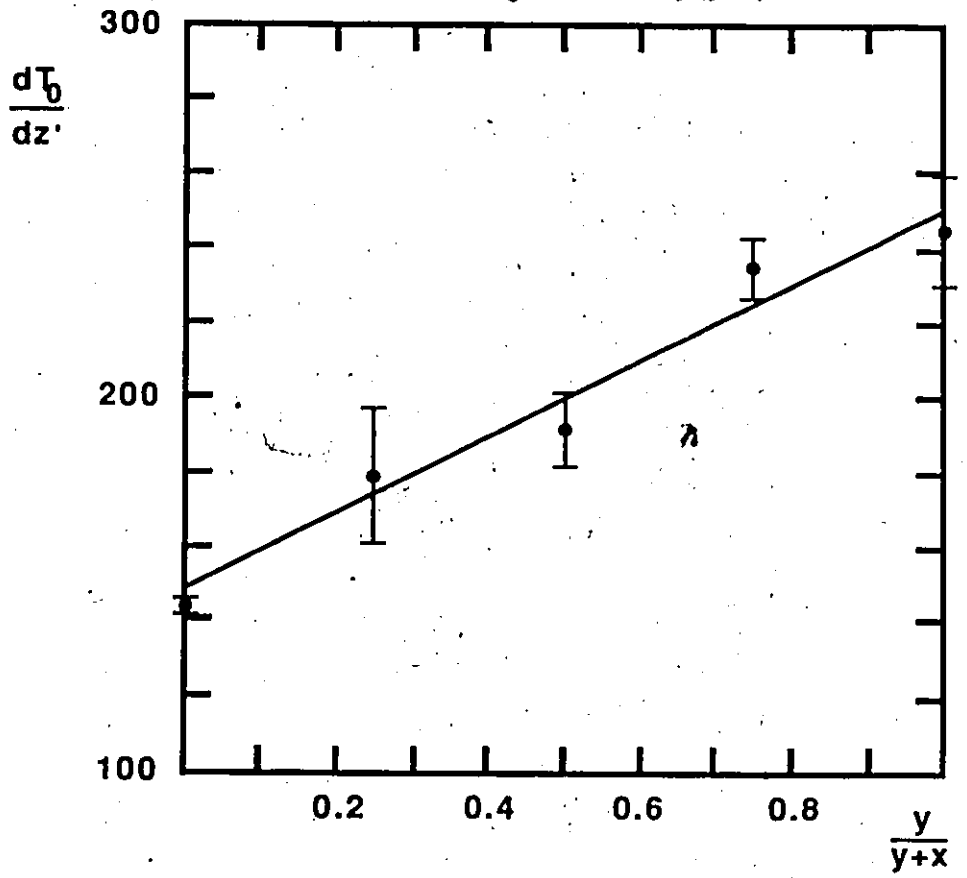

FIGURE 5.26(b). dT_0/dz' versus $y/(y+x)$.

The effects of the lattice parameter may be considered by repeating the above process using an effective value of Mn concentration, $z'=z(a_o/a)^3$, where a_o is the lattice parameter of CdTe and "a" is the lattice parameter of the particular sample. Using eq. 2.7, values of dT_o/dz' were calculated and plotted in fig. 5.26(b). The values plotted in this diagram still show an increase with y indicating that the lattice parameter may not be the only mechanism responsible for the increase in the height of the potential barrier as Zn replaces Cd on the cation sublattice. Some other property, such as electronegativity, (128), whose effect increases as the atomic number of the non-magnetic cation decreases, might explain this more completely.

The results of fig. 5.26(b) suggest that the values of dT_o/dz' obey the following expression;

$$\frac{dT_o}{dz'} = (a' + b'f)$$

with a' and b' constant, and with f=y/(y+x). Integrating this equation yields;

$$T_o = (a' + b'f)z' \qquad (5.7)$$

with the constant of integration going to zero because of the results of figs. 5.21(a) to 5.25(a). Thus, the variation of T_o with concentration could be approximated by a simple expression. Values for the constants in this equation were determined to be as follows;

$$a' = 146 + 5 \text{ K}$$

$$b' = 103 + 8 \text{ K}$$

It is interesting to note that a similar analysis for the $Cd_xZn_yMn_zSe$ alloy system, (92), resulted in a value for b´ which agreed with that quoted above. This would indicate that T_o varies with Zn in the same way for both of these alloy systems.

Considering now figs. 5.21(b) to 5.25(b), one can see that B varies linearly with Mn composition and seem to extrapolate to a non-zero intercept at z=0. The open circles represent values obtained from the slopes in figs. 5.16 to 5.18 which agree very well with the values obtained from eq. 5.6. Taking an average of the intercepts gives a value of approximately 80 gauss with a rather large standard deviation of about 50 gauss. Similar behaviour has been reported for the selenide systems, (91, 92), with a smaller degree of scatter. This finite quantity is smaller than the linewidth for isolated Mn impurities (~250 gauss, ref. 129) which indicates that there must be appreciable exchange narrowing of the ESR line at high temperatures and for the range of concentrations investigated here.

The variation of B with Zn concentrations may be examined in the same manner as was done for T_o. Values for dB/dz were calculated and plotted in fig. 5.27. In this case, no discernible variation could be observed within the limits of the error bars. Repeating this calculation using z´ did not affect this conclusion.

Values of Γ as a function of z were plotted in figs. 5.21(c) to 5.25(c). The degree of scatter was so great, in these cases, that trying to determine how this parameter varied with Zn

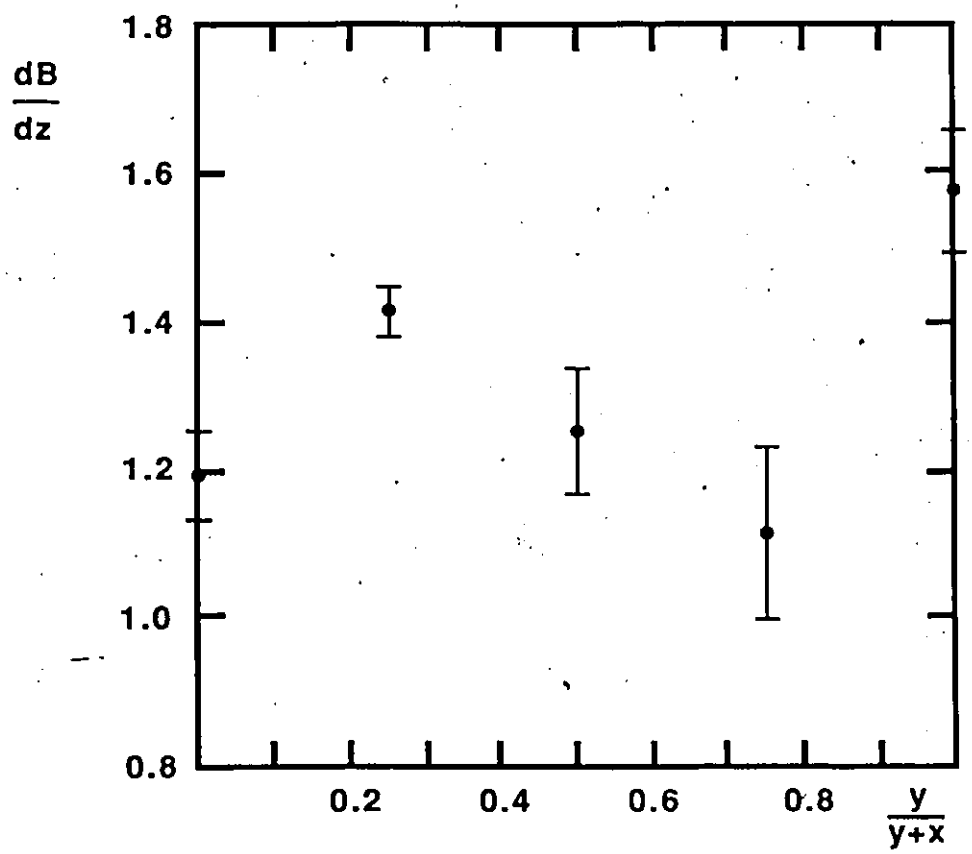

FIGURE 5.27 dB/dz versus y/(y+x).

concentration proved to be inconclusive. Thus only the variation with Mn will be considered. It was mentioned earlier that Γ is a measure of the width of the distribution of local fields. This distribution depends on the degree of randomness or the amount of disorder in the crystal. In alloy systems, the maximum amount of disorder is taken to be proportional to $z(1-z)$, i.e. the degree of randomness is zero for $z=0$ and for $z=1.0$ and a maximum at $z=0.5$. To apply it to the present case, one must multiply this by z to account for the effect of increasing the concentration of magnetic moments. This results in the following expression for Γ;

$$\Gamma = Az^2(z-1) \qquad (5.8)$$

where A is a constant. Note that eq. 5.8 predicts a maximum at $z=2/3$ which is very close to the limits of solid solution for this alloy system. With all of the Γ values plotted together as a function of z in fig. 5.28, it can be seen that the amount of scatter increases as the Mn concentration increases. Thus the points corresponding to the range of concentration in which Γ would be expected to decrease are not reliable enough to confirm. A least squares fit to eq. 5.8 yields;

$$A = 60+2 \text{ Kgauss}$$

The solid line in fig. 5.28 was drawn using this result.

The application of eq. 5.6 to the data has produced good results for the constants, T_o, Γ and B, despite the large amount of scatter. It has been noted that varying the Zn concentration affected the ESR properties more greatly than the susceptibility measurements. This indicated that the shift in the

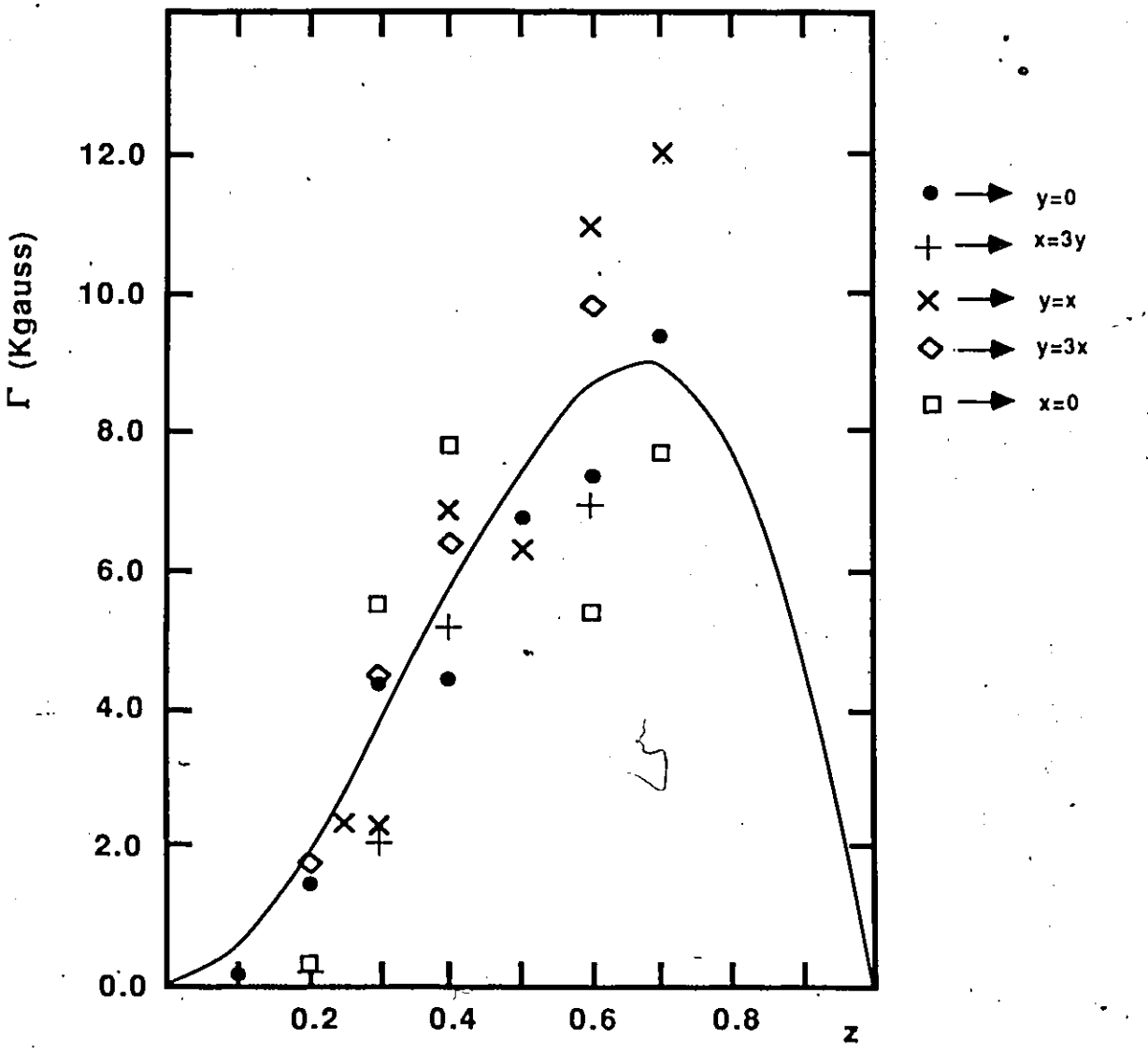

FIGURE 5.28 Γ versus z composition. The solid line represents the results of fitting the data to eq. 5.8.

lattice parameter was not the only factor involved in the case of ESR. The broadness of the lines, especially for the samples with high Zn and Mn concentrations, hindered the analysis. It is clear that more measurements in the temperature range greater than 500 K would be desirable.

CHAPTER 6

CONCLUSIONS

An investigation of some of the properties of the pseudo-ternary alloy, $Cd_xZn_yMn_zTe$, has been presented. Four main types of measurements were performed on this material; the determination of the lattice parameters, magnetic susceptibility, ESR linewidth and the energy gaps. Some of the results from one set of measurements were found to be quite useful in understanding those of another set. Hence, the results of magnetic susceptibility were used in the analysis of the thermal dependence of the energy gap and ESR linewidth. As well, the lattice parameters and the energy gaps were used in the discussion of the exchange interaction.

The ability to manipulate two composition parameters independently of each other, was used to study these properties as the concentration of either the magnetic or a non-magnetic component changed. When the concentration of Mn increased, it was found that the magnetic properties which depend on the strength of the magnetic interaction, also increased. Thus the critical temperatures and Curie-Weiss temperatures determined from measurements of magnetic susceptibility, as well as the ESR linewidths, all increased with z. Other properties which were affected by the Mn concentration are summarized in fig. 6.1. In this figure, an example of each of the measurements obtained from chapters 3 to 5 is sketched for three representative z concentrations. Also included is an example of a corresponding

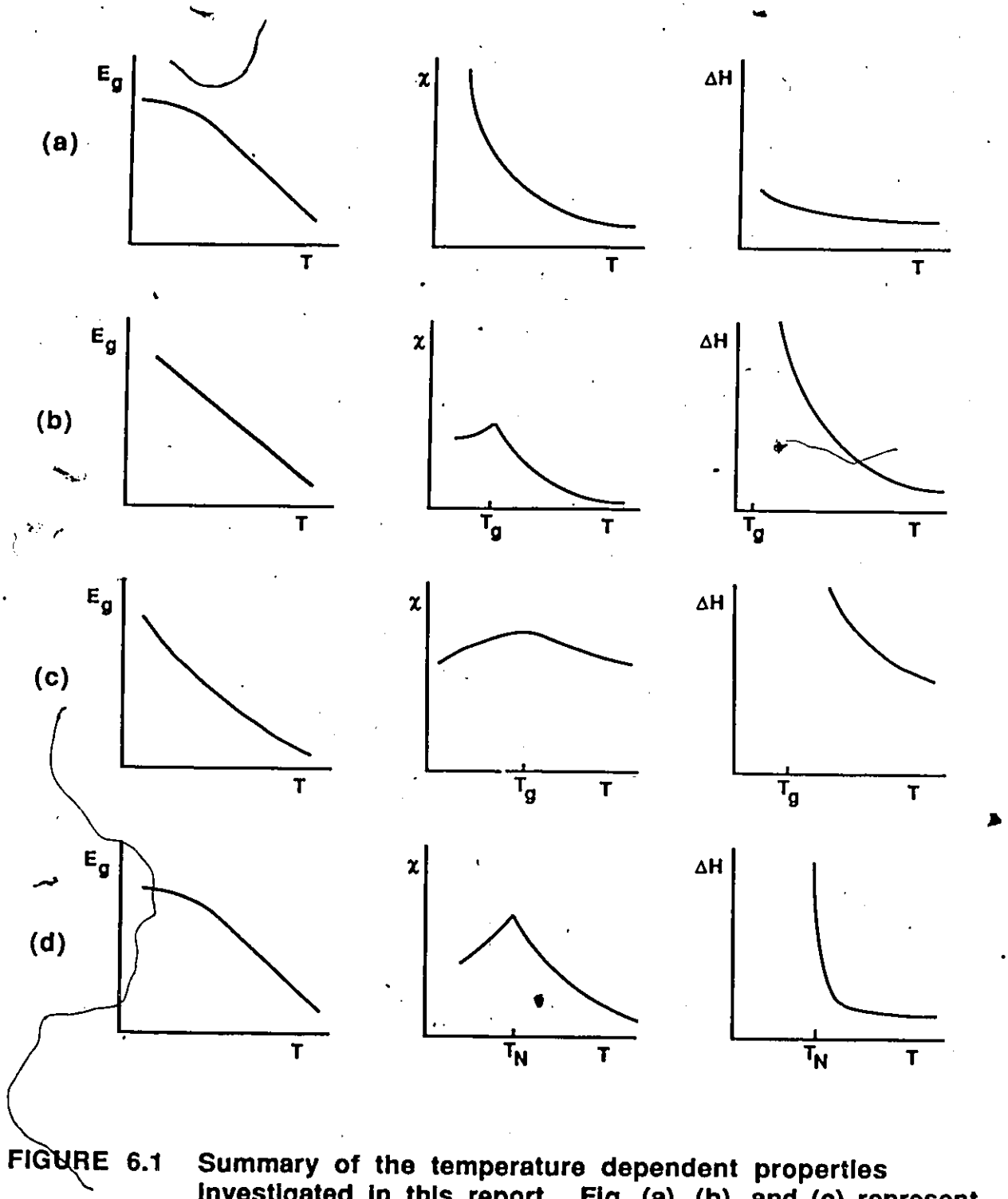

FIGURE 6.1 Summary of the temperature dependent properties investigated in this report. Fig. (a), (b), and (c) represent typical results for samples with z=0.1, 0.4 and 0.7, respectively. The energy gap diagram for Fig. (d) is for a normal non-magnetic semiconductor. The other diagrams in Fig. (d) represents the results for a normal antiferromagnetic material.

measurement for typical antiferromagnetic materials.

For the case of magnetic susceptibility, the example with z=0.1 indicates that there is no transition temperature above 4.2 K, the lowest temperature which could be reached. The example for which z=0.4 shows a very sharp cusp which is associated with the spin glass transition temperature. For z=0.7, the cusp becomes more rounded and now corresponds to a short range antiferromagnetic ordering. Comparing these to the example of MnF_2, (17), in fig. 6.1, indicates that the spin glass case bears the closest resemblance to an antiferromagnetic material.

The results for ESR linewidth in fig. 6.1 show that ΔH increases more rapidly at lower temperatures than at higher. It also becomes too large to measure at temperatures well above the magnetic critical points. This behaviour is very different from that of MnF_2 which gives a good measure of the antiferromagnetic Neel temperature.

The thermal dependence of the the energy gap for z=0.1 is very similar to that of typical non-magnetic semiconductors, figs. 6.1(a) and 6.1(d). When the Mn concentration is increased to 40%, the dependence remains linear down to the lowest temperatures which could be attained indicating that at these low temperatures, the energy gap is larger than what would be expected for ordinary semiconductors. This effect increases as the concentration is further increased so that, with z=0.7, a definite upturn is observed.

Increasing the concentration of the Zn component while

keeping the magnetic concentration constant, showed that the strength of the magnetic effects also increased. It was found that for both T_g and θ, this increase was directly attributable to an increase in the exchange energy which resulted from a decrease in the lattice parameter. This would also be responsible for the increase in the magnetic contribution to the energy gap, since the analysis in chapter 3 was based on the T_g values. The increase in the ESR linewidth with Zn was relatively larger that that observed for the other sets of measurements. It was decided that for this case, the decrease in lattice parameter was not the only factor involved.

Many of the results reported here for $Cd_xZn_yMn_zTe$ alloys were also observed in the other SMSC alloy systems which were mentioned in chapter 1 and investigated by this research group, (91, 92, 114, 115). Unlike the present case, these materials did not have a single crystallographic phase over a very wide range of composition. Consequently much of the phenomena observed at the highest Mn concentration were not seen in these alloys.

REFERENCES

1. J.B. Nelson, D.P. Riley, Proc. Phys. Soc. 57, 160 (1945).

2. R.R. Galazka, Physics of Semiconductors 1978, Conference Series No. 23 (Institute of Physics, London, 1979) p.133.

3. C.K. Williams, T.H. Glisson, J.R. Hauser, M.A. Littlejohn, J. Electronic Mat. 7, 639 (1978)

4. J.A. Gaj, Proc. 15th Int. Conf. Physics of Semiconductrs, Kyoto, (1980)
   J. Phys. Soc. Japan 49 Suppl. A, 797 (1980)

5. J.A. Gaj, R.R. Galazka, M. Nawrocki, Solid State Commun. 25, 193, (1978)

6. J. Stankiewicz, N. Bottka, W. Giriat, Proc. 15th Int. Conf. Physics of Semiconductor, Kyoto, (1980)
   J. Phys. Soc. Japan 49, Suppl. A, 827, (1980)

7. H.L. Frisch, J.M. Hammersley, D.J.A. Welsh, Phys. Rev. 126, 949 (1962)

8. R.A. Abreu, W. Giriat, M.P. Vecchi, Physics Letters, 85A, 399 (1981)

9. V.G. Sredin, M.V. Pashkovskii, Z.S. Vasilina, A.I. Evstigneev, Sov. Phys. Semicond. 7, 1566, (1974)

10. I.N. Borisov, V.V. Mikhailin, P.S. Kireev, S.N. Ivanov, Sov. Phys. Semicond. 4, 1521 (1971)

11. M. Cordona, D.L. Greenaway, Phys. Rev. 131, 98 (1963)

12. D.J. Chadi, J.P. Walter, M.L. Cohen, Phys. Rev. B 5, 3058 (1972)

13. J.P Walter, M.L. Cohen, Phys. Rev. B 1, 2661, (1970)

14. C. Kittel, Introduction to Solid State Physics, Fifth Ed., Chapter 11, p321. Wiley, Toronto, (1976)

15. C. Kittel, Introduction to Solid State Physics, Fifth Ed., Chapter 10, p285. Wiley, Toronto, (1976)

16. F.W. Sears, G.L. Salinger, Thermodynamics, Kinetic Theory and Statistical Thermodynamics, Third Ed., p190, Addison-Wesley, Don Mills, (1975)

17. T. Giebultowicz, W. Minor, H. Kepa, J. Ginter, R.R. Galazka, J. Magn. Magn. Mater. 30, 215 (1982)

18. R.R. Galazka, S. Nagata, P.H. Keesom, Phys. Rev. B 22, 3344 (1980)

19. C. Kittel, Introduction to Solid State Physics, Fifth Ed., Chapter 14, p433. Wiley, Toronto (1976)

20. I.S. Jacobs, C.P. Bean, Fine Particles, Thin Films and Exchange Anisotropy. in Magnetism III, edited by G.T. Rado, H. Suhl. p271. Academic Press, New York, (1963)

21. D.A. Smith, J. Phys. F 4, L266, (1974)

22. P.W. Anderson, Solid State Physics 14, 142 (1963)

23. L. de Seze, J. Phys. C 10, L353 (1977)

24. G.S. Grest, E.G. Gabl, Phys. Rev. Lettl 43, 1182, (1979)

25. S.B. Oseroff, R. Calvo, W. Giriat, Solid State Commun. 35, 539 (1980)

26. C.M. Soukoulis, K. Levin, Phys. Rev. Lett. 39, 581 (1977)

27. D.L. Huber, Phys. Rev. B 6, 3180 (1972)

28. S. Oseroff, R. Calvo, W. Giriat, J. Appl. Phys. 50, 7738 (1979)

29. N. Bloembergen, T.J. Rowland, Phys. Rev. 97, 1679 (1955)

30. N.T. Khoi, J.A. Gaj, Phys. Stat. Sol. (b) 83, K133 (1977)

31. D. McKie, C. McKie, Chrystalline Solids. p208. Nelson, Don Mills, (1980)

32. N.F.M. Henry, H. Lipson, W.A. Wooster, The Interpretation of X-Ray Diffraction Photgraphs. p240, MacMillan & Co. (1951)

33. A. Manoogian, A. Leclerc, Can. J. Phy. 57, 1766 (1979)

34. A. Manoogian, A. Leclerc, Phys. Stat. Sol. (b) 92, K23 (1979)

35. A. Manoogian, Unpublished Results.

36. G. Goodchild, J.C. Woolley, J. Gonzales, Proceedings of the 4th International Conference on Ternary and Multinary Compounds, Tokyo, 1980
Jap. J. Appl. Phys. 19, 123 (1980)

37. S.A. Lopez-Rivera, R.G. Goodchild, O.H. Hughes, J.C. Woolley, B.R. Pamplin, Can. J. Phys. 60, 10 (1982)

38. A. Manoogian, Private Communication

39. P.J. Ford, Contemp. Phys. 23, 141 (1982)

40. A.H. Morrish, The Physical Principles of Magnetism, p106. Krieger, New York, (1980)

41. G. Bastard, C. Rigaux, Y. Guldner, J. Mycielski, A. Mycielski, J. Physique 39, 87 (1978)

42. C.M. Soukoulis, K. Levin, Phys. Rev. B 18, 1429 (1978)

43. CRC. Handbook Of Chemistry and Physics, CRC Press, Boca Raton, Florida

44. F. Keffer, C. Kittel, Phys. Rev. 85, 329 (1952)

45. R. Triboulet, G. Didier, J. Crystal Growth 52, 614 (1981)

46. B.O. Seraphin, Electroreflectance. In Semiconductors and Semimetals, 9, 1 (1972)

47. I. Balslev, Piezooptical Effects. In Semiconductors and Semimetals, 9, 403 (1972)

48. K.L. Shaklee, J.E. Rowe, Appl. Optics 9, 627 (1970)

49. A.H. Morrish, The Phsyical Principles of Magnetism, p46. Krieger, New York. (1980)

50. T.M. Holden, G. Dolling, V.F. Sears, J.K. Furdyna, G.Giriat, Sol. State Commun. 40, 281, (1981)

51. T. Giebultowicz, H. Kepa, B. Buras, K. Clausen, R.R. Galazka, Sol. State Commun. 40, 499, (1981)

52. J.A. Mydosh, Spin Glasses: The Experimental Situation. From Magnetism in Solids, Some Current Topics, Proceedings of the Twenty-second Scottish Universities Summer School in Physics. Edited by A.P. Cracknell and R.A. Vaughan, p85 (1981)

53. S.P. McAlister, J.K. Furdyna, W. Giriat, Phys. Rev. B 29, 1310 (1984)

54. S.B. Oseroff, Phys. Rev. B 25, 6584 (1982)

55. M.A. Novak, O.G. Symko, D.J. Zheng, S. Oseroff, J. Appl. Phys. 57, 3518 (1985)

56. M.F. Sykes, J.W. Essam, Phys. Rev. 133, A310 (1964)

57. S. Fujiki, T. Suenaga, S. Katsura, J. Magn. Magn. Mater. 31-34, 1457 (1983)

58. C. Domb, N.W. Dalton, Proc. Phys. Soc. 89, 859 (1966)

59. D. Stauffer, Am. J. Phys. 45, 1001 (1977)

60. K. Levin, C.M. Souloulis, G.S. Grest, J. Appl. Phys. 50, 1695 (1979)

61. G. Bhat, A. Mody, A. Ragwala, Phys. Stat. Sol. (b) 121, K135 (1984)

62. S. Oseroff, F. Acker, Solid State Commun. 37, 19 (1980)

63. M. Escorne, A. Mauger, Phys. Rev. B 2, 4674 (1982)

64. G.D. Khattak, C.C. Amarasekara, S. Nagata, R.R. Galazka, P.H. Keesom, Phys. Rev. B 23, 3533 (1981)

65. S. Nagata, R.R. Galazka, D.P. Mullin, H. Akbarzadeh, G.D. Khattak, J.K. Furdyna, P.H. Keesom, Phys. Rev. B 22, 3331 (1980)

66. G. Toulouse, Lecture Notes in Physics 149, 166 (1981)

67. R.R. Galazka, Lecture Notes In Physics 152, 294 (1981)

68. H. Savage, J.J. Rhyne, R. Holm, J.R. Cullen, C.E. Carroll, E.P. Wohlfart, Phys. Stat. Sol. (b) 58, 685 (1973)

69. M.A. Novak, S. Oseroff, O.G. Symko, Physica 107B, 313 (1981)

70. U. Sonderman, J. Magn. Magn. Mater. 2, 216 (1976)

71. J. Souletie, R. Tournier, J. Low Temp. Phys. 1, 95, (1969)

72. J. Ginter, J. Kossut, L. Swierkowoski, Phys. Stat. Sol. (b) 96, 735 (1979)

73. P. Oelhafen, M.P. Vecchi, J.L. Feeouf, V.L. Moeruzzi, Solid State Commun. 44, 1547 (1982)

74. A.H. Morrish, The Physical Principles of Magnetism, p464. Krieger, New York, (1980)

75. G. Bastard, J.A. Gaj, R. Planel, C. Rigaux, J. Physique Colloque 41, C5-247 (1980)

76. G. Bastard, C. Lewiner, Phys. Rev. B 20, 4256 (1979)

77. C. Lewiner, J.A. Gaj, G. Bastard, J. Physique Colloque 41, C5-289 (1980)

78. C.A. Taft, R.M. Xavier, S. Lara, J. Physique Colloque 41, C5-375 (1980)

79. A.A. Abrikosov, Adv. Phys. 29, 869 (1980)

80. N.B. Brandt, V.V. Moshchalkov, Adv. Phys. 33, 193 (1984)

81. M. Escorne, A. Mauger, R. Triboulet, J.L. Tholence, Physica 107B, 309 (1981)

82. Z. Gulacsi, M. Gulacsi, M. Crisan, J. Magn. Magn. Mater. 40, 247 (1984)

83. C.E.T. Goncalves da Silva, L.M. Falicov, J. Phys. C 5, 63 (1972)

84. G.A. Sawatzky, W. Geertsma, C. Haas, J. Magn. Magn. Mater. 3, 37 (1976)

85. W. Geertsma, C. Haas, G.A. Sawatzky, G. Vertogen, Physica 86-88B, 039 (1977)

86. Y. Shapira, S. Foner, D.H. Ridgley, K. Dwight, A. Wold, Phys. Rev. 30, 4021 (1984)

87. J.S. Smart, Evaluation of Exchange Interactions From Experimental Data. From Magnetism III. Edited by G.T. Rado and H. Suhl. p63. Academic Press, New York. (1963)

88. A.C. Rose-Innes, E.H. Rhoderick, Introduction to Superconductivity, Second Edition, p170. Pergamon Press, Toronto. (1978)

89. A.H. Morrish, The Physical Principles of Mangetism, p78. Krieger, New York. (1980)

90. R.E. Kremer, J.K. Furdyna, Phys. Rev. B31, 1 (1985)

91. S. Chehab, Ph.D. Thesis, University of Ottawa

92. S. Manhas, Master's Thesis, University of Ottawa

93. J.W. Searl, R.C. Smith, S.J. Wyard, Proc. Phys. Soc. 78, 1174 (1961)

94. J.W. Searl, R.C. Smith, S.J. Wyard, Bullryin Ampere, fasc, special, 9th year, p236 (1960)

95. J.W. Searl, R.C. Smith, S.J. Wyard, Proc. Phys. Soc. 74, 491 (1959).

96. S.B. Oseroff, R. Calvo, Z. Fisk, F. Acker, Phys. Letters 80A, 311 (1980)

97. E. Dormann, V. Jaccarino, Phys. Letters, 48A, 81 (1974)

98. D.J. Webb, S.M. Bhagat, J.K. Furdyna, J. Appl. Phys. 55, 2310 (1984)

99. S.B. Bhagat, M.L. Spano, J.N. Lloyd, Solid State Comm. 38, 261, (1981)

100. W.Y. Ching, D.L. Huber, Phys. Rev. B 26, 6164 (1982)

101. A.M. Stoneham, Rev. Mod. Phys. 41, 82 (1969)

102. A. Manoogian, B.W. Chan, R. Brun del Re, T. Donofrio, J.C. Woolley, J. Appl. Phys. 53, 8934 (1982)

103. P.R. Bevington, Data Reduction and Error Analysis for the Physical Sciences, p204. McGraw-Hill Book Company, Toronto. (1969)

104. P.R. Bevington, Data Reduction and Error Analysis for the Physical Sciences, p187. McGraw-Hill Book Company, Toronto. (1969)

105. R.E. Kremer, J.K. Furdyna, J. Magn. Magn. Mater. 40, 185 (1983)

106. N. Bottka, J. Stankiewicz, W. Giriat, J. Appl. Phys. 52(b), 4189 (1981)

107. B.S. Sundersheshu, T. Kendelwicz, Physics of Semiconduction Compounds. Proceedings of the XI Conference, Jaszowiec, Poland. 26 April - 3 May 1981 (Warsaw, Poland: Polish Acad. Sci. 1982) p213.

108. B. Montegu, A. Laugier, R. Triboulet, J. Appl. Phys. 56, 3061 (1984)

109. H-h. Chou, H.Y. Fan, Phys. Rev. B 10, 901 (1974)

110. T. Kendelewicz, Physics of Semiconductiong Compounds, p253. Jaszowiec, Poland, (1980)

111. S. Alexander, J.S. Helman, I. Balberg, Phys. Rev. B 13, 304 (1976)

112. T. Kasuya, A. Kondo, Solid State Commun. 14, 249 (1974)

113. P. Haasen, Physical Metallurgy, p133. Cambridge University Press, New York. (1974)

114. M. Quintero, Ph.D. Thesis, University of Ottawa

115. C. Gnanatissa, Master's Thesis, University of Ottawa

116. M. El Amrani, J.P. Lascaray, J. Diouri, Solid State Comm. 45, 351 (1983)

117. E.I. Grancharova, J.P. Lascaray, J. Diouri, J. Allegre, Phys. Stat. Sol. (b) 113, 503 (1982)

118. M. Ayadi, P. Nordblad, J. Ferre, A. Mauger, R. Triboulet. Preprint, (1985)

119. S. Oseroff, F.G. Gandra, J. Appl. Phys. 57, 3421 (1985)

120. A.W. Simpson, Phys. Stat. Sol. 40, 207 (1970)

121. H.H. Heikens, R.S. Kuindersma, C.F. Van Bruggen, C. Haas, J. Magn. Magn. Mater. 8, 130 (1978)

122. D. Fiorani, S. Viticoli, J. Magn. Magn. Mater. 49, 83 (1985)

123. K. Zanio, Semiconductors and Semimetals 13, 91 (1978)

124. J. Lambe, C Kikuchi, Phys. Rev. 119, 1256 (1960)

125. H.A. Sayad, S.M. Bhagat, Phys. Rev. B 31, 591 (1985)

126. See for example; S.E. Barnes, Phys. Rev. B 30, 3944 (1984)

127. M.N. Aliev, L.R. Tagirov, Phys. Stat. Sol. (b) 127, K61 (1985)

128. K. Zanio, Semiconductors and Semimetals 13, 62 (1978)

129. H. Kimmel, Z. Naturforsch. 18a, 650 (1963)

130. J.K. Furdyna, J. Appl. Phys. 53, 7637 (1982)

131. J.A. Gaj, J. Ginter, R.R. Galazka, Phys. Stat. Sol. (b) 89, 655 (1978)

132. J.K. Furdyna, J. Vac. Sci. Technol. 21, 220 (1982)

133. M. Grynberg, Physica 117B & 118B, 461 (1983)

134. T. Dietl, Proc. O.J.I. Int. Seminar on Application of High Magn. Field in Phys. of Semicond. and Magn. Mat., Hakone 1980, Springer.
Solid State Science 24, 344 (1981)

135. A.P. Young, J. Stat. Phys. 34, 871 (1984)
K.H. Fischer, Phys. Stat. Sol. (b) 116 (1983)
J.A. Mydosh, J. Magn. Magn. Mater. 7, 237 (1978)
D. Chowdhury, A Mookerjee, Physics Reports 114, 1 (1984)

136. B.R. Coles, J. Magn. Magn. Mater. 15-18, 103 (1980)
J.A. Mydosh, J. Magn. Magn. Mater. 15-18, 99 (1980)
G. Toulouse, Physica 109B & 110B, 1912 (1982)
J. Tholence, Physica 126B, 157 (1984)
M. Mezard, G. Parisi, N. Sourlas, G. Toulouse, M. Virasoro, Phys. Rev. Lett. 52, 1156 (1984)

137. J.K. Furdyna, W. Giriat, D.F. Mitchell, G.I. Sproule, J. Sol. Stat. Chem. 46, 349 (1983)

138. M.M. Moriwaki, R.Y. Tao, R.R. Galazka, W.M. Becker, J.W. Richardson, Physica B&C 117-118, pt. 1, 467 (1983)

139. Y.R. Lee, A.K. Ramdas, Solid State Comm. 51, 861 (1984)

140. P.H. Keesom, private communication.

141. J. Diouri, J.P. Lascaray, M. El Amrani, Phys. Rev. B 31, 7995 (1985)

142. B.E. Larson, K.C. Haas, H. Ehrenreich, A.E. Carlsson, Solid State Commun. 56, 347 (1985)

143. U. Debska, M. Dietl, G. Grabecki, E. Janik, E. Kierzek-Pecold, M. Klimkiewicz, Phys. Stat. Sol (a) 64, 707 (1981)

144. M. Matlak, A. Ramakanth, K. Skrobis, Z. Phys. B 48, 227 (1982)

145. Y.P. Varshni, Physica 34, 149 (1967)